A study of amorphous transition metal oxide films

Himanshu Jain

A thesis submitted for the degree of

Doctor Of Philosophy

at the

University Of Oxford

Department Of Chemistry, Inorganic Chemistry Laboratory



Michaelmas 2020

Contents

Contents i

List of Figures xi

List of Tables xix

Abstract xxiii

Extended abstract xxv

Acknowledgments xxix

Dedication xxxv

Declaration xxxvii

List of Abbreviations xxxix

List of Symbols xlv

List of Materials lvii

1 Motivation and overview 1

1.1 Introduction 1

1.2 Transparent oxide films: commercial and environmental context 1

1.2.A Security of supply considerations for indium 8
1.3 Mandate for the academic research community, and corresponding aspects of this study 9
1.4 This study 10
1.4.A Introduction 10
1.4.B Operational aspects 10
1.4.C Interdisciplinary underpinnings 12
1.4.D Timeliness 15
1.5 Overview of chapters 16
1.5.A Introduction 16
1.5.B Chapter 1 entitled 'Motivation and overview' 16
1.5.C Chapter 2 entitled 'Literature survey' 16
1.5.D Chapter 3 entitled 'Film deposition: design of experiment, sputtering, and the substrate holder cum sputter flux collimator array' 17
1.5.E Chapter 4 entitled 'Materials, methods, and analysis frameworks' 18
1.5.F Chapter 5 entitled 'The sub-plantation layer' 19
1.5.G Chapter 6 entitled 'The thin-film layer' 20
1.5.H Chapter 7 entitled 'Conclusions and scope for future work' 21
1.5.I Appendix A entitled 'Elements of analysis I: refinement and modeling of experimental data' 22
1.5.J Appendix B entitled 'Elements of analysis II: calculations based on experimental data' 22
1.6 Original contributions of this thesis 23

2 Literature survey **25**

2.1 Introduction . . . 25

2.2 Amorphous oxide semiconductors . . . 25

2.2.A Introduction . . . 25

2.2.B Binary oxides . . . 26

2.2.C Ternary and quaternary oxides . . . 28

2.3 Transition metal oxide film deposition . . . 30

2.3.A Introduction . . . 30

2.3.B General considerations . . . 31

2.3.C Various approaches . . . 31

2.3.C.1 Introduction . . . 31

2.3.C.2 Sol-Gel . . . 32

2.3.C.3 Spray Pyrolysis . . . 32

2.3.C.4 Pulsed Laser Deposition . . . 33

2.3.C.5 Sputtering . . . 34

2.4 The sub-plantation layer: film-substrate adhesion . . . 36

2.4.A Introduction . . . 36

2.4.B Commercial and technological significance . . . 36

2.4.C Transition metal oxide films . . . 37

2.5 Design of experiment studies on sputtered films . . . 40

2.5.A Introduction . . . 40

2.5.B Evolution of opto-electronic and mechanical properties of transition metal oxide films . . . 40

2.5.B.1 Deposition factors dependence . . . 40

2.5.B.2 Post deposition mechanical stressing dependence . . . 42

2.5.C Epilogue . . . 44

2.6 New transparent conducting oxide film development 44
2.6.A Introduction 44
2.6.B Primary goal 44
2.6.C Comparison: present vs published results 46

3 Film deposition: design of experiment, sputtering, and the substrate holder cum sputter flux collimator array 49

3.1 Introduction 49
3.2 Design of experiment methodology 50
3.2.A Introduction 50
3.2.B One factor at a time experimentation 51
3.2.C Design of experiment: applicable considerations 52
3.2.D Linear modeling and response surface analysis 53
3.2.E Design of experiment: this study 55
3.3 Deposition of semiconducting amorphous transition metal oxide films 57
3.3.A Introduction 57
3.3.B Radio frequency magnetron sputtering 58
3.3.C Amorphous films: adatom mobility on substrate . . . 61
3.4 Angular distribution of sputtered material flux 62
3.4.A Introduction 62
3.4.B At target: the cosine distributions 62
3.4.C At substrate 62
3.4.D The sputter flux collimator 65
3.4.D.1 Qualitative description 65
3.4.D.2 Quantitative description 66
3.5 The substrate holder cum sputter flux collimator array: high-throughput conduct of a designed experiment 72

3.5.A Introduction . . . 72
3.5.B Design considerations . . . 73
3.5.C Engineering designs . . . 75
3.5.D Deployment . . . 76
3.5.E Versatility . . . 76

4 Materials, methods, and analysis frameworks 81

4.1 Introduction . . . 81
4.2 Film deposition: radio frequency magnetron sputtering . . . 82
4.2.A Introduction . . . 82
4.2.B Substrate preparation protocol . . . 83
4.2.C Film deposition protocol . . . 83
4.3 Film layer structure: x-ray reflectometry . . . 86
4.3.A Introduction . . . 86
4.3.B Motivation . . . 86
4.3.C Theory and schema . . . 87
4.4 Film opto-electronic properties: spectroscopic ellipsometry . . . 91
4.4.A Introduction . . . 91
4.4.B Motivation . . . 91
4.4.C Theory and schema . . . 92
4.4.D Amorphous semiconducting films: oscillator models . . . 95
4.4.D.1 tauc-lorentz . . . 96
4.4.D.2 drude . . . 96
4.5 Film electronic properties: AC field Hall effect . . . 97
4.5.A Introduction . . . 97
4.5.B Motivation . . . 97
4.5.C Theory . . . 98
4.5.C.1 DC Hall effect technique . . . 98

4.5.C.2 DC Hall effect technique: limitations 101
4.5.C.3 AC field Hall effect measurements 102
4.5.D The absolute temperature dependence of conduction electron mobility: ionized impurity scattering 104
4.5.D.1 The Brooks-Herring model 106
4.5.E Measurement: practical aspects 108

5 The sub-plantation layer 113
5.1 Introduction 113
5.2 Observation of bi-layer sputtered transition metal oxide films 114
5.3 The film layer structure models 116
5.4 Refinement of film layer structures 116
5.5 Physical properties of film layers: trends 122
5.5.A Introduction 122
5.5.B The single-layer films 122
5.5.C The bi-layer films 124
5.5.C.1 Introduction 124
5.5.C.2 The thin-film layer 125
5.5.C.3 The sub-plantation layer 126
5.6 Film opto-electronic properties I 126
5.6.A Introduction 126
5.6.B Information flow among characterization techniques . 127
5.6.C Experimentally measured and modeled transmission fraction 127
5.7 Sub-plantation during film deposition 127
5.7.A Introduction 127
5.7.B The pressure distance product dependence of sub-plantation 128

5.7.C Assertion . . . 132
5.8 Film growth from collimated sputtered material flux . . . 134
5.8.A Introduction . . . 134
5.8.B Angular distribution of sputtered material flux . . . 135
5.8.C Modulation of film deposition-rate via the sputter flux collimator . . . 136
5.8.D Epilogue . . . 141
5.8.D.1 The phase-diagram for sub-plantation layer formation . . . 142
5.9 Manifestation and observation of sub-plantation layer: role of experimentation choices . . . 149
5.9.A Introduction . . . 149
5.9.B Substrate: Corning Eagle XG glass . . . 150
5.9.C Collimation: sputter flux collimator . . . 150
5.10 Bonafides of the sub-plantation layer . . . 150
5.10.A Introduction . . . 150
5.10.B Dimensional analysis . . . 152
5.10.C Response surface analysis . . . 156

6 The thin-film layer 163

6.1 Introduction . . . 163
6.2 Amorphous Si doped In_2O_3−$(ZnO)_3$ films . . . 164
6.2.A Introduction . . . 164
6.2.B X-Ray diffractograms . . . 164
6.2.C Amorphous In_2O_3−$(ZnO)_k$ (k = 0, 1, 2, 3, …) material system . . . 164
6.2.D Si doping . . . 166
6.3 Film opto-electronic properties II . . . 169

6.3.A Introduction . . . 169
6.3.B The transmission fraction of transparent conducting oxide films: general considerations . . . 170
6.3.C The transmission fraction of Si doped In_2O_3−$(ZnO)_3$ films . . . 171
6.3.D Optical and electrical determination of room-temperature electronic properties . . . 180
6.3.E The refractive index and the extinction coefficient . . . 180
6.4 Film electronic state I: compensation . . . 187
6.4.A Introduction . . . 187
6.4.B The absolute temperature dependence of conduction electron mobility . . . 187
6.4.C The Brooks-Herring analysis of ionized impurity scattering . . . 188
6.4.D The compensation ratio . . . 192
6.4.D.1 The absolute temperature dependence . . . 192
6.4.D.2 The oxygen content dependence . . . 192
6.5 Film electronic state II: oxygen induced progress towards a metal . . . 197
6.5.A Introduction . . . 197
6.5.B Ioffe-Regel and Mott analyses . . . 198
6.6 Response surface analysis . . . 200
6.6.A Introduction . . . 200
6.6.B Film electronic properties . . . 201
6.6.C Thin-Film layer physical properties . . . 205

7 Conclusions and scope for future work 213

7.1 Introduction . . . 213

7.2 A ready-reckoner 213
7.3 Epilogue 216
7.4 Scope for future work 217
7.4.A Introduction 217
7.4.B Future work: programme development 217
7.4.C Future work: potential research themes 218
7.4.C.1 Nature of amorphous state 218
7.4.C.2 Nature of electronic state 218
7.4.C.3 Data interpretation 226
7.4.C.4 Film-Substrate adhesion 226
7.4.C.5 Aerospace applications 229
7.4.C.6 Biomedical applications 229
7.4.C.7 Machine-Learning for automation of experimentation 232

Appendices **235**

Appendix A Elements of analysis I: refinement and modeling of experimental data **237**

A.1 Introduction 237
A.2 X-Ray reflectometry: further elements of analysis 237
A.3 Spectroscopic ellipsometry: further elements of analysis . . . 238
A.3.A Introduction 238
A.3.B Gaussian oscillator model 238
A.3.C Corning Eagle XG Glass substrate 239
A.3.C.1 Introduction 239
A.3.C.2 Transmission Fraction 239
A.3.C.3 Refractive index and extinction coefficient . . 240

Appendix B Elements of analysis II: calculations based on experimental data **243**

B.1 Introduction 243

B.2 Linear model of layer physical or electronic properties 244

B.2.A Introduction 244

B.2.B Computer program 244

B.3 The total donor concentration and total acceptor concentration according the Brooks-Herring model for ionized impurity scattering 250

B.3.A Introduction 250

B.3.B Computer program 250

Bibliography **255**

List of Figures

1.1 Historical and projected trends and milestones of the photovoltaic market. (From published literature.) 6

1.2 Historical and projected trends and milestones of the transparent display market. (From published literature.) 7

1.3 Geographical distribution and price history of In. (From published literature.) 11

1.4 Aspects integral to new materials R&D. 14

2.1 The orbital drawings of energy of minimum of conduction band in conventional covalent semiconductors (left), and in ionic oxide semiconductors (right). (From published literature.) 30

2.2 Film layer structures used for modeling of spectroscopic ellipsometry data. (From published literature.) 39

2.3 Calculated free carrier absorptance of films as functions of conduction electron concentration and conduction electron mobility. (From published literature.) 46

2.4 Electronic properties of the Si doped In_2O_3−$(ZnO)_3$ films per the present study, compared to those of material system comprised of In, Ga, Zn, and O films per published studies. (From published literature.) 48

3.1 Navigation of hypothetical contour plot on basis of OFAT vs DOE principles. 52

3.2 Formal considerations and representation of a three-factor two-level designed experiment. 54

3.3 The three-factor two-level with center-point designed experiment employed in this study. 58

3.4 The angular distribution of material flux as emerges from a point on the target during sputtering. 63

3.5 Description (qualitative) of sputtering chamber, and of effect of deployment of sputter flux collimator on angular distribution at substrate of sputtered material flux. 67

3.6 Description (quantitative) of substrate side with sputter flux collimator, and of angular distribution of sputtered material flux, as obtains during collimated sputtering. 68

3.7 Radial dependence of maximum angle of incidence of sputtered material flux received at given radial location on substrate from SFC aperture. 71

3.8 Engineering drawings of the substrate holder cum sputter flux collimator array. 75

3.9 Engineering drawings of the shield as accompanies the substrate holder cum sputter flux collimator array. 76

3.10 Photographs of substrate holder cum sputter flux collimator array post film deposition via radio frequency magnetron sputtering. 77

3.11 Deployment of substrate holder cum sputter flux collimator array and shield in sputtering chamber of radio frequency magnetron sputtering equipment. 78

3.12 Canonical descriptive list showing the designed experiment of the present study, and other designed experiments that are accessible immediately via the substrate holder cum sputter flux collimator array. 79

4.1 Schema for specular reflection x-ray reflectometry. 89

4.2 Information content of a Kiessig fringes profile recorded via x-ray reflectometry. 90

4.3 Schema for spectroscopic ellipsometry. 93

4.4 Practical aspects of the Hall effect measurements as conducted for the present study. 110

5.1 Experimentally recorded (via x-ray reflectometry) Kiessig fringes profile of Si doped In_2O_3−$(ZnO)_3$ films. 117

5.2 The fourier transform of the experimentally recorded Kiessig fringes profile of Si doped In_2O_3−$(ZnO)_3$ films. 118

5.3 The layer structures (single-layer and bi-layer) arrived upon on basis of fourier transform of experimentally recorded Kiessig fringes profile of Si doped In_2O_3−$(ZnO)_3$ films. 119

5.4 Experimentally recorded (via x-ray reflectometry), and modeled Kiessig fringes profile of ISZO films. 121

5.5 Portion (expanded) of the ready-reckoner presented in figure 7.1, showing information-flow between the various independent characterizations, and the estimations (physical or electronic property) that they enable. 129

5.6 Experimentally measured and thence modeled energy or wavelength of light dependence of transmission fraction of film-substrate-combine. 130

5.7 Experimentally measured DC target-potential as developed during radio frequency magnetron sputtering deposition of Si doped $In_2O_3-(ZnO)_3$ films. 133

5.8 Suggested phase-diagram for bonafide sub-plantation layer manifestation. 151

5.9 The dimensionless group for P_{RF} dependence of sub-plantation layer physical properties. 158

5.10 The pareto plots of linear models (respective) for room-temperature physical properties of sub-plantation layer of Si doped $In_2O_3-(ZnO)_3$ films. 159

5.11 The contour plots — at bottom-plane, center-plane (horizontal), and top-plane of experiment design — of linear model of room-temperature physical properties of sub-plantation layer of Si doped $In_2O_3-(ZnO)_3$ films. 161

6.1 Experimentally measured room-temperature x-ray diffraction profiles of Si doped $In_2O_3-(ZnO)_3$ films. 165

6.2 Structural and electronic properties of homologous series of $In-Zn-O$ material system material system from perspective of transparent conductive applications. (From published literature.) 168

6.3 Experimentally measured wavelength of light dependence of room-temperature transmission fraction of Si doped $In_2O_3-(ZnO)_3$ films. 172

6.4 Representative maximum acceptable sheet resistance as a function of touchscreen size. (From published literature.) . . 178

6.5 Contour-plots of skin depth and resistivity in the conduction electron mobility and conduction electron concentration region relevant for Si doped In_2O_3−$(ZnO)_3$. 179

6.6 Experimentally measured and fitted energy dependence of SE Ψ-parameter and of SE Δ-parameter for Si doped In_2O_3−$(ZnO)_3$ films. 184

6.7 Modeled room-temperature energy dependent refractive index and extinction coefficient of Si doped In_2O_3−$(ZnO)_3$ film layer(s). 186

6.8 Experimentally measured absolute temperature dependences of electronic properties of Si doped In_2O_3−$(ZnO)_3$ films. . . . 189

6.9 Estimation of absolute temperature dependences of total donor concentration, total acceptor concentration, and compensation ratio for Si doped In_2O_3−$(ZnO)_3$ films, on basis of Brooks-Herring model of ionized impurity scattering. 193

6.10 The sub-gap density of states of the amorphous doped material system comprised of In, Zn, and O material systems. . . . 195

6.11 Determination of Tauc gap energy of Si doped In_2O_3−$(ZnO)_3$ films. 197

6.12 The absolute temperature dependences of Ioffe-Regel parameter for Si doped In_2O_3−$(ZnO)_3$ films. 200

6.13 Locations, within experiment design, of those Si doped In_2O_3−$(ZnO)_3$ films that presented electronic properties feasible for measurement. 202

6.14 The pareto plots of linear models for room-temperature electronic properties of Si doped In_2O_3−$(ZnO)_3$ films. 204

6.15 Scheme for contour plots of electronic properties of Si doped In_2O_3−$(ZnO)_3$ films, presenting detailed layout of front-plane, of the center-plane (vertical), and of the back-plane of experiment design. 205

6.16 The contour plots — at front-plane, center-plane (vertical), and back-plane of experiment design — of linear model of room-temperature conduction electron concentration, for Si doped In_2O_3−$(ZnO)_3$ films. 206

6.17 The contour plots — at front-plane, center-plane (vertical), and back-plane of experiment design — of linear model of room-temperature conduction electron mobility, for Si doped In_2O_3−$(ZnO)_3$ films. 207

6.18 The contour plots — at front-plane, center-plane (vertical), and back-plane of experiment design — of linear model of room-temperature resistivity, for Si doped In_2O_3−$(ZnO)_3$ films. 208

6.19 The contour plots — at front-plane, center-plane (vertical), and back-plane of experiment design — of linear model of room-temperature Ioffe-Regel parameter, for Si doped In_2O_3−$(ZnO)_3$ films. 209

6.20 The pareto plots of linear models (respective) for room-temperature physical properties of Si doped In_2O_3−$(ZnO)_3$ films. 210

6.21 The contour plots — at bottom-plane, center-plane (horizontal), and top-plane of experiment design — of linear model of room-temperature physical properties of thin-film layer of Si doped In_2O_3−$(ZnO)_3$ films. 211

7.1 A ready-reckoner (ten-thousand-foot-view walk through) this thesis. 214

7.2 The deposition temperature dependence of crystalline fraction in indium sesquioxide films. (From published literature.) 221

7.3 Possible representation of electrical conduction through the In_2O_3−$(ZnO)_k$ (k = 0, 1, 2, 3, ...) material system. 222

7.4 The oxygen partial pressure dependence of conductivity in amorphous digallium monoxide / transition metal oxide films. (From published literature.) 227

7.5 A machine-learning approach for automatic tuning of a quantum device. (From published literature.) 233

A.1 The energy and wavelength of light dependences of transmission fraction of Corning Eagle XG glass substrate. 240

A.2 Modeled energy dependence of refractive index and of extinction coefficient of Corning Eagle XG glass substrate. 242

List of Tables

1.1 Comparison of sputtering and other industrially relevant TC and TS oxide film deposition techniques. 5

3.1 Listing of physical and opto-electronic properties of interest, of film or of its layer(s) (sub-plantation layer, thin-film layer) thereof. 56

3.2 Grouping of the nine Si doped In_2O_3−$(ZnO)_3$ films that are the subject of this thesis, according to the plane of the designed experiment on which they reside. 59

3.3 The designed experiment according which were deposited the films that are the subject of this study. 59

3.4 Interconversion between coded unit and real world unit representations of the process factors considered. 60

4.1 Characterization techniques listed according to the information furnished. 82

5.1 Refined detailed layer structure for Si doped In_2O_3−$(ZnO)_3$ films. 123

5.2 The oscillator models for Si doped In_2O_3−$(ZnO)_3$ films on Corning Eagle XG glass substrates. 128

5.3 Estimated pressure distance product dependence of energy at substrate of sputtered material flux. 132

5.4 Determination (semi-quantitative) of angular distribution at substrate of sputtered material flux. 139

5.5 Results of dimensional analysis — in light of radio frequency magnetron sputtering — of sub-plantation layer physical properties. 154

6.1 The first coordination sphere of oxygens, and crystal radius, of metal in metal-oxide, for metals of interest. (From published literature.) 167

6.2 Electrical (experimentally measured) and optical (modeled) determinations of electronic properties of Si doped In_2O_3−$(ZnO)_3$ films. 181

6.3 Determination of charge on impurity in units of elementary charge per the Brooks-Herring model of ionized impurity scattering. 191

6.4 Estimation of distance between impurity centers at the composition induced MIT for Si doped In_2O_3−$(ZnO)_3$. 201

6.5 Experimentally measured room-temperature electronic properties of Si doped In_2O_3−$(ZnO)_3$ films. 203

7.1 Scientific and technological questions and application areas that may be addressed based on this study. 219

7.2 Structural and physical aspects of selected homologues of the In_2O_3−$(ZnO)_k$ (k = 0, 1, 2, 3, …) material system in the crystalline state. 223

7.3 Commercial product types servicing the aerospace industry. . 230

A.1 Relevant goodness of fit metrics of modeling Kiessig fringes profile of Si doped In_2O_3−$(ZnO)_3$ films. 239

A.2 The G plus TL optical model for Corning Eagle XG glass substrate. 241

Abstract

Transparent and conductive (TC) transition metal oxide (TMO) films are integral to many of the electronic devices ubiquitous in the modern world. Such devices include touchscreens of smart-phones, the light emitting diodes (LEDs) used in flat-panel televisions, smart-windows for temperature or lighting control within enclosed spaces, transparent electrodes for solar cells, and static charge control coatings for aerospace applications. The rigidity, and flat form-factor, are notable features of such devices and applications. An underserved commercial play for the aforementioned and kindred applications is their extension into the 'flexible' domain. Such extension requires devices designed to withstand flexing during installation or service. Consideration of said extension brings to fore the question of physical integrity (during installation or service) of any — e.g., opto-electronically active TMO — films present. The first and foremost locus that this question concerns is the film-substrate interface. Equally, opto-electronic properties of the film scope its applications. Thus, the film-substrate interface, and the film itself, are two loci of topical interest. This study addresses both. We present the discovery of a bonafide nanoscale film layer — the sub-plantation layer (SPL) — at (comprising) the film-substrate interface of TMO films deposited on glass substrates, via the industrially relevant process of sputtering. Furthermore, we report process control over manifestation and properties of the SPL. Amorphous phase films are most compatible with the constraints — e.g., maximum permissible substrate temperature during deposition — as are at issue due to use of flexible substrates. Additionally, amorphous films present abiding advantages from a fabrication-costs standpoint. Furthermore, concerns attend the security of supply of indium (In), which is a critical material resource enabling the commercial TC applications noted above. Given these considerations, we selected a reduced In content oxide material system comprising the metals silicon (Si), zinc (Zn), and In for study. Thereby, an amorphous microstructure does not (overly) disadvantage opto-electronic performance. We conduct an experimentally driven analysis of the electronic state of our films, and relate it to the chemistry and physics of the film microstructure and material system.

Extended abstract

We present an experimentally guided study of film layer structure and opto-electronic properties of transition metal oxide (TMO) films. The oxide material system studies comprised the metals silicon (Si), zinc (Zn), and indium (In). The films were deposited via radio frequency magnetron sputtering (RFMS) on room-temperature Corning Eagle XG Glass (CEXG) substrates. Distinct (bi-layer (BL) vs single-layer (SL)) layer structures manifest as a function of angular distribution or pressure distance product (ϕ) of sputtered material flux sourcing film growth. The films are amorphous, transparent and semiconducting.

Experimental determination of absolute temperature (T) dependence of resistivity (ρ) revealed that at temperatures close to room-temperature, ionized impurity scattering (IIS) is the dominant conduction electron scattering mechanism. Thence, application of the Brooks-Herring (BH) model of IIS permitted analysis of the electronic state of the films. Thereby, the electronic state was revealed to be highly compensated.

The design of experiment (DOE) and (associated) response surface analysis (RSA) frameworks were recruited from the very first stage — namely, the stage of film fabrication — of this study. This provisioned a self-referencing set of (nine) films (the 'samples') that are the subject of this study.

The two layers of the BL films are / will-be-referred-to-as the sub-plantation

layer (SPL) and the thin-film layer (TFL). The SPL is situated mediate substrate and TFL, and constitutes thereby the film-substrate interface. For consistent nomenclature, the term 'TFL' will be used to refer to the sole (film) layer of SL films.

The layer structures of the films were established via x-ray reflectometry (XRR). The films were interrogated optically via spectroscopic ellipsometry (SE) (at room-temperature), and electrically via AC Field Hall Effect (ACFHE) measurements (between $\mathrm{T} = 10.1\,\mathrm{K}$ to $300\,\mathrm{K}$).

An account of the understanding of the film layers — viz., SPL, and TFL — as has been achieved, is as follows:

~ The sub-plantation layer (SPL) ~

We report the controlled emergence of a bonafide nanoscale layer — the SPL — at (comprising) the film-substrate interface. The determination of presence of a SPL is direct — that is, sans any assumptions, or modeling — via Fourier analysis of XRR results.

We present three independent — experimental, empirical, and theoretical — threads of analysis to rationalize emergence of the SPL, as follows:

- In terms of deposition process conditions under which a SPL manifests. Our semi-quantitative analysis is in terms of angular distribution or ϕ of the material flux sourcing film growth.

  Evidently, this thread of analysis is beholden to the specific physics of the deposition process, namely, RFMS.

- Via RSA of SPL physical properties (SPL thickness ($\mathrm{d_{SPL}}$), SPL density ($\mathrm{D_{SPL}}$), and SPL roughness ($\mathrm{r_{SPL}}$)). This analysis reveals the following two process factors to be relevant: RF power ($\mathrm{P_{RF}}$), and process gas pressure (p).

While the analysis is on the basis of experimentally observed process factors dependence of the physical properties noted, it is not beholden to the physics of the deposition process (RFMS).

- Via dimensional analysis (DA) of the physical properties noted previously, in light of RFMS process. The dimensionless group for P_{RF} (P_{RF}^{*}) thus determined reveals precisely the two previously noted process factors to be relevant.

  This analysis is ab initio.

We highlight implications of our results for the industrially important problem of sputtered-film-on-substrate adhesion. Thereby, our results bear commercial promise, particularly for research and development (R&D) of flexible electronics applications.

~ The thin-film layer (TFL) ~

We quantify the semiconducting nature of the films (TFLs) on basis of optical (via SE) and electrical (via ACFHE) measurements of their room-temperature electronic properties.

We interrogate the film (material system) electronic state on basis of the experimentally determined T dependences of conduction electron concentration (n) and conduction electron mobility (μ). Presence of a T-range (in the vicinity of and including room-temperature) where IIS is the dominant conduction electron scattering mechanism is established.

Application of the BH model of IIS then lead to the (quantitative) determination that the electronic state is (highly) compensated. This determination — consistent with the experimentally observed anomalous oxygen content dependence of μ — is consistent with trap limited conduction. Thereby, we

relate the electronic state to the chemistry and physics of film microstructure and material system.

~ The ready-reckoner ~

Figure 7.1 presents another and visual walk through — a 'ready-reckoner' — of this study.

~ Epilogue ~

This study represents new lines of investigation for the Professor Peter P. Edwards FRS ML Group.

Acknowledgments

Yama's counsel* to Nachiketa had for long bounced about without settlement in my mind: *only* through the Guru may you know Atman. And so I acknowledge my debt of gratitude towards my supervisor Professor Peter P. Edwards FRS ML. For taking me under his fold, and for affording me a peek into the great project of science. For nurturing, giving the freedom to roam about science and whatnot (if you find your way to the Metal Insulator Transition, so much the better!), for always making time for a chat and for his loving hospitality during it, for always sending me on my way happy. His tutelage has been the privilege of my life. I'd like to respectfully offer him the following śloka†,

आचार्यं मां विजानीयान्नावमन्येत कर्हिचित् |
न मर्त्यबुद्ध्यासूयेत सर्वदेवमयो गुरुः

I must record my most respectful regards towards Professor C. N. R. Rao FRS of IISc. But for his indulgent prodding and kindly support, from when I was yet the bumbling student repairing my bike outside his labs, I may forever have remained the satisfied Koop Mandook. I acknowledge the singular honour of his sponsorship.

*Yama to Nachiketa, Kathopanishad 1.1.21, and 1.2.7 through 1.2.9.
†Krishna to Uddhava, Bhagavata Purana 11.17.27.

I'd like to express my most respectful regards to Professor Sir Michael Pepper FRS FREng of UCL. For being so very generous with his time, and for his support of this work. I vividly recall, and thank him again, for his patience when I first presented early results to him amidst the din of the Paddington Station in London!

I duly acknowledge my co-supervisor Professor Peter G. Bruce FRS, for his generosity and patience.

I remain most grateful to Professor Lars Kloo of KTH. He is among the kindest persons I have had the good fortune to meet. The double-quick stabilization of my situation at Oxford would not have been possible but for his grace. I've also benefited much from our science discussions over the years.

I convey my most sincere regards to Ms Linda Webb for her great and couthy care over the years. Her skills and thoughtfulness as an administrator are a sight for sore eyes. I hope I've learnt some of how she does things: from ensuring that you can't poke yourself with a staple(!), to ministering Prof. Edwards' visitors (whether they be students, academics, Nobel laureates, knights, or royalty!), and indeed, the Edwards Group.

I'm thankful to the staff of the Chemistry Mechanical Workshop, especially, Mr Les Hill, Mr Dennis Chikwanha, and Mr Andrew Green. There's nothing quite as fulfilling than to see your baby (well, experimental kit designs) come to life in a lathe. But for their ever patient ear and guidance and great pride in their work, the endless back and forth tweaking of the design's wouldn't have been as much fun. A tip of the hat to you gentlemen!

I'm most grateful to Dr Jefferey Lindemuth and to Professor John Swartz of Lake Shore Cryotronics for their wonderful hospitality during my multiple visits, and for their generosity in affording me unimpeded access to their

superb facilities. A fair bit of the analysis presented in this thesis is based on Hall Effect data that was collected during the visits. Jeff's workmanship and enthusiasm to figure out 'cold electrons' is a sight to behold, truly.

I sincerely thank Ms Aga Borkowska for her patient and ever pleasant assistance and care over the years.

I warmly thank Ms Hillary Fraser for her care and for our conversations over the years.

I'd like to express my warm regards and thanks to Dr Jamie Ferguson FRSC of Oxford University Innovation (OUI), for his support and mentorship over the years. I recollect fondly our monthly chats re things 'inventive and innovative' over at the University Club.

I'd like to thank Dr Chandra Ramanujam of OUI for his support of this work.

I'd like to acknowledge Dr Fiona Story and Ms Catherine Spence of OUI. The access to OUI's trainings calendar that they facilitated so generously has been to my enormous benefit. I remain grateful for their sponsorship over the years.

I owe hearty thank yous to Dr Steve Etienne, Ms Vijay Lakshmi, and Mr Rohit Khanna of the LCN. The films that are the basis of this study were deposited in the clean-room facilities that they keep humming so very well! Their cheerful pluck in letting me fiddle about endlessly with their (very expensive!) sputtering kit was key to the successful development of the new hardware that is central to this study.

I'd also like to thank the Kurt J. Lesker Company, and particularly, Mr Richard Dyer, for sharing the engineering drawings of, and for always making time for some very detailed discussions about, their Model PVD 75 sputtering kit. Their inputs crucial for our hardware development efforts.

I thank Dr James Hilfiker, Professor J. A. Woollam, and Dr Thomas Wagner of J. A. Woollam for our discussions of spectroscopic ellipsometry data modeling.

I thank Professor Moritz Riede for facilitating my access to his lab, and particularly to the ellipsometer.

I thank Dr Sameer Vajjala Kesava for training me on the ellipsometer.

I thank Dr Josue Martinez Hardigree for training me on the x-ray reflectometer.

Dr Vladimir Kuznetsov has been very kind, and ever willing to share his enormous technical knowledge. I'd like to take this opportunity to extend a personal thanks to him.

I thank Dr Daniel Slocombe for introducing me to the many tricks that microwaves are capable of. Our after-work (sometimes during-work!) conversations were among the sharpest ever, and I'm very glad for them. I'd like to acknowledge Dr Tiancun Xiao's kind help over the years.

I would like to thank the members of the Edwards Group for their company over the years.

I'd like to acknowledge, most warmly and gratefully, the wonderful generosity and sponsorship of Professor Marc J. Ventresca of SBS. Perhaps the only thing that beats the effortless grace of his lectures, is the deeply rigorous ways in which he thinks, and teaches his students to think, about matters business. I've learnt so much from him.

I'd like to thank Ms Natalie Berge for her great care and support over the years.

I'd like to thank Ms Libby Wood for her encouragement and facilitation over the years.

I'd like to thank Dr Alfred Tan of HKBU for his care and hospitality.

I'd like to thank Professor Ikhlaq Sidhu of Berkeley for making time for a conversation, and for his care, attentiveness, and insightful guidance during it. Sometimes, the one conversation is all that's needed!

I'd like to thank Dr David Stanley of the Henry Royce Institute, and Ms Yupar Myint and Dr Alexandra Huener of Cambridge, for their generous and cheerful support to develop the commercial prospects of this study.

I'd like to thank Mr Ken Shaw for his counsel. His mentorship and our conversations were very fruitful for me, and I'm grateful for the privilege of his time and company.

I'd like to thank Mr Karan Bilimoria for his encouragement. I'm grateful for his time and consideration.

I'd like to thank Mr Maurice McCartney for his counsel and for our conversations.

I would not have had the pleasure of acknowledging those forenamed, but for Professor Prabhakar G. Vaidya. He was the wind beneath my wings, and I miss him. And I could never acknowledge enough Mrs Beverley L. Vaidya, for sharing so much of her husband with the world, and particularly with me. Among my fondest memories are from our years in Bangalore, and the Vaidyas' are at the center of them. Those were the most artless of days — to be able to pop over to the Vaidya's, assured of a warm meal, and warmer company. I'm so glad that I got a top-up of their love and care more recently.

I'd like to respectfully acknowledge the conversations, and the succor, provided by Ambassador Dr Virander Paul. He is among the kindest, most giving, and gentlest of persons I have had the privilege of knowing.

I'd like to respectfully acknowledge the care, counsel, and succor provided by Dr S. Y. Quraishi. It's a rare privilege Sir, and I remain grateful.

I'd like to respectfully acknowledge the friendship and help over the years of Ms Amandeep Chatha. Her great craftsmanship in sewing words into poems is surpassed only by her kindness. Ah! To be able to say it like it is, and make it rhyme at the same time! It's truly a privilege and honour to have you and your poems in my life Ma'am.

My family — Ammaji, Papaji, Mummy, Prashantji, Keerti Didi, Pammi, Chiku Chiku, Nanhe, Divyanshu — is the bedrock of my life. They spoil me, and I couldn't be happier for it!

This thesis is dedicated

to my mum, who by name and nature is Sudha,

and

to my father Dr Mahesh Chander Jain, who would have been pleased to

see me come home to Chemistry,

and

to the 21 Indian military personnel who laid down their lives for our Flag

on June 15, 2020 at Galwan in Ladakh, India

जननी जन्मभूमिश्च स्वर्गादपि गरीयसी[‡]

[‡]Bharadwaja to Rama, Ramayana 6.124.17.

Declaration

The work described in this thesis was conducted under supervision of Professor Peter P. Edwards FRS ML, at the Inorganic Chemistry Laboratory of the University Of Oxford. All of the work is my own unless otherwise stated, and has not been previously submitted for a degree at this or any other university.

Himanshu Jain

Student Number: 766 815

List of Abbreviations

A

Alternating Current (AC)

Atomic Layer Deposition (ALD)

Amorphous Oxide Semiconductor (AOS)

Atmospheric Pressure Chemical Vapour Deposition (APCVD)

B

Brooks-Herring (BH)

Bi-Layer (BL)

C

Conduction Band Edge (CBE)

Conduction Band (CB)

Coded Unit (CU)

Chemical Vapour Deposition (CVD)

D

Dimensional Analysis (DA)

Direct Current Magnetron Sputtering (DCMS)

Direct Current Sputtering (DCS)

Direct Current (DC)

Designed Experiment (DE)

Design Of Experiment (DOE)

Density Of States (DOS)

Drude (D)

E

Evaporation Deposition (ED)

F

Figure Of Merit (FOM)

Flat Panel Display (FPD)

Fourier Transform (FT)

G

Gaussian Plus Tauc-Lorentz (G+TL)

Gaussian (G)

H

Hong Kong Baptist University

I

Ionized Impurity Scattering (IIS)

Infra Red (IR)

J

J. A. Woollam (JAW)

K

Kiessig Fringes Profile (KFP)

Kurt J. Lesker Company (KJLC)

Kramers Kronig (KK)

L

Liquid Crystal Display (LCD)

Light Emitting Diode (LED)

Lorentz Oscillator (LO)

Low Pressure Chemical Vapour Deposition (LPCVD)

Lake Shore Cryotronics (LSC)

M

Metal Insulator Transition (MIT)

Machine-Learning (ML)

Mean Square Error (MSE)

Magnetron Sputtering (MS)

N

Not Applicable (NA)

O

One Factor At A Time (OFAT)

P

Pulsed Laser Ablation (PLA)

Pulsed Laser Deposition (PLD)

Physical Vapour Deposition (PVD)

Photovoltaic (PV)

R

Research And Development (R&D)

Radio Frequency Magnetron Sputtering (RFMS)

Radio Frequency Sputtering (RFS)

Radio Frequency (RF)

Root Mean Square (RMS)

Response Surface Analysis (RSA)

Real World Unit (RWU)

S

Science And Technology (S&T)

Säid Business School

Spectroscopic Ellipsometry (SE)

Sputter Flux Collimator (SFC)

Substrate Holder Cum Sputter Flux Collimator Array (SHCSFCA)

Single-Layer (SL)

Sub-Plantation Layer (SPL)

Spray Pyrolysis (SP)

T

Temperature Coefficient of Mobility (TCM)

Transparent Conducting Oxide (TCO)

Temperature Coefficient of Resistivity (TCR)

Transparent Conductive (TC)

Thin-Film Layer (TFL)

Thin-Film Transistor (TFT)

Tauc-Lorentz Plus Drude (TL+D)

Tauc-Lorentz (TL)

Transition Metal Oxide (TMO)

Transparent Semiconductive (TS)

U

Ultra Violet (UV)

V

Valence Band Edge (VBE)

Valence Band (VB)

Van der Pauw (VDP)

X

X-Ray Diffraction (XRD)

X-Ray Reflectometry (XRR)

List of Symbols

A

Given First Process Factor (A)

Amplitude Of $\varepsilon^*_{\mathrm{G}}$ (A)

Amplitude Of Imaginary Part Of $\varepsilon^*_{\mathrm{TL}}$ (A)

Point On Boundary Of a_0 (A_{B})

Point On Central-Axis of a_0 (A_{C})

Point At Arbitrary Location On a_0 (A_{G})

SFC Aperture Side (a) $\mathrm{a} = 1.1\,\mathrm{cm}$

Absorption Coefficient (α)

Geometry Parameter (α) $0 \leq \alpha \leq 1.11$ (Lindemuth and Mizuta, 2011)

Critical Angle For X-Ray (α_{c})

Angle Of Final Wave-Vector (α_{f})

Angle Of Incident Light (α_{i})

Angle Of Initial Wave-Vector (α_{i})

Bounding-Plane Of SFC On Aperture Side (a_0)

Intersection-Line Of c_0 **And** a_0 (s^1_0)

Film Side (a_{f}) $\mathrm{a}_{\mathrm{f}} = 1.1\,\mathrm{cm}$

B

Amplitude Of AC Magnetic Field (B)

Given Second Process Factor (B)

Broadening Of $\varepsilon^*_{\mathrm{G}}$ (B)

Broadening Of Imaginary Part Of $\varepsilon^*_{\mathrm{TL}}$ (B)

RMS Value Of $\mathrm{B_{AC}}$ ($\mathrm{B_{AC,\,RMS}}$)

AC Magnetic Field ($\mathrm{B_{AC}}$)

DC Magnetic Field ($\mathrm{B_{DC}}$)

Proportionality Factor Relating Time Derivative Of $\mathrm{B_{AC}}$ **To** $\mathrm{V_i}$ (β)

XRR β**-Parameter** (β)

Response Surface Model Intercept (β_0)

Response Surface Model Coefficient For Main Effect Of A (β_{A})

Response Surface Model Coefficient For Interaction Effect Of A **And** B (β_{AB})

Response Surface Model Coefficient For Interaction Effect Of A, B, **And** C (β_{ABC})

Response Surface Model Coefficient For Interaction Effect Of A **And** C (β_{AC})

Response Surface Model Coefficient For Main Effect Of B (β_{B})

Response Surface Model Coefficient For Interaction Effect Of B **And** C (β_{BC})

Response Surface Model Coefficient For Main Effect Of C (β_{C})

Inverse Of Screening Length (β_{s})

C

Given Third Process Factor (C)

Cu K $-\,\alpha_1$ **X-Radiation** (Cu K $-\,\alpha_1$) $\lambda(\mathrm{Cu\ K} - \alpha_1) = 1.5406 \times 10^{-1}\,\mathrm{nm}$

Central-Axis Of SFC (cc′)

Goodness Of Fit Metric For Modelling KFP Obtained Via XRR (χ^2)

Axial-Plane Of SFC (c_0)

D

Density (As Applicable) Of Film Or Of Film Layer (D)

SE Δ-Parameter (Δ)

CEXG Density (D_{CEXG}) $D_{CEXG} = 2.38\,g/cm^3$

ISZO Density (D_{ISZO}) $D_{ISZO} \simeq 6.29\,g/cm^3$

SPL Density (D_{SPL})

Dimensionless Group For D_{SPL} ($D_{SPL}{}^*$)

TFL Density (D_{TFL})

Substrate Density (D_s) $D_s = D_{CEXG} = 2.38\,g/cm^3$

Thickness (As Applicable) Of Film Or Of Film Layer (d)

Film Thickness (d)

Film (Single-Layer) Thickness (d)

Skin Depth (δ)

XRR δ-Parameter (δ)

Van der Waals Diameter Of Ar Atom (d_{Ar}) $d_{Ar} = 376\,pm$

SPL Thickness (d_{SPL})

Dimensionless Group For d_{SPL} ($d_{SPL}{}^*$)

Nominal Si To Si Distance (d_{Si-Si})

TFL Thickness (d_{TFL})

Distance Between Impurity Centers At The Composition Induced MIT (d_c)

Process Gas Relevant Diameter (d_g)

Impurity To Impurity Distance (d_{i-i})

CEXG Substrate Thickness ($d_{s,\,CEXG}$) $d_{s,\,CEXG} = 700\,\mu m$

Target Diameter (d_t)

Substrate Thickness (d_s)

E

Energy (E)

Energy At Peak Of Imaginary Part Of ε^*_{TL} (E_0)

Fermi Energy (E_F)

Energy Of Minimum Of Conduction Band (E_c)

Tauc Gap Energy ($E_{g,\,Tauc}$)

Band-Gap Energy (E_g)

Center Energy (E_n)

Plasma Edge Energy (E_p)

Energy Of Sputtered Material Flux At Substrate ($E_{smf,\,s}$)

Energy Of Maximum Of Valence Band (E_v)

Elementary Charge (e) $e = 1.6022 \times 10^{-19}\,C$

Static Permittivity (ε)

High Frequency Dielectric Permittivity (ε_∞)

Permittivity Of Vacuum (ε_0) $\varepsilon_0 = 8.85 \times 10^{-12}\,F/m$

Real Part Of ε^*_D ($\varepsilon_{1,\,D}$)

Real Part Of ε^*_{TL} ($\varepsilon_{1,\,TL}$)

Real Part Of ε^* (ε_1)

Imaginary Part Of ε^*_D ($\varepsilon_{2,\,D}$)

Imaginary Part Of ε^*_{TL} ($\varepsilon_{2,\,TL}$)

Imaginary Part Of ε^* (ε_2)

Complex Permittivity (ε^*)

ε^* **Of CEXG** (ε^*_{CEXG})

Drude ε^* ($\varepsilon^*_{\mathrm{D}}$)

G ε^* ($\varepsilon^*_{\mathrm{G}}$)

TL ε^* ($\varepsilon^*_{\mathrm{TL}}$)

Electric Field Vector ($\vec{\mathrm{E}}$)

F

Ratio Between Two Solid Angles (f) Per Equation 5.2a

Metal Atomic Fraction Of In ($\mathrm{f_{In}}$)

Experimentally Observed Factor By Which Is Depressed, With Respect To Uncollimated (Unconstrained) Situation, Film Deposition-Rate Due Sputtered Material Flux Having A Uniform Angular Distribution (Which Corresponds To Fully Thermalized Sputtered Material Flux), Due Deployment Of An SFC ($\mathrm{f_{SFC,\,observed}}$) Scaled Deposition-Rate Observed In This Study Divided By The Deposition-Rate Observed By Fortunato et al., 2006 (=230 Å/min).

Expected (Theoretical) Factor By Which Is Depressed, With Respect To Uncollimated (Unconstrained) Situation, Film Deposition-Rate Due Sputtered Material Flux Having A Uniform Angular Distribution (Which Corresponds To Fully Thermalized Sputtered Material Flux), Due Deployment Of An SFC ($\mathrm{f_{SFC,\,thermalized}}$)

Metal Atomic Fraction Of Si ($\mathrm{f_{Si}}$)

Metal Atomic Fraction Of Zn ($\mathrm{f_{Zn}}$)

G

Compensation Ratio (Γ)

Convergence Series For Line-Shape Of Real Part Of $\varepsilon^*_{\mathrm{G}}$ (Γ)

H

Planck Constant (h) $h = 4.1357 \times 10^{-15}\,\mathrm{eV\,s}$

SFC Aperture Depth (h) $h = 1.0\,\mathrm{cm}$

Reduced Planck Constant ($\hbar$) $\hbar \equiv h/2\pi = 6.5821 \times 10^{-16}\,\mathrm{eV\,s}$, Where h Is The Planck Constant

I

Electric Current (I)

Final Intensity Of X-Ray (I_f)

Initial Intensity (Fixed) Of X-Ray (I_i)

K

Number Of Main Factors Of The DE (k)

Composition Index For Homologous Series '$In_2O_3-(ZnO)_k$ (k = 0, 1, 2, 3, ...)' (k)

Extinction Coefficient (k)

Boltzmann Constant (k_B) $k_B = 8.6173 \times 10^{-5}\,\mathrm{eV/K}$

Magnitude Of Fermi Wave-Vector (k_F)

Ioffe-Regel Parameter ($k_F l_e$)

Wave-Vector Of Final X-Ray ($\vec{k_f}$)

Wave-Vector Of Initial X-Ray ($\vec{k_i}$)

L

Mean Free Length Of Process Gas (l)

Wavelength Of Light (λ) As Was Employed For SE; $210\,\mathrm{nm} \leq \lambda \leq 1690\,\mathrm{nm}$

Wavelength Of X-Rays (λ) As Was Employed For XRR; $\lambda = 1.5406 \times 10^{-1}\,\mathrm{nm}$

Wavelength Of Interest Less Than λ_p (λ_0)

Plasma Edge Wavelength (λ_p)

Electron Mean Free Length (l_e)

Target-Substrate Distance (l_{t-s})

Perpendicular Distance From Target Surface (l_t)

M

Smallest Value, Expressed In CU, Of Chosen Range For Given Process Factor $(-)$

Effective Mass Of Electron At CBE (m)

Effective Mass Of Electron (m)

Rest Mass Of Electron (m_e) $m_e = 9.1094 \times 10^{-31}\,\text{kg}$

Effective Mass Of Electron In Units Of Rest Mass Of Electron (m^*)

Conduction Electron Mobility (μ)

BH Mobility (μ_{BH})

Maximal Mobility (μ_{max})

N

Ionized Impurity Concentration (N)

Avogadro Constant (N) $N = 6.022 \times 10^{23}/\text{mol}$

Total Acceptor Concentration (N_A)

Total Donor Concentration (N_D)

Nominal Concentration of Dopant / Si (N_{Si})

Conduction Electron Concentration (n) Note that this symbol is the same as the symbol for 'Refractive Index'. The usage of the symbols is as per convention. The context of use should dispel any ambiguity re the intended meaning of this symbol.

Refractive Index (n) Note that this symbol is the same as the symbol for 'Conduction Electron Concentration'. The usage of the symbols is as per convention. The context of use should dispel any ambiguity re the intended meaning of this symbol.

Complex Refractive Index (n^*)

Complex Refractive Index In The X-Ray Energy Range (n^*)

Film Deposition-Rate (ν)

Frequency Of B_{AC} (ν)

TFL Deposition-Rate (ν_{TFL})

Conduction Electron Concentration (n)

O

Oxygen Percent (O)

Solid Angle (Ω)

Solid Angle Subtended At Substrate Center By SFC Aperture (Ω_{SFC})

Dimensionless Group For Ω_{SFC} (Ω^*_{SFC})

Solid Angle From Which Material Flux Is Received In Unconstrained Conditions ($\Omega_{unconstrained}$)

Dimensionless Group For O (O^*)

Angular Frequency (ω)

Angular Frequency Of Interest Greater Than ω_p (ω_0)

Plasma Edge Angular Frequency (ω_p)

P

Largest Value, Expressed In CU, Of Chosen Range For Given Process Factor (+)

Cauchy Principal Value (P)

DC Target-Potential ($\Phi_{DC,\,t}$)

SE Ψ-Parameter (Ψ)

RF Power (P_{RF})

Dimensionless Group For P_{RF} (P_{RF}^{*})

Reciprocal Of Fraction Level Of A Two-Factor DE (p)

Process Gas Pressure (p)

Pressure Distance Product (ϕ)

Haacke Figure Of Merit (ϕ_{TC})

Given Pressure Distance Product (ϕ_{t-s}) $\phi_{t-s} \equiv \phi(l_t = l_{t-s})$

Mathematical Constant (π) $\pi = 3.1416$

Base Pressure (p_b)

X-Component Of Angular Momentum (Averaged) Of Sputtered Material Flux, At Substrate ($p_{x,\,s}$) x-component of angular momentum (averaged) of sputtered material flux sourcing film growth

X-Component Of Angular Momentum (Averaged) Of Sputtered Material Flux (p_x)

Y-Component Of Angular Momentum (Averaged) Of Sputtered Material Flux, At Substrate ($p_{y,\,s}$) y-component of angular momentum (averaged) of sputtered material flux sourcing film growth

Y-Component Of Angular Momentum (Averaged) Of Sputtered Material Flux (p_y)

Q

Magnitude of Transfer Wave-Vector (Q_z)

Transfer Wave-Vector ($\vec{Q}_z$)

R

Goodness Of Fit Metric For Modelling KFP Obtained Via XRR (R – value)

Ideal Gas Constant (R) $R = 62.3639\,m^3\,mTorr/(mol\,K)$

Reflectivity (R)

Hall Coefficient (R_H)

Sheet Resistance (R_s)

Power Reflection Coefficient ($\Re$)

Roughness (As Applicable) Of Film Or Of Film Layer (r)

Radial Distance From Impurity Ion (r)

Resistivity (ρ)

Ratio Of r_p To r_s (ρ)

Electron Density (ρ_e)

SPL Roughness (r_{SPL})

Dimensionless Group For r_{SPL} ($r_{SPL}{}^*$)

TFL Roughness (r_{TFL})

SFC Aspect Ratio (r_a)

Classical Electron Radius (r_e) $r_e = 2.8 \times 10^{-6}\,nm$

Reflectivity For p-Polarized Light (r_p)

CEXG Substrate Roughness ($r_{s,\,CEXG}$) $r_{s,\,CEXG} = 0.5\,nm$ to $1\,nm$

Reflectivity For s-Polarized Light (r_s)

S

Point On Boundary Of s_0 (S_B)

Point On s_0^1 (S_G)

Conductivity (σ)

Mott Minimum Metallic Conductivity (σ_{min})

Bounding Plane Of SFC On Substrate Side (s_0)

Intersection-Line Of c_0 And s_0 (s_0^1)

Solid Angle (Ω)

T

Absolute Temperature (T)

Process Gas Temperature (T)

Angle Of Incidence Of X-Rays (Θ)

Substrate Temperature (Θ_s)

Dimensionless Group For Θ_s (Θ_s^*)

Transmission Fraction (Tr)

Deposition Temperature (T_d)

Substrate Temperature (T_s)

Power Transmission Coefficient ($\mathfrak{T}$)

Time (t)

Mean Free Time Between Collisions (τ)

Mean Free Time Between Collisions With Ionized Impurities (τ_{ii})

Mean Free Time Between Collisions With Phonons (τ_p)

U

SFC Aperture Body-Diagonal (u) $u = 1.9\,cm$

V

Impurity Potential (V)

Mis-Alignment Voltage (V_0)

Hall Voltage (V_H)

Thermal Electric Voltage (V_{TE})

Inductance Voltage (V_i)

Experimentally Measured Voltage In Hall Geometry (V_m)

Experimentally Measured Voltage In Hall Geometry Minus V_{TE} (V'_m)

Voltage Read At X-Channel Of Lock-In Voltmeter (V_x)

Voltage Read At Y-Channel Of Lock-In Voltmeter (V_y)

X

Resolution Of The DE (X)

Point On s_0^1 (x_G)

Y

Function Relating $d_{SPL}{}^*$ To $P_{RF}{}^*$ (Υ_1)

Function Relating $D_{SPL}{}^*$ To $P_{RF}{}^*$ (Υ_2)

Function Relating $r_{SPL}{}^*$ To $P_{RF}{}^*$ (Υ_3)

Z

Middle Value, Expressed In CU, Of Chosen Range For Given Process Factor (0)

Charge On Impurity In Units Of Elementary Charge (Z)

Impedance Of Free Space (Z_∞) $Z_\infty \approx 377\,\Omega/\varepsilon_\infty^{1/2}$

Direction Perpendicular To Film During XRR (z)

Maximum Angle Of Incidence Of Sputtered Material Flux Received At Given Radial Location On Substrate From SFC Aperture (ζ)

List of Materials

A

Al Doped ZnO (AZO)

Silver (Ag)

Aluminum (Al)

Argon Ion (Ar^+)

Argon (Ar)

C

Corning Eagle XG Glass (CEXG)

Iso-Propyl Alcohol ($(CH_3)_2CHOH$)

Methanol (CH_3OH)

Cadmium (Cd)

Copper (Cu)

F

Fluorine (F)

G

Gallium Ion (Ga_3^+)

Gallium (Ga)

Amorphous Digallium Monoxide (a−Ga_2O_x)

I

High Quality a-IGZO (HQ a-IGZO) Per Kamiya, Nomura, and Hideo Hosono, 2013.

Low Quality a-IGZO (LQ a-IGZO) Per Kamiya, Nomura, and Hideo Hosono, 2013.

Ga Doped In_2O_3−$(ZnO)_3$ (IGZO)

Si Doped In_2O_3−$(ZnO)_3$ (ISZO)

Indium Tin Oxide (ITO)

Single Crystal $InGaZnO_4$ (sc-IGZO (m=1)) Per Kamiya, Nomura, and Hideo Hosono, 2013.

Single Crystal $InGaO_3(ZnO)_5$ (sc-IGZO (m=5)) Per Kamiya, Nomura, and Hideo Hosono, 2013.

k = 3 **Homologue Of The In_2O_3−$(ZnO)_k$ (k = 0, 1, 2, 3, ...) Material System** (In_2O_3−$(ZnO)_3$)

k = 5 **Homologue Of The In_2O_3−$(ZnO)_k$ (k = 0, 1, 2, 3, ...) Material System** (In_2O_3−$(ZnO)_5$)

Homologous Series Of In−Zn−O Material System (In_2O_3−$(ZnO)_k$ (k = 0, 1, 2, 3, ...))

Indium Sesquioxide (In_2O_3)

Material System Comprised Of In, Ga, Zn, And O (In−Ga−Zn−O)

Material System Comprised Of In, Ga, And Zn (In−Ga−Zn)

InO_2 (InO_2)

Material System Comprised Of In, Si, Zn, And O (In−Si−Zn−O)

Material System Comprised Of In, Zn, And O (In−Zn−O)

Indium (In)

N

Nitrogen (N)

O

Oxygen Ion (O^{2-})

Oxygen Molecule (O_2)

Oxygen (O)

P

Polyethylene Terephthalate (PET)

S

Silicon Dioxide (SiO_2)

Silicon (Si)

Tin(IV) Oxide (SnO_2)

Tin (Sn)

Z

Material System Comprised Of Zn, In, And O (Zn−In−O)

Zinc Oxide (ZnO)

Zinc (Zn)

Chapter 1

Motivation and overview

1.1 Introduction

This DPhil thesis presents a study of sputtered amorphous and semiconducting transition metal oxide (TMO) films. We begin by considering the commercial and environmental context of the study (section 1.2). This is followed by a discussion of the resulting mandate for the academic research community (section 1.3). This leads to a discussion of the operational aspects, interdisciplinary underpinnings, and timeliness of this thesis (section 1.4). With the backdrop thus, we present the overview of chapters of this thesis (section 1.5). Finally, we summarize the original contributions of this thesis (section 1.6).

1.2 Transparent oxide films: commercial and environmental context

Transparent oxide films may be prepared with a variety of metal (tin (Sn), indium (In), zinc (Zn), and cadmium (Cd)) ions, and in crystalline, polycrystalline, and amorphous microstructures. The electronic properties of

the films may be tuned, to display nearly insulating to degenerate semiconducting conductivity. The tuning goes hand in hand with control over film transparency in the visible region. Furthermore, such films may be prepared via scalable and industrially relevant non-vacuum (viz., spray pyrolysis, sol-gel, electrodeposition, atmospheric pressure chemical vapour deposition (APCVD)), or vacuum (viz., sputtering, atomic layer deposition (ALD), pulsed laser deposition (PLD), evaporation, low pressure chemical vapour deposition (LPCVD)) techniques. For such reasons, transparent oxide films are excellent candidates for delivering current and upcoming transparent electronics applications (Gordon, 2000; Ohta and Hideo Hosono, 2004; Ruske, 2012).

The last two decades bear witness to a great increase in the availability and uptake of transparent electronics devices in everyday life. Such devices include portable and large electronics gadgets incorporating touch sensitive displays, architectural applications such as smart-windows (Jelle, Kalnæs, and Gao, 2015; C. Granqvist, 2014; Mallick, Ghosh, and Basak, 2020), and energy applications such as such as solar cells (Hideo Hosono, 2010b).

The applications noted above are macro-scale (human-scale), where the transparent component has an areal extent between a few cm and up to $10^2\,\mathsf{cm}$. Notably, they are 'passive' applications (see figure 6.4) where the film serves as an electrode (Klaus Ellmer, 2012; Tadatsugu Minami, 2005; Peter P. Edwards et al., 2008). Such transparent conductive (TC) films collect charges from nearby functional layers (such as in the case of solar cells), or to supply these functional layers with charge carriers (such as in the case of light emitting diodes (LEDs) displays). Typically, the goal of research and development (R&D) for such applications is to achieve the highest conductivity (σ) possible for given minimum acceptable transmission fraction (Tr)

in the visible part of the electromagnetic spectrum (John F Wager, Keszler, and Presley, 2008).

The transparent thin-film transistor (TFT) is a more recent addition to the list of applications (R. L. Hoffman, Norris, and J. F. Wager, 2003; Nomura, Ohta, Ueda, et al., 2003; Nomura, Ohta, Takagi, et al., 2004; Barquinha et al., 2012). Device circuits based on the transparent TFT are fashioned from TC and transparent semiconductive (TS) oxide films. This is distinct from conventional semiconducting device circuits that are fashioned from, e.g., silicon (Si) based TFTs and metal based interconnects.

The TFT based applications are micro-scale, where the transparent component has an areal extent of up to a few 10s of nm. Notably, it is an 'active' application, whereby the film serves as the channel-layer in a TFT. Typically, the goal of R&D for such applications is to achieve the highest possible conduction electron mobility (μ) simultaneous with lowest (highest acceptable) conduction electron concentration (n) (P. P. Edwards et al., 2004; John F Wager, Keszler, and Presley, 2008).

Evidently therefore, transparent TMO based films (macro-scale and micro-scale) are a key technology enabling modern life. Thus, their application areas noted above present significant current and potential commercial opportunities (Rowell and McGehee, 2011; U.S. Department of Energy Solar Energy Technologies Office, n.d.; G. M. Wilson et al., 2020). Particularly, the architectural and energy application areas aforementioned represent important current and potential environment stewardship (climate change mitigation) opportunities (Slocombe et al., 2012; V. Kuznetsov and P. Edwards, 2010; Hoffmann, 2011; T. A. Gessert, 2010; C.-G. Granqvist, 2008; C. G. Granqvist, 2012).

The societal utility of such applications may be gauged in light of the market

size (current) and opportunity (projected) of exemplary devices representative of the application areas aforementioned.

Accordingly, figure 1.2 presents historical and projected market size opportunity for an exemplary energy (passive) application (photovoltaic (PV) modules) where transparent conducting oxide (TCO) films are a key enabling technology.

Similarly, figure 1.2 presents historical and projected market size opportunity for an exemplary active application (transparent and other flat panel display (FPD) displays) where TC and TS oxide films are a key enabling technology.

The devices servicing the aforementioned application areas are fabricated from diverse materials (Babbitt et al., 2020). Such materials include ceramics and glasses, semiconductors and metals, and organics and plastics. As such, the development of compatible transparent oxide films servicing such applications requires detailed considerations of film material system, of film deposition process and protocols, of film microstructures and morphologies, and of film opto-electronic performance requirements (John F Wager, Keszler, and Presley, 2008).

Particularly within industrial settings, the scrutiny of cost vs benefit also informs the aforementioned considerations (Fischhoff, 2015a; Fischhoff, 2015b). Additional significant considerations include security of supply of raw materials (particularly, for the presently relevant application areas, of In) and their cost (Weiser et al., 2015; Jasiński et al., 2018), and environmental considerations (C. G. Granqvist, 2007; Armaroli and Balzani, 2007). The technique of sputtering presents abiding advantages for industrial scale oxide film deposition, as illustrated via table 1.1.

Costing studies for thin-film PV modules (Shah et al., 1999) manufacturing

Film deposition technique	Deposition rate	Durability	Ease of doping	Low temperatures	On-line	Volatile precursor	Process controllability	Optical performance
CVD	High	High	No	No	Yes	Yes	Difficult	Normal
Sol-Gel	Normal	Normal	No	Yes	No	Yes	Normal	Normal
MS	Normal	Normal	Yes	Yes	No	No	High	High

Table 1.1: Comparison of magnetron sputtering (MS) and other industrially relevant transparent conductive (TC) and transparent semiconductive (TS) oxide film deposition techniques (chemical vapour deposition (CVD), sol-gel). Table adapted from Rezaei, Shannigrahi, and Ramakrishna, 2017.

for candidate technologies show that, with increasing technological maturity, material (all that are needed for module manufacture) costs will come to dominate the overall module cost (Ken Zweibel, 1995; K. Zweibel, 1999; K. Zweibel, 2000; Chopra, Paulson, and Dutta, 2004). New TCO materials R&D thereby is a core aspect for costs optimization of the manufacturing processes of semiconductor cell device and of their modules, for a(ny) given suite of materials and technologies.

This thesis touches upon the considerations discussed above. We investigate a reduced In content material composition (compared to the 'standard' TCO material composition indium tin oxide (ITO) (C. Granqvist and Hultåker, 2002)). Our films are deposited via the industrially relevant sputtering technique.

Our experimentation protocol — which is enabled by new hardware, viz., the substrate holder cum sputter flux collimator array (SHCSFCA) developed by us — permits high-throughput R&D experimentation. Furthermore, design features of the hardware (the sputter flux collimator (SFC)), permit control of angular distribution of sputtered material flux* sourcing film growth. This enables control over the physical properties (density, thickness, and roughness) of the film-substrate interface. Control as aforementioned presents evident and potentially fruitful implications for film-substrate adhesion (re-

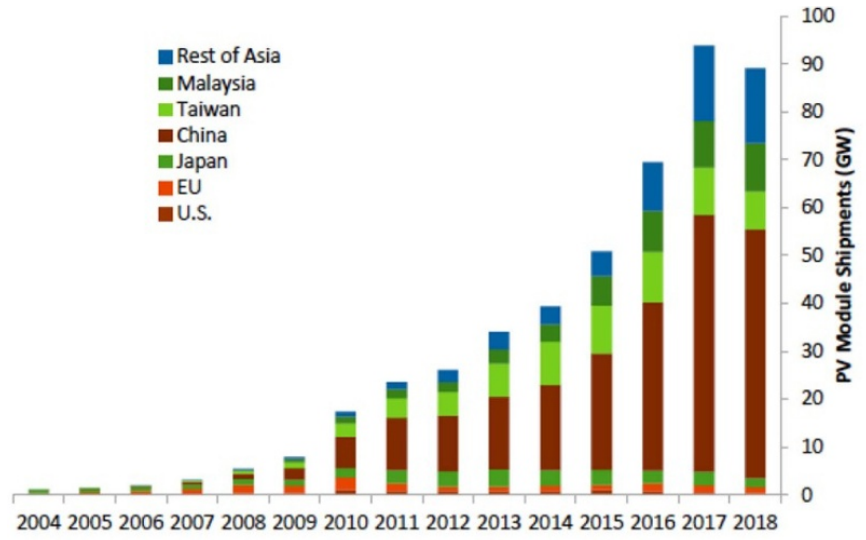

(a)

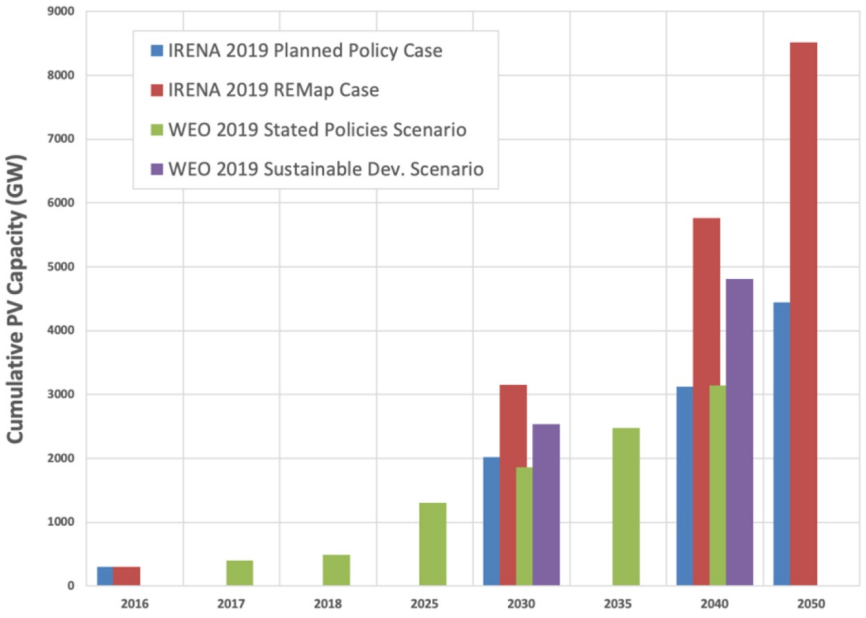

(b)

Figure 1.1: (a) Country-wise and cumulative module shipments over the period 2004 to 2018 by the photovoltaic (PV) industry. (b) Historical and projected cumulative PV capacity, per International Renewable Energy Agency (IRENA) and World Energy Outlook (WEO). Robust growth in capacity is projected, notwithstanding significant differences among the projections. Figures adapted from G. M. Wilson et al., 2020 and Feldman, D. and Margolis, R., 2019 and references cited therein.

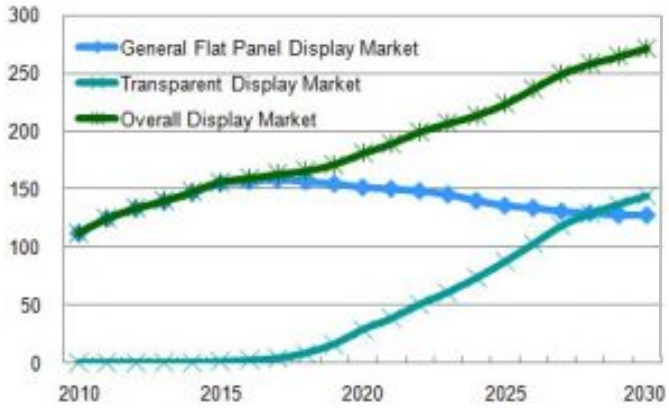

(a)

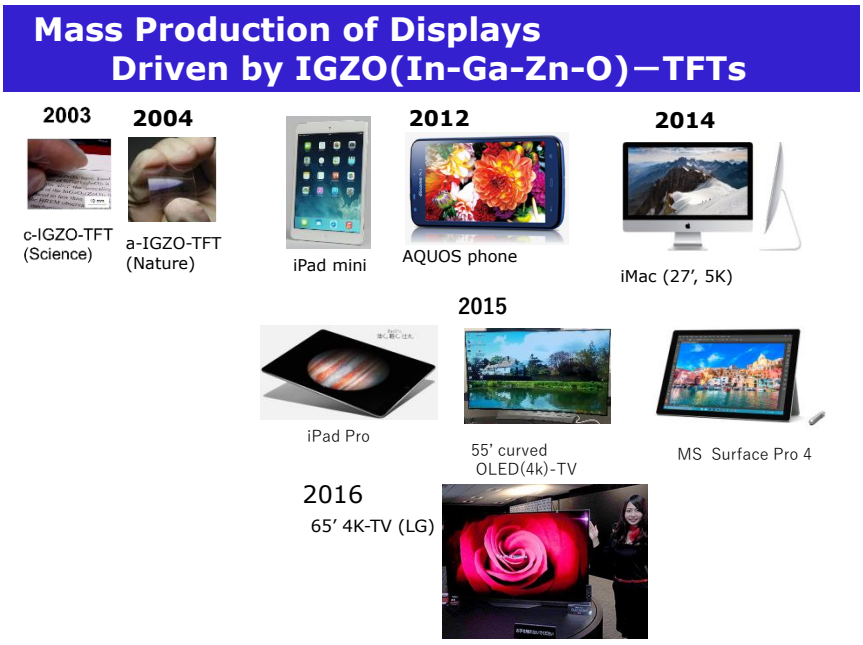

(b)

Figure 1.2: (a) Historical trends and forecasts for the transparent display market. It is estimated that the market will exceed \$87 billion in annual revenue by year 2025. This will be over a third of the estimated size of the total display market of \$223 billion. Furthermore, by year 2030, revenues from transparent displays will surpass those from non-transparent displays. Figure adapted from DisplayBank Co., Ltd, 2021. (b) Chronology of development, and of application to the backplane of various flat panel displays (FPDs), of In−Ga−Zn−O (IGZO) thin-film transistors (TFTs). Figure adapted from H. Hosono, 2017.

fer section 2.4).

As discussed, the development of a film material compositions for new applications is a complex exercise given the multitude of considerations at issue. New materials development is often called for, with (learnings from) extant material compositions serving as benchmarks. The task of such new materials development efforts fall, more often than not, on the shoulders of the academic research community.

The societal relevance of the science and technology (S&T) considerations described above is informed by the security of supply realities of critical raw materials, e.g., of In, needed to service the application areas aforementioned. We discuss the same next in section 1.2.A. Thereafter, we would be in a position to present the resulting mandate for the academic research community (in 1.3).

1.2.A Security of supply considerations for indium

Indium based TCO films are an essential component of the large scale commercial applications aforementioned (consumer electronics, and electricity supply and consumption management). Therefore, for the foreseeable future therefore, In will remain an industrially, societally, and environmentally critical material (Ali et al., 2017).

Thus, in addition to intrinsic S&T interest (D. S. Ginley and C. Paine, 2010), security of supply concerns motivate R&D into zero or reduced[†] In content transparent films. Here, we develop the background informing such security concerns (Richard Herrington, 2013; Vidal, Goffé, and Arndt, 2013). Security of supply concerns of a given material resource emerge upon con-

[*]For brevity and as appropriate, in this thesis the term "sputtered material flux" will often be contracted to 'material flux'.

[†]Compared, for instance, to the gold-standard composition indium sesquioxide (In_2O_3); refer 2.2.C.

sideration of its projected future requirement, environmentally acceptable mode(s) of its extraction, its national distribution around the world, and its international market price. We address these aspects for the material resource In.

The projected future requirement for In is expected to triple (at least) by the year 2050, compared to the requirement in year 2018. Substantive environmental concerns emerge and have been flagged re the impact of In mining activities needed to supply such increased requirement (Raw materials for a truly green future, 2021; R. Herrington, 2021; Boldy et al., 2021). The environmental aspects are confounded with the (currently known) national distribution (refer figure 1.3(a)), and production distribution (refer figure 1.3(b)) of In. Consideration of the volatility in the international market price of In (refer figure 1.3(c)) makes evident that the national and production distributions aforementioned are not amenable to price, that is, supply security of In.

1.3 Mandate for the academic research community, and corresponding aspects of this study

In light of preceding discussions, the academic research community is tasked to provide a pipeline of innovations in service of the following societally and commercially relevant goals.

- Enabling new commercial applications, e.g., on flexible substrates (M. Simon, 2019; M. Simon, 2020a; M. Simon, 2020b).
- Lowering costs of R&D. This is equivalent to enhancing the efficiency of R&D. Demonstrable and quantifiable enhancement of the return per unit R&D expenditure is required.

- Lowering costs of extant commercial applications.
- Mitigate the risks arising from raw material availability constraints. This is achievable by developing new materials that do not present security of supply concerns.

We overview (in sections 1.4 and 1.6) aspects of this study. The same may be considered in light of the preceding mandate. The overview will also ring-fence this study, that is, distinguish it from prior studies.

1.4 This study

1.4.A Introduction

Prior to allocating the discussions of this thesis into its chapters (which we will do in section 1.5), we present the operational aspects of this study (1.4.B). This will motivate a discussion of the naturally interdisciplinary underpinnings of this study (1.4.B). Finally, we will consider the timeliness of this study (1.4.C).

1.4.B Operational aspects

The following are the operational aspects of this thesis. It will be recognized that they attend upon the mandate described in section 1.3.

1. The design and development of new hardware (the SHCSFCA), and experimentation protocols (to accompany and exploit the features of the new hardware), guided by design of experiment (DOE) principles (G. E. P. Box and K. B. Wilson, 1951; N. C. Giri and Das, 1979; D. Montgomery, 2000).

   The development efforts so were informed by the desire (imperative) to conduct the designed experiment (DE)[‡] at high-throughput.

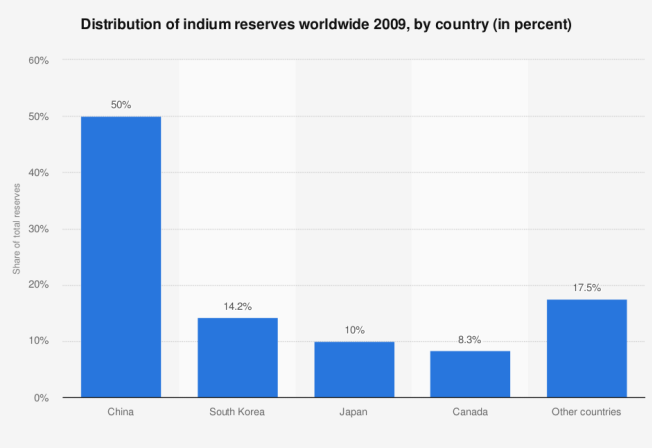

(a)

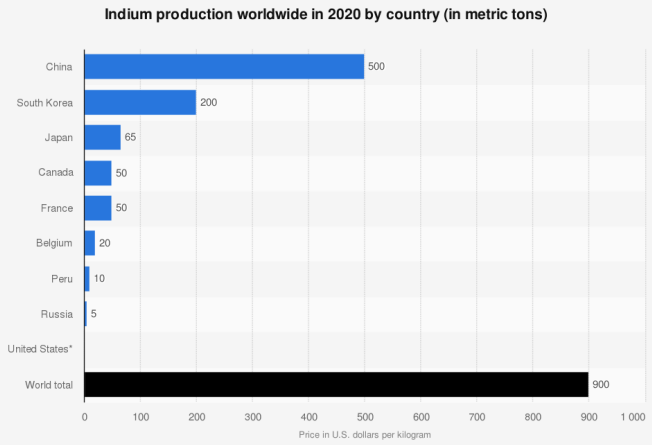

(b)

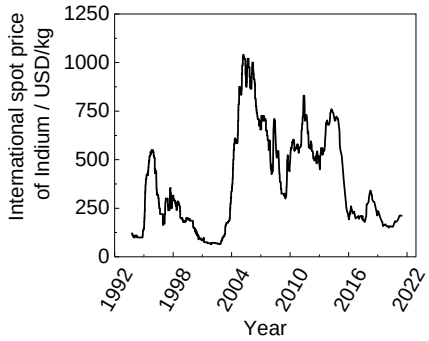

(c)

Figure 1.3: (a) Distribution of indium (In) reserves in year 2009 by country. Figure adapted from Statista, 2020. (b) Distribution of In production in year 2020 by country. Figure adapted from Statista, 2021. (c) International spot price history of In. Data from Eikon, 2021.

2. The choice of a commercially promising material system, viz., In_2O_3−$(ZnO)_k$ (k = 0, 1, 2, 3, ...) (Negar Naghavi et al., 2000; N. Naghavi et al., 2001), and fabrication of its films via an industrially relevant technique, viz., sputtering.

   Also, the fabrication and characterization of films of this material system in a manner consonant with the previous aspect.

3. The quantitative theoretical investigation of new results, such as the observation of the sub-plantation layer (SPL).

   We utilized an ab initio dimensional analysis (DA) (Sonin, 2001), and an experimentally driven response surface analysis (RSA) (Davies, 1954; G. E. P. Box and Draper, 1987; Khuri and Cornell, 1987), for such investigations.

   On basis of such investigations, we suggest a phase-diagram for SPL formation.

4. The theoretical interpretation of electronic property results to yield quantitative information about the nature of the electronic state of the film (Chattopadhyay and Queisser, 1981; Kamiya, Nomura, and Hideo Hosono, 2010a).

   The interpretations are relevant for room-temperature applications.

1.4.C Interdisciplinary underpinnings

Readily accessible theory with predictive power to guide new TMO materials development is as yet unavailable (Hideo Hosono, 2010b). Therefore the role

[‡]By "Designed Experiment", or its abbreviation "DE", is meant a set of experiments ('runs') that are conducted in light of DOE principles. In this study, each experiment so yielded, in turn, a set of nine films (multiple replicates of each).

of experimentation and empirical analysis is central in new TC film materials development.

Typically, the starting point of a new materials development effort is the identification of a material composition of interest. Figure 1.4 depicts the situation as inheres thereafter, viz., at the stages of sample fabrication and characterization. The naturally interdisciplinary underpinnings of this study are evident on its basis. Ideally, the throughput, that is, time-scale, of characterizations should be in consonance with the fabrication throughput (Maier, Stöwe, and Sieg, 2007).

We suggest that the epithet "high-throughput", is naturally inherent to experimentation performed according to DOE principles (including RSA). This is since experimentation so conducted is demonstrably rational and quantifiably efficient (compared to one factor at a time (OFAT) methodologies) (J. S. Hunter, 1987; George E. P. Box, J. S. Hunter, and W. G. Hunter, 2005).

The new experimentation capability — developed by us in-house and from scratch — to conduct a given DE within the shortest possible time duration adds further velocity to the throughput, thereby proceeding it (the throughput) to the highest values possible. That is, the experimentation throughput demonstrated by us is limited (in the main) only by the (user specified) time duration for film deposition.

Our use of the qualifier "high-throughput" for the experimentation described in this thesis encompasses both of the aforementioned considerations.

Development of our high-throughput DOE experimentation capacity entailed melding of the following aspects (discussed in detail in chapters 3 through 4):

- Materials fabrication and their downstream characterizations aspects:

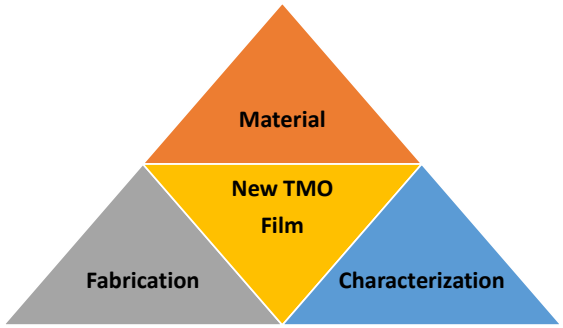

Figure 1.4: Aspects integral to rational new materials research and development (R&D) where theory with predictive power is unavailable (D. S. Ginley and C. Paine, 2010). We identify three aspects — 'Material', 'Fabrication', and 'Characterization' — that are integral to support development of a 'New transition metal oxide (TMO) Film'. By "Material" we mean the material composition (in this study: Si doped In_2O_3−$(ZnO)_3$ (ISZO)). By "New TMO Film" we mean a new film (including its stoichiometry and microstructure) having nominal composition of the chosen material composition. Once the material composition of interest has been fixed, a true high-throughput film fabrication strategy will be one where "Fabrication" and "Characterization" aspects keep up with, indeed contribute to, the velocity of each other. One understands that the fabrication technique and process factors set of choice are informed by film (material composition and microstructure) to be fabricated. Considering the present study, film fabrication (via sputtering) has traditionally been the rate-limiting-step. The limitation arises on account of the time duration and resources needed to create the low base pressure (that is, high vacuum) required for sputtering (refer section 4.2). he substrate holder cum sputter flux collimator array (SHCSFCA) developed by us effectively alleviates this limitation (Jain, Peter P. Edwards, and Pepper, 2018). The SHCSFCA provides us capacity to conduct (R&D-stage) film fabrication according to design of experiment (DOE) principles at high-throughput. Accordingly, it demonstrably enables a true high-throughput R&D workflow. The commercial promise of such workflows is in evidence.

  - Choice of material system, and the attending materials chemistry and physics considerations.

- Fabrication technique and equipment aspects:

  - New hardware design (including choice of material to construct it from) as constrained by the film deposition equipment.
  - The experimentation protocol, as constrained by the given functionalities and control software of the film deposition equipment.
  - The DOE framework for experimentation, and the RSA framework for analysis of the results therefrom.
  - The film deposition technique of interest (radio frequency magnetron sputtering (RFMS)).

Evidently therefore, this study is naturally interdisciplinary.

1.4.D Timeliness

The timeliness of this study emerges from the preceding discussions, particularly those presented in sections 1.3 and 1.4.C. Accordingly, this study is timely since it …

- … identifies and investigates a likely new TMO composition for transparent and semiconducting or conductive applications.
- … demonstrated the ability to tailor properties of nanoscale film interfaces, via control of 'macro' process factors (such as RF power (P_{RF}), process gas pressure (p), and oxygen percent (O)) of the commercially significant technique of sputtering.
- … demonstrated transferable DOE approaches to experimentation that may be leveraged widely and within the means as given (extant).

1.5 Overview of chapters

1.5.A Introduction

Here, we allocate description of the aspects of this study among chapters 1 through 7, and appendices A and B. The chapters present our results, and the appendices present elements of analyses (data, analysis, and computer programs) that accompany the discussions presented in the chapters.

1.5.B Chapter 1 entitled 'Motivation and overview'

In this, the present chapter, we introduce the study that is the subject of this thesis.

1.5.C Chapter 2 entitled 'Literature survey'

Dovetailing the aspects mentioned in section 1.4.B naturally ringfences this study from prior studies. We survey the published literature on the individual aspects of this study.

The survey focuses on TMO film studies where the experimentation was performed according to DOE principles, and / or where the film deposition technique is sputtering.

The section-wise overview of this chapter is:

- Detailed introduction to the chapter discussions. Refer section 2.1.
- Discussion of selected published results on binary, ternary, and quaternary amorphous oxide semiconductors (AOSs). Refer section 2.2.
- Discussion of selected published studies on the process-structure-property considerations that accompany sputtered TMO films. Comparative discussion thereby of various TMO film deposition techniques. Refer section 2.3.

- Discussion of sub-plantation phenomena in context of film-substrate adhesion. Discussion of published studies potentially relevant for our SPL related results. Refer section 2.4.
- Discussion of selected published DOE studies on TMO films. Presentation of an epilogue on such studies. Refer section 2.5.
- Discussion of the goals informing new TCO materials development. Comparative preview thereby of (some of) our, and corresponding published, results. Refer section 2.6.

1.5.D Chapter 3 entitled 'Film deposition: design of experiment, sputtering, and the substrate holder cum sputter flux collimator array'

We develop details of implementation, of the experimentation undertaken to address the aspects per section 1.4.B. The discussions will situate the aspects in relation to each other. This will help ring-fence (distinguish) this study within the art of TMO films.

The section-wise overview of this chapter is:

- Detailed introduction to the chapter discussions. Refer section 3.1.
- Motivation of the DOE and RSA frameworks for experimentation. Presentation of the DE used for this study. Refer section 3.2.
- Discussion of AOS films deposition via RFMS , which is the film deposition technique of choice. Refer section 3.3.
- Discussion of the angular distribution of sputtered material flux, at target and at substrate. Qualitative and quantitative discussions thereby, of the ability to control, via a SFC, the angular distribution of sputtered material flux sourcing film growth. Refer section 3.4.

- Discussion of the engineering designs, and re deployment and versatility, of the SHCSFCA developed by us for high-throughput conduct of a DE. Refer section 3.5.

1.5.E Chapter 4 entitled 'Materials, methods, and analysis frameworks'

We motivate the theory and detail the practice, of the film depositions, of the characterizations, and of the analyses, undertaken in this study.
The section-wise overview of this chapter is:

- Detailed introduction to the chapter discussions. Refer section 4.1.
- Presentation of the protocols for substrate preparation prior to, and for film deposition via, RFMS. Refer section 4.2.
- Presentation of the theory and practice details for film layer structure determination via x-ray reflectometry (XRR). Refer section 4.3.
- Presentation of the theory and practice details for film opto-electronic property determination via spectroscopic ellipsometry (SE). Presentation thereby of the oscillator models employed for modeling of the SE data, which are used for quantitative determination of said properties. Refer section 4.4.
- Presentation of the theory and practice details for film electronic property determination via AC Field Hall Effect (ACFHE). Presentation thereby of the Brooks-Herring (BH) model of ionized impurity scattering (IIS) of conduction electrons, which is used to interrogate the electronic state of our films. Refer section 4.5.

1.5.F Chapter 5 entitled 'The sub-plantation layer'

We report the observation, and present results of interrogation and analysis, of a SPL in TMO films.

The section-wise overview of this chapter is:

- Detailed introduction to the chapter discussions. Refer section 5.1.
- Presentation of experimental results attesting the growth of bi-layer (BL) sputtered TMO films, where the growth is sourced from a continuous stream of sputtered material flux. Refer section 5.2.
- Presentation of film layer structure models that are used for refining film Kiessig fringe profiles (KFPs) recorded via XRR. Refer section 5.3.
- Presentation of the individual film layer structures (physical properties of the layer(s) comprising a given film), as determined via refinement of respective KFPs. Refer section 5.4.
- Rationalization of the process factors dependences of (certain) trends observed in the (refined) film layer(s) physical properties. Refer section 5.5.
- Modeling experimentally recorded SE spectra via physically meaningful oscillator models, to obtain the energy (E) dependence of Tr of the Si doped In_2O_3−$(ZnO)_3$ (ISZO) film-substrate-combine. Comparison of the same with the experimentally determined dependences. Presentation and consideration of the inter-relationships, among the characterizations, that enabled said modeling. Refer section 5.6.

- Considerations and rationalization of our results in light of published results on the given pressure distance product ($\phi_{\mathrm{t-s}}$) dependence of sub-plantation during sputtering. Refer section 5.7.
- Consideration of the growth of films from collimated sputtered material flux. Suggestion thereby, of a phase-diagram for SPL formation. Refer section 5.8.
- Consideration of the role of our experimentation choices that in enabling the successful preservation and detection of a nanoscale SPL. Refer section 5.9.
- Discussion of the bonafides of the SPLs observed by us, via an ab initio DA, and an experimental RSA, of their physical properties. Refer section 5.10.

1.5.G Chapter 6 entitled 'The thin-film layer'

We present the results of interrogation of electronic and physical properties of the thin-film layer (TFL).

The section-wise overview of this chapter is:

- Detailed introduction to the chapter discussions. Refer section 6.1.
- Introduction to the amorphous In−Zn−O material system. Discussion of Si doping into the same. Refer section 6.2.
- Further quantitative discussion of electronic and electrical properties of commercial significance, of our ISZO films. The discussions are on basis of the Drude (D) model. Presentation of further results obtained from the modeling of experimentally recorded SE spectra. Comparison thereby of 'optical' and 'electrical' estimates of film opto-electronic properties. Refer section 6.3.

- Quantitative discussion of the electronic properties of our ISZO films, on basis of temperature dependent Hall Effect (HE) measurements. The measurements yielded the aforementioned "electrical" estimates. Determination thereby of the compensated nature of film (TFL) electronic state, on basis of the BH model of IIS of conduction electrons. Refer section 6.4.

- Quantitative discussion of the oxygen induced progress, of our ISZO films, towards a metal. The discussions are on basis of the Ioffe-Regel and Mott theories of the metal insulator transition (MIT). Refer section 6.5.

- Presentation of the results of a RSA of TFL physical properties, and of film electronic properties (at room-temperature). Refer section 6.6.

1.5.H Chapter 7 entitled 'Conclusions and scope for future work'

Here, we sum up the results of this study.

The section-wise overview of this chapter is:

- Detailed introduction to the chapter discussions. Refer section 7.1.

- Overview of the technical aspects and results of this study as presented in chapters 2 through 6, to highlight the inter-relationships among them. Thereby, we present a ready-reckoner for this thesis in figure 7.1. Refer section 7.2.

- Having overviewed the results of this study, we consider their significance in light of the film loci to which they pertain. We also consider the significance of the new hardware developed by us for high-throughput, rational, and efficient experimentation. Refer section 7.3.

- We signpost outstanding scientific / technological research themes that may be addressed on basis of this study. Refer section 7.4.

1.5.I Appendix A entitled 'Elements of analysis I: refinement and modeling of experimental data'

We present elements of analysis that accompany the characterization results per chapters 3, 5, and 6.

The section-wise overview of this appendix is:

- Detailed introduction to the appendix contents. Refer section A.1.
- Supporting analysis of XRR data. Refer section A.2.
- Supporting analysis of SE data. Refer section A.3.

1.5.J Appendix B entitled 'Elements of analysis II: calculations based on experimental data'

We present elements of analysis that accompany the calculations per chapters 5 and 6.

The section-wise overview of this appendix is:

- Detailed introduction to the appendix contents. Refer section B.1.
- An exemplary computer program as was developed for linear modeling of a given experimentally determined electronic or physical property of film layer(s), as were presented in chapters 5 and 6. Refer section B.2.
- The computer program as was written to compute total donor concentration (N_D) and total acceptor concentration (N_A) under a BH analysis of IIS of conduction electrons for our ISZO films, as presented in chapter 6. Refer section B.3.

1.6 Original contributions of this thesis

The results presented in this thesis advance the state of the art of sputter deposition of films, as also the state of the art of transition metal oxide (TMO) films. There are three principal results, as follows:

The first result is the development of a system for experimentation in light of design of experiment (DOE) principles. The development work involved custom design and fabrication of new hardware. The hardware referred to is the substrate holder cum sputter flux collimator array (SHCSFCA). The SHCSFCA additionally enabled film depositions to be performed at high-throughput.

Prior to outlining the second result, one might consider the words of Professor George Box, among the doyens of DOE (George E. P. Box, J. S. Hunter, and W. G. Hunter, 2005):

> "Discovering the unexpected is more important than confirming the known"

This leads us naturally to the second result, namely, the successful manifestation, preservation, and detection of a nanoscale SPL in sputtered films.

The third result concerns the electronic state of the film proper. Starting from experimentally measured absolute temperature (T) dependences of conduction electron concentration (n) and of conduction electron mobility (μ), we determine that the electronic state of the system is compensated.

In closing this chapter, the reader is invited to peruse and bookmark the ready-reckoner of this thesis, presented in figure 7.1.

Chapter 2

Literature survey

2.1 Introduction

In this chapter, we survey relevant literature by way of presenting a backdrop for this study. Accordingly, we introduce amorphous oxide semiconductors (AOSs) as the material system that is the subject of this study (section 2.2). This is followed by a comparative discussion of various approaches for transition metal oxide (TMO) film deposition (section 2.3). We then discuss the sub-plantation layer (SPL), and its role in film-substrate adhesion (section 2.4). This is followed by a discussion of design of experiment (DOE) studies on sputtered TMO films (section 2.5). Finally, we overview the general goals of new transparent conducting oxide (TCO) film development (section 2.6).

2.2 Amorphous oxide semiconductors

2.2.A Introduction

A survey of the published literature on transparent oxide films shows that the present phase of research and development (R&D) in the field commenced around the turn of this century (D. S. Ginley and C. Bright, 2000;

C. I. Bright, 2008). Leading into this phase, the field was characterised by empirical studies on oxide films of the (individual) metals indium (In), tin (Sn), and zinc (Zn) (Gregory J. Exarhos and Zhou, 2007).

The present phase has seen the introduction of a number of new TCO materials. Amorphous phases of 'mixed' oxides of In and Zn are an important case in point, and are the subject of this study (refer chapters 4 and 5 and 6). Section 2.2.B presents an overview of such phases, while section 6.2, presents a focussed discussion of the same with reference to the present study.

Notably, theoretical predictability of the transparent conductive (TC) properties of such (new) amorphous materials remains elusive (Hideo Hosono, 2010b; Kılıç and Zunger, 2002). We will address this point further in chapter 7, where we discuss, among other issues, machine-learning (ML) approaches for new materials discovery and development.

Here, we present an overview of the traditional binary TC film material systems, viz., indium sesquioxide (In_2O_3) and zinc oxide (ZnO). We will consider limitations of such binary materials for TC and transparent semiconductive (TS) applications. In particular, we will consider the constraints attaching to the development of In_2O_3 and ZnO films for TC or TS applications (section 2.2.B).

Consequent to such discussions, we will be positioned to consider the design concept of ternary and quaternary oxide material systems. Particularly, we will discuss how such materials alleviate the constraints referred to previously (section 2.2.C).

2.2.B Binary oxides

Transparent electrodes in liquid crystal displays (LCDs), electrochromic windows, and solar cells, antistatic coatings for aerospace applications, and heating stages for optical microscopes are among the traditional 'passive'

applications of TMO films (Hartnagel et al., 1995; C.-G. Granqvist, 2008).

Such applications require passive service (e.g., as an electrode) from the TMO film. Accordingly, a major focus of R&D effort is on enhancing the conductivity (σ) of the electrode (film). The upper limit of σ of TC TMO films has been estimated theoretically to be $2.5 \times 10^4\,\mathrm{S/cm}$ (Bellingham, W. Phillips, and Adkins, 1992; Robbins and Wolden, 2003).

Increasingly, transparent and conductive or semiconductive TMO films are finding 'active' duty in the transparent thin-film transistor (TFT). The TFT is the basis of a slew of modern electronic applications (Barquinha et al., 2012). Contrary to the aforementioned passive applications, active duty requires smaller conduction electron concentration (n), as one among a host of other considerations.

Electronic properties (e.g., σ, and n) of TMO films are governed by the unavoidable structural defects (oxygen (O) vacancies and / or metal interstitials), and by any introduced substitutional defects (which come to occupy cation sites, and have a valence different from the regular occupant of the site). The defects give rise to defect states (donor or acceptor) within the band-gap.

Two of the most common oxide material systems servicing passive transparent electronics applications are the binary material systems In_2O_3 and ZnO. The valence electron configurations of metal cations and of oxygen anions is respectively, ns^0 and $2s^2 2p^6$, wherein n = 4 for ZnO and n = 5 for In_2O_3. The empty s-orbitals of the metal species constitute the states at the energy of minimum of conduction band (E_c), while the full 2p-orbitals of the oxygens constitute the states at the energy of maximum of valence band (E_v). Given their spherical 's' nature, the states at E_c physically overlap, and therby enable electron transport.

Oxygen vacancies give rise to shallow donor levels, and thereby to n-type conduction in both aforementioned material systems. Particularly, for ZnO, neutral oxygen vacancies are electron traps that lie deep within band-gap. The properties of films of both material system are highly sensitive to the process conditions during deposition. In particular, ZnO films tend to be polycrystalline, which makes film uniformity and reproducibility difficult to achieve in practice. This disadvantages their use, particularly for large area applications. In_2O_3 films also tend to be polycrystalline. However, over a (narrow) range of process conditions, depositions performed at low temperatures (<150 °C) yield amorphous In_2O_3 films.

Grain boundary scattering limits the conduction electron mobility (μ) of such films, particularly at low n. At higher n (typically $>1.5\times10^{18}/cm^3$ for In_2O_3), μ is limited by ionized impurity scattering (IIS) (Ellmer, 2001). Furthermore, high temperature (>200 °C) processing is required (for films of both In_2O_3 or ZnO, either during or post deposition), before they are rendered suited for commercial service.

In light of the preceding, In_2O_3 and ZnO films are not ideal for service in upcoming TFT applications. This is, and as noted previously, since such applications require low n films that nevertheless display appreciable μ.

2.2.C Ternary and quaternary oxides

In light of the preceding discussions, multicomponent oxide films comprising transition metal and post transition metal (valence configuration $(n-1)d^{10}s^0$) were proposed and demonstrated (Hideo Hosono, Yasukawa, and Kawazoe, 1996; Hideo Hosono, 2006; Taylor et al., 2008). Such films present an amorphous microstructure over a very broad range of processing conditions (including to temperatures >500 °C), while simultaneously presenting μ values comparable to those achieved in degenerately doped binary

composition films (upto $10\,cm^2/(V\,s)$) (Dehuff et al., 2005).

Next we consider the chemical basis of the aforementioned observations. We do so via figure 2.1, and with reference to an exemplary ternary material system, viz., In−Zn−O.

The states at the E_c of multicomponent oxide films comprise isotropic 'ns' orbitals. For $n > 4$, the spatial extent of such orbitals exceeds the inter-cation distance. This is in contrast to the situation in single crystal silicon (Si), wherein the states at E_c are comprised of anisotropic sp^3 orbitals. Furthermore, given their isotropic (spherical) nature, the aforementioned overlap of ns orbitals is not sensitive to the degree of microstructural disorder present.

Typically however, $n(In-Zn-O) \geq 1 \times 10^{17}/cm^3$, which is yet too high for active semiconducting applications. The introduction of a suitable third metal into In−Zn−O addresses this aspect.

The most widely studied quaternary oxide material system thus, is In−Ga−Zn−O (IGZO). Given the high ionic potential of gallium ion (Ga_3^+), free carrier generation is suppressed. Furthermore, the amorphous state is stabilized due the additional microstructural disorder introduced via introduction of the additional cation (Ga_3^+).

In this study, we proceed in light of the aforementioned observations, whereby we selected Si as the source of the third cation (refer section 6.1). The specific material composition studied by us is presented in section 4.2, and is referred to in this thesis as 'ISZO'.

Among other desirable features, Si doped $In_2O_3-(ZnO)_3$ (ISZO) contains $52\,wt\,\%$ In_2O_3 (refer section 4.2.B). This may be compared to, say, the gold-standard TCO material, viz., indium tin oxide (ITO), which contains $90\,wt\,\%$ In_2O_3. Given the discussion of security of supply of In per section

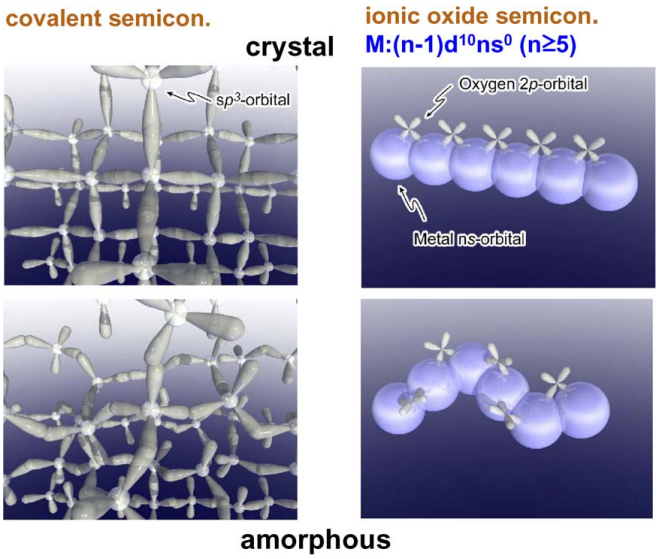

Figure 2.1: The orbital drawings of energy of minimum of conduction band (E_c) in conventional covalent semiconductors, and in ionic oxide semiconductors. Electron flow pathways are not disrupted in the amorphous state of ionic semiconductors given the spherical isotropic nature of the metal (M) ns^0 orbitals constituting the states at E_c. In contrast, given the anisotropic nature of the sp^3 orbitals that constitute the states at E_c in covalent semiconductors, disruption of crystalline order also disrupts electron flow pathways. Figure adapted from Hideo Hosono, 2006.

1.2.A, this is a commercially significant aspect of our study (Barquinha et al., 2012).

2.3 Transition metal oxide film deposition

2.3.A Introduction

We present the general process*-structure-property considerations that attend film deposition (section 2.3.B). We then overview the various approaches for TCO film deposition, and motivate thereby our choice for the same, viz., sputtering (section 2.3.C).

*Deposition process.

2.3.B General considerations

Evidently, the understanding of film process-structure-property relationships will be improved via development of new TCO materials. Alternatively, such understanding will help co-optimize the two defining properties (viz., transparency and conductivity) in existing ones (Gregory J. Exarhos and Zhou, 2007).

Such understanding will entail determination of the role of chemical bonding and structure, and of microstructure, in charge transport. Furthermore, film stoichiometry and stress affect its charge transport properties.

The role of film interfaces (surface and film-substrate interface, and grain boundaries if present) must also be accounted for. Thereby, an understanding of chemical interactions between the film and the substrate is called for (Quinto, 2007).

Evidently, the aforementioned considerations emerge consequent the film deposition process (including any post deposition processing steps). Next, we discuss various approaches for deposition of TCO films.

2.3.C Various approaches

2.3.C.1 Introduction

We discuss exemplary techniques of various approaches for TCO film deposition (Gregory J. Exarhos and Zhou, 2007). Generally speaking, solution based (atmospheric pressure) approaches offer deposition costs advantages, while vacuum based approaches enable superior quality films.

Accordingly, we discuss the exemplary solution based sol-gel technique (section 2.3.C.2). This is followed by a discussion of the spray pyrolysis (SP) technique, which combines advantages of solution-to-solid approaches (as aforementioned) and of gas-to-solid (physical vapour deposition (PVD)) ap-

proaches (section 2.3.C.3). Next, we consider two exemplary vacuum based techniques. The first of these is pulsed laser deposition (PLD) technique which generally yields the highest quality films (section 2.3.C.4). The second of these is sputtering which is the technique of choice for depositing high quality large area films (section 2.3.C.5).

2.3.C.2 Sol-Gel

The quality of TCO films deposited via atmospheric pressure solution based approaches is inferior to those obtained via vacuum based approaches (discussed in sections 2.3.C.3 and 2.3.C.4; see also, Donald M. Mattox, 2004). Nonetheless, they offer the potential of lowering device manufacturing costs given their intrisically lower capital (equipment) costs, and given their relative ease and scalability (Pasquarelli, D. Ginley, and O'hayre, 2011).

A sol-gel approach proceeds the evolution of inorganic networks starting with formation of a sol (colloidal suspension). Gelation of the sol results in formation of the continuous liquid phase inorganic network (gel). Spin casting of the gel onto substrates coats them (the substrates). A continuous oxide phase may now be formed by subjecting the coating to thermal treatment. The process can be repeated to yield thicker coatings. This is usually accompanied by improvement, e.g., densification, of the coating.

2.3.C.3 Spray Pyrolysis

The approach of SP is positioned midway between solution based and vacuum based approaches. It attempts to leverage the deposition costs advantages of the former, and the film quality advantages of the latter (Vai et al., 2014). This technique has been referred to as the "poor man's PLD"[†].

In this technique, a flowing gas carries droplets of a precursor solution

[†]By Professor C. N. R. Rao FRS. Private communication from Professor Peter P. Edwards FRS ML.

through a heated reactor towards a heated substrate. The droplets are obtained via an atomizer. The solvent evaporates during passage through the reactor. The solutes undergo thermal pyrolysis at, and coat, the substrate surface. Thereby, a film of the requisite oxide phase and morphology is obtained on the substrate (Rashidi et al., 2013).

The film stoichiometry of SP deposited films is expected to be as per the solution composition. This is since a submicrometer sized coating area is obtained per atomized droplet (Gregory J. Exarhos and Zhou, 2007). The ability to control film stoichiometry is an important advantage of SP, and has led to its wide use to deposit not just TCO films, but also superconducting and and piezoelectric ones. Other advantages include the ability to uniformly coat large areas of high aspect ratio geometries.

A high substrate temperatures (typically $\gtrsim$400 °C) is required during SP. The substrate temperature affects not just solvent drying and solute pyrolysis, but also the subsequent crystallization and grain growth (and orientation) as leads to film formation. As a matter of fact, the substrate temperature is recognized as the most important process determinant of film quality.

The aforementioned substrate temperature requirements effectively forbid use of plastic 'flexible' substrates (Zardetto et al., 2011; Agaiby, 2018). In turn, flexible electronics applications based on such substrates are ruled out (Lampert, 2012; Zervos, 2015). Given the requirements of the robustly upcoming field of flexible electronics (Bradley and Huang, 2017), this is a significant drawback of the SP technique.

2.3.C.4 Pulsed Laser Deposition

High quality phase pure multicomponent epitaxial films may effectively be deposited via the approach of PLD (Perkins et al., 2002; Donald M. Mattox,

2015a). Particularly, deposition of oxide films may be performed under moderate to ultrahigh vacuum (M. Grundmann et al., 2005).

In this technique, a ultra violet (UV) laser source is used to generate a train of high energy nanosecond laser pulses. The pulse train is focussed and rastered over a target, which could be a metal, or metal oxide (single crystal or powder). The rastering causes the formation of a 'laser plume', comprised of ablated atomic and molecular material from the target. A suitable substrate placed within the plume volume will thence receive a coating of the material. While the substrate could be unheated, typical end use applications necessitate it to be heated to temperatures in the range 450 °C to 700 °C.

The aforementioned processing is performed inside a vacuum chamber, which permits control over the oxygen partial pressure. Typical applications require the oxygen partial pressure to be below a few mTorr (Matsubara et al., 2002). A wide deposition-rates range is possible (10 nm/min to 6×10^4 nm/min), and such control ability serves as a handle to control the quality of the deposited film.

A survey of the published literature shows that the lowest resistivity ($\lesssim 1 \times 10^{-5}\,\Omega\,\mathrm{cm}$) TCO films as have been reported were typically deposited via PLD (Suzuki et al., 2002; Agura et al., 2005). Nonetheless, the technique of sputtering is another commercially important technique within the industry, owing especially to its capability to coat large areas. We discuss this technique next.

2.3.C.5 Sputtering

Sputtering is among an industrially important film deposition approach (Donald M. Mattox, 2015b; Sproul, 2008). This is given the abiding costs vs film quality advantages that it presents, particularly for large area appli-

cations (Hill, Nadel, and Andreasen, 2008).

Sputtering approaches include direct current magnetron sputtering (DCMS), radio frequency magnetron sputtering (RFMS), and reactive sputtering (Wasa, Kitabatake, and Adachi, 2004; Adachi et al., 2012; Donald M. Mattox, 2010b). Targets of electrically conductive (metal) materials are conducive for DCMS, while those of insulating (semiconducting) material compositions are conducive for RFMS (Anderson, Mayer, and Wehner, 1962).

As noted, sputtering is widely practised for large area TCO applications (Tadatsugu Minami, 2005). However, it is often difficult to obtain a spatially homogenous plasma during DCMS and reactive sputtering approaches. This results in depression in quality of deposit film. Nonetheless, RFMS approaches help alleviate such issues (Gregory J. Exarhos and Zhou, 2007).

Furthermore, the schema in which sputtering is performed permits deployment of other film deposition techniques. Thereby, layers of other materials that are (more) properly deposited via such other techniques, may too be readily obtained. This feature is particularly useful to generate integrated multilayer device structures (Hagiwara, Nakada, and Kunioka, 2001).

In light of the preceding discussions, and given the electrically insulating nature of our target material, viz., ISZO (refer section 4.2.C), we have employed RFMS to deposit the films used in this study. Our scheme for film deposition is described in chapters 3 and 4.

2.4 The sub-plantation layer: film-substrate adhesion

2.4.A Introduction

We consider the commercial and technological significance of the SPL in section 2.4.B. We then consider the SPL in TMO films in section 2.4.C

2.4.B Commercial and technological significance

According to Donald M. Mattox, 2016, one may consider there to be 'good adhesion between a thin film/coating and a substrate' when 'the interfacial region (or "nearby material") does not fail ("deadhesion") during processing, or service conditions over its lifetime, nor at unacceptably low stress levels under test conditions' (refer also D. M. Mattox, 1978).

Evidently, the film-substrate interface is an (among others) important determinant of adhesion. Sub-surface implantation of sputtered material flux can result in the formation of a SPL, which constitutes a "pseudodiffusion interface" (Donald M. Mattox, 2016; Donald M. Mattox, 2013)[‡] between film and substrate (Lifshitz, Kasi, and Rabalais, 1989; Lifshitz, Kasi, Rabalais, and Eckstein, 1990).

The commercial significance of film-substrate adhesion is attested to by the fact that there are "more than 200 different methods for measuring film-substrate adhesion" that are "material, geometry and even industry specific" (Volinsky, Moody, and Gerberich, 2002).

The state of affairs so underscores (is a consequence of) film-substrate adhesion's "lack of susceptibility to measurement" (Chapman, 1974).

In section 2.5.B, we will consider studies investigating the evolution of opto-

[‡]Note that this is but one type of film-substrate interface according to the categorization by Donald M. Mattox, 2016.

electronic properties of TMO films under mechanical stressing (induced deadhesion).

2.4.C Transition metal oxide films

The phenomena of Sub-Plantation has been mentioned only in passing by published TMO film studies.

Kobrinsky et al., 2008 studied the gas sensing properties of sputtered ZnO films deposted on borosilicate glass substrates. They tailored saia properties by varying the O non-stoichiometry. They alluded to the deposition conditions dependent sub-plantation, and consequent trapping, of "energetic oxygen and zinc species ... [into] ... sub-surface sites". This was forwarded as a potential mechanism by which film stoichiometry may be varied. The study did not present any quantitative investigation of the sub-plantation phenomena.

Talagrand et al., 2015 present a spectroscopic ellipsometry (SE) study of RFMS deposited In−Ga−Zn oxide films. The target-substrate distance (l_{t-s}), process gas pressure (p), and RF power (P_{RF}) were $4\,\mathrm{cm}$, $5.3\,\mathrm{mTorr}$, and $100\,\mathrm{W}$ respectively (compare with the same deposition conditions of the present study, per tables 3.4 and 5.4).

It is instructive to compare experimentation details (such as the given pressure distance product (ϕ_{t-s}), and substrate-stage rotation) per the present study with those of the aforementioned study of Talagrand et al., 2015. Thereby, ones notes ...

- ... that ϕ_{t-s}(present study, films at the front-plane of the experiment design) = $180\,\mathrm{mTorr\,mm}$ (refer table 5.3), while ϕ_{t-s}(Talagrand et al., 2015) = $212\,\mathrm{mTorr\,mm}$; and furthermore,

- ... that, similarly to the case of the present study (refer discussions of

azimuthal rotation of the substrate-stage per section 3.4.C and figure 3.5, and section 5.8.D), Talagrand et al., 2015 too performed their film depositions in "static mode".

In light of the aformentioned comparisons, one may not rule out sub-plantation of sputtered material flux into the substrate during the film depositions performed by Talagrand et al., 2015.

Indeed, while Talagrand et al., 2015 found it expedient to analyze their SE data in terms of a "double pseudo-layer structure" (refer figure 2.2) they explicitly state that their results "cannot be interpreted by two strictly superposed layers". In fact, they interpret their results as, "an inhomogeneity of the optical properties through the thickness". Furthermore, they postulate the same to be a result of "Surface passivation, and/or contamination".

As will be seen in sections 5.3, 5.6.C, and 6.3.D, in the present study the film layer structure was determined experimentally and directly (that is, sans assumptions, or modeling) via x-ray reflectometry (XRR). The determination so was the basis of analysis of the SE data. However, Talagrand et al., 2015 do not present independent determination of the layer structure of their films.

In other words, Talagrand et al., 2015 do not recognize the potential occurence of sub-plantation into substrate, and invoke other phenomena to explain their choice of a two-layer film structure.

We address a further consideration re the film-substrate interface, since it concerns the commonly employed technique of post deposition annealing. Such annealing is commonly employed to improve the electronic transport properties of TMO films (Calnan and Tiwari, 2010).

In this regard, it is known that the effect of film annealing, on the film-substrate interface, and in turn, on film electronic properties, can be sig-

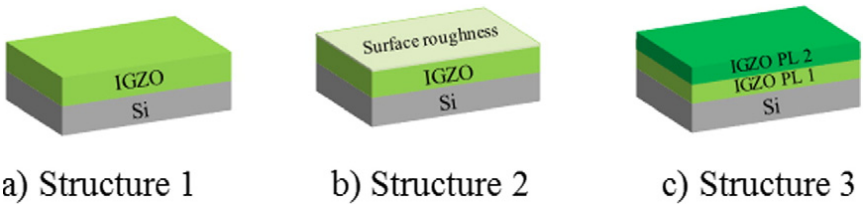

Figure 2.2: Film layer structures considered by Talagrand et al., 2015 to model their spectroscopic ellipsometry (SE) data. (a) Single layer structure, (b) structure with a surface roughness layer, and (c) double pseudo-layer (PL) structure. They analyze their data in terms of structure (c) (their "Structure 3").

nificant (Rose and Gregory J Exarhos, 1997). The existence of a substrate dependent critical temperature (which for ZnO, is in excess of 675 K) has been experimentally ascertained.

When annealing is performned at temperatures below the critical temperature, one observes the expected enhancement in density and crystalline fraction of, and stress in, a film. However, exposure (annealing) of the film to temperatures above the critical temperature, leads to the formation of an (in-situ) layer at the film-substrate interface. This layer manifests on account of chemical reactions that ensue between the film and substrate. Furthermore, reactions between the film and cations from the substrate result in the alteration of film electronic properties. With increasing temperature, the in-situ layer grows to cover the entire film.

The film depositions in the present study were performed on to unheated substrates (refer section 4.2.C), and the amorphous phase nature of the resulting films (refer section 6.2) confirms that no substantive excursion of the film / substrate temperature occured due bombardment (during film growth) of substrate by energetic sputtered material flux. Furthermore, our films were not subjected to any post deposition annealingt. As such, the aforementioned critical temperature (energy) scale is not pertinent for

interpretation of the results re the film-substrate interface, of the present study.

2.5 Design of experiment studies on sputtered films

2.5.A Introduction

A limited number of studies on sputtered TMO films have exploited DOE techniques. Such studies have, in the main, considered extensively studied material systems.

This has been with a view to demonstrate the 'guidance' capabilities of DOE and response surface analysis (RSA) methods to simultaneously optimize multiple film properties of interest. Here one bears in mind that the optimizations so are limited by the factor-ranges available in the sputtering equipment at issue. The properties of interest include opto-electronic properties. They also include mechanical properties that are relevant for film-substrate adhesion.

Such studies are surveyed in section 2.5.B. The survey so is concluded via an epilogue on the same, presented in section 2.5.C.

2.5.B Evolution of opto-electronic and mechanical properties of transition metal oxide films

2.5.B.1 Deposition factors dependence

S.-I. Jun et al., 2005 studied RFMS deposited ITO films. They considered the problem of simultaneously optimizing the sheet resistance (R_s) and transmission fraction (Tr) of their films. As discussed in section 6.3.C, both R_s and Tr increase with decrease in n. The usual technological goal is determine the film deposition process conditions to minimize R_s simultaneous

with maximizing Tr of the resulting films.

They considered four process factors — viz., P_{RF}, substrate temperature (T_s), p, O partial pressure — and utilized a four-factor three-level Taguchi DOE (Taguchi and Konishi, 1987; Nair, 1992), and conducted 9 experiments 'runs' to achieve their optimization goal. Their analysis also revealed the dependence of film crytalline fraction and its preferred orientation on the process factors aforementioned. Thereby, via investigation of film microstructure, they illumined the causal chain linking the process factors to the observed changes in properties of interest.

Hu et al., 2020 studied RFMS deposited 'Al / AZO' double layers. They considered the problem of optimizing the opto-electronic properties (maximizing the Haacke Figure Of Merit (ϕ_{TC}); (Haacke, 1976)) of the Al doped ZnO (AZO) layer, as a function of three factors (thickness, annealing temperature, annealing duration), related to the aluminum (Al) buffer layer. They utilized a three-factor two-level Taguchi DOE (Taguchi and Konishi, 1987; Nair, 1992) to achieve their stated optimization goal by conducting 4 experiments (runs).

Dhage and Badgujar, 2018 studied cylindrical rotating target DCMS deposited AZO films. They considered the problem of optimizing film opto-electronic properties (conductivity, uniformity, transparency) for large area photonic and electronic applications. They considered three factors (sputtering power, argon (Ar) / oxygen molecule (O_2) flow rate, substrate temperature). The DOE they present comprised 11 experiments (runs).

Kumar et al., 2013 studied sputtered amorphous In−Zn−O films deposited on (among others) flex glass substrates. They considered the problem of simultaneously optimizing their residual stress and electrical conductivity. For flexible electronics applications, the usual technological goal is to deter-

mine the film deposition process conditions that minimize residual stress, simultaneous with maximizing conductivity of the resulting films.

They considered four process factors (sputtering power, growth pressure, O partial pressure, radio frequency (RF) power ratio) and utilized a four-factor two-level full-factorial with center-point DOE (Dunn, 2016) to achieve their stated optimization goal by conducting 17 ($= 2^4 + 1$) experiments (runs).

Their analysis confirmed the role of the energetic nature of the sputtering process in determining film residual stress. Notably, they demonstrated the practice whereby prior knowledge of (presently, re growth parameter-conductivity relationship) was used to suitably extrapolate their results outside of the parameter space considered by their DOE. They were thus able to achieve their stated optimization goal.

Further to the aforementioned studies, particularly the study of Kumar et al., 2013, we next consider studies investigating the change in opto-electronic properties of TMO films under mechanical stressing. The same should be considered in light of the definition of "good adhesion" presented in section 2.4.B.

2.5.B.2 Post deposition mechanical stressing dependence

Alzoubi et al., 2011 studied pre-fabricated (commercially available) ITO on polyethylene terephthalate (PET) substrate films (ITO-PET structure). They sought to establish "a baseline for a comprehensive reliability study of ITO thin films on flexible substrate". In order to do so, they conducted high cycle bending fatigure experiments on their ITO-PET structures.

During service in flexible electronics applications, the film substrate structure undergoes mechanical flexing (bending). As such, the usual technological goal of the R&D re such applications is for the film to continue to display its (original) electrical conductivity during its service lifetime.

They considered three process factors (bending diameter, bending frequency, sample width) at fixed number of bending cycles. They present the DOE they utilized, on basis of which they determined the factors (bending diameter, and number of bending cycles) that influence the film conductivity.

Notably, this study (perhaps on account of being on commercially sourced ITO-PET structures) did not address the deposition process factors dependence of film mechanical properties; nor their influence, in turn, on the film conductivity.

Peng et al. (C.-Y. Peng et al., 2012; C. Peng, Hamasha, et al., 2013; C. Peng, Dhakal, et al., 2014) studied RFMS deposited AZO on Corning flexible Willow glass substrates. They investigated films grown on strained, and on normal, substrates. Specifically, they investigatd the degradation in film electrical and optical properties under a diverse set of cyclic bending conditions.

In order to do so, they conducted cycle bending fatigue experiments on their film-substrate structures. As noted previously, during service in flexible electronics applications, the film substrate structure undergoes mechanical flexing (bending). Accordingly, and as noted earlier, the usual technological goal of the R&D re such applications is for the film to continue to display its (original) electrical and optical properties during its service lifetime.

They considered three process factors (growth method, bending radius, tension) at fixed bending frequency. They utilized a three-factor two-level full-factorial DOE (Dunn, 2016), whereby they conducted 8 ($= 2^3$) experiments (runs). They determined that while strained growth method does change film properties, the same method does not lead to a significant improvement in film reliability post cyclic bending fatigue experiments.

Notably, this study did address the deposition process factors dependence of

film mechanical properties; and their influence in turn on the film electrical and optical properties.

2.5.C Epilogue

A consistent feature of the above studies is that they are confirmatory in nature. The reasons underlying the choice of experiment design, in terms of the goals sought, are not discussed. Significantly, analysis of the experimentation results has not been proceeded to guide theory development (refer sections 5.10.B and 5.8.D; see also, Palmer, 2008; Albrecht et al., 2013).

2.6 New transparent conducting oxide film development

2.6.A Introduction

We discuss the goals of new TCO materials development, and compares the options available to meet it (section 2.6.B). Hence, we compare our results against those in the published literature (section 2.6.C).

2.6.B Primary goal

A primary goal during TCO films development is to decrease (minimize) film resistivity (ρ) while retaining acceptable (maximizing) Tr. On face of it, the following two options present themselves to decrease film ρ (refer equation 4.11e), or $\mathrm{R_s}$ (at given fixed d; refer equation 6.5a): enhance n, or enhance μ.

Figure 2.3 helps understand the consequences for film Tr of traditional TCO materials (e.g., $\mathrm{In_2O_3}$; refer section 2.2.B), of proceeding either of the aforementioned options. The analysis (calculations) presented in the figures are on basis of the Drude (D) model.

Figure 2.3(a) presents the consequences of increasing n, at fixed μ, for a

representative traditional TCO film. One expects conduction electron absorption to increase with increase in $\mathbf{n}$, since more conduction electrons (per unit volume) are available to absorb photons. Indeed, the height of the absorption band increases with increasing $\mathbf{n}$ (equivalently, with decreasing ρ).

Note also that the absorption peak moves progressively closer to the (upper limit) of the visible range of wavelengths ($0.4\,\mu\mathrm{m}$ to $0.7\,\mu\mathrm{m}$) with increasing $\mathbf{n}$. This results in an increase in absorption of these wavelengths with increasing $\mathbf{n}$. Nonetheless, the absorption of these wavelengths remains low. This is owing to the inability of conduction (free) electrons to stay in phase with the exciting electromagnetic field at the wavelengths (equivalently, frequencies) at issue.

Figure 2.3(b) presents the consequences of increasing μ at fixed $\mathbf{n}$ for the (same and traditional) TCO films per figure 2.3(a). Variation (increase) in μ does not result in a change of the wavelength at which absorption peaks. However, one notes that the height of the absorption peak decreases with increasing μ (equivalently, with decreasing ρ).

This is in contrast to the situation presented in figure 2.3(a), whereby the height of the absorption peak increased with increase in $\mathbf{n}$. Thereby, one determines that the preferred option for developing improving the opto-electronic performance of films of traditional (binary TCO) materials (that is, films with lowered ρ) is via enhancement of μ, as opposed to enhancement of $\mathbf{n}$ (Morales-Masis et al., 2015; Macco et al., 2014).

Finally, note that in traditional TCO materials, increasing $\mathbf{n}$ is accompanied by a decrease in μ. This is understood as being due to decreases in the various free electron scattering times with increasing $\mathbf{n}$ (refer section 4.5.D). However, in AOS material system such as the one per this study, μ increases

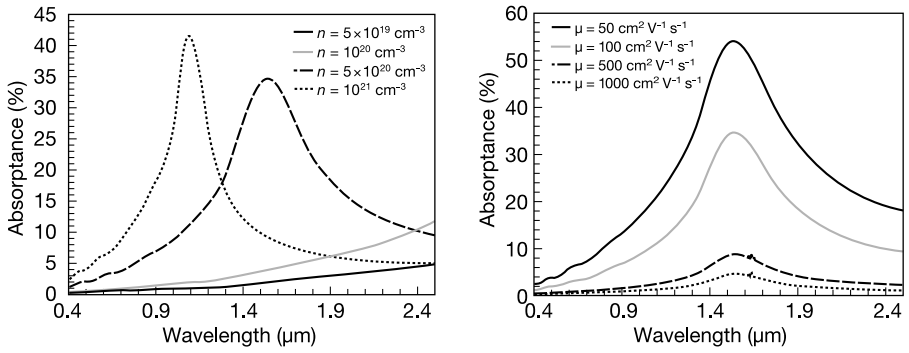

(a) (b)

Figure 2.3: Calculated free carrier absorptance of films with $\varepsilon_\infty = 4$ and $\mathrm{m} = 0.3\mathrm{m_e}$, $\mathrm{d} = 500\,\mathrm{nm}$. (a) The effect of increasing conduction electron concentration (n) at fixed $\mu = 100\,\mathrm{cm^2/(V\,s)}$. (b) The effect of increasing conduction electron mobility (μ) at fixed $\mathrm{n} = 5\times10^{20}/\mathrm{cm^3}$. Here, high frequency dielectric permittivity (ε_∞), effective mass of electron (m), rest mass of electron ($\mathrm{m_e}$), thickness (as applicable) of film or of film layer (d). Figures adapted from Coutts, Young, and Li, 2000.

with increase in n (Nomura, Kamiya, Ohta, et al., 2004; Nomura, Ohta, Takagi, et al., 2004; Hideo Hosono, 2006; Kim et al., 2017; Ide et al., 2019; see figure 2.4).

Section 6.3.C (particularly, figure 6.5) presents quantitative analyses, on basis of the D model, of the experimentally determined λ dependence of Tr of the ISZO films that are the subject of this study. The analyses will expand upon the discussions presented above.

2.6.C Comparison: present vs published results

Figure 2.4 presents the experimentally determined (n, μ) of the ISZO films that are the subject of this study, and of films of kindred material systems as reported in exemplary published studies (Kamiya, Nomura, and Hideo Hosono, 2013). The figure enables ready assessment of our results in light of the discussions presented above.

Evidently, at (any) given n, our films (by which is meant here material

system and film deposition protocol; refer section 4.2) present enhanced (in comparison to published results) $\mu(\mathsf{n})$. This is a contribution of the present study to advancing the state of the art, in addition to the results and discussions presented in chapters 3, 5, 6, and 7.

Furthermore, with reference to table 5.1, the ISZO films obtained per our film deposition protocol (section 4.2) present nanoscale surface roughness. This represents another potential commercially relevant feature.

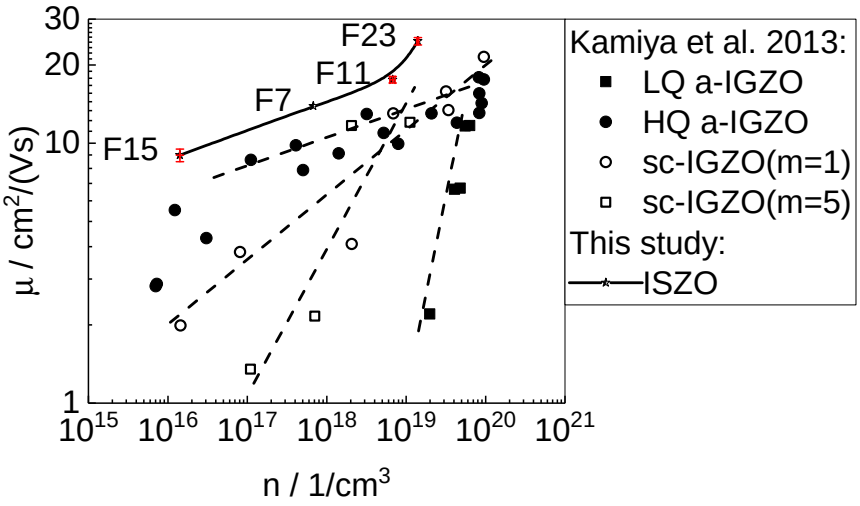

Figure 2.4: Electronic properties of the Si doped $In_2O_3{-}(ZnO)_3$ (ISZO) films per the present study, compared to those of In−Ga−Zn−O (IGZO) films per published studies. The four ISZO films per table 6.5 — viz., F15, F7, F11, F23 — are presented alongside published results (Kamiya, Nomura, and Hideo Hosono, 2013; Kamiya, Nomura, and Hideo Hosono, 2010a). The published results shown were obtained on films deposited via pulsed laser deposition (PLD); and furthermore, some of the films were subjected to post-deposition annealing at 400 K. The four ISZO films at issue were deposited via radio frequency magnetron sputtering (RFMS), and were not subjected to post-deposition annealing. As such, our results on ISZO films are on as-deposited films. The standard error bars in our results are shown in red (refer also figure 6.8 and table 6.5). Evidently, the electronic properties of our ISZO films compare favorably with those of kindred films per the published results shown. That is, our results (electronic properties) on ISZO films are appreciably better than those presented in published studies, despite having been deposited via a lower energy density process (RFMS vs PLD). Also, our fabrication process is simpler and less energy intensive since it does not involve post-deposition annealing. The commercial significance of our results is furthermore enhanced since RFMS is a large area film deposition technique widely practised in the industry. The curve (re our results), and dashed lines (re published results), are a guide for the eye. Here, 'single crystal $InGaZnO_4$' (sc-IGZO (m=1)), 'single crystal $InGaO_3(ZnO)_5$' (sc-IGZO (m=5)), 'high quality a-IGZO' (HQ a-IGZO), 'low quality a-IGZO' (LQ a-IGZO).

Chapter 3

Film deposition: design of experiment, sputtering, and the substrate holder cum sputter flux collimator array

3.1 Introduction

In this chapter, we present the two experimentation aspects that are key to this study. They are: experimentation conducted according to design of experiment (DOE) principles, and control of the angular distribution of sputtered material flux sourcing film growth. Both aspects were addressed from scratch.

We have designed and developed new experimentation hardware — the substrate holder cum sputter flux collimator array (SHCSFCA) — that dovetails the aforementioned aspects. Additionally, the SHCSFCA enables conduct a (our) designed experiment (DE) at high-throughput.

We demonstrate, as a direct consequence of deployment of the SHCSFCA, an order of magnitude improvement in experimentation (film deposition) throughput, relative the throughput of traditional film deposition protocols. Equivalently, the experimentation protocol enabled by the SHCSFCA (refer section 4.2) enables reduction of equipment and labour costs per film deposition by 3x-10x relative to the costs so due traditional protocols.

The aforementioned efficiencies are achieved simultaneous with enhancement in the quality (reliability) of film deposition. This is due the use of DOE principles.

While the SHCSFCA implemented by us is, of necessity, specific to the film deposition equipment used for this study (Kurt J. Lesker Company Model PVD 75), the implementation is capable of servicing a variety of full or fractional factorial (Bisgaard and Steinberg, 1997) DEs (refer figure 7.1). Furthermore, its design principles are extensible to service arbitrary DEs, and for given sputtered film deposition equipment.

Accordingly, we discuss DOE and the associated response surface analysis (RSA) methodology (section 3.2). We then discuss film deposition via radio frequency magnetron sputtering (RFMS) (section 3.3). Next, we discuss the angular distribution of sputtered material flux (section 3.4). With this background, we discuss the SHCSFCA (section 3.5).

3.2 Design of experiment methodology

3.2.A Introduction

We begin with an overview 'one factor at a time (OFAT)' experimentation (section 3.2.B). This positions us to discuss DOE experimentation (section 3.2.C). This then leads us to discus the RSA methodology for linear modeling of (film) properties (section 3.2.D). Thence, we present the experiment

design employed for this study (section 3.2.E).

3.2.B One factor at a time experimentation

Consider a system (e.g., a Si doped In_2O_3−$(ZnO)_3$ (ISZO) film), the properties of which are sensitive to a multiplicity of factors (e.g., film deposition process factors). It is required to determine the factors dependence of given properties (e.g., to determine quantitatively, the trade-offs necessary for simultaneous optimization of two or more said properties).

The film deposition technique of choice for this study is RFMS. As such, the following discussions are in context of process factors relevant for this technique.

It is known that the following deposition process factors are among the principal determinants of film properties: RF power (P_{RF}), and oxygen percent (O). A typical goal therefore, is to determine the dependence of film conductivity (σ) as a function of these process factors. Figure 3.1 describes the situation as inheres when such determination is attempted via OFAT experimentation.

Generally, OFAT approaches are ill-equipped to discriminate between main effects and interaction effects, that occur due the multiplicity of factors. Such effects are, not uncommonly, comparable in magnitude (refer for instance, pareto plots per figures 5.10, 6.14, and 6.20).

An OFAT approach would not permit the ascribing of an observed response to the main or interaction effects, of the single process factors that was varied (refer equation 3.1). Moreover, interaction effects can be specific to the given equipment.

As such, "experiments in which one factor at a time ...[is] ...varied ...[are] ...wasteful and misleading" (J. S. Hunter, 1987). In addition to being inherently self-referencing, the DOE methodology cures the aforementioned

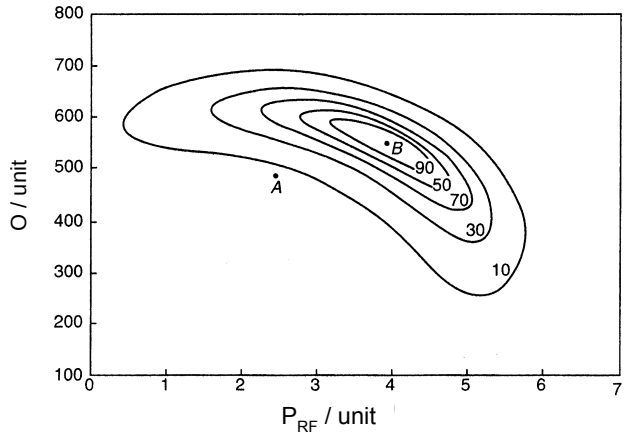

Figure 3.1: Navigation of given hypothetical contour plot on basis of one factor at a time (OFAT) vs design of experiment (DOE) principles. Given contour plot of property of interest (e.g., room-temperature conductivity (σ) of a Si doped In_2O_3–$(ZnO)_3$ (ISZO) film deposited via radio frequency magnetron sputtering (RFMS). The independent variables are RF power (P_{RF}) and oxygen percent (O); these are the process factors impressed during film deposition. If the goal is to determine (proceed towards) point B, starting from point A, then OFAT experimentation is sub-optimal (Dunn, 2016). This is since such experimentation does not systematically furnish information about the (likely) location of B relative A. The difficulty of determining B increases with the number of process factors at play. This is due the geometric (exponential) increase in the number of possible combinations of the process factors in a given real world situation. Experimentation performed according to DOE principles will result in progress towards point B in a rational and efficient (that is, cost-effective) manner, irrespective of number of process factors under consideration. Illustrative figure adapted from (Myers, D. C. Montgomery, and Anderson-Cook, 2011).

deficiencies of OFAT methodology (George E. P. Box, J. S. Hunter, and W. G. Hunter, 2005; Dunn, 2016).

3.2.C Design of experiment: applicable considerations

This study concerns layer structure and opto-electronic properties of transparent conductive (TC) transition metal oxide (TMO) films, deposited via RFMS. Three film deposition process factors, viz., P_{RF}, process gas pressure (p), and O, were identified to be of interest (refer, chapter 4).

As such, we adopted a three-factor two-level with center-point experiment design for our experimentation (film depositions). With reference to figure 3.12, this design does not suffer from confounding between the (main or interaction) effects due (of) a process factor.

The addition of an additional center-point experiment provisioned, in effect, an extra level for each of the process factors, for lowest possible increase in experimentation costs.

Figure 3.2 collates the formal considerations for a 'three-factor two-level' experiment design. This along with an additional 'center-point', is the experiment design used in this study. For simplicity, and without loss of applicability, the following discussions omit the center-point.

3.2.D Linear modeling and response surface analysis

A linear model of a given property of interest, valid over the process factors space spanned, may be determined from the set of experimentally determined responses (per section 3.2.C). The equation of the linear model, consistent with the experiment design per figure 3.2, is:

$$y = \beta_0 \quad \text{...baseline effect} \tag{3.1a}$$

$$+ \beta_A A + \beta_B B + \beta_C C \quad \text{...main effects} \tag{3.1b}$$

$$+ \beta_{AB} AB + \beta_{AC} AC + \beta_{BC} BC \quad \text{...two-factor interaction effects} \tag{3.1c}$$

$$+ \beta_{ABC} ABC \quad \text{...three-factor interaction effect} \tag{3.1d}$$

where, the meaning of the nine 'β-coefficients' are indicated. Physically, the β-coefficient β_0 (term 3.1a of equation 3.1) represents the baseline effect on a given response, of the three process factors. The baseline effect may be computed as the average of all observed responses. Each of the β-coefficients β_A, β_B, and β_C (terms 3.1b of equation 3.1) represent the main effects, on a

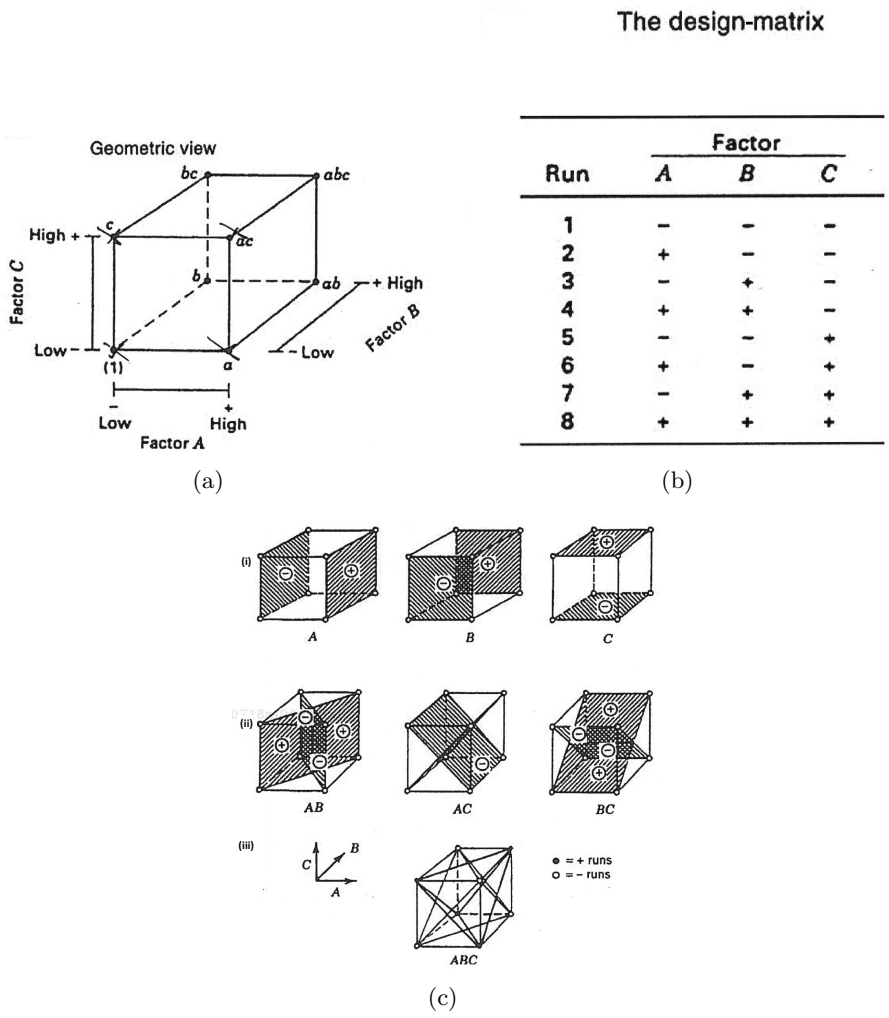

Figure 3.2: [Caption to this figure is presented on next page.]

given response, of the process factor to which they correspond. A main effect of a process factor may be computed as the average change in the response due a unit change in that process factor. The β-coefficients β_{AB}, β_{AC}, and β_{BC} (terms 3.1c of equation 3.1) represent the two-factor interaction effects, on a given response, due the (two) process factors to which they correspond. The β-coefficient β_{ABC} (term 3.1d of equation 3.1) represents the three-factor interaction effects, on a given response, due the (three) process factors at

Figure 3.2: [Figure corresponding to this caption is presented on the previous page.]
(a) Geometric representation of a three-factor two-level designed experiment (DE). The string of one, two, or three lowercase letters at each vertex represents the experimentally determined value of a property of interest, namely, the 'response'. For instance, "ac" is the response for (A, B, C) = (+, −, +). Here A, B, and C are the given three process factors; + and − are the given two levels, while 0 is the center-point (not shown) between the levels (the levels are expressed in coded units (CUs)). Table 3.1 presents the properties of interest for the present study. Refer figure 3.3 and table 3.4, and table 5.1. (b) The design-matrix representation of the DE per (a). Refer table 3.3. (c) Contrasts between the "−" and "+" levels, for (i) each of the three main effect, (ii) each of the three (symmetrical) two-factor interaction effects, and (iii) the sole three-factor interaction effect. Figure adapted from (Myers, D. C. Montgomery, and Anderson-Cook, 2011).

issue. The procedure to compute two-factor and three-factor interaction effects is described in Dunn, 2016.

With reference to figure 3.1 or table 3.4, one notes that the two-levels, viz., '−' and '+', for any given process factor, are separated by two units. In the present study, the factors '(A, B, C)' are '(P_{RF}, p, O)'.

Further details of (including the computer program developed for) the linear modeling (per equation 3.1), of various physical and opto-electronic properties of interest — on basis of their (respective) experimental measurements — are presented in appendix B. Properties of interest are listed in table 3.1.

3.2.E Design of experiment: this study

We detail the '3-factor, 2-level, full-factorial with center-point DE' employed for this study. Nine ($= 2^3 + 1$) films (multiple replicates of each) were deposited simultaneously, per the DE*.

The resolution of a DE for a given property is based upon (obtained subse-

*In this thesis, the terms 'designed experiment' (abbreviated as 'DE'), and 'experiment design' will be used interchangeably.

Property		Film layer	
Type	Symbol	SPL	TFL
Physical	d	✓	NA
	D	✓	✓
	r	✓	✓
	ν	✓	✓
Electronic*	ρ		✓
	μ		✓
	n		✓
	$k_F l_e$		✓

Table 3.1: Listing of physical and opto-electronic properties of interest, of film or of its layer(s) (sub-plantation layer (SPL), thin-film layer (TFL)) thereof. *Film only. Refer also table 4.1. Here, thickness (as applicable) of film or of film layer (d), density (as applicable) of film or of film layer (D), roughness (as applicable) of film or of film layer (r), film deposition-rate (ν), resistivity (ρ), conduction electron mobility (μ), conduction electron concentration (n), Ioffe-Regel parameter ($k_F l_e$), and not applicable (NA).

quent to) modeling, per equation 3.1, of given property. Thereby, for each film property of interest for which it proves feasible to measure (said property on) at least eight of the nine films, one is able to fully resolve the main, and the interaction (two-factor and three-factor), effects of the three process factors (viz., P_{RF}, p, and O) of interest. That is, in such a situation, the highest-possible (full-resolution) of the DE is achieved.

It proved feasible to measure physical properties on each of the 9 of 9 films (see table 5.1). Thereby, the results of the RSA of film layer(s) physical properties are fully resolved. See figures 5.10 and 5.11 (for RSA results on sub-plantation layer (SPL) physical properties), and figures 6.20 and 6.21 for RSA results on thin-film layer (TFL) physical properties.

On the other hand, it proved feasible to measure electronic properties on only a subset 2 to 4 of 9 films (see figure 6.8 and table 6.5). The RSA results

on film electronic properties therefore are indicative only; see figures 6.14 through 6.19.

One notes that, since the physical or electronic property measurements are performed post film deposition, ascertaining the feasibility / DE resolution (as mentioned) is is a post-facto exercise.

The nine films as obtained — F35, F15, F31, F19, F7, F27, F11, F23, and F3 — are shown in figure 3.3, alongside their respective process factors set in coded units (CUs). Table 3.4 presents the interconversion between CUs and real world units (RWUs), of the process factors sets per figure 3.3.

It will sometimes be convenient to refer to a film (or sets of films thereof) by the 'plane' of the DE (per figure 3.3) upon which it (they) reside. Table 3.2 presents the listing thus[†].

3.3 Deposition of semiconducting amorphous transition metal oxide films

3.3.A Introduction

Sputtering presents abiding advantages to industry, from the perspectives of scale and quality, for deposition of TMO films (Crawford, 2005). As such, given the semiconducting (insulating) electrical nature of our target material system (viz., ISZO), RFMS is the film deposition technique of choice.

We highlight aspects of the RFMS technique relevant for this study (section 3.3.B). We then present considerations that apply for deposition of amorphous films (section 3.3.C).

[†]For brevity and as appropriate, in this thesis the "center-point / center-plane" of the DE will sometimes be contracted to 'center-plane'.

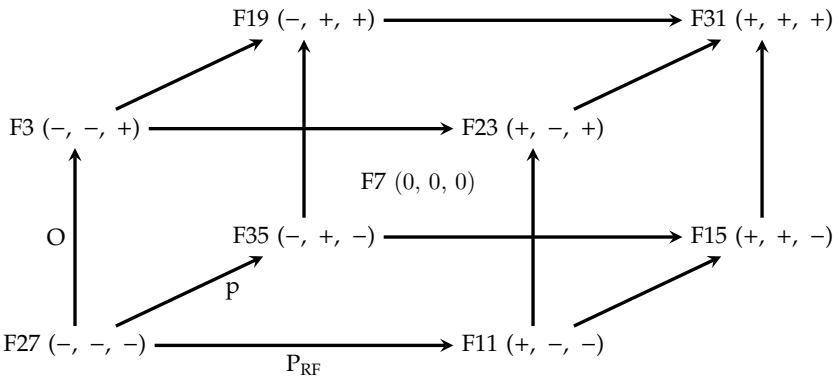

Figure 3.3: The three-factor two-level with center-point designed experiment (DE) employed in this study. Accordingly, nine films (multiple replicates of each) were deposited via radio frequency magnetron sputtering (RFMS). The nine films thus obtained, viz., F35, F15, F31, F19, F7, F27, F11, F23, and F3, are listed alongside the respective deposition process factors set, viz., '(P_{RF}, p, O)'. That is, the entries as presented are in the format "Film (P_{RF}, p, O)", where RF power (P_{RF}), process gas pressure (p), oxygen percent (O). The value of each process factor is expressed in coded units (CUs) (refer table 3.4). As discussed in the text, we have determined that a sub-plantation layer (SPL) manifests in only the front-plane (four films, viz., F27, F11, F23, and F3) and at the center-point (one film, viz., F7). Thereby, the process factor p separating the back-plane (p = +) and front-plane (p = −) is revealed to be a crucial determinant for emergence of a SPL. A response surface analysis (RSA) of the experimentally determined physical properties of the SPL (refer section 5.10.C) affirms and quantifies the role of p. An ab initio dimensional analysis (DA) of SPL physical properties (section 5.10.B) provides further affirmation of the role of p. For handy reference, table 3.2 lists the films by DE plane.

3.3.B Radio frequency magnetron sputtering

The deposition of films via sputtering entails physical dislodgement 'sputtering' of material from a 'target' (which serves as the cathode). Typically, as in our case, the target is a compacted disc of the material composition of interest. The sputtering of the target results in film deposition on a substrate that is placed in the path of the sputtered material flux.

The dislodgement is achieved via collision by energetic massive ions (typ-

Location in DE	Film(s)	Film layer structure
Back-Plane	F27, F11, F23, and F3	SL (TFL only)
Center-Point / Center-Plane	F7	BL (SPL and TFL)
Front-Plane	F35, F15, F31, and F19	
Bottom-Plane	F27, F11, F15, and F35	See above
Top-Plane	F3, F23, F31, and F19	

Table 3.2: With reference to figure 3.3, the nine Si doped In_2O_3−$(ZnO)_3$ (ISZO) films that are the subject of thesis grouped according the plane of the designed experiment (DE) on which they reside. For reference throughout this thesis, the layer structure of each film, viz., single-layer (SL) or bi-layer (BL), and the layer(s) thereof, viz., sub-plantation layer (SPL) and / or thin-film layer (TFL), is indicated (refer figure 5.3 and section 5.4).

DE		Factor			Film
Run order	Standard order	P_{RF} / CU	p / CU	O / CU	
1	5	−	−	+	F3
2	9*	0	0	0	F7
3	2	+	−	−	F11
4	4	+	+	−	F15
5	7	−	+	+	F19
6	6	+	−	+	F23
7	1	−	−	−	F27
8	8	+	+	+	F31
9	3	−	+	−	F35

Table 3.3: With reference to figures 3.2(b) and 3.3, the designed experiment (DE) according to which the films that are the subject of this study were deposited. Following design of experiment (DOE) principles, the "standard order" was randomized to obtain a "run order" (Dunn, 2016). Table 3.4 presents the interconversion between coded unit (CU) and real world unit (RWU) representations of the process factors. Here, RF power (P_{RF}), process gas pressure (p), oxygen percent (O).

		RWU		
		P_{RF} / W	p / mTorr	O / %
	–	25	2	0
CU	0	87.5	6	10
	+	150	10	20

Table 3.4: Interconversion between the coded unit (CU) and real world unit (RWU) representations of process factors considered. The RWUs are the physical values impressed during film deposition. Refer figure 3.3 and table 3.3. Here, smallest value, expressed in CU, of chosen range for given process factor (−), middle value, expressed in CU, of chosen range for given process factor (0), and largest value, expressed in CU, of chosen range for given process factor (+).

ically, as in our case, argon ion (Ar^+)), which are obtained by ionization of a process gas via collisions with energetic electrons. The electrons, and the Ar^+, constitute the process plasma, and the same is confined within the sputtering chamber.

The electrons are sourced from the cathode, and are accelerated towards the anode (substrate). This variant of the sputtering technique is referred to as diode or Direct Current Sputtering (DCS).

For semiconducting (insulating) targets however, it is advantageous to incorporate a radio frequency (RF) circuit, to generate the required voltage between anode and cathode. This variant of the sputtering technique is referred to as Radio Frequency Sputtering (RFS).

The RF circuit also transfers power to the process plasma, resulting in enhancement of the kinetic energy of the Ar^+ ions. This results, in turn, in enhancement of sputtering yield (number of target atoms sputtered per Ar^+

collision).

Finally, a suitable magnetic field, created by permanent magnets disposed beneath the target, enables concentration of the electrons in proximity of the target. This results in enhancement of the Ar^+ flux incident on the target. This results, in turn, in an enhancement of sputtered material flux. This variant of RFS is referred to as RFMS.

The power provisioned by the RF circuit to the plasma (as aforementioned) is referred to herein as P_{RF}. It has a direct bearing on the kinetic energy of the Ar^+ ions, and therefore on the sputtered material kinetic energy and flux (refer figure 5.7), and on film morphology (refer figures 6.20(b) and 6.20(c)). Similarly, the process pressure (on account of the process gases present) within the deposition chamber is referred to herein as p. It has an inverse bearing on film (TFL) deposition-rate (refer figure 6.20(a)). This is since scattering of sputtered material flux particles, as they transit the process plasma, is proportional to p.

Finally, introduction of oxygen in to the process gas, to an extent O of p, permits modulation of the oxygen stoichiometry of the film. This has a direct bearing on film opto-electronic properties (refer table 6.2, and figures 6.12 and 6.9).

3.3.C Amorphous films: adatom mobility on substrate

A low adatom mobility on substrate is necessary to obtain amorphous films. There are two contributions to adatom mobility on substrate: material flux bombardment induced, and thermal.

The first contribution, namely, bombardment induced adatom mobility, is an intrinsic outcome of sputtering given its high energy nature (refer figure 5.7), which results in hyperthermal sputtered material flux impinging upon (bombarding) the substrate. The use a sputter flux collimator (SFC)

per our film deposition protocol furnishes (limited) control to suppress this contribution to adatom mobility on substrate (refer section 3.4).

The second contribution, namely, thermal energy provisioning of adatom mobility, was suppressed by effecting film depositions on to substrates to which no heat is provisioned expressly (Messier, A. P. Giri, and Roy, 1984). That is, film depositions were performed on nominally unheated substrates.

3.4 Angular distribution of sputtered material flux

3.4.A Introduction

We discuss the angular distribution of sputtered material flux at target (section 3.4.B). This leads to consideration of the angular distribution of material flux sourcing film growth, that is, of the angular distribution of material flux at substrate (section 3.4.C). We are positioned thereby to discuss the control of angular distribution of material flux sourcing film growth (section 3.4.D).

3.4.B At target: the cosine distributions

The angular distribution of sputtered material flux, as emerges from the target, is usually modeled as a cosine distribution (Wehner and Rosenberg, 1960; Zalm, 1988; S. Rossnagel, 1995; S. M. Rossnagel, 1999; Cook, 1999; Ohring, 2002; Donald M. Mattox, 2010a). The distribution is discussed further via figure 3.4.

3.4.C At substrate

Due at least the following features of the sputtering technique (S. M. Rossnagel, 2003; J. E. Greene, 2017) ...

- the large area nature of the target;

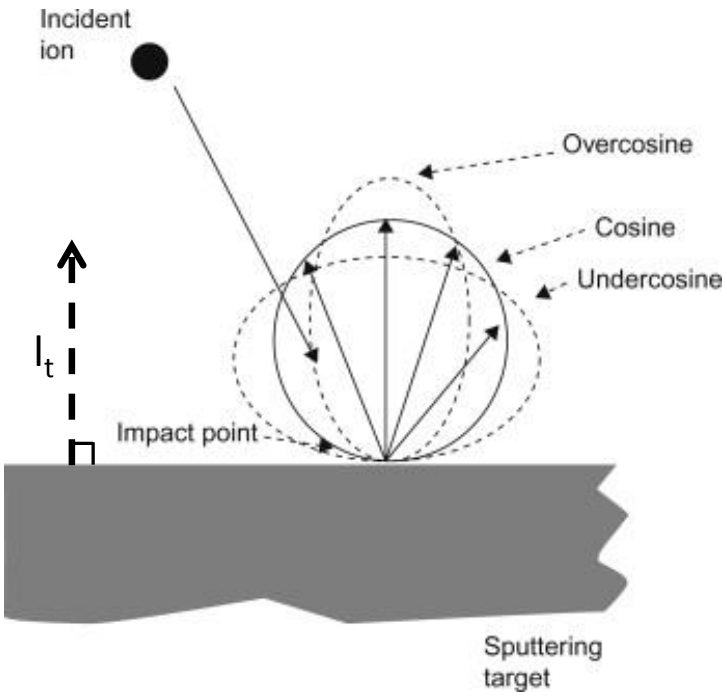

Figure 3.4: The angular distribution of material flux as emerges from a point on the target during sputtering. In the knock-on sputtering regime, the angular distribution so is approximately cosine. This regime manifests for normal-incidence bombardment by energetic massive ions (typically, as in our case, the ion is argon ion (Ar^+)). The ions so possess (kinetic) energy in the range 10^1 eV to 10^3 eV. This is the sputtering (energy) regime of deposition for the films considered in the present study (refer figure 5.7). Bombardment by higher (lower) energy ions results in an over-cosine (under-cosine) angular distribution. Figure adapted from A. H. Simon, 2012. Here, perpendicular distance from target surface (l_t) (refer section 5.7.B).

- the requirement of relatively high p (compared for instance, to other physical vapour deposition (PVD) techniques, such as, evaporation deposition (ED) or pulsed laser deposition (PLD)); and

- the multi-species composition of the process plasma;

... sputtered material flux, in general, is incident on the substrate at angles up to 90° with respect to the substrate normal (Barranco et al., 2016). Also, sputtering protocols practiced during academic research commonly provision

an azimuthal rotation to the substrate-stage[‡].

For such reasons, the maximum angle of incidence, alternatively, the angular distribution of material flux on substrate, are not controlled for during sputtering as it is commonly practiced within academia. Later, with reference to figure 3.7, we will introduce the maximum angle of incidence of sputtered material flux received at given radial location on substrate from SFC aperture (ζ), as a metric in terms of which to quantify the modulating effect of a (our) SFC, on the angular distribution of sputtered material flux sourcing film growth on substrate.

A state of affairs as aforementioned necessarily endows adatoms (material flux particles that have been received at the substrate surface, but are yet to condense therein), with momentum on the substrate surface. Adatom momentum so is determined, in part, by the component, in plane of the substrate surface, of the vector momentum at substrate of the (parent) material flux particle.

Adatom momentum in the substrate plane homogenizes the growing film. Indeed, that is often the goal of sputter film deposition protocols traditionally practiced within the academia (as noted above).

In our assessment (see also, section 5.8.D), a particular outcome of such traditional film growth protocols, is the averaging-out (non-preservation) of any bonafide physical features at the substrate-film interface. Accordingly, we conjecture that film growth protocols as above, are not conducive to preservation of a developing bonafide substrate-film interfacial structure (motif, or feature), that inheres due to — that is, which may be identified or correlated with — the process factors set (that is, the process conditions) impressed during film growth.

[‡]Rotation about axis perpendicular to plane of substrate-stage.

Control of angular distribution of material flux at substrate should result in (enhanced) preservation of said interfacial structure. Accordingly, substrate-film interface properties as emerge during 'controlled' growth (as aforementioned), of the substrate-film interface, or of the film, should be in-correlation-with (relatable-to), the process factors set impressed during substrate-film interface (e.g., SPL) growth.

As a matter of fact we show in this study that, the experimentally determined, via RSA, dependence of SPL physical properties, on the process factors set impressed during its growth, indeed agrees with the ab initio predictions of a dimensional analysis (DA), for the process factors set dependences of the same properties (refer sections 5.8.D and 5.10).

3.4.D The sputter flux collimator

3.4.D.1 Qualitative description

We have designed and developed a SFC compatibly the commercial RFMS equipment used in this study (Kurt J. Lesker Company Model PVD 75). The SFC enables us to exercise control over the angular distribution of sputtered material flux incident on substrate.

It is noted that effect, on film deposition, of the SFC occurs in conjunction with process factors — particularly, p and P_{RF} — that are at issue (refer equation 3.3). In leading up to a quantitative discussion of the SFC in section 3.4.D.2, we present a qualitative treatment of the considerations at issue via figure 3.5.

As alluded to in section 5.8.D, our ansatz is that control (depression) of adatom momentum in the substrate plane will aid the preservation of bonafide features (structure) at the substrate-film interface. The determination (of presence) of correlation between physical properties of the

substrate-film interface, and the process factors impressed during growth of said interface, will help interrogate (confirm) this ansatz.

To this end a SFC was designed, developed, and deployed, to control the maximum angle of incidence of sputtered material flux particles on substrate. This permitted the exercise of control as aforementioned (Jain, Peter P. Edwards, and Pepper, 2018). Further suppression of adatom mobility in the substrate surface was achieved, by undertaking growth on substrates to which no express provision of heat was made[§]. As discussed with reference to equation 3.3, control as aforementioned is available dependent on the p at issue.

3.4.D.2 Quantitative description

Via figure 3.6(a), we describe the substrate side as obtains in our film deposition protocol, wherein a SFC is disposed mediate target and substrate. In practice, the substrate is accommodated on the distal end (with respect to target) of the SFC aperture.

The discussions as follow are for a cylindrical SFC, while our SFC is a cuboid with a square cross section. The discussions so are for convenient development of a description of the SFC collimation (control of angular distribution, at substrate, of incident material flux) properties.

With reference to figure 3.6(b), let s_0 be a plane parallel to the substrate surface at an infinitesimal distance from it on the target facing / front side of the substrate, and let a_0 be the plane of the SFC aperture. Both planes s_0 and a_0 are circular.

We use the mean free length of process gas (l) to estimate the ballistic travel distance (length between two successive scattering events) of a material flux particle. The l may be estimated via the relation (S. Wilson, Tracy, and

[§]That is, upon nominally unheated substrates; assumed to be at room-temperature.

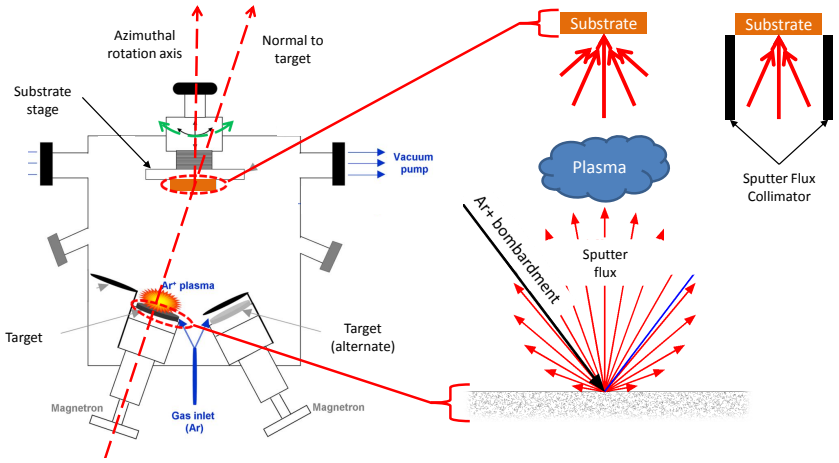

Figure 3.5: Description (qualitative) of sputtering chamber, and of effect of deployment of sputter flux collimator (SFC) on angular distribution at substrate of sputtered material flux. On the left is shown the situation as inheres in the radio frequency magnetron sputtering (RFMS) equipment used (refer figure 3.11). With reference to the center illustration in figure 3.11, the angle between the normal to target and azimuthal rotation axis of the substrate-stage is 10° (note: this angle is compensated for in the design of our substrate holder cum sputter flux collimator array (SHCSFCA); per the left most illustration in figure 3.8 (N. Honda and A. Honda, 2011)). Sputtering of the target causes material flux to emerge according a cosine angular distribution (refer figure 3.4). Upon passage through the process plasma, the material flux is incident on the substrate at angles up to the maximum possible 90° with respect to the substrate normal, as shown in the center illustration. Introduction of a SFC results in control of the angular distribution at substrate of the material flux, as shown on the right. Thereby, and with reference to figure 3.7, for certain process conditions, deployment of a SFC results in maximum angle of incidence of sputtered material flux received at given radial location on substrate from SFC aperture (ζ) to be a function of the location.

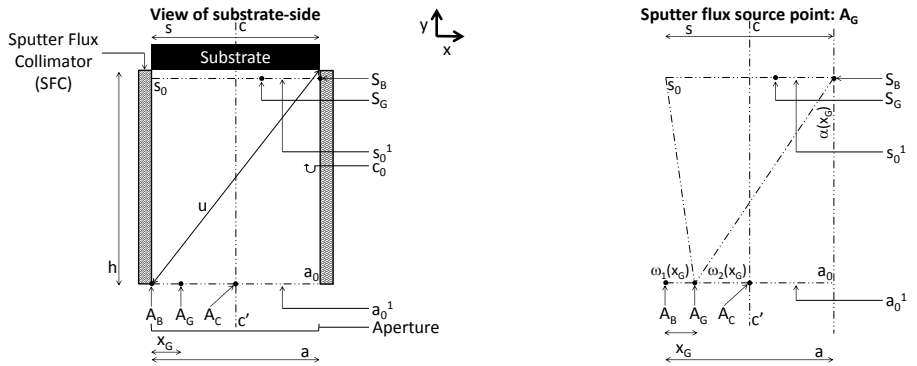

Figure 3.6: Description (quantitative) of substrate side with sputter flux collimator (SFC), and of angular distribution of sputtered material flux, as obtains during collimated sputtering. (a) The substrate side as obtains in our film deposition protocol, wherein a SFC is disposed intermediate substrate and target. The substrate is accommodated at the distal (with respect to target) end of the SFC. The SFC is shown in axial-plane c_0 (that is, a plane through the central-axis cc′), and is bounded by planes s_0 (on the substrate side) and a_0 (on the aperture side). Planes c_0 and s_0 intersect in line s_0^1, while planes c_0 and a_0 intersect in line s_0^1. Three points, A_B (on boundary of plane a_0), A_C (on central-axis cc′), and a point A_G at arbitrary location x_G on line s_0^1, are identified. Two further points, S_B (on boundary of plane s_0) and a point S_G at arbitrary location on line s_0^1, are also identified. Dimension "s" is the diameter of the substrate, and dimension "a" (= s) that of the aperture. Dimension "h" is the depth of the SFC. Relation 3.3b informs the choice of body diagonal dimension "u". Not to scale. (b) The range of angles of incidence of material flux on substrate, over sufficiently long time period, on the line s_0^1 from a general point A_G on line s_0^1. The angles $\omega_1(x_G)$, $\omega_2(x_G)$, and $\alpha(x_G)$ are obtained per equations 3.4a, 3.4b, and 3.4d respectively. Refer (a) for description of the other indicated features. Not to scale.

Freeman, 1993):

$$l = \frac{R}{2^{1/2}\pi {d_g}^2 N}\left(\frac{T}{p}\right) \tag{3.2}$$

where, ideal gas constant (R), process gas relevant diameter (d_g), avogadro constant (N), process gas temperature (T), process gas pressure (p). Given that the process gas (plasma) is comprised predominantly of Ar (refer table 3.4), we use $d_g = d_{Ar}$, the Van der Waals diameter of Ar atom. Furthermore and further to Powell and Stephen M. Rossnagel, 1999 we use $T = 500\,K$.

With reference to figure 3.6(a) and equation 3.2, two regimes of material flux deposition are identified, as follows:

$l(p) < u$ … Lowered energy material flux substrate side; SFC inactive; Material flux sourcing film deposition is uncollimated. (3.3a)

$l(p) \gtrsim u$ … Energetic material flux substrate side; SFC active; Material flux sourcing film deposition is collimated. (3.3b)

where, mean free length of process gas (l), SFC aperture body-diagonal (u).

We choose u of the SFC so that it is feasible to span, via control of p, the two conditions represented by equations 3.3. Table 5.3 presents further relevant discussions.

We next consider the range of angles of incidence of material flux on substrate, under the constraint imposed by equation 3.3b. The range so will be

quantified via the angle ζ.

Figure 3.6(b) shows three points on line a_0^1 that lies at the intersection of plane a_0 and c_0: point A_B on the boundary of plane a_0, A_C (on central axis $c - c'$), and a point A_G at arbitrary location x_G on line a_0^1. The angles ω_1 and ω_2 subtended by point A_G on the line s_0^1 are shown, and are:

$$\omega_1(x_G) = \cos^{-1}\left(\frac{x_G}{(x_G{}^2 + d^2)^{1/2}}\right) \tag{3.4a}$$

$$\omega_2(x_G) = \cos^{-1}\left(\frac{a - x_G}{\left((a - x_G)^2 + d^2\right)^{1/2}}\right) \tag{3.4b}$$

$$\omega(x_G) = \min\left(\omega_1(x_G),\ \omega_2(x_G)\right) \tag{3.4c}$$

$$\alpha(x_G) = \pi/2 - \omega(x_G) \tag{3.4d}$$

$$\zeta(x_G) = \alpha(x_G) \tag{3.4e}$$

In equation 3.4c, the function 'min' returns the minimum (lesser) of the two values (viz., $\omega_1(x_G)$ and $\omega_2(x_G)$) supplied to it as argument. Angle $\alpha(x_G)$ is the maximum angle of incidence (with respect to substrate normal) at which material flux is received by the substrate plane s_0 from a general point x_G on the aperture a_0 of the SFC. Noting the symmetry of the situation between aperture and substrate, $\zeta(x_G)$ per 3.4e is the maximum angle of incidence of material flux received at radial location x_G on substrate.

In the model (figure 3.6 and equations 3.4a – 3.4e), the distance from edge of aperture a_0) x_G determines the adatom momentum that is provisioned to the growing film. In general, adatoms that have a substantial momentum component in the plane of the substrate are received closer to the boundary of the substrate from the 'far' boundary of the aperture.

Figure 3.7 plots the maximum angle of incidence (of material flux on substrate) as a function of radial distance from the substrate center, for a cylin-

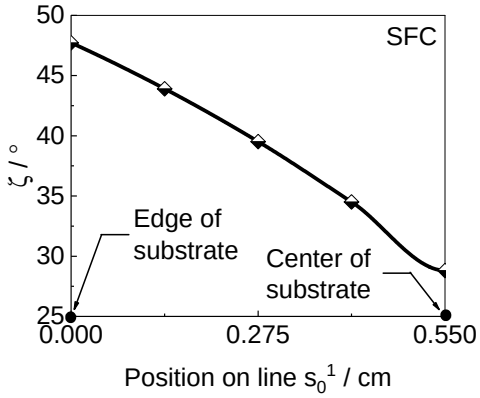

Figure 3.7: Radial dependence of maximum angle of incidence of sputtered material flux received at given radial location on substrate from SFC aperture (ζ). For a SFC with square cross-section having side 'a' and depth 'h'. Evidently, the angular range at which material flux is received at substrate becomes progressively less normal as one moves radially outwards from the substrate center. Here intersection-line of c_0 and s_0 (s_0^1) (refer figure 3.6).

drical SFC. The diameter and depth of said SFC equal the side and depth respectively of our cuboidal SFC; thereby, SFC aperture side (a) and SFC aperture depth (h).

Evidently, the SFC aspect ratio ($\mathsf{r_a}$) of the SFC deployed for this thesis (figure 3.6(a)) is:

$$\mathsf{r_a} = \frac{\mathsf{h}}{\mathsf{a}} \tag{3.5a}$$

$$\simeq 0.91 \tag{3.5b}$$

3.5 The substrate holder cum sputter flux collimator array: high-throughput conduct of a designed experiment

3.5.A Introduction

The SHCSFCA dovetails the considerations as obtain due each of the aforementioned aspects of our experimentation programme: DOE methodology (per section 3.2), RFMS (per section 3.3), and control of angular distribution of sputtered material flux sourcing film growth (per section 3.4).

It does so compatibly the inescapable practical constraints due to the film deposition equipment, and due to the multiplicity of characterization modalities (primarily, x-ray reflectometry (XRR), AC Field Hall Effect (ACFHE), and spectroscopic ellipsometry (SE)).

In particular, the SHCSFCA is designed to meet the mechanical and electromagnetic constraints of the precision engineered commercial sputtering equipment: Kurt J. Lesker Company Model PVD 75[¶]. In particular, the SHCSFCA is designed to accommodate substrates sized to simultaneously meet the sample sizing and quality constraints of the state of the art characterization equipments: Rigaku Model SmartLab (for XRR), Lake Shore Cryotronics 8400 Series HMS Hall effect measurement system (for ACFHE), J. A. Woollam Model RC2 (for SE).

Furthermore, the SHCSFCA permits high-throughput conduct of our DE.

Accordingly, we motivate the design of the SHCSFCA, and discuss the film deposition throughput demonstrated via its deployment (section 3.5.B). This is followed by presentation of the engineering designs of the SHCSFCA, and

[¶]This equipment is stationed in the clean-room of the London Centre for Nanotechnology (LCN).

of the associated 'shield' (section 3.5.C). We then discuss deployment of the SHCSFCA and shield hardware inside the RFMS equipment at issue (section 3.5.D). Finally, we discuss the versatility of the SHCSFCA to service DEs in general (section 3.5.E).

3.5.B Design considerations

We present the experimentation hardware designed and developed by us — the SHCSFCA and associated shield — that enables conduct of a DE (e.g., our DE per figure 3.3) at high-throughput. The SHCSFCA comprises an array of SFCs per section 3.4.D. The number of SFCs is determined by the DE of interest.

Figures 3.8 and 3.10 present respectively the engineering design drawings, and the photographs of the SHCSFCA as fabricated. Thereby, given its 36 individual SFCs, our SHCSFCA is able to service the 3-factor, 2-level, full-factorial with center-point DE per figure 3.3 for (up to) 4 replicates per run.

Used in conjunction with the shield per figure 3.9, the SHCSFCA enabled conduct of the DE described in section 3.2.E, at (up to) an order of magnitude decrease in costs (refer section 4.2). The throughput so demonstrated by us translates to a 3x improvement (decrease in equipment costs per film deposition) to 10x improvement (decrease in average time duration per film deposition), over traditional film deposition protocols.

The improvements referred to are a direct consequence of deployment of the SHCSFCA, which enabled conduct of each of the nine (per figure 3.3) required film depositions upon a single vacuum pumpdown (refer section 4.2.C). Traditional film deposition protocols would have permitted only the one film deposition per vacuum pumpdown. Further details re our film deposition protocol are presented in section 4.2.

The SHCSFCA is designed to meet the mechanical and electromagnetic constraints at issue due the precision engineered and in-operation commercial RFMS equipment at issue (Kurt J. Lesker Company Model PVD 75).

The sputtering chamber hosts (is part of) the electrical circuit to prepare the RF plasma for sputtering. Thereby, the primary electro-magnetic constraint was to ensure the compatibility of the 'non-native' (that is, not part of original equipment design) SHCSFCA, in to the sputtering chamber, and thereby, in to the RF circuit.

A number of mechanical constraints imposed trade-offs as follows: between minimum film size requirements of characterization modalities, and the number of substrates (refer section 3.5.B) that needed to be accommodated within the sputtering chamber.

Two of the main characterization modalities employed by us, viz., XRR and SE, interrogate the sample via a macro-scale beam of radiation. The size of the footprint on sample of such beams determines the minimum acceptable film size. The size of the sputtering chamber / substrate-stage then determined the maximum number of substrates that may be accommodated within (on) the SHCSFCA.

For close to the minimum acceptable sample sizes dictated by the characterization modalities, it proved feasible to design and deploy a SHCSFCA capable of accommodating a complement of 36 substrates, which was sufficient to conduct the chosen DE (up to 4 replicates of 9 films).

This permitted conduct of the chosen DE at (close to) the highest possible (time) throughput, at significantly lower equipment related costs, and by avoiding experiment analysis complexities that arise due time lapse between the individual runs comprising the DE (Altman and Krzywinski, 2015; Kowalski and Potcner, 2003) (refer section 4.2.C).

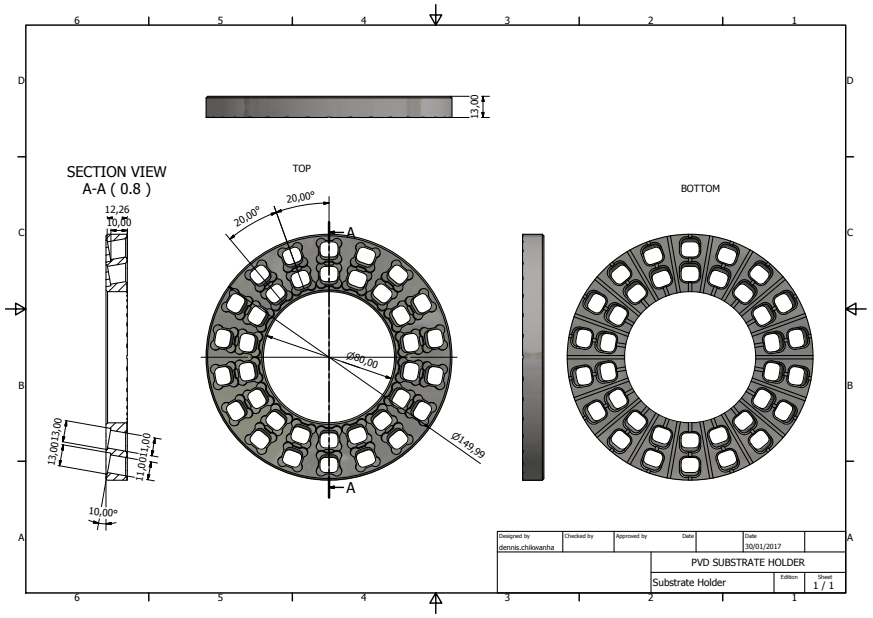

Figure 3.8: Engineering drawings of the substrate holder cum sputter flux collimator array (SHCSFCA). It is deployed within the sputtering chamber of the radio frequency magnetron sputtering (RFMS) equipment (refer figure 3.11) in conjunction with the shield per figure 3.9.

3.5.C Engineering designs

Figure 3.8 presents the engineering drawings of the SHCSFCA.

Figure 3.9 presents the engineering drawings of the shield. The shield was deployed intermediate the SHCSFCA and the target, and served to block passage of material flux to all SHCSFCA SFCs, except to those that were bought to be positioned (via azimuthal rotation of the substrate-stage, performed with aid of pre-existing control software), immediately behind the shield-window.

The shield was designed to present two different window sizes, so that one may position 2 or 4 SFCs / substrates behind it.

Figure 3.10 shows the front and distal views of the SHCSFCA as fabricated. The as-deposited samples (film-substrate-combine; one per SFC) are also

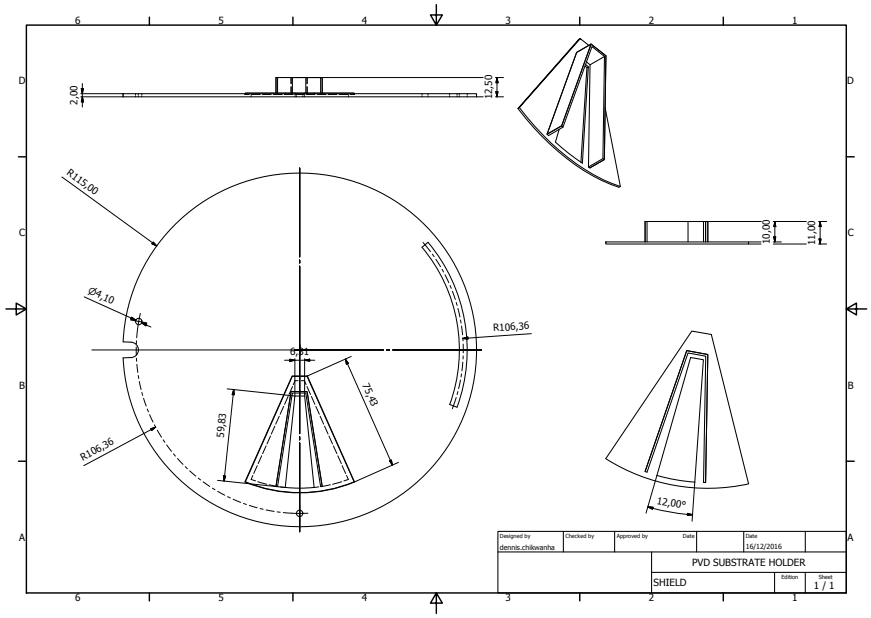

Figure 3.9: Engineering drawings of the shield. It is deployed within the sputtering chamber of the radio frequency magnetron sputtering (RFMS) equipment (refer figure 3.11) in conjunction with the substrate holder cum sputter flux collimator array (SHCSFCA) per figure 3.8.

seen.

3.5.D Deployment

Figure 3.11 presents the placement of the SHCSFCA, and of its associated shield, within the RFMS equipment sputtering chamber, prior to commencement of sputtering.

3.5.E Versatility

The SHCSFCA as designed and fabricated is capable of servicing a variety of DEs, as discussed with reference to figure 3.12.

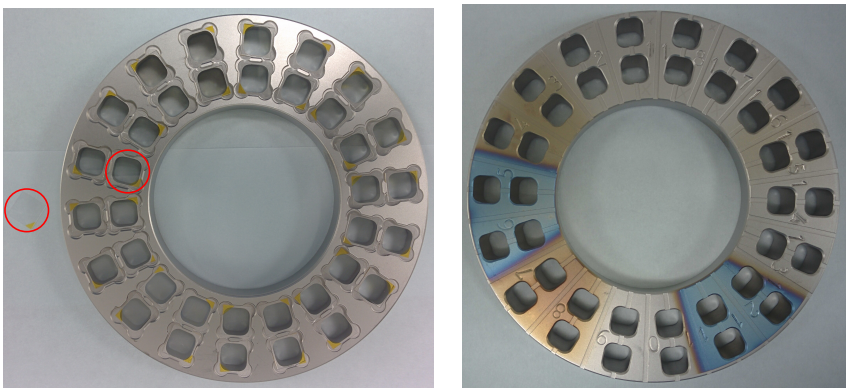

(a) (b)

Figure 3.10: Photographs of substrate holder cum sputter flux collimator array (SHCSFCA) post film deposition via radio frequency magnetron sputtering (RFMS). (a) Substrate-side view of the substrate holder cum sputter flux collimator array (SHCSFCA) with substrates mounted. The circles highlight representative film-substrate-combines (as-deposited films). (b) Target-side view. The rainbow colours are due the transition metal oxide (TMO) coatings received by the SHCSFCA body during the course of film deposition.

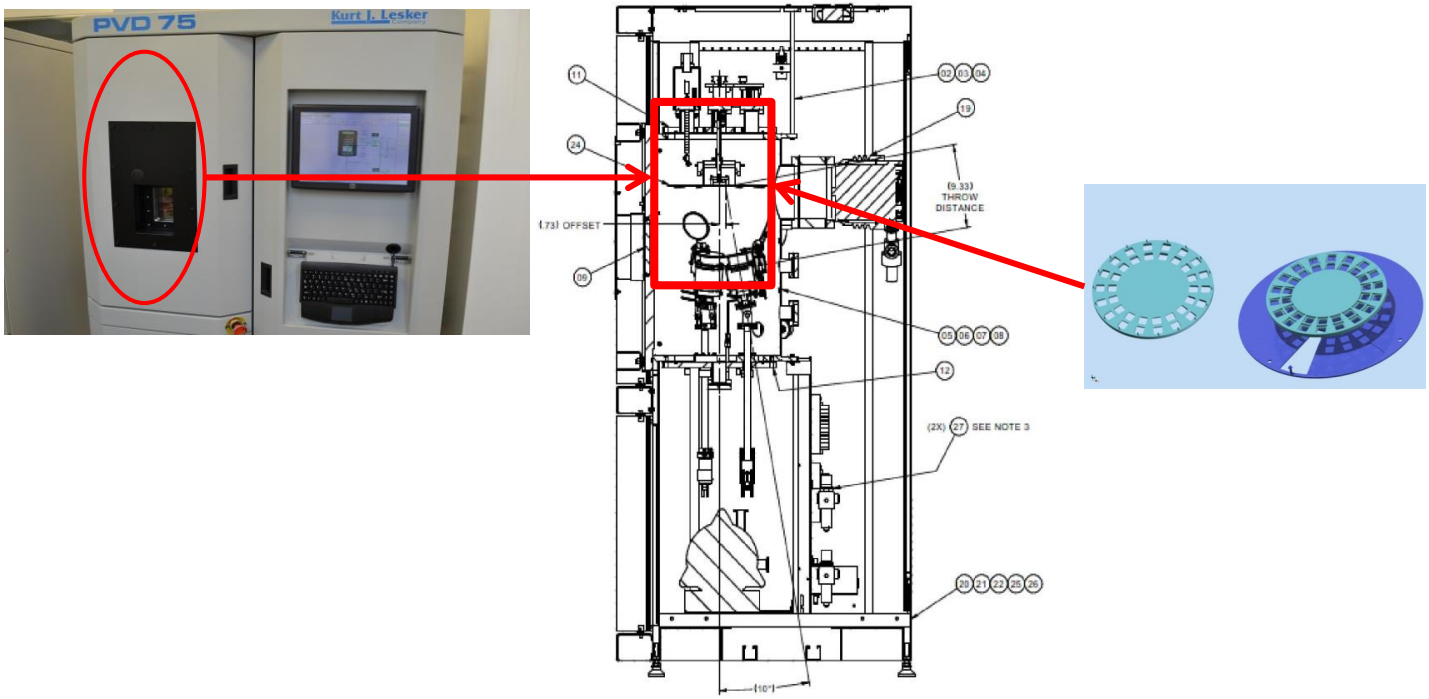

Figure 3.11: Deployment of substrate holder cum sputter flux collimator array (SHCSFCA) (refer figure 3.8) and shield (refer figure 3.9) in sputtering chamber of radio frequency magnetron sputtering (RFMS) equipment used in the present study. The center figure is the engineering drawing of the commercial RFMS equipment (Kurt J. Lesker Company (KJLC) Model PVD 75) on the left. The SHCSFCA and shield are shown on the right, are deployed in conjunction with each other, at the substrate side of the sputtering chamber. Engineering drawing used with permission of KJLC.

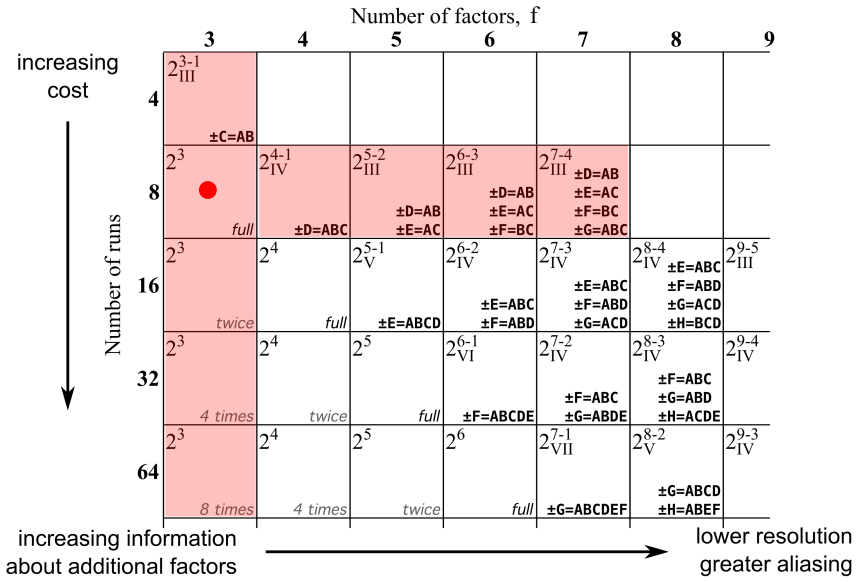

Figure 3.12: Canonical descriptive list showing the designed experiment (DE) of the present study, and other DEss that are accessible immediately via the substrate holder cum sputter flux collimator array (SHCSFCA). The information content of each DE is indicated. The DEs accessible (as mentioned, via the SHCSFCA (per figure 3.8) and RFMS equipment (per figure 3.11) at issue are highlighted (red shading). The dot indicates the DE employed in the present study. Figure adapted from Dunn, 2016; George E. P. Box, J. S. Hunter, and W. G. Hunter, 2005. See also figure 7.1.

Chapter 4

Materials, methods, and analysis frameworks

4.1 Introduction

In this chapter, we consider the film deposition and characterization techniques, as were informed by the film material system (composition, opto-electronic properties, and microstructure) at issue. We will also present relevant theoretical results, and frameworks for analysis of the experimental results.

We begin by presenting the film deposition protocol (section 4.2). We then present the principal film characterization techniques. The technique of x-ray reflectometry (XRR) revealed and quantified the film layer structure (section 4.3). Building upon the results from XRR, the technique of spectroscopic ellipsometry (SE) furnished information re film opto-electronic properties at room-temperature (section 4.4). The technique of AC Field Hall Effect (ACFHE) permitted determination of the absolute temperature (T) dependence of film electronic properties (section 4.5). The determination

Information re	For instance	Characterization technique			
film / layer...	re...	XRR	SE	ACFHE	XRD
Layer structure	SPL, TFL	✓	✓		
Physical properties	d, $D^{\dagger}$, r	✓	✓		
Optical properties	n, k		✓		
Electronic properties	μ, n, ρ, $E_g{}^{\ddagger}$		✓	✓	
Microstructure					✓

Table 4.1: Characterization techniques listed according to the information furnished. Film properties (physical, or opto-electronic) were estimated and corroborated via independent experimental techniques. Refer table 3.1. Here, sub-plantation layer (SPL), thin-film layer (TFL), x-ray reflectometry (XRR), spectroscopic ellipsometry (SE), AC Field Hall Effect (ACFHE), x-ray diffraction (XRD), thickness (as applicable) of film or of film layer (d), density (as applicable) of film or of film layer (D), roughness (as applicable) of film or of film layer (r), refractive index (n) (optical), extinction coefficient (k), conduction electron mobility (μ), conduction electron concentration (n) (electronic), resistivity (ρ), band-gap energy (E_g). †Via XRR only. ‡Via SE only.

underpinned quantitative analysis — on basis of the Mott theory of the metal insulator transition (MIT), and the Brooks-Herring (BH) model of ionized impurity scattering (IIS) — of nature of the electronic state of Si doped In_2O_3−$(ZnO)_3$ (ISZO) films.

Thus, table 4.1 lists the characterization techniques according the information furnished.

4.2 Film deposition: radio frequency magnetron sputtering

4.2.A Introduction

We present, the substrate preparation protocol (section 4.2.B). Thereafter, alongside motivation of its features, we present the film deposition protocol

(section 4.2.C).

4.2.B Substrate preparation protocol

All film fabrication (substrate preparation and film deposition) related processes were performed in a Class 1000 (ISO 6) clean-room. The CEXG substrate roughness, $r_{s,\,CEXG} = 0.5\,nm$ to $1\,nm$, while the CEXG substrate thickness, $d_{s,\,CEXG} = 700\,\mu m$, per guarantee by the manufacturer (Corning Inc., 2017). The substrate preparation protocol involved ex-situ and in-situ cleaning of the substrates, as follows:

Ex-situ cleaning of the substrates was performed via standard wet bench procedures (sonification successively in CH_3OH, $(CH_3)_2CHOH$, and de-ionized water, followed by drying in anhydrous N flow), prior to mounting them on the substrate holder cum sputter flux collimator array (SHCSFCA), and the assembly thus in to the sputtering chamber of the radio frequency magnetron sputtering (RFMS) equipment.

In-situ cleaning of the thus mounted substrates was performed in / via a low energy undirected Ar^+ plasma at an P_{RF} density $\simeq 0.34\,W/cm^2$ of substrate area prior to commencement of sputtering (Donald M. Mattox, 2014).

4.2.C Film deposition protocol

The nine ISZO films per the experiment design presented in figure 3.3 and table 3.4 were deposited via RFMS of a single target comprised of metal-oxides in ratio In_2O_3:SiO_2:ZnO = 1:0.2:3. Accordingly, the aforementioned composition may be considered as a silicon (Si) doped k=3 homologue of the $In_2O_3{-}(ZnO)_k$ (k = 0, 1, 2, 3, ...) material system. Thereby, metal atom percentages in the ISZO films nominally are (In, Si, Zn) = (38.5, 3.8, 57.7). Accordingly, we determine $N_{Si} = 1.45 \times 10^{21}/cm^3$ and $d_{Si-Si} = 0.9\,nm$, where nominal concentration of dopant / Si (N_{Si}), nominal Si to Si distance

(d_{Si-Si}), and $d_{Si-Si} \sim 1/N_{Si}{}^{1/3}$.

Sputtering of the target was performed via argon ion (Ar^+) bombardment in the knock-on regime (refer figures 3.4 and 5.7). The sputtering system employed is a modified Kurt J. Lesker Company Model PVD 75, with $d_t = 7.62\,cm$ and $l_{t-s} \simeq 9\,cm$, where target diameter (d_t) and target-substrate distance (l_{t-s}) (refer figure 3.11 and Kurt J. Lesker Company, 2012).

The modifications referred to were due and included deployment of a plug-and-play SHCSFCA comprising sputter flux collimators (SFCs), wherein SFC aperture side (a) (refer section 3.5.D). The SHCSFCA is fabricated using BS970 Grade 304 Stainless Steel. The distal end (with respect to target) of each SFC of the SHCSFCA accommodated a substrate such that the substrate surface normal is parallel to the target surface normal. Accordingly, square films with side $a_f = a$ are obtained.

The sputtering chamber was evacuated to a $p_b \leq 10^{-3}\,mTorr$. The vacuum pumpdown time required for said evacuation was $\gtrsim 12\,h$.

As discussed in section 3.4.D the SFC permits control of angular distribution of material flux sourcing film growth. In particular, for process gas pressure (p) per relation 3.3b, deployment of an SFC results in film growth from collimated material flux. With reference to tables 3.2 and 5.3, such a situation manifests for the the center-plane and front-plane films.

The films were deposited on Corning Eagle XG Glass (CEXG) substrates (further discussion follows; see also (Donald M. Mattox, 2011)) to which no heat was provisioned expressly (refer section 3.3.C). Also, the substrate temperature (T_s) during film deposition was unregulated. Given that each as-deposited film is amorphous (further discussion follows), and whereas that the crystallization temperature of the $In-Zn-O$ material system is $>500\,K$, it follows that the heat deposited in to the substrate / growing film by the

incident material flux, was insufficient to cause a significant temperature rise (Hideo Hosono, 2010a; Walsh, Silva, and S.-.-H. Wei, 2011).

The microstructure of the as-deposited films was interrogated via x-ray diffraction (XRD) measurements, and was revealed (confirmed) to be amorphous (refer figure 6.1). The x-ray diffractograms were collected via a commercial PANalytical X'Pert Pro x-ray diffractometer.

Each film was obtained upon sputtering of the target for time duration = 20 min. Figure 3.3 and table 3.4 present the deposition process factors set corresponding to each film.

The films were deposited according the run order per table 3.3. Each film deposition was completed in a total time duration of approximately 30 min. The additional time period (about 10 min) was required for positioning (via azimuthal rotation of the substrate-stage / SHCSFCA) of a new set of substrates in to the shield-window, implementing and allowing stabilization of the required process factors set, and other sundry experimental considerations. Accordingly, note that by "each" film is meant the film-replicates-set deposited at a given process factors set.

Thus, the SHCSFCA furnished us with the capacity to conduct a designed experiment (DE) at high-throughput. For the particular experiment design chosen by us (3-factor, 2-level, full-factorial with center-point, per figure 3.3), we demonstrate a film deposition throughput that is close to the highest possible. The throughput so demonstrated by us translates to a 3x improvement (decrease in equipment costs per film deposition) to 10x improvement (decrease in average time duration per film deposition).

4.3 Film layer structure: x-ray reflectometry

4.3.A Introduction

We motivate the technique of XRR in light of the nature of films at issue (section 4.3.B). We then present the theory and the schema for specular XRR (section 4.3.C).

4.3.B Motivation

Determination of physical properties (thickness, density, roughness) of the layer(s) comprising a film was made on basis of the XRR technique (refer table 4.1). Here, we motivate the reasons underlying our choice of this technique (Nolot and André, 2011).

The technique of XRR presents abiding advantages for film layer structure determination (A. Gibaud, Chebil, and Beuvier, 2013). It is non-destructive, microstructure agnostic, and capable of determining length-scales down to sub-nanometer. However, constraints on film surface and interface morphology apply. In particular, successful experimental observation of a Kiessig fringes profile (KFP) via XRR is requires that roughness of film interface(s) (surface and in-situ interface(s)) be $\lesssim 3\,\mathsf{nm}$ to $5\,\mathsf{nm}$ (LaPuma and Zimmermann, 2010).

Given the stringent constraint on film interface(s) smoothness, special attention was paid to the selection of low-roughness substrates (viz., CEXG) and their pre-deposition cleaning (refer section 4.2.C) (Corning Inc., 2017; Donald M. Mattox, 2014). With reference to table 5.1, it is (post-facto) determined that each of the nine films at issue meet this constraint. Another principal result is that the center-point and the front-plane films of the experiment design per figure 3.3 are bi-layer (BL).

4.3.C Theory and schema

The technique of specular reflection XRR (refer figure 4.1) measures $R(\alpha_i)$, or equivalently, $R(Q_z)$ of a film (refer figure 4.2). Given finite layer(s) thicknesses, interference, that is 'Kiessig fringes' are observed in the $R(Q_z)$ profile; the same is referred to as a KFP.

Peaks corresponding to film layer thickness(es) are positioned in the fourier transform (FT) of the KFP. Thus, the number of layers (each with a distinct density) comprising the film is revealed. It is noted that no assumption or modeling is required to determine the number of layers; that is, this determination is directly on basis of experimentally measured KFP data.

At this stage of analysis, for a multi-layer film, the relative placement of layers is yet undetermined. The film layer structure as arrived upon based on the FT may now be refined. The refinement is on basis of the experimentally measured KFP, and yields the thickness, roughness, and density of each film layer. Tallying the thus obtained layer thickness(es) with the position of peaks in the FT provides a straightforward and independent confirmation of reliability of the refinement.

In the x-ray energy range, it is convenient to express the complex refractive index in the x-ray energy range (n^*) of a material (film) as:

$$n^* = 1 - \delta + \iota\beta \tag{4.1a}$$

$$\delta = \frac{\lambda^2}{2\pi} r_e \rho_e \tag{4.1b}$$

$$\alpha_c = (2\delta)^{1/2} \tag{4.1c}$$

where, complex refractive index in the x-ray energy range (n^*), XRR δ-parameter (δ), XRR β-parameter (β), wavelength of x-rays (λ), classical electron radius (r_e), electron density (ρ_e), critical angle for x-ray (α_c).

Evidently, in addition to wavelength of x-rays (λ), XRR δ-parameter (δ) depends on film composition and density. Typically, δ lies in the range 10^{-6} to 10^{-5}, and thus critical angle for x-ray (α_c) lies in the range $0.1°$ to $0.5°$. The parameter XRR β-parameter (β) is related to x-ray absorption within the film, and is typically 10x smaller than δ (Daillant and Alain Gibaud, 1999).

Figure 4.1 shows the schema in which specular reflection XRR is performed.

In light of figure 4.1, for the specular part of reflection:

$$\alpha_f = \alpha_i \tag{4.2a}$$

$$Q_z = \frac{4\pi}{\lambda} \sin \alpha_i \tag{4.2b}$$

where, angle of final wave-vector (α_f), angle of initial wave-vector (α_i), magnitude of transfer wave-vector (Q_z), wavelength of x-rays (λ).

The x-rays as reflect from different interfaces of the film-substrate-combine interfere, and the final intensity oscillates as a function of angle of initial wave-vector (α_i) — or equivalently, in light of equation 4.2b — as a function of magnitude of transfer wave-vector (Q_z). As noted, the oscillating intensity (fringes) profile is the KFP (Kiessig, 1931). For a single-layer (SL) film having thickness d, the wavelength of the KFP equals $2\pi/d$.

With reference to figure 4.1, the reflectivity (R) is:

$$R = \frac{I_f(\alpha_i)}{I_i} \tag{4.3a}$$

Or, in light of equation 4.2b

$$= \frac{I_f(Q_z)}{I_i} \tag{4.3b}$$

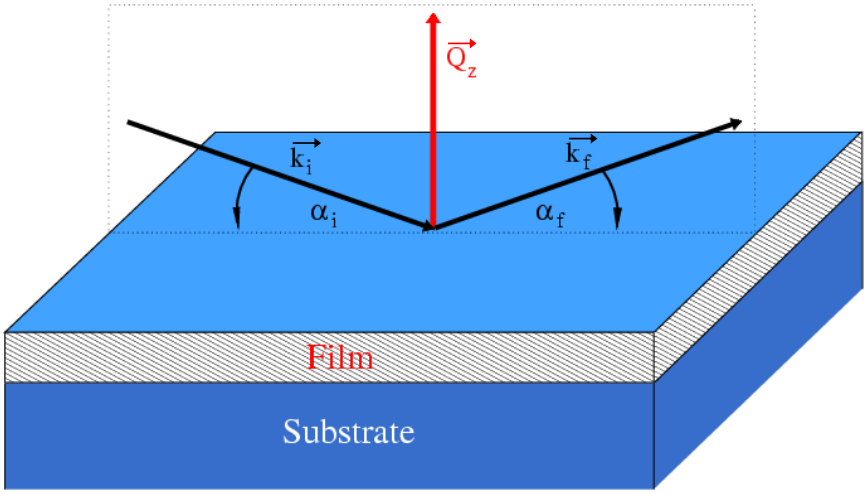

Figure 4.1: Schema for specular reflection x-ray reflectometry (XRR). Each of the three vectors shown lie in the same plane. Refer figure 4.2 also. Figure adapted from Schreiber and A. Gerlach, 2004. Here, wave-vector of initial x-ray ($\vec{k_i}$), wave-vector of final x-ray ($\vec{k_f}$), transfer wave-vector ($\vec{Q_z}$), angle of initial wave-vector (α_i), angle of final wave-vector (α_f).

where, final intensity of x-ray (I_f), initial intensity (fixed) of x-ray (I_i), α_i. Evidently, R is a normalized quantity.

Under kinematical approximation, and for $\alpha_i \gg \alpha_c$, the R for an arbitrary electron density profile $\rho_e(z)$ may be described as:

$$R(Q_z) \propto \left| \int \frac{d\rho_e(z)}{dz} \exp(\iota Q_z z)\, dz \right|^2 \tag{4.4}$$

where, magnitude of transfer wave-vector (Q_z), direction perpendicular to film during XRR (z).

Evidently from equation 4.4, the FT of $R \propto d\rho_e(z)/dz$. This feature is crucial for determination thickness of film layer(s) (Sakurai and Iida, 1992). Refinement of film layer structure (revealed via FT of $R(Q_z)$) with interface roughness(es) (Sinha et al., 1988) included, given knowledge of chemical composition of the film, yields a plethora of information, as indicated in figure 4.2. The KFPs were recorded via a Rigaku Model SmartLab x-ray

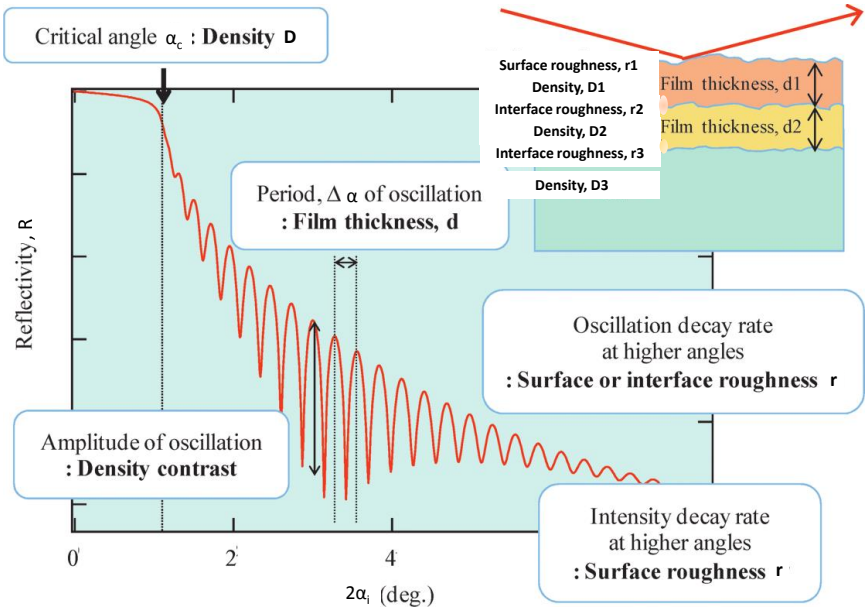

Figure 4.2: Information content of a Kiessig fringes profile (KFP) recorded via x-ray reflectometry (XRR) per figure 4.1. In specular reflection XRR, the reflectivity (R) may be expressed as a function of angle of initial wave-vector (α_i) (as shown). Equivalently, in light of equation 4.2b, the R so may be expressed as a function of magnitude of transfer wave-vector (Q_z). Accordingly, figure 5.1 presents experimentally recorded $R(Q_z)$ of the films that are the subject of this study. Figure adapted from Yasaka, 2010.

diffractometer with $\mathrm{Cu\ K-}\alpha_1$ x-radiation ($\mathrm{Cu\ K-}\alpha_1$) between α_i range of 0° to 1.5°, which corresponds to a Q_z range of $0/\mathrm{nm}$ to $2.14/\mathrm{nm}$ (Stierle and Vlieg, 2012). The angle α_i was scanned in step size of 0.0026°. The Fourier analysis and refinement of the KFP was performed via the Rigaku GlobalFit software. The following values were used during refinement: ISZO density (D_{ISZO}) (assumed to be as for single-crystalline phase of base material composition $In_2O_3{-}(ZnO)_3$ per Yoshinari et al., 2009), and CEXG density (D_{CEXG}) (per Corning Inc., 2017).

4.4 Film opto-electronic properties: spectroscopic ellipsometry

4.4.A Introduction

We motivate the technique of SE in light of the nature of films at issue (section 4.4.B). We then present its theory and schema (section 4.4.C). We conclude by motivating and presenting the oscillator models as were used for extracting film opto-electronic properties on basis of SE measurements (section 4.4.D).

4.4.B Motivation

The technique of SE was employed to estimate film room-temperature electronic properties such as conduction electron mobility (μ), conduction electron concentration (n), and band-gap energy ($\mathrm{E_g}$) (Fujiwara, 2007). The analysis is on basis the film layer structure obtained via XRR (refer figure 5.3(d)). The analysis also yields the energy (E) dependence of complex refractive index (n^*).

We introduce the SE technique and the framework for analysis of the E dependences of SE Ψ-parameter (Ψ) and SE Δ-parameter (Δ) that it furnishes. Choice of physically meaningful oscillator models — viz., Tauc-Lorentz (TL) and Drude (D) — as were employed for the analysis is based upon film microstructure (amorphous) and electronic state (semiconducting). The E dependence of the transmission fraction (Tr) of exemplary film-substrate-combines is calculated on basis of the Tauc-Lorentz plus Drude (TL+D) oscillator model (for film) and Gaussian plus Tauc-Lorentz (G+TL) (for substrate). The same are compared to the experimentally measured dependences so (see figure 5.6).

A film with thickness $\lesssim 10\,\mathrm{nm}$ is not amenable for interrogation via SE, given the equipment (J. A. Woollam (JAW) Model RC2) at issue (J. A. Woollam Co., 2017; Hillier et al., 2020). Given the aforementioned, and with reference to figure 3.3 and table 5.1), three of the nine films — viz., F7, F11, and F23 — were amenable for interrogation via SE. Each of these films is BL, and hence the use as mentioned of the BL film layer structure per figure 5.3(d).

Thereby, SE also furnished, additionally to XRR, further experimental validation of the sub-plantation layer (SPL).

4.4.C Theory and schema

The technique of SE employs polarized light to characterize a film, according the schema shown in figure 4.3. One proceeds by measuring the change in the polarization of the incident light beam as occurs upon interaction (reflection off of, and transmission through) with the film (Woollam et al., 1999; Johs et al., 1999).

The change in polarization so is described via two ellipsometric parameters which are related via the 'fundamental equation of ellipsometry', as follows:

$$\rho = \frac{\mathrm{r_p}}{\mathrm{r_s}} \tag{4.5a}$$

$$= (\tan \Psi) \exp \iota\Delta \tag{4.5b}$$

where, reflectivity for p-polarized light ($\mathrm{r_p}$), reflectivity for s-polarized light ($\mathrm{r_s}$), ratio of $\mathrm{r_p}$ to $\mathrm{r_s}$ (ρ), SE Ψ-parameter (Ψ), SE Δ-parameter (Δ).

The n^*, complex permittivity (ε^*), and (Ψ, Δ) of a bulk material are inter-

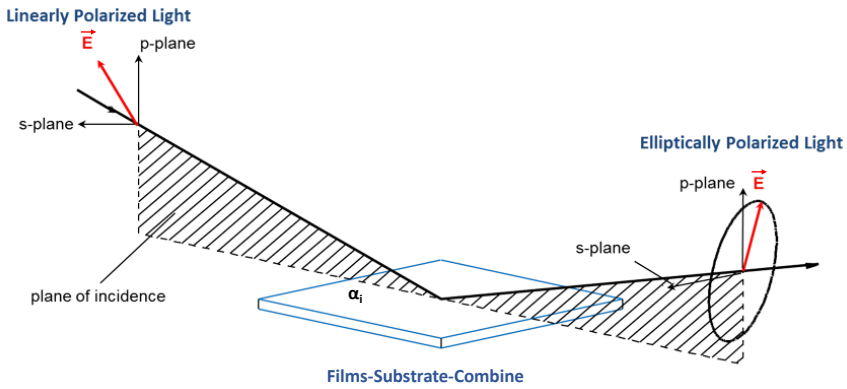

Figure 4.3: The schema in which spectroscopic ellipsometry (SE) is performed. Circularly polarized light is incident upon the film. Due interaction with (reflection off of, transmission through) the film, it undergoes a change in its polarization state. Thereby and in general the light is rendered elliptically polarized. The electric field vector ($\vec{E}$) before and after reflection, and the s-plane and p-plane are shown. Figure adapted from J. A. Woollam Co., 2014.

related as:

$$n^* = (\varepsilon^*)^{1/2} \tag{4.6a}$$

$$= \left(\sin^2 \alpha_i \left(1 + \tan^2 \alpha_i \left(\frac{1-\rho}{1+\rho} \right)^2 \right) \right)^{1/2} \tag{4.6b}$$

where,

$$n^* = n + \iota k \tag{4.6c}$$

and,

$$\varepsilon^* = \varepsilon_1 + \iota \varepsilon_2 \tag{4.6d}$$

where, complex refractive index (n^*), complex permittivity (ε^*), angle of

incident light (α_i), ratio of r_p to r_s (ρ), refractive index (n), extinction coefficient (k), real part of ε^* (ε_1), imaginary part of ε^* (ε_2).

The technique of SE proceeds by measuring the wavelength of light (λ) or E dependence of (Ψ, Δ) of the film-substrate-combine. Thereafter, the λ or E dependence of optical constants refractive index (n) and extinction coefficient (k) of the film layer(s) may be determined on basis of modeling employing appropriate oscillator models (refer table 5.2 and figure 6.7). In our case, the determination so is expedited given our independent knowledge, on basis of XRR results (refer figure 5.3), of film layer structure along with layer(s) thickness(es). Thus, film layer structure models determined via XRR were employed for the modeling as aforementioned.

Thereby, for each sample, SE spectra (Ψ(E), Δ(E)) were recorded (via a JAW Model RC2 ellipsometer) at eight equally spaced angle of incident light (α_i) between 45° to 66° over the E (λ) range 5.9 eV to 0.73 eV (210 nm to 1690 nm). The range referred to covers wavelengths of interest for micro-scale and macro-scale applications alluded to in chapter 1.

As mentioned, the starting point for modeling of the experimentally obtained SE spectra of a film, was its refined film layer structure obtained via XRR. The modeling was performed using Kramers Kronig (KK) consistent dispersion functions (oscillator models) to yield physically plausible ε^*(E), and in turn (via equation 4.6a) n^*(E).

Given the transparency of the film (ISZO) and of the substrate (CEXG), ordinarily the experimentally recorded SE spectra will be contributed in part by electro-magnetic energy reflected from the film-substrate-combine 'back-side' (that is, from the substrate-air interface). Such contributions compromise the ability to model the SE spectra. This problem is the more severe in the present case, since the signal to noise ratio of the present

SE measurements is depressed on account of the low layer thicknesses ($<$ 100 nm; refer table 5.1). Nonetheless, back-side reflections were effectively suppressed by applying a refractive index-matching material (cloudy tape) to the substrate-air interface (Synowicki, 2008).

The modeling of the SE spectra was performed via the JAW CompleteEASE software (J. A. Woollam Co., 2014). The ε^*(E) of the CEXG substrate (viz., ε^* of CEXG ($\varepsilon^*_{\text{CEXG}}$)), necessary for the modeling the film SE spectra, was in turn modeled per the guidance of, and consistent with, published literature as a G+TL two oscillator system (Cushman et al., 2016) (refer section A.3.C).

4.4.D Amorphous semiconducting films: oscillator models

Oscillator models help quantify the interaction of (oscillatory) electromagnetic energy with matter (the film) in terms of its electronic properties such as E_g and μ. The lorentz oscillator (LO) is the basis for the physically meaningful TL and D oscillator models. The same result upon the incorporation of context-specific physics into the LO.

The TL oscillator model (refer section 4.4.D.1) is a KK consistent model for amorphous semiconducting materials at energies comparable to E_g (typically, 2 eV to 4 eV) (Jellison Jr. and Modine, 1996). At lower energies yet greater than the plasma edge energy (E_p) (typically, $\lesssim$ 1 eV), free electron absorption dominates. Over this energy range, the D model is more appropriate (refer section 4.4.D.2).

The aforementioned models are responsive at well separated energy-scales, that is, address different aspects of the physics of the semiconductor material (film). We employ a TL+D oscillator model to model experimentally measured response (that is, Tr(E)) of amorphous semiconducting samples (film-substrate-combine) over the energy range $\gtrsim E_g$ to $\gtrsim E_p$.

The SE spectra, viz., (Ψ(E), Δ(E)) were measured over E range 0.76 eV to 5.9 eV energy range. Modeling of the aforementioned spectra (on basis also of results from Hall Effect (HE) measurements; refer section 4.5) permitted the prediction / calculation of Tr(E) of the film-substrate-combine. The computed and experimentally measured results were compared (refer figure 5.6).

4.4.D.1 tauc-lorentz

The TL dispersion function models the main absorption of an amorphous material via a LO with zero absorption below a defined E_g energy (Kamiya, Nomura, and Hideo Hosono, 2009). The model proceeds from the Tauc absorpton formula:

$$\varepsilon_{2,\,TL}(E) \propto \left(1 - \frac{E_g}{E}\right)^2 \tag{4.7}$$

The TL ε^* (ε^*_{TL}) of the TL oscillator model is:

$$\varepsilon_{2,\,TL} = \begin{cases} \frac{AE_0B(E-E_g)^2}{(E^2-E_0^2)^2+B^2E^2} \cdot \frac{1}{E} & \dots E > E_g \\ 0 & \dots E \leq E_g \end{cases} \tag{4.8}$$

$$\varepsilon_{1,\,TL} = \frac{2}{\pi} P \int_{E_g}^{\infty} \frac{\xi \varepsilon_{2,\,TL}(\xi)}{\xi^2 - E^2}\, d\xi \tag{4.9}$$

where: real part of ε^*_{TL} ($\varepsilon_{1,\,TL}$), imaginary part of ε^*_{TL} ($\varepsilon_{2,\,TL}$), cauchy principal value (P), band-gap energy (E_g), amplitude of imaginary part of ε^*_{TL} (A), broadening of imaginary part of ε^*_{TL} (B), energy at peak in imaginary part of ε^*_{TL} (E_0), energy (E).

4.4.D.2 drude

The classic D oscillator model describes free electron effects on the dielectric response of a material. It is a LO with center energy equal to zero.

The Drude ε^* (ε^*_D) oscillator model is:

$$\varepsilon^*_D = \frac{-\hbar^2 e^2 n \mu}{\varepsilon_0(\mu m^* m_e E^2 - \iota e \hbar E)} \tag{4.10}$$

where: reduced Planck constant ($\hbar$), elementary charge (e), conduction electron concentration (n), conduction electron mobility (μ), permittivity of vacuum (ε_0), effective mass of electron in units of rest mass of electron (m^*), rest mass of electron (m_e), energy (E).

Section 6.3.C presents further discussion and analysis of ISZO film opto-electronic properties on basis of the D model.

4.5 Film electronic properties: AC field Hall effect

4.5.A Introduction

We motivate the technique of ACFHE in light of the nature of films at issue (section 4.5.B). We describe the data analysis framework for the direct current (DC) HE technique. We then present the theory (analytical-framework of the ACFHE technique (section 4.5.C). We conclude by motivating and presenting the BH model of IIS which was used to elucidate the electronic state of the films on basis of T dependent HE measurements (section 4.5.D).

4.5.B Motivation

The low values of conduction electron mobility (μ) and conduction electron concentration (n) exhibited by (some of) our films (refer table 6.5) rendered the set of films unsuited for HE measurements via the traditional DC magnetic field technique. The unsuitability arises in part due the standard analysis protocol that is employed to extract Hall voltage (V_H) from experimentally measured voltage in Hall geometry (V_m). Further discussion of limitations of the DC HE technique, given our films-set, is presented in

section 4.5.C.2.

Due this reason — as also due paucity of published (benchmark) results on the Si doped In−Si−Zn−O material system in general, and for the ISZO material composition in particular — it was imperative to recruit the ACFHE technique. This enabled reliable determination of electronic properties, and in turn, of electronic state, of our films (Hall, 1879; Pauw, 1958; Lindemuth and Mizuta, 2011; Lindemuth, 2020).

4.5.C Theory

4.5.C.1 DC Hall effect technique

The experimentally measured voltage in Hall geometry (V_m) is given by:

$$V_m = V_H + V_0 + V_{TE} \tag{4.11a}$$

$$= \frac{R_H I B_{DC}}{d} + V_0 + V_{TE} \tag{4.11b}$$

$$= \frac{\rho I}{d}(\mu B_{DC} + \alpha) + V_{TE} \tag{4.11c}$$

using,

$$V_H = \frac{I B_{DC}}{ned} \tag{4.11d}$$

$$\rho = \frac{1}{ne\mu} \tag{4.11e}$$

$$R_H = \mu\rho \tag{4.11f}$$

and,

$$V_0 = \frac{\alpha I}{d}\rho \tag{4.11g}$$

where, Hall voltage (V_H), mis-alignment voltage (V_0), thermal electric voltage (V_{TE}), Hall coefficient (R_H), resistivity (ρ), electric current (I), DC magnetic field (B_{DC}), conduction electron concentration (n), elementary charge (e). film thickness (d), conduction electron mobility (μ), geometry parameter (α).

The thermal electric voltage (V_{TE}) arises due the contact between different materials (In−Si−Zn−O / film, and indium (In) / electrical contact on film), and depends on thermal gradients across the film. Furthermore, it is independent of electric current (I). As such, current reversal may be employed to determine experimentally measured voltage in Hall geometry minus V_{TE} (V'_m) thus:

$$V'_m = IR \tag{4.12a}$$

where,

$$R = \frac{V_m(I) - V_m(-I)}{2I} \tag{4.12b}$$

Thus, further to procedure / equation 4.12 and with reference to equation 4.11c, we write:

$$V'_m = \frac{\rho I}{d}(\mu B_{DC} + \alpha) \tag{4.13}$$

where, $\alpha = 0$ for a perfectly square film with point electrical contacts at the four corners. Each of our films is nominally a square with side $a_f = 11\,\text{mm}$, and the hand-made electrical contacts were $\simeq 0.5\,\text{mm}$ in diameter.

We estimate, based on calculations by Lindemuth and Mizuta, 2011:

$$\alpha \gtrsim 10^{-2} \tag{4.14a}$$

For a (typical, for instance, via in-house equipment) DC HE measurement performed at $B_{DC} = 0.5\,T$, for our films per table 6.5,

$$\mu B_{DC} \quad \text{lies in the range} \quad 4.4 \times 10^{-4} \text{ to } 1.2 \times 10^{-3} \tag{4.14b}$$

Whereby, for our films in a typical DC HE measurement,

$$\mu B_{DC} \ll \alpha \tag{4.14c}$$

Thus, per equation 4.13, the measured V'_m is predominantly mis-alignment voltage (V_0).

The V_0 depends on film resistivity (ρ), T*, I, and geometry parameter (α); and is independent of DC magnetic field (B_{DC}). As such, magnetic field reversal may be employed to determine Hall coefficient (R_H) thus:

$$R_H \equiv \rho\mu \tag{4.11f}$$

$$= \frac{d}{I}\left(\frac{V'_m(B_{DC}) - V'_m(-B_{DC})}{2B_{DC}}\right) \tag{4.15a}$$

With R_H determined via equation 4.15a and ρ determined via independent experimental measurement (via, for instance, the van der pauw (VDP) method (Weeks, 1985)), μ may be determined via equation 4.11f. With ρ and μ having been determined thus, n may be determined via relation 4.11e.

*V_0 depends on T, since ρ does.

4.5.C.2 DC Hall effect technique: limitations

In light of the discussions of section 4.5.C.1, following considerations arise:

- The standard analytical framework of the DC magnetic field HE technique assume that zero to a negligible portion of I flows through the voltmeter. For high resistivity ($\rho \gtrsim 10\,\Omega\,\mathrm{cm}$) films having thickness $\mathrm{d} \simeq 10\,\mathrm{nm}$, the $\mathrm{R_s} \sim 10\,\mathrm{M\Omega/\square}$; for instance, for film F15 (refer table 6.5). At such (high) film resistances, the aforementioned assumption may not hold true. Relatedly, in order to keep the $\mathrm{V_m}$ within range of the voltmeter, it may become necessary to excite the film with a small I ($\lesssim 10\,\mu\mathrm{A}$). At such low levels of excitation, absent especial attention towards their attenuation, noise and thermal drifts may render HE measurements unreliable.

- Thermal drifts in the HE equipment, and in turn in the film, cause $\mathrm{V_{TE}}$ to vary. This degrades the ability to remove its contribution to $\mathrm{V_m}$ via current reversal (equation 4.12b).

- Given dependence of $\mathrm{V_0}$ on T, its removal from $\mathrm{V_m}$ via magnetic field reversal, per procedure / equation 4.15a, requires that T be the same during the $\mathrm{V'_m(B_{DC})}$ and $\mathrm{V'_m(\text{-}B_{DC})}$ measurements. Thermal drifts within the HE equipment counteract this requirement.

- With reference to equations 4.13 and 4.15a, $\mathrm{R_H}$ is obtained via determination of the difference ($\mathrm{V'_m(B_{DC})}$ - $\mathrm{V'_m(\text{-}B_{DC})}$). In light of relation 4.14c, the aforementioned determination involves the subtraction between two comparable numbers to yield a number which is relatively much smaller. Any noise during the measurement of, or and independently, loss of significance due rounding off, of the two starting / large

numbers may render the determination unreliable.

On account of the aforementioned considerations, and given furthermore the paucity of published benchmark results noted in section 4.5.B, we conducted HE measurements via the ACFHE technique. Whenever feasible, the alternating current (AC) measurements so were corroborated with DC magnetic field HE measurements. In all such cases, the results of measurement via AC and DC techniques were in agreement.

4.5.C.3 AC field Hall effect measurements

The ACFHE technique employs a low frequency (25 mHz to 100 mHz) AC magnetic field (B_{AC}). Due the inductance of the electrical circuit used to measure the HE, this causes a inductance voltage (V_i) proportional to the time derivative of B_{AC} to be generated. The V_m thence is given by:

$$V_m = V_H + V_i + V_0 + V_{TE} \tag{4.16a}$$

$$= \frac{R_H I B_{AC}}{d} + \beta \frac{dB_{AC}}{dt} + V_0 + V_{TE} \tag{4.16b}$$

Expressing,

$$B_{AC} = B \cos 2\pi\nu t \tag{4.16c}$$

one obtains,

$$V_m = \frac{R_H I B}{d} \cos 2\pi\nu t - 2\pi\nu\beta B \sin 2\pi\nu t + V_0 + V_{TE} \tag{4.16d}$$

$$= \frac{R_H I B}{d} \cos 2\pi\nu t + 2\pi\nu\beta B \cos\left(2\pi\nu t + \frac{\pi}{2}\right) + V_0 + V_{TE} \tag{4.16e}$$

where, Hall voltage (V_H), mis-alignment voltage (V_0), thermal electric voltage (V_{TE}), Hall coefficient (R_H), electric current (I), film thickness (d). am-

plitude of AC magnetic field (B), AC magnetic field (B_{AC}), proportionality factor relating time derivative of B_{AC} to V_i (β), frequency of B_{AC} (ν), time (t).

Evidently, V_H and B_{AC} are in phase, and V_i lags them both by a phase-angle of $\pi/2$. Furthermore, and with reference to equation 4.16e, while the aforementioned voltages are AC, V_0 and V_{TE} are DC.

Use of a lock-in (phase sensitive) voltmeter now accomplishes two measurement tasks. First, it removes the DC voltage. Second, it makes available the two phase separated AC voltages individually. Thus, the voltage read at x-channel of lock-in voltmeter (V_x) and the voltage read at y-channel of lock-in voltmeter (V_y), are:

$$V_x = \frac{R_H I}{d} B_{AC,\,RMS} \tag{4.17a}$$

$$V_y = -2\pi\nu\beta B_{AC,\,RMS} \tag{4.17b}$$

where,

$$B_{AC,\,RMS} = \frac{B}{2^{1/2}} \tag{4.17c}$$

where, Hall coefficient (R_H), electric current (I), film thickness (d). RMS value of B_{AC} ($B_{AC,\,RMS}$), proportionality factor relating time derivative of B_{AC} to V_i (β), frequency of B_{AC} (ν).

Evidently, with R_H determined via relations 4.17a and 4.17c, and ρ determined via independent experimental measurement (via, for instance, the VDP method), μ may be determined via equation 4.11f. With ρ and μ having been determined thus, n may be determined via relation 4.11e.

Furthermore and significantly, the measurement protocol of the ACFHE

technique — whereby R_H is recovered from V_m upon removal of V_0 and V_{TE} — does not entail current reversal and magnetic field reversal. The limitations of the DC magnetic field HE measurement (per section 4.5.C.2) are thereby alleviated.

4.5.D The absolute temperature dependence of conduction electron mobility: ionized impurity scattering

The temperature dependence of conduction electron mobility (μ) arises due its dependence on mean free time between collisions (τ), given as:

$$\mu = \frac{e}{m}\tau \tag{4.18a}$$

where, per Matthiessen rule (Lundstrom, 2000)

$$, \frac{1}{\tau} = \frac{1}{\tau_{ii}} + \frac{1}{\tau_p} \tag{4.18b}$$

wherein,

$$\tau_p \propto T^{-3/2} \tag{4.18c}$$

and,

$$\tau_{ii} \propto T^{3/2} \tag{4.18d}$$

and therefore there exists,

$$T(\mu_{max}) \tag{4.18e}$$

where, elementary charge (e), effective mass of electron at CBE (m), mean free time between collisions with phonons (τ_p), mean free time between collisions with ionized impurities (τ_{ii}), absolute temperature (T), maximal mobility (μ_{max}).

Evidently, given relations 4.18c and 4.18d, the importance of mean free time between collisions with phonons (τ_p) relative mean free time between collisions with ionized impurities (τ_{ii}) increases as absolute temperature (T) decreases, which leads therefore to result 4.18e. Also, T(μ_{max}) increases, and μ_{max} decreases, with increase in impurity and defect concentrations. At sufficiently high impurity / defect concentration, T(μ_{max}) can approach or exceed room-temperature.

The experimentally measured μ(T) data for films F11 and F23 are shown in figure 6.8(b). Per the preceding discussion, the data bears out the persistence of IIS (equation 4.18d) till (at least) room-temperature, and shows furthermore that T(μ_{max}) lies above room-temperature.

Next, we present the BH model of scattering due ionized impurities. We discuss the T-range of its applicability for the present films / material composition. On its basis, we will be able to calculate total donor concentration (N_D)(T) and total acceptor concentration (N_A)(T) in the aforementioned T-range. Consideration of the same alongside experimentally measured conduction electron concentration (n), and alongside nominal concentration of dopant / Si (N_{Si}) will enable us to describe the experimentally observed variation of μ between films F11 and F23.

We next consider the BH model of IIS, which model assumes fully ionized impurities. Accordingly, for a compensated (n-type) semiconductor (Look et al., 2011):

$$n(T) = N_D(T) - N_A(T) \tag{4.19}$$

where, conduction electron concentration (n), total donor concentration (N_D), total acceptor concentration (N_A), absolute temperature (T).

4.5.D.1 The Brooks-Herring model

The BH model of IIS proceeds from a screened coulomb potential of independent scattering centers (impurities), to obtain, under Boltzmann statistics (Brooks, 1955; Chattopadhyay and Queisser, 1981; Ellmer, 2001; C. M. Wolfe, G. E. Stillman, and Dimmock, 1970; Korshunov et al., 2000):

$$V(r) = \frac{Ze}{4\pi\varepsilon r}\exp\left(-\beta_s r\right) \tag{4.20a}$$

where,

$$\beta_s = \left(\frac{ne^2}{\varepsilon k_B T}\right)^{1/2} \tag{4.20b}$$

and from which one may obtain,

$$\mu_{BH} = \frac{2^{15/2}\pi^{1/2}{k_B}^{3/2}}{e^3}\frac{\varepsilon^2 T^{3/2}}{m^{1/2}Z^2 N}\left(\ln\left(\frac{24m{k_B}^2}{\hbar^2 e^2}\frac{\varepsilon T^2}{n}\right)\right)^{-1} \tag{4.20c}$$

where,

$$n = N_D(1-\Gamma) \tag{4.20d}$$

$$N = N_D(1+\Gamma) \tag{4.20e}$$

since,

$$n = N_D - N_A \tag{4.20f}$$

$$\Gamma = \frac{N_A}{N_D} \tag{4.20g}$$

and where,

$$m = m_e m^* \tag{4.20h}$$

where, impurity potential (V), radial distance from impurity ion (r), charge on impurity in units of elementary charge (Z), elementary charge (e), mathematical constant (π), static permittivity (ε), inverse of screening length (β_s), reduced Planck constant ($\hbar$), conduction electron concentration (n), boltzmann constant (k_B), absolute temperature (T), BH mobility (μ_{BH}), ionized impurity concentration (N), charge on impurity in units of elementary charge (Z), total donor concentration (N_D), total acceptor concentration (N_A), compensation ratio (Γ), effective mass of electron at CBE (m), rest mass of electron (m_e), effective mass of electron in units of rest mass of electron (m^*).

As will be seen in section 6.4.C, for the two films for which it had proved feasible to determine (μ(T), n(T)) — viz., F11 and F23 — and over the respective T-range in which IIS is the dominant mode of scattering, n(T) does not display any significant change. That is, the respective impurity populations are completely ionized over the respective T-ranges in question. As such, in the present discussions, N_D and N_A represent respectively the ionized donor and ionized acceptor concentrations. The expression 4.20b follows in light of the aforementioned observations (Chattopadhyay and Queisser, 1981).

We have proceeded analysis of (μ(T), n(T)) starting from determination of the T-range over which IIS is the dominant scattering mechanism. The BH model for IIS per equation 4.20 was employed thence to calculate ionized impurity concentration (N), N_D, and N_A. The determination of charge on impurity in units of elementary charge (Z) — consistent with (film / target) material composition, and additional experimental results that are in attendance — will also be described in section 6.4.C.

We determine, via relation 4.20c, N at given T from the corresponding experimentally measured (μ, n) and by setting (assuming) $\mu_{BH} = \mu$. This procedure is justified given the domination of IIS (refer figures 6.9(b) and 6.9(a)) over other scattering mechanisms in the T-ranges (respective) under consideration.

A computer program was written to implement calculations per the BH model. The program computes, at given T, (N_D, N_A) on basis of corresponding experimentally measured (μ, n). The same is presented in appendix B.

4.5.E Measurement: practical aspects

A Lake Shore Cryotronics 8400 Series HMS Hall effect measurement system (Lakeshore Cryotronics Inc., 2020) connected to a closed cycle refrigerator was used to determine μ(T) and n(T) of our ISZO films (refer figure 4.4(a)). The aforementioned determination is predicated upon the fabrication of ohmic electrical contacts with the film. This is critical, given the semiconducting (low n) nature of our films. Accordingly, we experimented with several potential solders such as silver (Ag) paste (various grades), In−Sn (various grades), and In, for affixing electrical contact wires to the film.

We determined that molten In (99.999 % pure metal basis; sourced from Alfa Aesar) wets the films with relative ease. Together with use of a clean point tip (a stainless steel paper-pin), which was attached (via copper (Cu) wire)

to the rod of a temperature controlled soldering station, it proved feasible to fashion small sized (refer description of equation 4.13) In electrical contact pads on a film.

Subsequently, Ag wires (100 µm in diameter, 99.997 % pure metal basis; sourced from Alfa Aesar) were soldered (also via In) onto the films via the contact pads fashioned previously (figure 4.4(b)). The other end of each Ag wire so was soldered to the correct receiving contact pad on the sample card (figure 4.4(c)). Subsequently, the sample card was mounted on to the standard insert (figure 4.4(d)) of the Hall effect measurement system (figure 4.4(a)).

As mentioned, via use of a point soldering tip and with practiced care, it is possible to control (minimize) the size of the electrical contact pad. This is an important requirement, since the analyses presented in section 4.5.C.1 assume (four) point electrical contacts. We were able to fabricate four 'point' ohmic electrical contacts at a relatively low temperature ($\gtrsim$157 °C, the melting point of In), on each of our nine films.

Furthermore, care must be exercised to minimize the springiness (tension) present in the soldered wires. This is relevant to ensure that the electrical contacts survive and continue to be of service, especially during cycling between room and cryogenic temperatures. The length of wire used should be minimized, and sharp changes in angle should be avoided.

Excitation current values as used were in the range I = 10^1 µA to 10^2 µA. The HE measurement system has an input impedance >200 GΩ.

It proved feasible to conduct room-temperature HE measurements on but four of the films (viz., F15, F7, F11 and F23; refer table 6.5). Furthermore, it proved feasible to conduct T dependent HE measurements on but two of the films (viz., F11 and F23; refer figure 6.8).

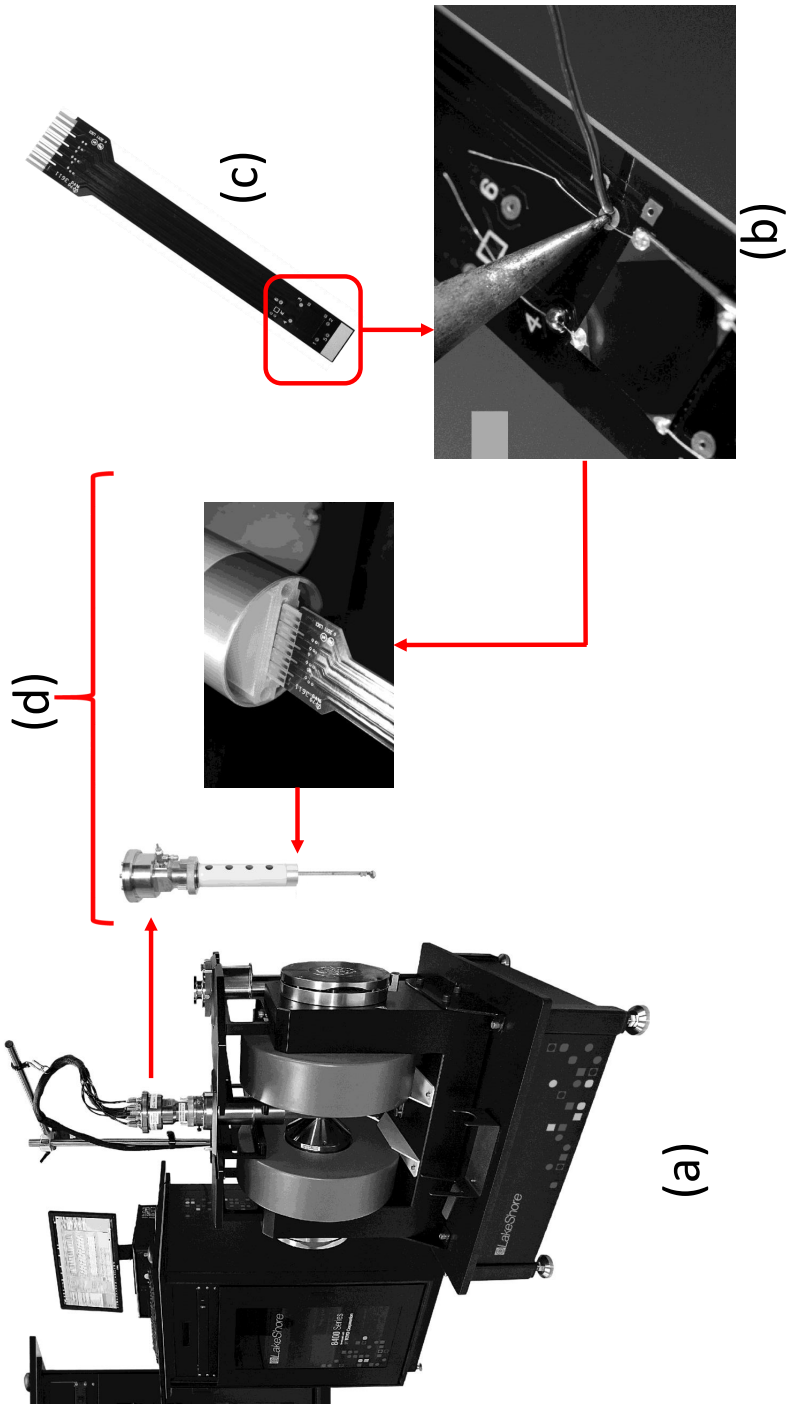

Figure 4.4: [Caption to this figure is presented on next page.]

Figure 4.4: [Figure corresponding to this caption is presented on the previous page.]
Practical aspects of the Hall Effect (HE) measurements as conducted for the present study. (a) The Lake Shore Cryotronics 8400 Series HMS Hall effect measurement system (Lakeshore Cryotronics Inc., 2020). (b) Film with electrical contact wires already attached being mounted on the sample card. Note that the soldering rod as seen does not the possess the "point" tip described in the text. As shown, a wire is being soldered on to the correct receiving contact pad of the sample card. (c) The sample card. (d) The standard insert. The arrows depict interrelationship between the various steps leading up to the mounting of a film in to the HE measurement system. The figures (a)–(d) are not to scale.

Chapter 5

The sub-plantation layer

5.1 Introduction

In this chapter, we report the direct experimental observation of a sub-plantation layer (SPL) in transition metal oxide (TMO) films. Our report is based on x-ray reflectometry (XRR) measurements, and are corroborated via spectroscopic ellipsometry (SE) measurements. Further corroboration is furnished by the agreement between predictions of an ab initio theoretical dimensional analysis (DA) of SPL physical properties, and the results of response surface analysis (RSA) of experimental measurements of the same properties.

Thus, we present Fourier analysis of film Kiessig fringe profiles (KFPs) recorded via XRR. The analysis revealed that while certain films are single-layer (SL) (as expected), others are bi-layer (BL) (section 5.2). We then present the film layer structure models, to be refined, as were arrived upon in light of the aforementioned analysis (section 5.3). We then present the refined film layer structures, which show the additional layer in BL films to be situated mediate the substrate and film proper (thin-film layer (TFL));

and the recognition thereby of it being a SPL (section 5.4). This permits discussion of the process factors dependence of the physical properties of the refined film layers (section 5.5). We then present and compare the experimental (via SE) and modeled determinations of film-substrate-combine transmission fraction (Tr) (section 5.6).

We now double back to discuss the process factors dependence of our sub-plantation results (section 5.7). We consider the effect of collimation of sputtered material flux on film deposition, by presenting a semi-quantitative comparative analysis of our and published experimental results; here, we also develop and present a SPL phase-diagram (section 5.8). We then consider the enabling role of our experimental choices for the manifestation and observation of the SPL (section 5.9).

Finally, we consider the bonafides of the SPL by presenting an ab initio DA of its physical properties, given the radio frequency magnetron sputtering (RFMS) process factors at issue; and compare its predictions to the results a RSA of experimental measurements of the same properties (section 5.10).

5.2 Observation of bi-layer sputtered transition metal oxide films

In section 3.2.E, we presented the experiment design of this study. Accordingly, a set of nine films — viz., F35, F15, F31, F19, F7, F27, F11, F23, and F3 — have been deposited via RFMS.

The KFP of each film was successfully recorded via XRR. The requirements necessary for the successful conduct of specular XRR have been presented in section 4.3.B. This yielded direct and refined determinations of film layer(s) thickness(es) per figure 5.2 and table 5.1 respectively.

The experimentally determined KFPs were recorded via Cu K $-\alpha_1$ x-

radiation ($\mathsf{Cu\ K} - \alpha_1$), and are presented in figure 5.1. It is expedient to consider the fourier transform (FT) of each KFP so. The same are presented in figure 5.2, organized according to the experiment design plane to which the corresponding film belongs (refer table 3.2).

Consideration of the FTs per figure 5.2, in light of the experiment design per figure 3.3, leads to the following observations:

- The films at the experiment design front-plane — viz., F27, F11, F23, F3; figure 5.2(c) — and at the center-plane — viz., F7; figure 5.2(b) — are BL.

- The films at the experiment design back-plane — viz., F35, F15, F31, F19; figure 5.2(a) — are SL (as expected).

- The process gas pressure (p) is significant for the manifestation of BL films. This follows from the preceding observations, since the growth of each individual film (whether it belongs to the front-plane, or to the center-plane, or to the back-plane of the experiment design) was sourced from a continuously received stream of material flux (refer section 4.2.C).

  We will have occasion to consider this observation further in terms of the given pressure distance product ($\phi_{\mathsf{t-s}}$) (refer section 5.7.B). Nonetheless, it is noted that since all films were deposited at the same target-substrate distance ($\mathsf{l_{t-s}}$), it is not possible to distinguish between the effects of the process factors p and pressure distance product (ϕ).

The DA and RSA presented in section 5.10 will provide further rationalization of manifestation of the additional layer, in terms of the physics of RFMS. At that stage of discussions, the additional layer would have been

determined to be a SPL. Notably, the aforementioned analyses will reveal, independently of and consistently with each other, that the process factors p and RF power (P_{RF}) are significant determinants of manifestation of a SPL.

5.3 The film layer structure models

In section 5.2, we presented the direct experimental determination of the number of layers comprising each individual film of the experiment design per figure 3.3. That is, we presented the gross layer structure for each individual film so. Thereby, it was determined that the films at the back-plane of the experiment design are SL (refer figure 5.3(a)), while those at the center-plane and front-plane are BL (refer figure 5.3(b)).

Accordingly, the general and detailed SL and BL film layer structures of the film-substrate-combine are presented in figure 5.3(c) and 5.3(d) respectively. The film layer structure models were, as applicable, refined as described in section 5.4.

5.4 Refinement of film layer structures

Refinement of the applicable general detailed film layer structures on basis of the experimentally recorded film KFP yields length-scales and mass-scales of individual film layer(s).

In particular, refinement yielded the film layer(s) thicknesses. Accurate determination of the same is crucial for quantitative analyses of experimental SE and AC Field Hall Effect (ACFHE) results. Determination so of the same is crucial also for quantitative (linear) modeling, via RSA, of experimentally determined properties (physical and opto-electronic) of film layer(s). In turn, (particular) RSA results help test the predictions of DA re SPL physical properties.

Refinement also permitted determination of the technologically relevant

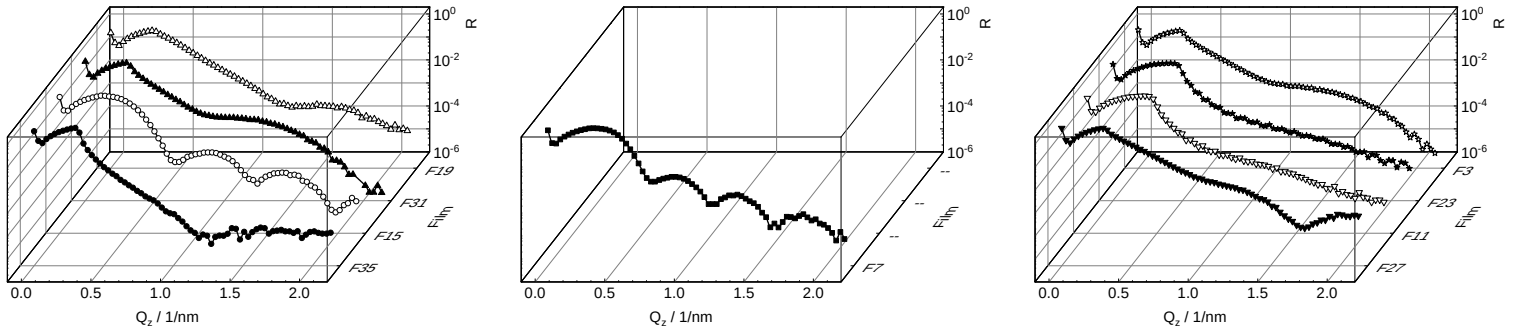

(a) (b) (c)

Figure 5.1: With reference to experiment design per figure 3.3 and table 3.2 experimentally recorded Kiessig fringes profile (KFP) for a particular (typical) set of nine Si doped In_2O_3−$(ZnO)_3$ (ISZO) films obtained at the (a) back-plane, (b) center-plane, and (c) front-plane. The KFPs were recorded via x-ray reflectometry (XRR). Refer also figure 5.2. Note: the data and results presented in the remainder of this chapter are on individual members of the aforementioned particular films-set, except when noted otherwise.

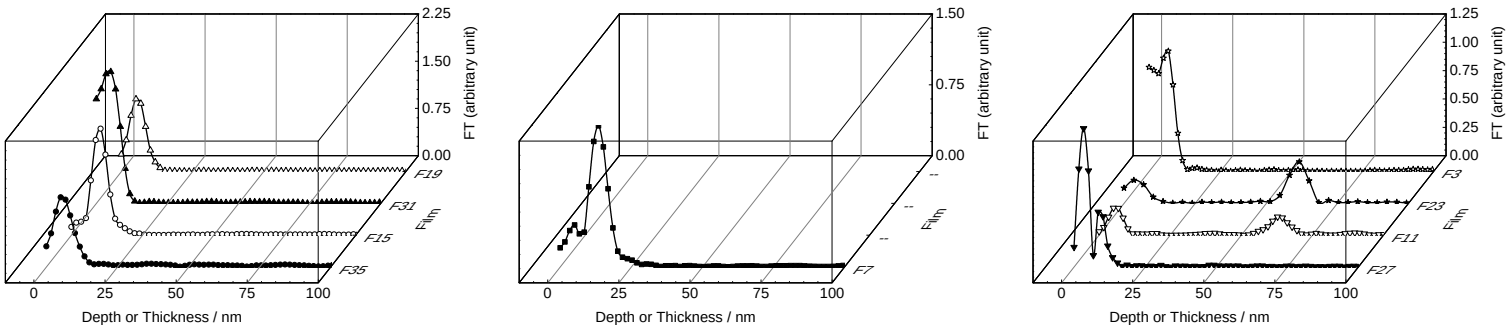

(a) (b) (c)

Figure 5.2: The fourier transform (FT) of experimentally recorded Kiessig fringes profile (KFP) of the particular Si doped $In_2O_3-(ZnO)_3$ (ISZO) films-set per figure 5.1. With reference to the experiment design per figure 3.3 and table 3.2, the FT of the experimentally recorded KFP for the (a) four back-plane films, viz., F35, F15, F31, and F19. The sole peak in each FT profile disclose presence of two interfaces — viz., the film surface, and the film-substrate interface — in the film-substrate-combine. The presence of two interfaces implies that the film is single-layer (SL), per figure 5.3(a); (b and c) one center-plane film, viz., F7, and four front-plane films, viz., F27, F11, F23, and F3. The two peaks in each FT profile disclose presence of three interfaces. Of these three, two interfaces are as mentioned in (a). The third interface, like the film-substrate interface, must also be in-situ the film-substrate-combine. The presence of three interfaces implies that the film is bi-layer (BL), per figure 5.3(b). It is noted that the relative placement of the the two layers (within given BL film) is as yet unknown.

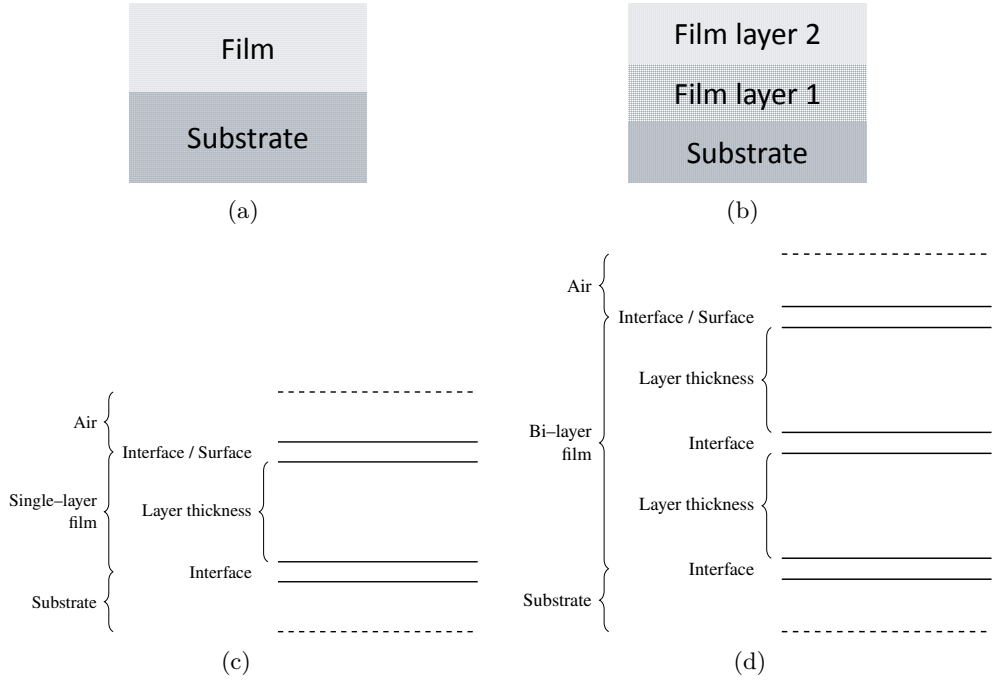

Figure 5.3: (a and b) The 'gross' layer structures arrived upon of the single-layer (SL) (per figure 5.2(a)) films, and of the bi-layer (BL) films (per figures 5.2(b) and 5.2(c)). (c and d) The general 'detailed' layer structure per (a) and (b) respectively. These were refined, as applicable, for each film via the respective Kiessig fringes profile (KFP). This led to determination of the physical properties per table 5.1 for each film (for SL films), or for each film layer (for BL films). For the BL films, the refinement process also established the relative placement of the two layers. Representative refined KFP profiles are presented in figure 5.4.

length-scale of roughness of in-situ (that is, buried interface(s)), and / or of the surface. The substrate roughness was fixed at the manufacturer supplied value for Corning Eagle XG Glass (CEXG) (refer section 4.2.C).

Furthermore, refinement yielded the density of film layer(s), on basis of ISZO density (D_{ISZO}) (Yoshinari et al., 2009) and CEXG density (D_{CEXG}) (Corning Inc., 2017).

The film layer structure applicable for each film was refined via the Rigaku GlobalFit software. Figure 5.4 presents representative refined KFP profiles, overlaid atop respective experimentally measured KFP profile (refer figure 5.1).

The refinements are for (assume) an SPL composition of CEXG and Si doped $In_2O_3{-}(ZnO)_3$ (ISZO) in a 1:1 ratio. Full details of the refinement procedure are presented in section A.2. Table A.1 presents values of goodness of fit metrics as obtained for each refinement. Final results of refinement are presented in table 5.1.

With reference to discussions per section 5.2, the refinements established the relative placement of the two layers of each BL film (refer figures 5.2(b) and 5.2(c)). Consideration of the refined density of the film layer(s) — in light of the densities of starting materials (viz., ISZO and CEXG), of the relative placement of the film layer(s), and of the energetic nature of the deposition process (RFMS) — led to appreciation of presence of sub-plantation phenomena. This led in turn to the determination of the additional layer — "Film layer 1" per figure 5.3(b) — as a 'SPL' (Lifshitz, Kasi, and Rabalais, 1989; Lifshitz, Kasi, Rabalais, and Eckstein, 1990; Boyd et al., 1998).

Reasoning similarly, one appreciates that the "Film" layer per figure 5.3(a) and the "Film layer 2" per 5.3(b) are kindred layers. Accordingly, for consistency of nomenclature, they will both be addressed via the term 'TFL'.

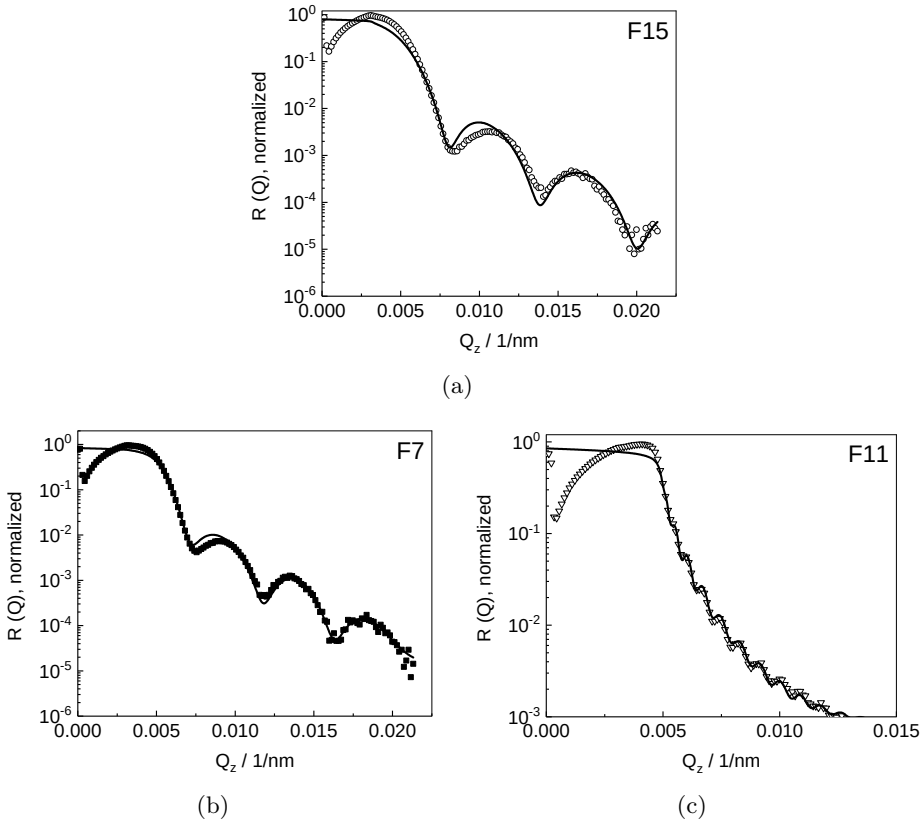

Figure 5.4: The experimentally recorded and modeled Kiessig fringes profile (KFP) of selected individual members of the particular Si doped $In_2O_3{-}(ZnO)_3$ (ISZO) films-set per figure 5.1, (a) back-plane (single-layer (SL)) film F15, (b) center-plane (bi-layer (BL)) film F7, and (c) front-plane (BL) film F11. Here, reflectivity (R), magnitude of transfer wave-vector (Q_z).

The refined layer structures of each of the nine films per experiment design figure 3.3 are presented in table 5.1.

Perusal of the refined values so of TFL density (D_{TFL}) determines the nominal TFL material composition as (being close to) ISZO. Similarly, perusal of the refined values of SPL density (D_{SPL}) determines their composition, consistent with their manifestation via sub-plantation, to be an admixture of CEXG and ISZO.

5.5 Physical properties of film layers: trends

5.5.A Introduction

With reference, for instance, to figure 5.10, or to figure 6.20, it is evident that main and interaction effects of RFMS process factors are comparable in magnitude. Furthermore, a given effect (main or interaction; per equation 3.1) may be antagonistic for a given first property of interest, and sympathetic for a given second property of interest. As such, RSA is an appropriate technique for quantitative determination of process factors dependence of properties of interest.

Nevertheless, we consider and systematize trends as are in evidence among the refined physical properties presented in table 5.1.

Accordingly, we consider the RFMS process factors dependence of physical properties of the SL films, that is, those films which are at the experiment design back-plane (section 5.5.B). Next, we consider similarly the BL films, that is, those films which are at the experiment design center-plane and at the front-plane (section 5.5.C).

5.5.B The single-layer films

These are the four films at the back-plane of the experiment design per figure 3.3 and table 3.4.

We observe increase in TFL thickness (d_{TFL}) concomitant with increase in D_{TFL} from F35 to F15, at fixed p = + and O = -. This is consistent with the increase in P_{RF}, from P_{RF} = - to P_{RF} = +. The reason is that increase in P_{RF} leads to an increase in sputtering-yield, simultaneous with an increase in energy of sputtered material flux. In this regard, reference may be made also to figure 5.7.

We observe decrease in d_{TFL} concomitant with increase in D_{TFL} from F19

Factor (CU)			Back-Plane				Front-Plane			
p →			+				−			
P_{RF} ↓	O ↓	Film layer	Film	D / g/cm^3	d / nm	r / nm	Film	D / g/cm^3	d / nm	r / nm
−	−	TFL	F35	1.1	2.5	0.4	F27	6.5	3.8	0.4
		SPL		NA	NA	NA		4.1	3.8	0
+	−	TFL	F15	6.0	9.7	0.6	F11	6.4	61.6	1.1
		SPL		NA	NA	NA		3.1	5.8	2.4
+	+	TFL	F31	6.0	3.2	0.6	F23	6.2	58.8	0.6
		SPL		NA	NA	NA		2.8	5.1	2.3
−	+	TFL	F19	5.4	5.7	0.5	F3	6.8	2.8	0.6
		SPL		NA	NA	NA		4.0	4.0	0
0	0	TFL	NA	NA	NA	NA	F7*	6.5	12.0	0.7
		SPL		NA	NA	NA		3.3	4.6	0.8

Table 5.1: The refined detailed layer structure of the nine films according the experiment design per figure 3.3 and table 3.4. The organization of the table highlights the importance of the radio frequency magnetron sputtering (RFMS) process factor process gas pressure (p) for emergence of the sub-plantation layer (SPL). For completeness, the two other process factors of the experiment design, viz., RF power (P_{RF}) and oxygen percent (O) are also indicated. It is readily verified for each film that the layer (SPL, or thin-film layer (TFL)) thickness(es) arrived upon refinement agree with the respective direct (experimental) prediction of the fourier transform (FT) of the corresponding Kiessig fringes profile (KFP) (per figure 5.2). *The sole center-plane film; this film, being bi-layer (BL), is listed along with the other BL (front-plane) films. Given the sub-nanometer resolution of x-ray reflectometry (XRR) (refer section 4.3.B), the results here are presented to the first place of decimal only. Here, coded unit (CU), not applicable (NA), thickness (as applicable) of film or of film layer (d), density (as applicable) of film or of film layer (D), roughness (as applicable) of film or of film layer (r).

to F31, at fixed p = + and O = +. This is consistent with the increase in P_{RF} from P_{RF} = - to P_{RF} = +. The aforementioned reason applies here as well. However, in this case, in light of figure 5.7, we hypothesize that O^{2-} bombardment of the growing film is enhanced, owing to an enhancement of DC target-potential ($\Phi_{DC,\,t}$) in the sputtering chamber.

A particular outcome of such a state of affairs would be the depression of film thickness accumulated per unit time duration, that is, of TFL deposition-rate (ν_{TFL}). For fixed sputtering time duration, this would result in decrease in the final d_{TFL}. This is indeed observed from F19 to F31.

The observed increase in TFL roughness (r_{TFL}) from F19 to F31 is a further signature of this effect.

5.5.C The bi-layer films

5.5.C.1 Introduction

These are the five films at the center-plane (one film), and at the front-plane (four films), of the experiment design per figure 3.3 and table 3.4.

Proceeding forth the discussion of section 5.5.B re the back-plane films (wherein p = +) we see that d_{TFL} decreases from F19 to F31, while it increases from F35 to F15. However, on the front-plane (wherein p = -) d_{TFL} increases, from F3 to F23, as well as from F27 to F11. The aforementioned foretell an antagonistic three-way interaction term p:(O:P_{RF}), that is, O:p:P_{RF} (refer term 3.1d per equation 3.1). This observation is corroborated by the sign (negative) of this interaction term, as determined via the RSA results presented in figure 6.20(a).

Consideration of the O:p:P_{RF} interaction term assumes significance — for instance, if one considers the oxygen content dependence of electronic state of amorphous TMO (ISZO) films (refer figures 6.12 and 6.9) — given the

commercial imperative towards higher ν_{TFL} and / or, towards higher D_{TFL}. Next, we consider the TFL and the SPL in turn.

5.5.C.2 The thin-film layer

The discussions re d_{TFL} as presented in section 5.5.B for the SL films, apply to the TFL of the BL films. The implications of the change in value of p, between the back-plane (p = +) and front-plane (p = -), are nonetheless significant.

The increase in d_{TFL} from F27 to F11 (at fixed p = - and O = -), as also from F3 to F23 (at fixed p = - and O = +), may be understood along the lines of the discussion re d_{TFL} as presented in section 5.5.B.

However, contrary to the state of affairs on the back-plane, the aforementioned increases in d_{TFL} is concomitant with decreases (pair-wise respectively) in D_{TFL}. This is likely due to a depression of film (TFL) densification with increasing ν_{TFL}. Thus, one expects (predicts) differences in the amorphous morphology between the opposite numbers in the aforementioned film pairs. The d_{TFL} and D_{TFL} values of the sole center-plane film F7 are consistent with the preceding discussion.

The trends noted above indicate an interaction between P_{RF} and p (refer terms 3.1c per equation 3.1). This observation is corroborated by the presence of significant p:P_{RF} interaction term in the RSA results presented in figures 6.20(a) and 6.20(b). The change in sign of the aforementioned interaction term — viz., p:P_{RF} — between the two (exemplary) properties of interest — viz., ν_{TFL} and D_{TFL} — is a case in point re the complexities attending the (simultaneous) optimization of multiple properties of sputtered multifunctional films (G. E. P. Box and K. B. Wilson, 1951; Derringer and Suich, 1980; Khuri and Cornell, 1987).

5.5.C.3 The sub-plantation layer

The emergence of the SPL is observed as one proceeds from the back-plane (p = +) to the front-plane (p = -) of the experiment design per figure 3.3. With reference to table 3.4, the p range of the experiment design spanned approximately an order of magnitude. The lower limit of the range is determined by the lowest p necessary to maintain conditions (within the sputtering chamber) conducive to the striking and sustenance of a process plasma. The upper limit of the range is determined by the p necessary to ensure arrival, at substrate, of material flux in meaningful* quantity.

The direction of change in SPL thickness (d_{SPL}) and D_{SPL} from F27 to F11, and from F3 to F23, are opposite each other. With reference to figure 5.7, the increase in P_{RF}, in both of the aforementioned cases, leads to enhancement of energy of sputtered material flux impinging, and sourcing film growth, on the substrate. This would result in a depression of SPL densification concomitant with an increase in its growth-rate, as observed.

5.6 Film opto-electronic properties I

5.6.A Introduction

With the ISZO film layer structures having been quantified (per table 5.1), we proceed interrogation of the film electronic state. The characterization techniques for opto-electronic investigations had been introduced briefly in table 4.1. Here, we address inter-relationships among them.

Thereby, we present the information-flow among characterization techniques employed in this study (refer section 5.6.B). We then compare the experimentally measured and the calculated energy (E) dependences of Tr (refer

*Sufficient to obtain a sufficient ν_{TFL}, so that a measurable d_{TFL} is accumulated within the deposition time duration (refer section 4.2.C).

section 5.6.C).

5.6.B Information flow among characterization techniques

Figure 5.5 previews a portion of the ready-reckoner per figure 7.1. It highlights the inter-relationships, and the information-flow, among the characterization techniques employed in this study.

5.6.C Experimentally measured and modeled transmission fraction

The ISZO film layer structures determined via XRR (refer table 5.1) were used to model the experimentally obtained SE spectra via Kramers Kronig (KK) consistent and physically meaningful oscillator models per table 5.2.

In particular, the modeling permitted calculation of the E dependence of Tr of the film-substrate-combine. Accordingly, the experimentally measured and modeled room-temperature Tr(E) for the BL films F7, F11, and F23, are compared in figure 5.6.

The modeling additionally furnished estimations of opto-electronic properties of interest; further discussions of the same are presented in table 6.2. The discussions and comparison as aforementioned furnish independent corroboration of the film layer structures per table 5.1.

5.7 Sub-plantation during film deposition

5.7.A Introduction

We are now in a position to address considerations attending our assertion of sub-plantation (section 5.7.C). This will be followed by consideration of the pressure distance product (ϕ) dependence of sub-plantation (section 5.7.B).

Film /	Oscillator Model	
Sample	Film	Substrate
F7	B-Spline	G+TL
F11	TL+D	
F23		

Table 5.2: With reference to experiment design per figure 5.6, the oscillator models for Si doped $In_2O_3{-}(ZnO)_3$ (ISZO) films on Corning Eagle XG Glass (CEXG) substrates. The oscillator models were used to compute (Ψ(E), Δ(E)) given the film layer structure per figure 5.3(d), with d_{SPL} and / or d_{TFL} per table 5.1, and $d_s = 700\,\mu m$. The thus obtained 'optical' (modeled) estimates of (n, μ) are compared with the 'electrical' (direct) estimates in table 6.2. The general agreement between the two (electrical and optical) estimations is noted. The low thickness of film F7 disallowed use of the Tauc-Lorentz plus Drude (TL+D) oscillator model (J. A. Woollam Co., 2017). Further details re the Tauc-Lorentz (TL) and Drude (D), and re the Gaussian (G) oscillator models are presented in sections 4.4.D and A.3.B respectively. Here, Tauc-Lorentz plus Drude (TL+D),Gaussian plus Tauc-Lorentz (G+TL), spectroscopic ellipsometry (SE), SPL thickness (d_{SPL}), TFL thickness (d_{TFL}), substrate thickness (d_s), conduction electron concentration (n), conduction electron mobility (μ), SE Ψ-parameter (Ψ), SE Δ-parameter (Δ), energy (E).

5.7.B The pressure distance product dependence of sub-plantation

For discussions in sections 5.7.C, 5.8 and 5.9, it is expedient to introduce the process factor ϕ:

$$\phi = p l_t \tag{5.1a}$$

whereby,

$$\phi_{t-s} \equiv \phi(l_t = l_{t-s}) = p l_{t-s} \tag{5.1b}$$

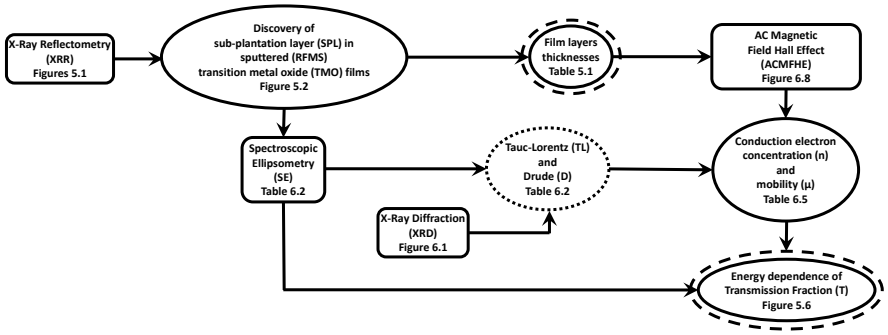

Figure 5.5: With reference to table 4.1, portion (expanded) of the ready-reckoner presented in figure 7.1. We show the information-flow between the various independent characterizations and the estimations (physical or electronic property) that they enable. Starting at the top-left, x-ray reflectometry (XRR) yielded the detailed film layer structure for each film. This permitted quantification of Hall Effect (HE) measurements, yielding 'electrical' estimates of conduction electron concentration ($\mathbf{n}$) and conduction electron mobility (μ) for each film. Knowledge of the detailed layer structure, and of room-temperature ($\mathbf{n}$, μ) permitted modeling (for films F11 and F23) of experimentally recorded (via SE) room-temperature (Ψ(E), Δ(E)) in terms of a Tauc-Lorentz plus Drude (TL+D) oscillator model. The aforementioned oscillator model is apposite in light of the amorphous microstructure (determined via x-ray diffraction (XRD)) of the Si doped In_2O_3−$(ZnO)_3$ (ISZO) films. The modeling yielded 'optical' estimates of room-temperature ($\mathbf{n}$, μ), and the same are in general agreement with the aforementioned electrical 'direct' estimates. Computed $\mathbf{Tr}$(E), of film-substrate-combines further to said modeling are in general agreement with respective experimentally measured counterparts, depicted at the bottom-right. Rectangular boxes house characterization modalities, while results are housed in elliptical boxes. Dotted lines indicate theoretical determination, while dashed lines indicate determination via data refinement or modeling. Here, SE Ψ-parameter (Ψ), SE Δ-parameter (Δ), energy (E).

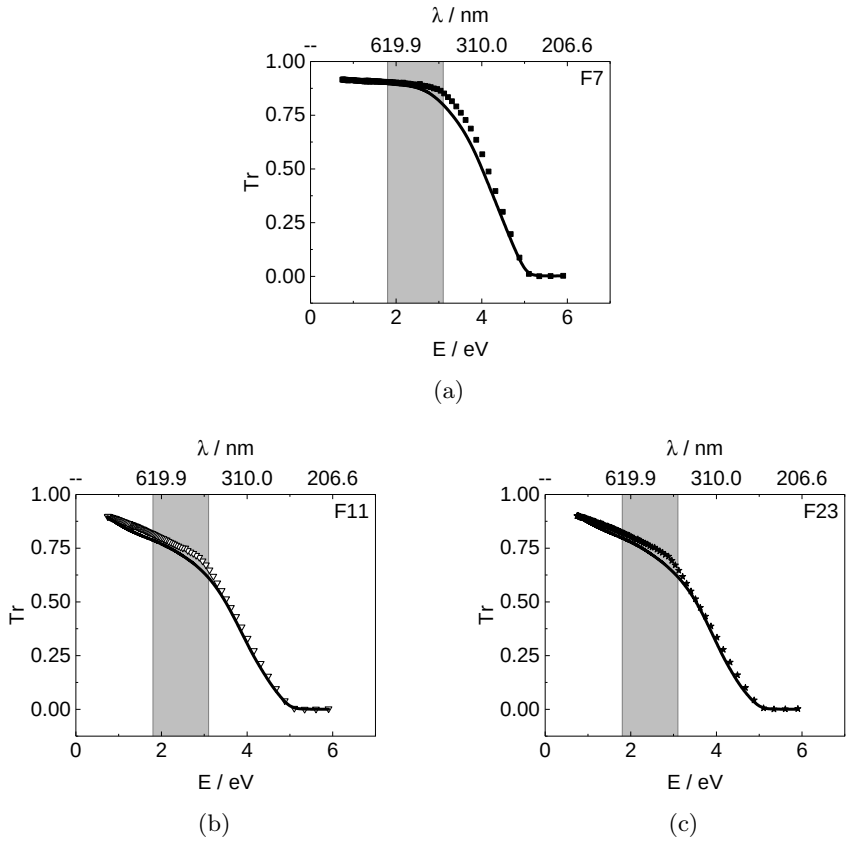

Figure 5.6: With reference to figure 3.3, experimentally measured (symbols) and thence modeled (solid curve) energy (E) or wavelength of light (λ) dependence of transmission fraction (Tr) of selected individual members of the particular Si doped In_2O_3−$(ZnO)_3$ (ISZO) films-set per figure 5.1. The general agreement between the experimentally measured and modeled dependences affirms the bi-layer (BL) layer structure per figure 5.3(d). The dependences were modeled based upon Kramers Kronig (KK) consistent oscillator models per table 5.2. The shaded E-range demarcates the visible electromagnetic spectrum. (a) center-point / Center-Plane film F7, (b) front-plane film F11, and (c) front-plane film F23.

where, pressure distance product (ϕ), process gas pressure (p), perpendicular distance from target surface ($\mathrm{l_t}$), given pressure distance product ($\phi_{\mathrm{t-s}}$), target-substrate distance ($\mathrm{l_{t-s}}$).

As noted in section 3.4.D, process plasma temperatures during RFMS are in the range room-temperature to a few hundred K, $\simeq$25 meV to 50 meV. On the other hand, for sub-plantation into a substrate, the energy at substrate of incident material flux should (typically) be $\gtrsim$1 eV (Lifshitz, Kasi, Rabalais, and Eckstein, 1990).

The energy of sputtered material flux at substrate ($\mathrm{E_{smf,\,s}}$) decreases with increasing $\phi_{\mathrm{t-s}}$. We estimate, on basis of published results (Somekh, 1984), and on basis of experimental observation of $\Phi_{\mathrm{DC,\,t}}$, the (kinetic) energy at substrate of material flux particles, for comparison with the process plasma energy-scale as aforementioned.

Table 5.3 presents conservative estimates of the kinetic energy per particle (on average) of sputtered material flux at substrate, for the back-plane, center-plane, and front-plane of our experiment design (per figure 3.3). The estimates are based upon published results (Somekh, 1984) for the (target) metal atoms at issue, viz., indium (In), zinc (Zn), and silicon (Si). Evidently, $\mathrm{E_{smf,\,s}}(\phi_{\mathrm{t-s}})$ is sufficient for sub-plantation during depositions of the front-plane and center-plane films; while that is not the case during depositions of the back-plane films.

Furthermore, figure 5.7 presents the $\Phi_{\mathrm{DC,\,t}}$ as develops at each individual process factors set (read alongside figure 3.3). Since a significant fraction of kinetic energy of the bombarding argon ion (Ar^+) ions is transferred to the target (Winters et al., 1990), the material flux particles emitted from the target are expected to possess energies of up to tens of eV. In light of the estimates of mean free length of process gas (l) presented in table 5.3, the

Experiment	p		l	l_{t-s}	ϕ_{t-s}		$E_{smf,\,s}$	
design	(CU)	/ mTorr	/ mm	/ mm	/ mTorrmm	/ Pa mm	/ K	/ eV
Back-Plane	+	10	8		900	123	2×10^4	< 2
Center-Plane	0	6	14	90	540	74	5×10^4	$\lesssim 4$
Front-Plane	–	2	41		180	25	1.3×10^5	> 11

Table 5.3: With reference to experiment design per figure 3.3 and table 3.4, and following Somekh, 1984, we present conservative estimates of given pressure distance product (ϕ_{t-s}) dependent energy of sputtered material flux at substrate ($E_{smf,\,s}$) for a material flux comprised predominantly (as is the case in this study) of indium (In) and zinc (Zn). For reference and further to equation 3.2, process gas pressure (p) dependent mean free length of process gas (l) in the process gas (plasma) is listed. For reference we also list the target-substrate distance (l_{t-s}) for the radio frequency magnetron sputtering (RFMS) equipment used in the present study.

material flux is expected to retain a substantial fraction of this energy at substrate during deposition of front-plane and center-plane films.

5.7.C Assertion

We now address our use of the descriptive term "sub-plantation layer (SPL)" for the film layer that lies mediate (sandwiched between) the TFL and substrate, viz., "film layer 1" (refer experimental results per figures 5.2(b) and 5.2(c), and the film layer structure model per 5.3(b)). The assertion that the sandwiched layer manifests due sub-plantation of material flux is in light of the following observations:

- First, with reference to table 5.1, for each of the five BL films, $D_{CEXG} < D_{SPL} < D_{ISZO}$. This is consistent with expectation consequent the "phase formation" and "internal subsurface growth", as occurs during sub-plantation per Lifshitz, Kasi, Rabalais, and Eckstein, 1990.

- Second, and further to section 4.2, each of the (nine) substrates were prepared identically prior to sputter deposition of films upon them.

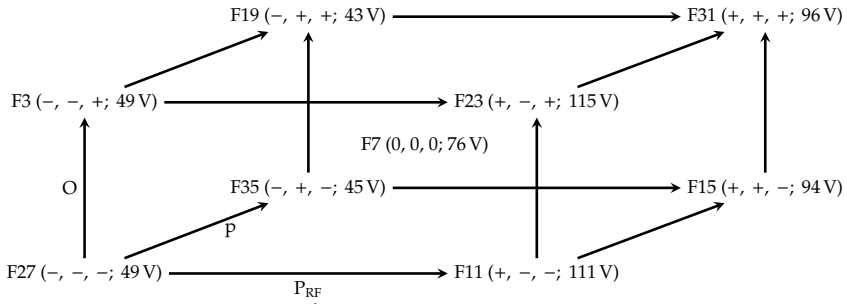

Figure 5.7: The DC target-potential ($\Phi_{DC,\,t}$) as developed during the nine individual radio frequency magnetron sputtering (RFMS) film depositions, according the experiment design per figure 3.3 and table 3.4. The data is presented in the format "Film (P_{RF}, p, O; $\Phi_{DC,\,t}$)". The $\Phi_{DC,\,t}$ was stable to within a few percent, and its stability improved with increase in its magnitude. Here, RF power (P_{RF}), process gas pressure (p), oxygen percent (O).

With further reference to figure 3.3, film layer 1 manifests in each of the four front-plane films, but not at the respective opposite number film on the back-plane.

The process factors sets of each opposite number pair differ but in the value of p, or since l_{t-s} is constant, of ϕ_{t-s}. That is, the value of the process factor ϕ_{t-s} is decisive for the presence (at the front-plane), or the absence (at the back-plane), of sub-plantation.

Recall from section 5.7.B that ϕ_{t-s} is a principal determinant of the final energy (thermalization state) at substrate of the sputtered material flux (refer table 5.3), whereas the final energy so decreases with increasing ϕ_{t-s}.

That is, the ϕ_{t-s} of transit from target to substrate determines the capacity of sputtered material flux to cause (be) subplantation (subplanted) into substrate, whereas the capacity so decreases with increasing ϕ_{t-s}.

We have observed an additional nanoscale layer situated mediate, and having a density intermediate that of, the substrate and overlying film (TFL) proper, in each of the four front-plane films and not in the respective opposite number film at the back-plane. This observation is well explained by the expected presence and absence respectively, of sub-plantation, at the front-plane and back-plane (given the ϕ_{t-s} values at said planes).

A related inference flows from the first observation above: since SPL growth — provisioned by hyperthermal material flux — entails "an outward expansion of the substrate layer" (Lifshitz, Kasi, Rabalais, and Eckstein, 1990), one observes that d_{SPL} may not be straightforwardly identified as (is greater than) the depth to which sputtered material flux is implanted into substrate.

5.8 Film growth from collimated sputtered material flux

5.8.A Introduction

We consider film growth from collimated sputtered material flux. On basis of comparison with published results (Fortunato et al., 2006) on kindred films grown from uncollimated sputtered material flux, we quantify the effect of deployment of our sputter flux collimator (SFC) (per section 3.4.D) on film deposition-rate. Thereby, we demonstrate the capacity of the SFC to modulate the ϕ_{t-s} dependence of film deposition-rate. With this background, we present a reasoned conjecture re the role of the SFC in the manifestation of a set of SPLs with physical properties relatable to the deposition process conditions.

Accordingly, we consider the angular distributions of sputtered material flux

at substrate (section 5.8.B). This will be followed by a semi-quantitative analysis of the effect of deployment of our SFC, on film deposition-rate (section 5.8.C). Finally, we present a conjecture re the role of the SFC in manifestation of a bonafide set of SPLs, and present a phase-diagram for SPL formation (section 5.8.D).

5.8.B Angular distribution of sputtered material flux

The material flux as emerges from target during sputtering is hyperthermal (refer section 5.7.B; Ohring, 2002; D. M. Mattox, 1965), and furthermore its angular distribution is cosine (refer section 3.4.B). The cosine angular distribution relaxes as a function of increasing ϕ, towards a uniform angular distribution (Kurt J. Lesker Company, 2010; Ohring, 2002). The relaxation occurs concomitant with thermalization of the material flux via scattering as it transits through the process plasma.

Accordingly, two extremal cases may be considered, based on the thermalization state of material flux provisioning film growth per our protocol, whereby a SFC is present mediate the target and substrate (per figure 3.6(a)) (Cook, 1999):

1. The material flux provisioning film growth (on substrate) is substantially hyperthermal. Whereby, the material flux received at substrate is traveling substantially perpendicular to plane of the substrate.

   With reference to figure 3.3 and table 5.3, this situation inheres during deposition of the experiment design front-plane and center-plane films; in particular, films F11, F23, and F7.

2. The material flux provisioning film growth on substrate is substantially thermalized. Whereby, the material flux received at substrate does not have a preferred travel direction.

With reference to figure 3.3 and table 5.3, this situation inheres during deposition of the experiment design back-plane films; in particular, films F15 and F31.

We interrogate the aforementioned cases quantitatively, via comparison of deposition-rate of films deposited from collimated (present study), and from uncollimated (Fortunato et al., 2006) sputtered material flux.

5.8.C Modulation of film deposition-rate via the sputter flux collimator

Let Ω be the solid angle from which sputtered material flux may be received at substrate (e.g. upon deployment of a SFC), and $\Omega_{\text{unconstrained}}$ be the maximum possible solid angle from which sputtered material flux may be received at substrate. One may define the following ratio:

$$\begin{aligned} f &= \frac{\Omega}{\Omega_{\text{unconstrained}}} \\ &= \frac{\Omega}{2\pi} \end{aligned} \tag{5.2a}$$

whereas, the solid angle subtended on the substrate center by the aperture of our SFC (per figure 3.6(a)) is:

$$\begin{aligned} \Omega &= \Omega_{\text{SFC}} \\ &\simeq \frac{\pi}{4.3}\text{sr} \end{aligned} \tag{5.2b}$$

Thus, for material flux having uniform angular distribution — corresponding to it being fully thermalized — deployment of our SFC may be expected[†] to depress (compared to the unconstrained situation) deposition-rate by a factor:

$$f_{\text{SFC, thermalized}} \equiv f(\Omega = \Omega_{\text{SFC}}) \sim 0.1 \tag{5.2c}$$

Relation 5.2c furnishes us with a first quantitative estimate of effect — on film deposition-rate — of deployment of our SFC.

In light of table 5.3 and equations 3.3, the front-plane films were deposited from collimated sputtered material flux. In order to interrogate the prediction per relation 5.2c, one requires the film deposition-rate as obtains in a commensurable deposition from uncollimated sputtered material flux.

A "commensurable" deposition would be one in which the material system (viz., In−Zn−O), the film deposition technique (viz., RFMS), the substrate temperature during deposition (viz., nominally room-temperature), and film morphology (viz., amorphous) are comparable.

Nonetheless, differences in deposition process factors that have the most bearing on film deposition-rate, viz., P_{RF}, and p (refer figure 6.20(a)), and l_{t-s} (refer Kurt J. Lesker Company, 2010), must be accounted for prior to comparison.

Accordingly, table 5.4 presents data that permits quantitative comparison of deposition-rates from uncollimated (Fortunato et al., 2006), and from collimated (present study), sputtered material flux. The films in question are

[†]For a situation where substrate and target have a common perpendicular. This was taken in to account in the design of the substrate holder cum sputter flux collimator array (SHCSFCA) / SFC (refer discussion of 3.5).

commensurable according to the criteria mentioned. The following observations are forthcoming re the deposition-rate …

- … of films F11 and F23:

  The observed deposition-rate is about 2 times slower than that observed by Fortunato et al., 2006, and with reference to equation 5.2c, about 5 times faster than expectation for fully thermalized material flux. As such, observations per item number 1 in section 5.8.B apply.

- … of film F7:

  The observed deposition-rate is about 5 times slower that that observed by Fortunato et al., 2006, and with reference to equation 5.2c, about 2 times faster than expectation for fully thermalized material flux. As such, observations per item number 1 in section 5.8.B apply.

  Validity of the preceding conclusion is underscored by the fact that it is reached given that the process factor p for film F7 is 5x the value of the same factor in the study of Fortunato et al., 2006[‡].

- … of films F15 and F31:

  The observed deposition-rate is at least 10 times lower than that observed by Fortunato et al., 2006. Thus, the material flux is fully thermalized. As such, observations per item number 2 of section 5.8.B apply.

  At the lower end of the deposition-rate range presented by these two films, the deposition-rate is about 30 % of the value expected per equation 5.2c. This further depression by a factor of 3x or so is attributed to the process factor p being over 8x that in the study of Fortunato et al., 2006[‡].

[‡]Film deposition-rate depends inversely on p (Kurt J. Lesker Company, 2010).

Study	Film	p		d_t	P_{RF}			l_{t-s}	ν		$f_{SFC,\ observed}$	Sputtered Material Flux
							Density		Actual	Scaled		at substrate directed
		(CU)	/ mTorr	/ cm	(CU)	/ W	/ W/cm^2	/ cm	/ nm/min			into substrate?
Fortunato et al., 2006	Refer caption	NA	1.2	5	NA	175	8.9	10	23	23 (Self)	1 (Self)	NA
	F11, F23	–	2		+	150	3.3		3.2–3.4	10.7–11.3	$\simeq 0.5$	✓✓✓
Present	F7	0	6	7.62	0	87.5	1.9	9	0.8	4.6	$\simeq 0.2$	✓
	F15, F31	+	10		+	150	3.3		0.2–0.5	0.7–1.8	$\lesssim 0.1$	✗

Table 5.4: Experimentally observed film deposition-rate (ν) of commensurable films per Fortunato et al., 2006, and per the present study (refer figure 3.3 and table 3.4). Further to figure 6.20(a), the process factors that have the most bearing on film film deposition-rate (ν) — viz., RF power (P_{RF}), process gas pressure (p) (refer figure 6.20(a), and target-substrate distance (l_{t-s}) (refer Kurt J. Lesker Company, 2010) — are listed. The scaled values as listed (present study) were obtained from the respective experimentally observed values according to established principles (Kurt J. Lesker Company, 2010). Such scaled values account for the differences, in the values of the aforementioned process factors, between the present study and that of Fortunato et al., 2006. Thus, the listed scaled values as listed for ν observed per Fortunato et al., 2006, and per the present study, are comparable. The quantity $f_{SFC,\ observed}$ estimates the quantity f (equation 5.2a). Comparison thence of $f_{SFC,\ observed}$ to $f_{SFC,\ thermalized}$ per relation 5.2c furnishes information re the angular distribution (refer figure 3.4) — alternatively, re the thermalization state — of the sputtered material flux that sourced the deposition of our films.
[This caption continues on next page.]

Table 5.4: [This caption continues from previous page.]
Given the listed values of mean free length of process gas (l) per table 5.3, in light of equations 3.3, the sputtered material flux that sourced growth of our front-plane films (F11 and F23) was collimated. On the other hand, the film of Fortunato et al., 2006 was deposited from uncollimated sputtered material flux. For our films F11 and F23 (front-plane), and F7 (center-plane) $f_{SFC,\ observed} > f_{SFC,\ thermalized}$, that is, the film ν is faster than expected for deposition from thermalized sputtered material flux in presence of our sputter flux collimator (SFC). Given fixed $\Omega = \Omega_{SFC}$, the aforementioned result implies that the in-plane (of substrate) momentum component distribution of sputtered material flux incident upon the substrate (that is, upon the growing film) is skewed to lower values. We believe this to be a contributory factor for manifestation of a bonafide set of sub-plantation layers (SPLs) in our front-plane and center-plane films-set (refer section 5.8.D). For our films F15 and F31 (back-plane), $f_{SFC,\ observed} < f_{SFC,\ thermalized}$, that is, the ν is as expected for deposition from thermalized sputtered material flux in presence of our SFC. One notes the consistency of the aforementioned analysis with that presented — and arrived upon independently — in table 5.3. Here, coded unit (CU), experimentally observed factor by which is depressed, with respect to uncollimated (unconstrained) situation, film deposition-rate due sputtered material flux having a uniform angular distribution (which corresponds to fully thermalized sputtered material flux), due deployment of an SFC ($f_{SFC,\ observed}$), ratio between two solid angles, expected (theoretical) factor by which is depressed, with respect to uncollimated (unconstrained) situation, film deposition-rate due sputtered material flux having a uniform angular distribution (which corresponds to fully thermalized sputtered material flux), due deployment of an SFC ($f_{SFC,\ thermalized}$), solid angle (Ω), solid angle subtended at substrate center by SFC aperture (Ω_{SFC}), target diameter (d_t).

5.8.D Epilogue

In light of the preceding discussions, we conjecture that the selective depletion of the adatom (material flux) momentum in-plane of the substrate, as occurred due deployment of the SFC, promoted the conservation (from nascency) of the developing sub-planted layer, in face of continual degradation or disadvantage (sputtering away) due bombardment by sputtered material flux from target. This helped manifest a bonafide set of SPLs.

We clarify our use of the qualifier "bonafide". It conveys that the (physical) property of the object to which the qualifier applies are in lawful[§] correlation with the process factors set under which the object manifests.

Two results underpin the bonafide nature of the SPLs observed in our films-set. They are, in sequence: the ab initio prediction, and the experimentally driven determination, of the process factors dependence of SPL physical properties. We consider these results next (refer also, section 3.4.C).

(I) The ab initio (theoretical) determination of possible laws relating SPL physical properties (such as d_{SPL}, r_{SPL}, D_{SPL}) to the process factors sets under which the properties emerge:

This determination is based on DA (Sonin, 2001) of the physical properties, in light of the specific film deposition technique at issue. viz., RFMS (Depla, Mahieu, and J. Greene, 2010). The results of the DA are presented in table 5.5.

Given the form of the dimensionless group P_{RF}^{*}, and for our particular experimental arrangement whereby D_s and l_{t-s} are held constant[¶] (see section 4.2), the process factors p and P_{RF} are predicted to determine the aforementioned physical properties.

[§]Equivalently: 'lawfully expected'.

[¶]$D_s = D_{CEXG} = 2.38\,g/cm^3$, and $l_{t-s} \simeq 90\,mm$.

(II) The quantitative (experimental) determination that the process factors p and P_{RF} are the principal determinants of SPL physical properties such as d_{SPL}, D_{SPL}, r_{SPL}:

This determination is based on RSA (G. E. P. Box and Draper, 1987; Dunn, 2016) of the (respective) experimentally determined physical properties. The results of the RSA are summarized in figure 5.10.

One observes that the two process factors determined to be of consequence according to the experimental RSA (per result II), are the two predicted to be of consequence according to the ab initio DA (per result I).
Our assertion re the bonafides of the observed SPLs is in light of the above discussions, whereby: their experimentally manifested physical properties, depend on the process factors set under which they emerged, in the (precise) manner predicted by ab initio analysis.

5.8.D.1 The phase-diagram for sub-plantation layer formation

We consider the role of the SFC (refer figure 3.6) as deployed by us (refer figures 3.5 and 3.11), for manifestation of a bonafide SPL. The discussions will position us to propose a phase-diagram for SPL formation.
Via figure 5.8, we consider three successive experimental scenarios. Recall (refer figure 3.4) that the angular distribution of sputtered material flux, as emerges from points on the target, is cosine. The material flux undergoes scattering as it transits the process plasma.
The calculation of angular distribution of material flux as a function of perpendicular distance from target surface (l_t) will be an (involved) undertaking specific to the given sputtering chamber arrangement. It will have to account for, among other factors, the specific geometry of the sputtering chamber including placement of the target and process gas inlets inside of

it, the p, the process plasma composition, the ion employed for sputtering, the target composition, and the P_{RF}.

Nonetheless, the following inferences re the l_t dependence of said angular distribution are plausible in general (with reference to figure 3.4):

- For $l_t = 0$:

  This is the plane in the sputtering chamber that is flush with the target surface. No scattering events could have occurred, and therefore the angular distribution of material flux at all points on this plane is cosine.

  This situation corresponds to (one of the three possible situations under) experimental scenario (a) discussed later.

- For $l_t > 0$:

  This is a plane in the sputtering chamber which is at a (given) distance from the target surface. Scattering (thermalizing events) have occurred (owing to transit through the process plasma), and the angular distribution of material flux at all points on such given plane has relaxed, and is closer to uniform.

  Uniformization of the angular distribution of material flux occurs concurrently with its thermalization. We refer to the aforementioned concurrent occurrences as 'de-cosining' of the sputtered material flux.

  It is convenient to quantify the de-cosining strength of a given process plasma via the ϕ_{t-s} at issue. In particular, and with reference to the figure 3.6(a), given:

$$p_{y,\,s} \equiv p_y(l_t = l_{t-s}) \tag{5.3a}$$

$$p_{x,\,s} \equiv p_x(l_t = l_{t-s}) \tag{5.3b}$$

the following condition is plausible[‖]:

$$\frac{p_{y,\,s}}{p_{x,\,s}}(\text{SFC deployed: yes}) > \frac{p_{y,\,s}}{p_{x,\,s}}(\text{SFC deployed: no}) \tag{5.3c}$$

where, x-component of angular momentum (averaged) of sputtered material flux, at substrate ($p_{x,\,s}$), x-component of angular momentum (averaged) of sputtered material flux (p_x), perpendicular distance from target surface (l_t), target-substrate distance (l_{t-s}), y-component of angular momentum (averaged) of sputtered material flux, at substrate ($p_{y,\,s}$), y-component of angular momentum (averaged) of sputtered material flux (p_y).

As has been discussed with aid of table 5.3, the ϕ_{t-s} values corresponding to the front-plane and center-plane of the experiment design did not preclude sub-plantation. Additionally, we believe that condition 5.3c underpinned the "conservation" referred to earlier in this section, and the manifestation thereby of a bonafide set of SPLs.

Accordingly, we refer to a substrate-film interface created due sub-plantation, but absent deployment of an SFC, as 'dirty' (further discussion is presented in context of experimental scenarios (b) and (c), and corresponding figures 5.8(b) and 5.8(c) respectively).

Also, since the effect of deployment of the SFC is to mitigate the de-cosining as aforementioned, we refer to it (said effect) as 'de-de-cosining'. It is convenient to quantify the de-de-cosining strength of a given SFC via its SFC aspect ratio (r_a) (per definition 3.5a).

The ideas introduced above permit us to develop a phase-diagram for SPL

[‖]One realizes that the l_{t-s} is not a straightforward distance when a SFC is deployed mediate the target and substrate. Nonetheless, equation 5.1b should remain valid for film depositions performed with an SFC deployed, so long as $h \ll l_{t-s}$. For the present film depositions, the $h/l_{t-s} = 1\,\text{cm}/9\,\text{cm} \ll 1$.

formation, in the (ϕ_{t-s}, r_a) plane. Thereby, we propose control of sub-plantation of sputtered material flux — equivalently, of development of the substrate-film interface — via interplay of the opposing tendencies towards de-cosining (due ϕ_{t-s}; inherent during sputtering), and de-de-cosining (due r_a; as can be imposed during sputtering via deployment of a collimator)**. We arrive upon the aforementioned phase-diagram, via consideration of three successive experimental scenarios in figure 5.8, as follows:

(a) Experimental scenario with $\phi_{t-s} = 0$, refer figure 5.8(a):

Films may not be deposited according this scenario. This is since each of the (three) ways in which this scenario may be achieved correspond to experimental configurations that make sputtering untenable. Recalling equation 5.1b, the aforementioned value for ϕ_{t-s} is obtained only if either or both of p and l_{t-s} equal 0.

In each case so, sputtering is not possible, as follows: sputtering is not possible for $p = 0$, since no material is available for the process plasma to form. Sputtering is again not possible for $l_{t-s} = 0$, since no volume is available for the process plasma to form.

We next consider the two experimental scenarios at non-zero values of ϕ_{t-s}.

(b) Experimental scenario with $\phi_{t-s} > 0$, and absent deployment of a SFC, refer figure 5.8(b):

In this scenario the angular distribution of sputtered material flux relaxes towards a uniform distribution — that is, it undergoes de-cosining — as it transits the process plasma (for instance, from target

**The potential commercial significance of this proposal, for instance, for controlling substrate-film adhesion in service of flexible electronics applications, is noteworthy.

towards substrate).

Up to a certain value of ϕ_{t-s} the material flux sourcing film deposition is sufficiently energetic to cause sub-plantation. However, a substantial in-plane-of-substrate component of (total) adatom momentum too is present.

We suggest that this would result in a dirty substrate-film interface. By a 'dirty' substrate-film interface is meant one whose properties are not in lawful correlation (for instance, per laws presented in table 5.5) to the process conditions under which it (the substrate-filminterface) manifests.

This would imply also that, trends within and among properties of individual members of a set of interfaces obtained under different process conditions so (that is, absent de-de-cosining via a collimator), do not furnish information that is reliable for formulation, or for verification, of 'SPL formation theory'.

At still higher values of ϕ_{t-s}, the material flux sourcing film deposition does not possess energy sufficient to cause sub-plantation. The insufficiency referred to is on account of the material flux having been thermalized towards the plasma temperature (due scattering within the process plasma; refer section 3.4.D.2).

The 'boundary' (actually a range over ϕ_{t-s}) between the "Substrate-Film interface: Dirty" and "Sub-Plantation: Absent" regions is named as "Boundary-I".

Finally, one does not expect boundary-I to be sharp. This is given the statistical nature of the angular distribution of material flux sourcing film deposition via sputtering.

(c) Experimental scenario with $\phi_{t-s} > 0$, and with deployment of SFC, refer figure 5.8(c):

This experimental scenario is the subject of this thesis. As at experimental scenario (b), here too the angular distribution of sputtered material flux relaxes towards a uniform distribution — that is, it undergoes de-cosining — as it transits the process plasma. However, unlike as at experimental scenario (b), the deployment of a SFC (per figure 3.6(a)), results in de-de-cosining of the material flux (just) before it sources film growth.

Physically, de-de-cosining refers to the selective subtraction (removal) of in-plane-of-substrate momentum component of material flux (sourcing film growth). In practice, when the material flux sourcing film growth is not thermalized, then de-de-cosining of material flux may be effected via deployment of a SFC mediate target and substrate (for instance, per figure 3.6(a)).

As noted earlier, the manifestation of a bonafide SPL is considered as an outcome of interplay between two opposing phenomena (where each phenomena affects the angular distribution of material flux) as follows: the phenomena of de-cosining of material flux due scattering in the process plasma (quantifiable via the given ϕ_{t-s}), and the phenomena of de-de-cosining of material flux due the SFC (quantifiable via the given $\mathrm{r_a}$).

In essence, the SFC (via its $\mathrm{r_a}$) opens up opportunity for a bonafide SPL to manifest. That is, deployment of a SFC results in creation of a "SPL: Bonafide" region in the (ϕ_{t-s}, $\mathrm{r_a}$) plane. The boundary thereby created, between the "Substrate-Film interface: Dirty" and

"SPL: Bonafide", regions is named as "Boundary-II".

Furthermore, it is plausible that increasing $\mathsf{r_a}$ will cause increase in the $\phi_{\mathsf{t-s}}$ to which exists the "opportunity" as mentioned, as follows. Recall the large area nature of the target (section 3.4.C), and furthermore that the angular distribution of material flux as emerges from a(ny) point on the target is cosine (figure 3.4). Thence, increasing $\mathsf{r_a}$ should increase the proportion of unscattered, that is, unthermalized material flux, within the material flux sourcing film deposition. Thereby, we hypothesize that, with increasing $\phi_{\mathsf{t-s}}$, boundary-II will present a slope as shown.

Thus, increase in $\mathsf{r_a}$ should decrease the angular spread of material flux sourcing film deposition. Decreasing the angular spread of material flux sourcing film deposition will decrease the in-plane-of-substrate component of adatom momentum.

This will help "the conservation (from nascency) of the developing SPL layer" as suggested earlier (refer section 5.8.D).

Also, it follows that increasing $\mathsf{r_a}$ will decrease the area of the target from which is sourced the material flux sourcing film deposition.

Reasoning as preceding, we hypothesize that the boundary of the 'Substrate-Film: Dirty' region with the 'Sub-Plantation: Absent' region, viz., boundary-I, will present a slope as shown with increasing $\phi_{\mathsf{t-s}}$.

The preceding also implies that boundary-I and boundary-II will approach each other with increasing $\mathsf{r_a}$). This is physically plausible since a SFC with a very large $\mathsf{r_a}$ will permit passage (through itself) of material flux at (only) a sharply defined momentum with $\mathsf{p_x} \rightarrow 0$.

The aforementioned implies that increasing $\mathrm{r_a}$ will decrease the width of the 'Substrate-Film: Dirty' region.

Furthermore, one expects that ν will decrease with with increasing $\mathrm{r_a}$ (the discussion of table 5.4 is relevant).

In light of the preceding discussions, we situate, 'by hand', the nine films per this study (refer table 5.3, and value 3.5), and the various aforementioned regions, within figure 5.8(c). This helps bring a measure of quantification (in terms of $\phi_{\mathrm{t-s}}$ and $\mathrm{r_a}$ ranges spanned) to the regions and boundaries introduced in the preceding discussions.

The observed manifestation of a bonafide (understood per results (I) and (II)) set of 5 SPLs (refer figure 3.3 and table 5.1) — viz., in the 4 front-plane ($\phi_{\mathrm{t-s}} = 180\,\mathrm{mTorr\,mm}$) films F27, F11, F23, F3, and in the 1 center-plane ($\phi_{\mathrm{t-s}} = 540\,\mathrm{mTorr\,mm}$) film F7 — may now be rationalized in light of the preceding discussions, as follows: compared to experimental scenario (b), in experimental scenario (c) (this study), the deployment of a SFC with $\mathrm{r_a} = 0.91$ (refer relation 3.5b) effected a rightwards shift of boundary-II to beyond $(\phi_{\mathrm{t-s}}, \mathrm{r_a}) = (540\,\mathrm{mTorr\,mm}, 0.91)$.

5.9 Manifestation and observation of sub-plantation layer: role of experimentation choices

5.9.A Introduction

We have had occasion to consider the specific details of our film deposition protocol (per section 4.2.C), in relation to those of film deposition protocols practiced widely (Fortunato et al., 2006). Accordingly, and with benefit of

hindsight, we are in position to conjecture re those features of our experimentation (as regards film deposition, and as regards film characterization), that facilitated the creation, preservation, and observation of the SPL. We believe that a confluence of experimentation choices facilitated the successful manifestation and observation of the SPL.

Accordingly, we consider our choice of substrate (section 5.9.B). This is followed by consideration of the effect of deployment of a SFC (section 5.9.C).

5.9.B Substrate: Corning Eagle XG glass

The choice of a substrate, namely, CEXG with sub-nanometer scale surface roughness ($r_{s,\,CEXG} = 0.5\,nm$ to $1\,nm$) did not preclude the manifestation of a bonafide nm scale layer, namely, the SPL (refer table 5.1).

Relatedly, the same choice of substrate did not preclude successful observation of the SPL via the technique of XRR, given the constraints on in-situ interface(s) and / or surface roughness, as attach to the technique (refer section 4.3.B).

5.9.C Collimation: sputter flux collimator

As discussed in section 5.8.D.

5.10 Bonafides of the sub-plantation layer

5.10.A Introduction

We address the submission made in section 5.8.D, namely, that the observed set of SPLs (in the films that are at the center-plane and at the front-plane of the experiment design per figure 3.3) is bonafide. For this, we proceeded two independent analyses of SPL physical properties.

An ab initio DA of the process factors in play during RFMS (which is the technique used for depositing our films), furnishes predictions re the pro-

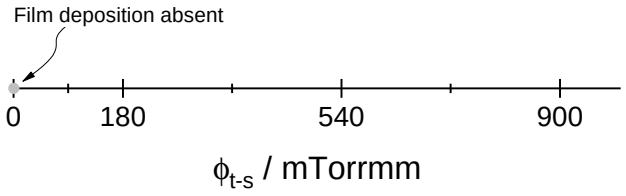

(a)

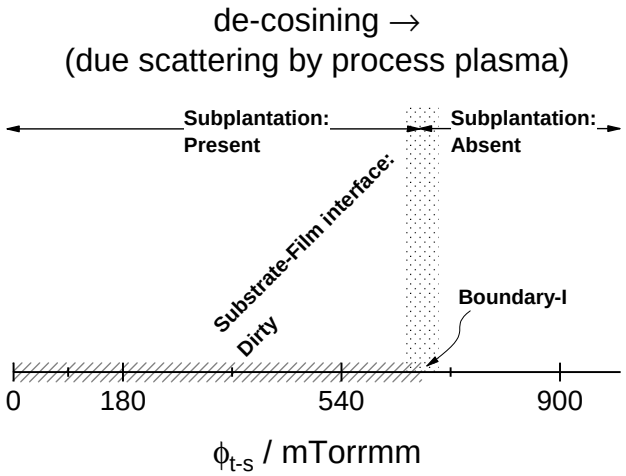

(b)

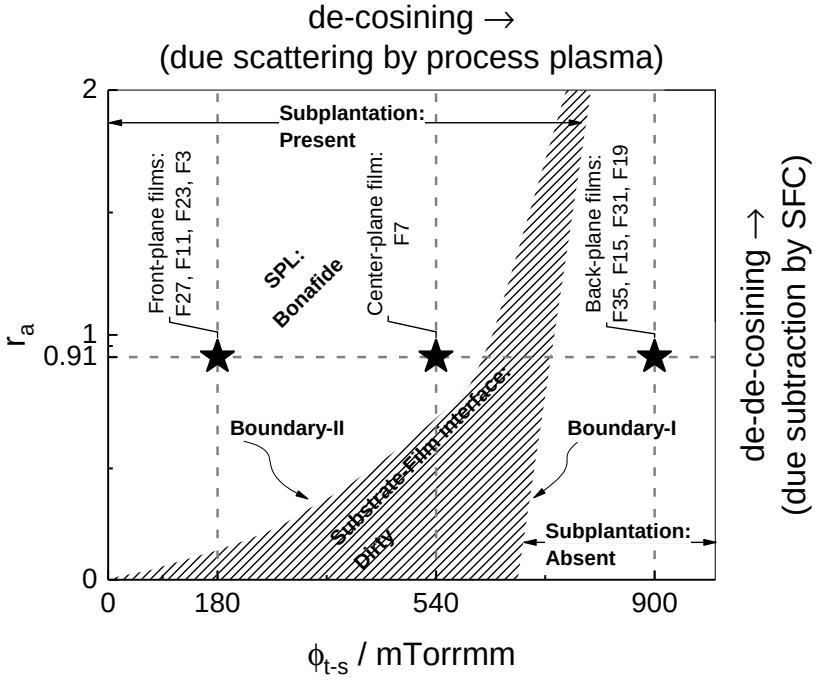

(c)

Figure 5.8: [Caption to this figure is presented on next page.]

Figure 5.8: [Figure corresponding to this caption is presented on the previous page.]
We suggest (at (c)) a 'phase-diagram for sub-plantation layer (SPL) formation' via consideration of three (successive) experimental scenarios. Detailed discussion of each scenario is presented in section 5.8.D.1. (a) Experimental scenario with $\phi_{t-s} = 0$. (b) Experimental scenario with $\phi_{t-s} > 0$, and absent deployment of a sputter flux collimator (SFC). Here, boundary-I separates the "Substrate-Film Interface: Dirty" and "Sub-Plantation: Absent" ϕ_{t-s} ranges. The dotted range (region) indicates that boundary-I is not expected to be sharp. (c) Experimental scenario with $\phi_{t-s} > 0$, and with deployment of SFC. Boundary-I separates the two regions as at (b). Boundary-II, on the other hand, separates the "Substrate-Film Interface: Dirty" and "SPL: Bonafide" ϕ_{t-s} regions. Neither boundary-I, nor boundary-II, is expected to be sharp, per refer aforementioned detailed discussions. Here, given pressure distance product (ϕ_{t-s}), SFC aspect ratio (r_a); refer the aforementioned detailed discussions for definition of the terms "de-cosining" and "de-de-cosining".

cess factors that are significant in determination of SPL physical properties (Sonin, 2001; Gorse, Johnston, and Pritchard, 2020; V. Simon, Weigand, and Gomaa, 2017).

An independent RSA of the manifest (experimentally determined) values of SPL physical properties (per table 5.1) revealed precisely the same process factor (as were revealed by the DA) to be significant.

Accordingly, we present the DA (section 5.10.B). This is followed by the RSA (section 5.10.C).

5.10.B Dimensional analysis

Table 5.5 presents the results of a DA of SPL physical properties. The following are noteworthy observations re the DA results:

- First, it has reduced (to about half of the original number), the number of variables (process factors) relevant for analysis of the problem (of determining the process factor dependence of SPL physical properties.

- Second, and with reference to the dimensionless group P_{RF}^{*}, it predicts the significance of the two process factors P_{RF} and p for determining SPL physical properties (viz., d_{SPL}, D_{SPL}, SPL roughness (r_{SPL})).

  This observation (which is on basis of a DA) may be compared to the RSA results presented in figures 5.10 (which are on basis the experimental results per table 5.1). Evidently, the aforementioned RSA results reveal, independently of the DA, precisely the same two process factors, to be significant for determining the aforementioned physical properties of an SPL obtained via RFMS.

Proceeding forth from the DA results presented in table 5.5, in general one would express each of the 'dependent' dimensionless groups — viz., dimensionless group for d_{SPL} (d_{SPL}^{*}), dimensionless group for D_{SPL} (D_{SPL}^{*}), and dimensionless group for r_{SPL} (r_{SPL}^{*}) — individually in terms of all of the surviving 'independent' dimensionless groups — viz., dimensionless group for P_{RF} (P_{RF}^{*}), dimensionless group for O (O^{*}), dimensionless group for Ω_{SFC} (Ω_{SFC}^{*}), and dimensionless group for Θ_s (Θ_s^{*}).

However, our experimentation (refer figure 3.3) results are unable to address the dependence, if any, of SPL physical properties (d_{SPL}, D_{SPL}, and r_{SPL}) on solid angle subtended at substrate center by SFC aperture (Ω_{SFC}) and substrate temperature (Θ_s). At any rate, DA is unable to account for the process factor oxygen percent (O), or for the process factor Ω_{SFC}, since they both are dimensionless.

Variable type	RFMS Process Factor		Dimensionless Group	
	Name	Symbol	Symbol	Definition
Independent	RF Power	P_{RF}	${P_{RF}}^*$	$\frac{{D_s}^{1/2} P_{RF}}{{l_{t-s}}^2 p^{3/2}}$
	Process Gas Pressure	p	p^*	1
	Oxygen Percent	O	O^*	O
	Target-Substrate Distance	l_{t-s}	${l_{t-s}}^*$	1
	Substrate Density	D_s	${D_s}^*$	1
	Target Density	D_t	${D_t}^*$	1
	Solid Angle Subtended At Substrate Center By SFC Aperture	Ω_{SFC}	Ω^*_{SFC}	Ω_{SFC}
	Substrate Temperature	Θ_s	Θ^*_s	Θ^*_s
Dependent	SPL Thickness	d_{SPL}	${d_{SPL}}^*$	$\frac{d_{SPL}}{l_{t-s}}$
	SPL Density	D_{SPL}	${D_{SPL}}^*$	$\frac{D_{SPL}}{D_s}$
	SPL Roughness	r_{SPL}	${r_{SPL}}^*$	$\frac{r_{SPL}}{l_{t-s}}$

Table 5.5: [Caption to this table is presented on next page.]

Table 5.5: [Table corresponding to this caption is presented on the previous page.]
Results of dimensional analysis (DA) — in light of radio frequency magnetron sputtering (RFMS) — of sub-plantation layer (SPL) physical properties. The SPL was obtained on a substrate from collimated sputtered material flux. The sputtered material flux was obtained via RFMS of a target, and collimated via a sputter flux collimator (SFC). The process factors at issue are as listed, and they constitute the set of independent variables for DA. Accordingly, SPL physical properties are obtained as a result of conspiracy between the process factors (independent variables) so. The physical properties of interest are the dependent variables. A set of dimensionless groups arrived upon via DA is listed. Figure 5.9 shows the dependences $d_{SPL}(P_{RF}{}^{*})$, $D_{SPL}(P_{RF}{}^{*})$, and $r_{SPL}(P_{RF}{}^{*})$ for the five films that manifest a SPL (refer experiment design per figure 3.3 and table 3.4). Note that the symbol substrate temperature (Θ_s) is the same as the symbol substrate temperature (T_s) as is used elsewhere in this thesis; this is merely to avoid confusion with the dimension [T] of time. Also, the definition of Θ_s^* is retained as its name itself; this is since a dimension for temperature, viz., $[\Theta]$ is not supplied by any of the other (independent) variables.

As such, we proceed on basis of the following simplified relations:

$$d_{SPL}{}^{*} = \Upsilon_1 (P_{RF}{}^{*}) \tag{5.4a}$$

$$D_{SPL}{}^{*} = \Upsilon_2 (P_{RF}{}^{*}) \tag{5.4b}$$

$$r_{SPL}{}^{*} = \Upsilon_3 (P_{RF}{}^{*}) \tag{5.4c}$$

where, function relating $d_{SPL}{}^{*}$ to $P_{RF}{}^{*}$ (Υ_1), function relating $D_{SPL}{}^{*}$ to $P_{RF}{}^{*}$ (Υ_2), function relating $r_{SPL}{}^{*}$ to $P_{RF}{}^{*}$ (Υ_3).

Accordingly, given SPL physical properties per table 5.1, we consider the dependences $d_{SPL}{}^{*}(P_{RF}{}^{*})$ (refer equation 5.4a), $D_{SPL}{}^{*}(P_{RF}{}^{*})$ (refer equation 5.4b), and $r_{SPL}{}^{*}(P_{RF}{}^{*})$ (refer equation 5.4c). Plots of the same are shown in figure 5.9.

Consideration of equations 5.4a and 5.4b, in light of figures 5.9(a) and 5.9(b), predicts Υ_1 and Υ_2 to be inversely related. This is consistent with expectation and with experimental observation, as was discussed in section 5.5.C.3.

Finally, we note that due the expected drop in process pressure (p) due gas rarefaction (D. W. Hoffman, 1985; Jimenez, Ekpe, and Dew, 2006; S. M. Rossnagel, 1988) at high P_{RF}, the plots per figure 5.9 are likely contracted along the x-axis. This is further to the expression for $P_{RF}{}^{*}$ per table 5.5, and since nominal values for p per table 3.4 were used for the data plots.

5.10.C Response surface analysis

We present the RSA conducted on basis of the experimentally measured room-temperature physical properties of the SPL, as were presented in table 5.1. As noted earlier, the RSA results of a given property comprise two (inter-related) types: the pareto plots, and the response surfaces (refer section 5.10.C).

Figure 5.10 presents the linear models, via respective pareto plots, of said SPL physical properties. The pareto plots make convenient the comparison of magnitude and of sign of main and interaction (two-factor or three-factor) effects, of the three process factors, viz., P_{RF}, p, and O (refer equation 3.1b). As discussed in section 5.5.C.2, such quantitative comparisons, within and among process factors, have utility for simultaneous optimization of multiple film properties.

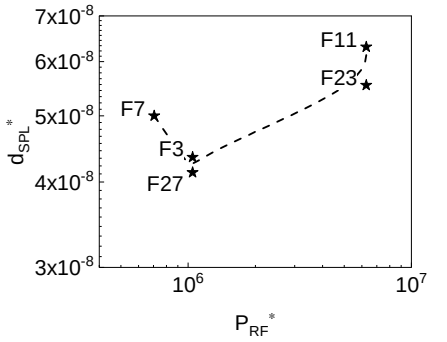

(a)

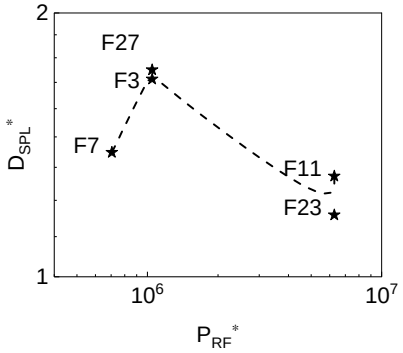

(b)

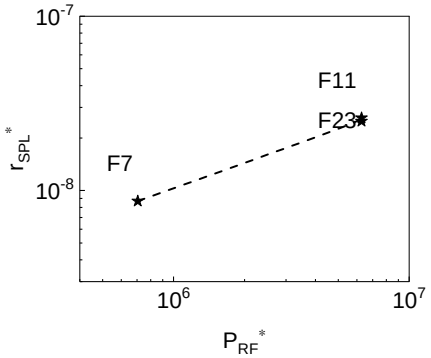

(c)

Figure 5.9: With reference to table 5.5 and equations 5.4, the dependences of dimensionless groups for sub-plantation layer (SPL) physical properties of interest (viz., SPL thickness (d_{SPL}), SPL density (D_{SPL}), SPL roughness (r_{SPL})), as a function of dimensionless group for P_{RF} (P_{RF}^*). (a) $d_{SPL}^*(P_{RF}^*)$, (b) $D_{SPL}^*(P_{RF}^*)$, and (c) $r_{SPL}^*(P_{RF}^*)$. The dashed line is a guide for the eye.

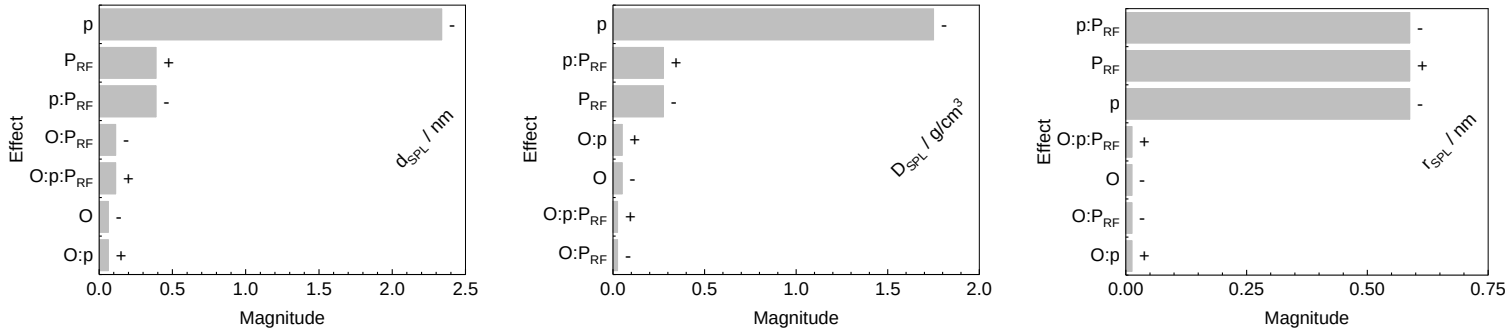

(a) (b) (c)

Figure 5.10: The pareto plots of linear models (respective) for room-temperature physical properties of sub-plantation layer (SPL) of Si doped In_2O_3−$(ZnO)_3$ (ISZO) films. Results of linear modeling (per equation 3.1 and table 5.1) of physical properties of interest of the SPL. Each bar-plot presents the seven β-coefficients corresponding to the main effects (three; terms 3.1b of equation 3.1), two-factor interaction effect (three; terms 3.1c of equation 3.1), and three-factor interaction effect (one; term 3.1d of equation 3.1). The coefficients are presented in descending order of magnitude, with their sign (-, or +) indicated next to the respective bar. Thereby, each bar-plot enables ready comparison of relative magnitude and direction (sign) of the main effects due, and of the interaction effects among, the three experimentally controlled factors, viz., RF power (P_{RF}), process gas pressure (p), and oxygen percent (O). Each of the seven bars per plot bear the label of the effect (individual β-coefficient) which they represent, as follows; main effects: O, p, and P_{RF}; two-factor interaction effects: p:P_{RF}, O:p, and O:P_{RF}; three-factor interaction effect: O:p:P_{RF}. (a) d_{SPL}, (b) D_{SPL}, and (c) r_{SPL}. Evidently, p and P_{RF} are the two principal process factors. Furthermore, it is noted that magnitudes of the main effect and of two-factor interaction effect are comparable.

We next present the response surfaces of SPL physical properties that bear upon its technological application, over the process factors space spanned by the designed experiment (DE) per figure 3.3 and table 3.4. As earlier, the properties considered so are d_{SPL}, D_{SPL}, and r_{SPL}.

The pareto plots corresponding to the response surface for each of the aforementioned properties were presented in figure 5.10. The response surface make convenient the quantitative representation of the property of interest over the process factors space spanned by the DE.

Evidently, figure 5.10 reveals P_{RF} and p to be process factors of significance for the SPL properties in question. Accordingly, contour plots constituting each response surface will be presented in terms of these process factors, according the scheme shown in figures 5.11(a) through 5.11(c).

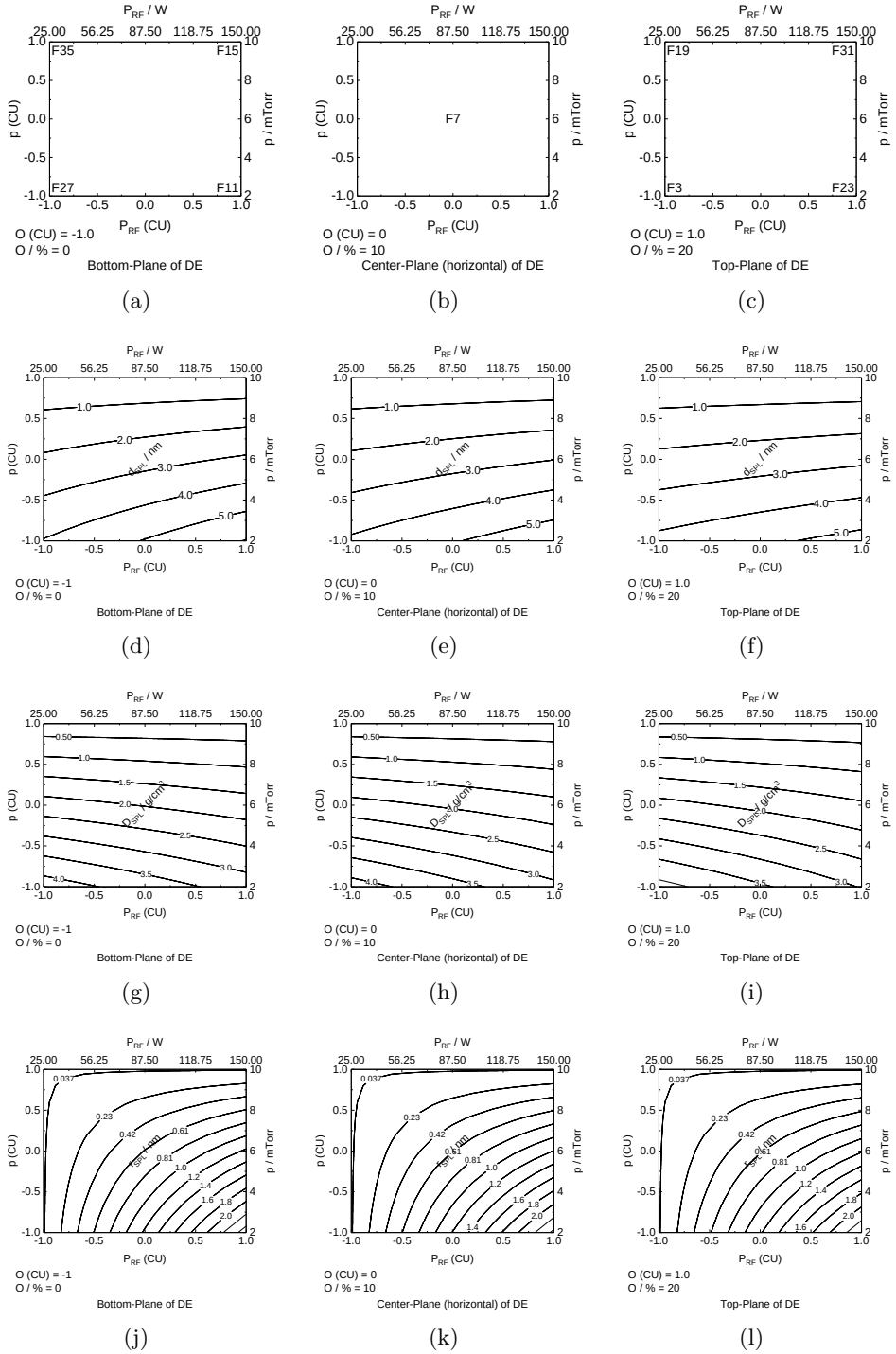

Figure 5.11: [Caption to this figure is presented on next page.]

Figure 5.11: [Figure corresponding to this caption is presented on the previous page.]
With reference to the experiment design per figure 3.3 and table 3.4, sub-plantation layer (SPL) response surfaces corresponding to the factors set (P_{RF}, p, O) indicated. The response surfaces are presented as contour plots at the bottom-plane, center-plane (horizontal), and top-plane of the experiment design. A simultaneous reading of the response surfaces of each property of interest may be used to determine the process factors set needed to obtain a SPL that manifests a requested set of physical properties. The ranges over which may be varied the individual process factor is determined by the film deposition equipment (Kurt J. Lesker Company Model PVD 75, for the present study). (a to c) Respectively, the bottom-plane, center-plane (horizontal), and top-plane of DE. (d to f) SPL thickness (d_{SPL}), (g to i) SPL density (D_{SPL}), (j to l) SPL roughness (r_{SPL}). Here, oxygen percent (O), process gas pressure (p), RF power (P_{RF}).

Chapter 6

The thin-film layer

6.1 Introduction

In this chapter, we consider the thin-film layer (TFL). Discussion of the TFL was initiated in chapter 5, with determination of its physical properties (refer table 5.1). Here, we present further discussion of the physical properties, and of opto-electronic properties, of the TFL. Furthermore, this chapter will elucidate the nature of electronic state of the amorphous TFL (film).

We begin by considering the microstructure of our films (section 6.2). This is followed by detailed quantitative (further to section 5.6.C) analysis of experimentally determined room-temperature opto-electronic properties of film layers (section 6.3). We then determine (on basis of absolute temperature (T) dependence of their electronic properties) that the electronic state of the films is compensated (section 6.4). Having determined the electronic state to be insulating (semiconducting), we demonstrate that oxygen (O) incorporation results in its progress towards a metal (section 6.5). Finally, we present results of response surface analysis (RSA) of film electronic, and physical properties (section 6.6).

6.2 Amorphous Si doped In_2O_3–$(ZnO)_3$ films

6.2.A Introduction

We establish that the microstructure of our Si doped In_2O_3–$(ZnO)_3$ (ISZO) films is amorphous (section 6.2.B). Thence we consider relevant published results on the amorphous In_2O_3–$(ZnO)_k$ (k = 0, 1, 2, 3, …) material system (section 6.2.C). Finally, we discuss the doping of silicon (Si) into said material system (section 6.2.D).

6.2.B X-Ray diffractograms

With reference to experiment design per figure 3.3 and table 3.4, figure 6.1 presents the x-ray diffractograms of our ISZO films. For each film, the sole broad peak confirms the absence of crystalline phases (respectively) (Hideo Hosono, 2010b).

This is as per expectation, since film growth was performed on unheated substrates (that is, substrates to which no express provision of heating was made; refer section 4.2.C) (Messier, A. P. Giri, and Roy, 1984).

6.2.C Amorphous In_2O_3–$(ZnO)_k$ (k = 0, 1, 2, 3, …) material system

The In–Zn–O material system forms line compounds according to the homologous series In_2O_3–$(ZnO)_k$ (k = 0, 1, 2, 3, …). The following discussions are for film deposition via pulsed laser ablation (PLA) of a target with nominal composition according a given composition index for homologous series 'In_2O_3–$(ZnO)_k$ (k = 0, 1, 2, 3, …)' (k).

When depositions were performed onto substrates maintained at high temperature (ca. 500 K), the resulting films were polycrystalline, where each grain comprised a multitude of line compounds of composition according to

Figure 6.1: The x-ray diffraction (XRD) profiles of the nine Si doped $In_2O_3-(ZnO)_3$ (ISZO) films constituting the designed experiment (DE) of this study (refer figure 3.3 and table 3.2). The single broad peak in each diffractogram reveals that the corresponding film is amorphous. (a) designed experiment (DE) back-plane films: F35, F15, F31, and F19. (b) DE center-plane / center-point film: F7. (c) DE front-plane films: F27, F11, F23, and F3. Here, angle of incidence of x-rays (Θ).

the aforementioned homologous series (Negar Naghavi et al., 2000). Each grain comprised polytype domains, where the composition of a domain was at a single k value. Further, the atomic arrangement within a domain was layered (see figure 6.2(a)). Within a grain, the predominant domain composition was at the k value of the original nominal composition of the target. When depositions are performed on substrates at lower (nominally room-temperature), the resulting films were amorphous. Calculations (figure 6.2(b)) show that, the amorphous state maintains the local coordination motifs as are present in the crystalline state of the In−Zn−O system (Walsh, Silva, and S.-.-H. Wei, 2011; Khanal et al., 2015).

Figure 6.2(c) presents experimentally observed electronic properties of the aforementioned homologous series of In−Zn−O material system (In_2O_3−$(ZnO)_k$ (k = 0, 1, 2, 3, …)) material system (Negar Naghavi et al., 2000). Calculated absolute band alignment of the valence and conduction bands of the starting transparent conducting oxide (TCO) materials, namely, ZnO and In_2O_3, and that of the k = 1 homologue are shown in figure 6.2(d).

6.2.D Si doping

Structural disorder introduced into a material system due doping by a species having a size (significantly) different from that of the replaced species helps stabilize an amorphous phase within the system (Mattes, 1980; Funabiki, Kamiya, and Hideo Hosono, 2012). Table 6.1, compares the sizes of the metal species involved during doping of Si into the In−Zn−O material system. The structural disorder introduced upon Si doping, given its size relative the other metals (viz., In and Zn) at issue, will stablize the amorphous phase of the resulting multinary system.

With reference to experiment design per figure 6.2(a) and table 6.1, upon

Metal	Number of coordinating oxygens in metal-oxide	Crystal radius of metal ion / nm
In	6	9.4×10^{-2}
Zn	4	7.4×10^{-2}
Si	4	4.0×10^{-2}

Table 6.1: The first coordination sphere of oxygens, and crystal radius, of metal in metal-oxide. Note the difference in crystal radius of silicon (Si) from that of indium (In), and from that of zinc (Zn). Data from Shannon, 1976.

doping Si into the $In_2O_3{-}(ZnO)_k$ (k = 0, 1, 2, 3, ...) material system, one expects the Si species to inhabit the Zn−In−O network in preference to the InO_2 network (refer figure 6.2(a)). This is since Si, like zinc (Zn), prefers four coordinating oxygens. This may be contrasted to the preference of indium (In), which prefers a six coordinated oxygen environment (C. S. G. Phillips and Williams, 1965).

Consideration, more so at higher k values, of strain energy also support such reasoning. This is since the positive strain energy introduced into the $In_2O_3{-}(ZnO)_k$ (k = 0, 1, 2, 3, ...) system, due incorporation of Si, will be diminished by the availability, to the originating strain field, of an adequate length scale (thickness of Zn−In−O network; refer figure 6.2(a)) over which to relax (refer also, section 7.4.C.2) (S.-H. Wei, 2004).

Furthermore, Si is capable of donating electrons to the conduction band when doped into ZnO (Wang et al., 1996; Klaus Ellmer and Bikowski, 2016). Polycrystalline films of Si doped ZnO have shown promise for high temperature applications (Tadatsugu Minami et al., 1986; T. Minami et al., 1989).

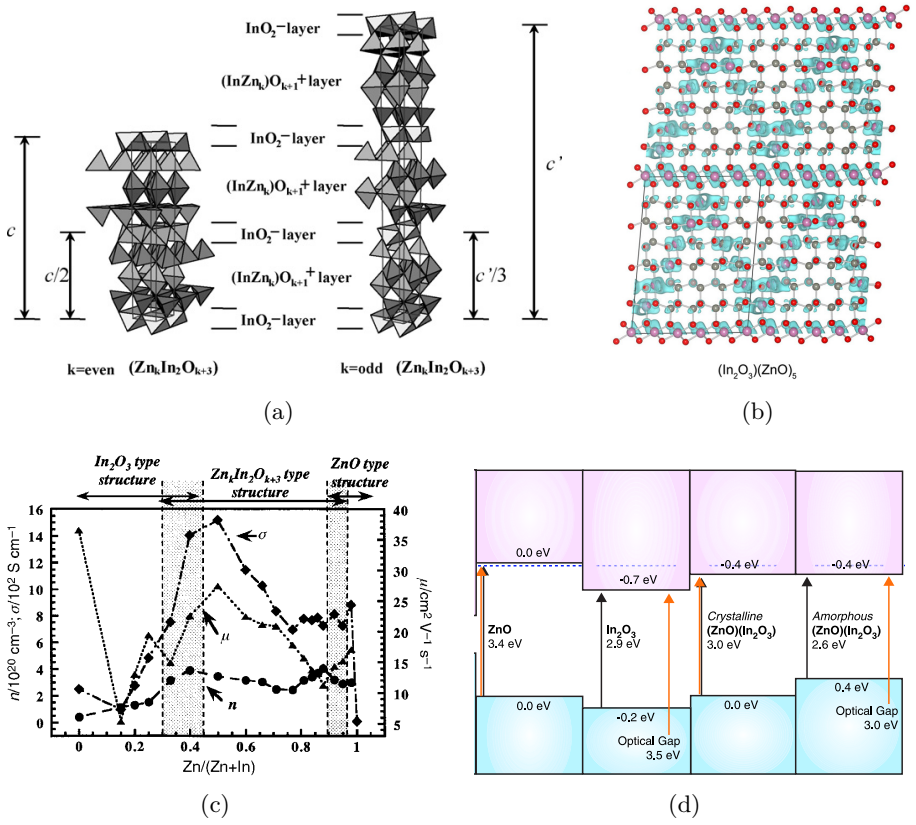

Figure 6.2: (a) The layered crystal structure of homologous series of In−Zn−O material system (In_2O_3−$(ZnO)_k$ (k = 0, 1, 2, 3, …)) (for reference also in context of table 7.2). Figure adapted from Yoshinari et al., 2009. (b) The layered structure of amorphous k = 5 homologue of the 'In_2O_3−$(ZnO)_k$ (k = 0, 1, 2, 3, …)' material system (In_2O_3−$(ZnO)_5$) material system showing that the local coordination motifs are maintained in comparison to the crystalline state. (c) The variation of room-temperature electronic properties (conduction electron concentration (n), conduction electron mobility (μ), and conductivity (σ); see equation 4.11e, where $\sigma = 1/\rho$) for In_2O_3−$(ZnO)_k$ (k = 0, 1, 2, 3, …) films deposited via pulsed laser ablation (PLA). In the figure, zinc (Zn) and indium (In) refer to the number of corresponding metal atoms in corresponding homologue formula unit. Note that the peak in conductivity (σ) and in conduction electron mobility (μ) occur at a metal ratio of 1:1. A silicon (Si) doped k = 3 homologue is the subject of this study (refer section 4.2.C and table 7.2). Figure adapted from Negar Naghavi et al., 2000.
[This caption continues on next page.]

Figure 6.2: [This caption continues from previous page.]
(d) Absolute alignment of the valence band edge (VBE) and of the conduction band edge (CBE) of the starting materials, namely, zinc oxide (ZnO) and indium sesquioxide (In_2O_3) and that of the $k = 1$ homologue. For any homologue, the valence band edge (VBE) is determined by the zinc oxide (ZnO) VBE while the conduction band edge (CBE) is determined by the indium sesquioxide (In_2O_3) CBE. Thus, with increasing k (which results in a decrease in the In:Zn ratio in the Zn−In−O network per (a)), the states from which is constituted the CBE of In_2O_3−$(ZnO)_k$ (k = 0, 1, 2, 3, ...) are localized progressively on the InO_2 networks. That is, with increasing k, the InO_2 networks are progressively the preferred seat (channel) for electrical conduction within In_2O_3−$(ZnO)_k$ (k = 0, 1, 2, 3, ...). We have attempted to modulate electrical transport parameters (n, μ) by introducing Si, which is expected to preferentially substitute at Zn sites in the Zn−In−O network (Walsh, Silva, and S.-.-H. Wei, 2011).

Also, In doping of ZnO has been shown to result in marked improvement in conduction electron concentration (n), accompanied albeit with a depression of μ (Vai et al., 2014).

6.3 Film opto-electronic properties II

6.3.A Introduction

We present quantitative estimations of room-temperature opto-electronic properties of our ISZO films. We do so on basis of the basic physics of the transparent conductive (TC) state. We then proceed to model the optical (spectroscopic ellipsometry (SE)) measurements, on basis of physically meaningful (Kramers Kronig (KK) consistent) oscillator models. We compare the modeling results so with those obtained 'directly' via electrical (AC Field Hall Effect (ACFHE)) measurements. The discussions will be on basis of two exemplary ISZO films, viz., F11 and F23.

Accordingly, we present general considerations relevant for a quantitative understanding of the wavelength of light (λ) dependence of transmission

fraction (Tr) for TCO material films (section 6.3.B). We then present and analyze the experimentally measured $\mathrm{Tr}(\lambda)$ (uncorrected for substrate) of our ISZO films (section 6.3.C). Thence, we present and compare the results of modeled (optical), and of direct (electrical), determinations of electronic properties of the aforementioned two ISZO films (section 6.3.D). This will be followed by the modeled λ dependence of optical constants of the same two ISZO films (section 6.3.E).

6.3.B The transmission fraction of transparent conducting oxide films: general considerations

The low (ultra violet (UV), and lower) and high (near infra red (IR)) λ ends of the desired optical transmission window of TC oxide film are determined respectively by the (wavelength corresponding to) material band-gap energy ($\mathrm{E_g}$), and the material plasma edge wavelength (λ_p). The Drude (D) free electron model provides a satisfactory (in agreement with experiment) description of the optical behaviour at energy (E) (much) less than $\mathrm{E_g}$ (Wooten, 1972).

The D model, per equation 6.1, defines the Drude ε^* (ε^*_D) as a function, among others, of λ (alternatively, of E), and film resistivity (ρ) (alternatively, of n and μ; refer equation 4.11e). Via the complex refractive index (n^*) (calculable from ε^*_D; refer equation 4.6a), one may calculate the λ and d dependent absorptance of the film (Coutts, Young, and Li, 2000).

As discussed in section 2.6.A, such calculations reveal that, for traditional TCO materials whereby increasing n results in decrease of μ, the preferred strategy for enhancing film opto-electronic properties to increase μ in preference to increase of n.

On basis of figure 2.4, one sees that $\mu(\mathsf{n})$ for our ISZO films is enhanced in comparison to kindred Ga doped $\mathrm{In_2O_3}-(\mathrm{ZnO})_3$ (IGZO) films. In section

6.3.C we present a quantitative analysis, on basis of the D model, of the experimentally measured λ dependence of Tr for our ISZO films.

6.3.C The transmission fraction of Si doped In_2O_3–$(ZnO)_3$ films

Figure 6.3 presents the experimentally recorded room-temperature $\mathrm{Tr}(\lambda)$ (uncorrected for substrate) for the nine films constituting our DE. One observes that the plasma edge is not yet reached at the upper limit of the λ range, viz., 1690 nm, of the Tr measurements.

Further to equations 6.1 and 4.6d, and accounting for high frequency dielectric permittivity (ε_∞) (Horiba Jobin Yvon, 2006), one writes (P. P. Edwards et al., 2004; Porch et al., 2004):

$$\varepsilon_{1,\,D} = \varepsilon_\infty - \left(\frac{e^2\hbar^2}{\varepsilon_0}\right)\frac{1}{\left(\hbar^2 + E^2\tau^2\right)}\frac{\tau^2 n}{m_e m^*} \tag{6.1a}$$

and,

$$\varepsilon_{2,\,D} = \left(\frac{e^2\hbar^3}{\varepsilon_0}\right)\frac{1}{E\left(\hbar^2 + E^2\tau^2\right)}\frac{\tau n}{m_e m^*} \tag{6.1b}$$

where,

$$E = \hbar\omega \tag{6.1c}$$

or equivalently,

$$E = \frac{2\pi\hbar c}{\lambda} \tag{6.1d}$$

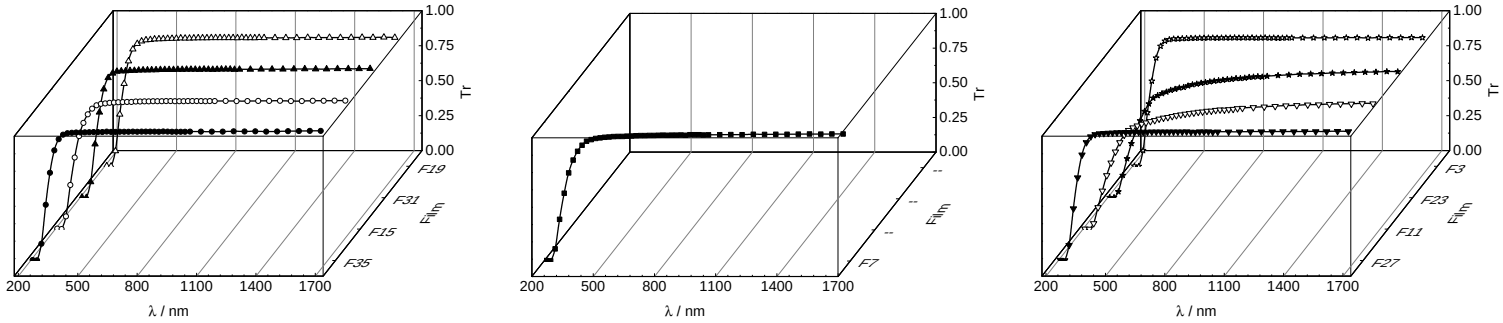

(a) (b) (c)

Figure 6.3: The wavelength of light (λ) dependent transmission fraction (Tr) (uncorrected for substrate) of the nine Si doped $In_2O_3-(ZnO)_3$ (ISZO) films constituting the designed experiment (DE) of this study (refer figure 3.3 and table 3.2). (a) DE back-plane films: F35, F15, F31, and F19. (b) DE center-plane / center-point film: F7. (c) DE front-plane films: F27, F11, F23, and F3.

Whereas, the condition:

$$\varepsilon_{1,\,D}(E_p) = 0 \tag{6.1e}$$

defines the plasma edge energy (E_p), or equivalently (given equation 6.1c):

$$\omega_p = \frac{E_p}{\hbar} \tag{6.1f}$$

Thereby, given equation 4.18a:

$$\omega_p = \frac{e}{m_e m^*}\left(\frac{n m_e m^*}{\varepsilon_\infty \varepsilon_0} - \frac{1}{\mu^2}\right)^{1/2} \tag{6.1g}$$

where, plasma edge angular frequency (ω_p), high frequency dielectric permittivity (ε_∞), real part of ε^*_D ($\varepsilon_{1,\,D}$), imaginary part of ε^*_D ($\varepsilon_{2,\,D}$), reduced Planck constant ($\hbar$), elementary charge (e), mathematical constant (π), speed of light in vacuum (c), conduction electron concentration (n), conduction electron mobility (μ), permittivity of vacuum (ε_0), effective mass of electron in units of rest mass of electron (m^*), rest mass of electron (m_e), mean free time between collisions (τ), energy (E).

The analysis as follows proceeds with reference to the film with the highest observed n, namely, F23 (refer tables 6.2 and 6.5) (P. P. Edwards et al., 2004). As discussed later, it (the analysis) is pertinent for our films-set (refer DE per figure 3.3 and table 3.4), and is in light of the following results re film F23, in comparison to the other (eight) films of the DE:

- That this film displays the highest n and the highest μ (refer table 6.5, and consequent figures 6.16 and 6.17);
- That this film, while semiconducting (refer figure 6.8(c)), is in vicinity

of the metal insulator transition (MIT) (refer figure 6.12). In particular, film F23 is degenerate in vicinity of room-temperature (refer its n(T) per figure 6.8(a)).

In the limit $n \gtrsim 10^{19}/cm^3$ and $\mu \gtrsim 2 \times 10^1\, cm^2/(V\,s)$ (refer table 6.2 for values of the relevant quantities for film F23), the first term in parenthesis of equation 6.1g is much greater than the second term.

Thereby, ignoring the second term, one may write:

$$\omega_p = \left(\frac{e^2 n}{\varepsilon_\infty \varepsilon_0 m_e m^*} \right)^{1/2} \tag{6.2a}$$

That is, in the limit under consideration, the plasma edge angular frequency (ω_p) is a function only of n, as follows:

$$\omega_p \propto n^{1/2} \tag{6.2b}$$

Thus, for ω_0 such that:

$$\omega_p < \omega_0 \tag{6.2c}$$

the film will be non-reflective. Inverting expression 6.2a using condition 6.2c, we obtain the inequality:

$$n < \frac{4\pi^2 c^2 \varepsilon_\infty \varepsilon_0 m_e m^*}{e^2} \frac{1}{\lambda_0^2} \tag{6.2d}$$

where, wavelength of interest less than λ_p (λ_0).

Whereby, for ISZO, on basis of results for F23 presented in table 6.2:

$$\mathrm{n}\ (1/\mathrm{cm}^3) < 1.7 \times 10^{26} \frac{1}{\lambda_0^2}\ (1/\mathrm{nm}^2) \tag{6.2e}$$

is the condition on n for transmission of given λ_0.

Thus, at the upper limit of the present wavelength-range, viz., $1690\,\mathrm{nm}$, the condition on n for transmission to occur is:

$$\mathrm{n} < 6.0 \times 10^{19}/\mathrm{cm}^3 \tag{6.2f}$$

From figure 6.3, it is clear that λ_p is not reached till the upper limit of the present wavelength-range. That is, the theoretically determined relation 6.2f for ISZO is consistent with the experimentally determined n for ISZO / F23 presented in table 6.5.

We consider next the λ dependences of reflection from, and transmission through, our ISZO films, over the investigated wavelength-range, viz., $210\,\mathrm{nm} \leq \lambda \leq 1690\,\mathrm{nm}$. In general:

$$\Re(\lambda) = \left| \frac{\varepsilon_\mathrm{D}^*(\lambda)^{1/2} - 1}{\varepsilon_\mathrm{D}^*(\lambda)^{1/2} + 1} \right|^2 \tag{6.3a}$$

Whence,

$$\Re(\lambda > \lambda_\mathrm{p}) \lesssim 1 \tag{6.3b}$$

$$\Re(\lambda < \lambda_\mathrm{p}) \ll 1 \tag{6.3c}$$

where, power reflection coefficient ($\Re$), wavelength of light (λ), plasma edge wavelength (λ_p), Drude ε^* (ε_D^*).

Further quantitative discussion of reflection properties of the films is not

feasible here. This is since we do not possess $\Re(\lambda)$ data.

We consider next the $\mathrm{Tr}(\lambda)$ of our ISZO films. In general:

$$\frac{\mathfrak{T}(d)}{\mathfrak{T}(0)} \propto \exp\left(\frac{-2d}{\delta}\right) \tag{6.4a}$$

where,

$$\delta = \frac{2\lambda}{\pi}\left(\frac{1}{\varepsilon_{1,\,D}^2 + \varepsilon_{2,\,D}^2 - \varepsilon_{1,\,D}}\right)^{1/4} \tag{6.4b}$$

Specifically, for wavelengths $\lambda_0 < \lambda_p$:

$$\delta \approx \frac{8\pi^2 c^2 (m_e m^*)^2}{Z_\infty e^3}\left(\frac{\mu}{n\lambda_0^2}\right) \tag{6.4c}$$

That is, at wavelengths λ_0 below λ_p:

$$\delta \propto \left(\frac{m^{*2}\mu}{n}\right)\frac{1}{\lambda_0^2} \tag{6.4d}$$

here, normalized power transmission coefficient '$\mathfrak{T}(d)/\mathfrak{T}(0)$' determines $\mathrm{Tr}(\lambda_0)$, and whereas, power transmission coefficient ($\mathfrak{T}$), thickness (as applicable) of film or of film layer (d), skin depth (δ), speed of light in vacuum (c), wavelength of light (λ), real part of ε_D^* ($\varepsilon_{1,\,D}$), imaginary part of ε_D^* ($\varepsilon_{2,\,D}$), effective mass of electron in units of rest mass of electron (m^*), impedance of free space (Z_∞) (refer table A.2 for value of ε_∞), rest mass of electron (m_e), conduction electron mobility (μ), conduction electron concentration (n), wavelength of interest less than λ_p (λ_0).

In light of the experimental and modeled estimations presented in table 6.2, we determine the pre-factor in relation 6.4d to be $3.8 \times 10^{-20}\,\mathrm{cm}^5/(\mathrm{V\,s})$ for film F11, and $3.4 \times 10^{-20}\,\mathrm{cm}^5/(\mathrm{V\,s})$, for film F23. The quantitative proximity

of the two aforementioned pre-factors is indeed borne out by the closeness — despite differences in respective μ and n values — of their respective $\mathrm{Tr}(\lambda_0)$ profiles as presented in figure 6.3(c).

A principal quantity of interest for macro-scale technological applications (e.g., transparent electrodes for touchscreen and photovoltaic (PV) applications) is $\mathrm{R_s}$ (Walker, 2014; Bivour et al., 2014), given as:

$$\mathrm{R_s} = \frac{\rho}{\mathsf{d}} \tag{6.5a}$$

which, expressed in terms of film electronic properties (per equation 4.11e), yields:

$$\mathrm{R_s} = \frac{1}{\mathsf{n}\mathrm{e}\mu\mathsf{d}} \tag{6.5b}$$

In light of the preceding discussions, optimization of two of the film parameters critical for technology development in the transparent electronics area, viz., $\mathrm{Tr}(\mathsf{d})$ and $\mathrm{R_s}(\mathsf{d})$, are in fundamental opposition to each other. Figure 6.4 presents quantitative practical considerations that arise due the aforementioned observation, in context of the commercially important touchscreen applications area.

Figures 6.5(a) and 6.5(b) presents contour plots of $\delta(\mathsf{n},\, \mu)$ and $\rho(\mathsf{n},\, \mu)$.

Similarly, figure 6.5(c) presents contour plot of $\mathrm{R_s}(\mathsf{n},\, \mu,\, \mathsf{d} = 75\,\mathsf{nm})$. The choice of value of d for calculation of $\mathrm{R_s}$ is a representative one based on a typical use case whereby an indium tin oxide (ITO) film is used as the front contact on a heterojunction solar cell. For this value of d, the ITO film has a reflection minimum near $\lambda = 600\,\mathsf{nm}$. Thereby, in addition to serving as an electrode, it (the ITO TCO film) serves also as an anti-reflection coating on the solar cell (Holman et al., 2012).

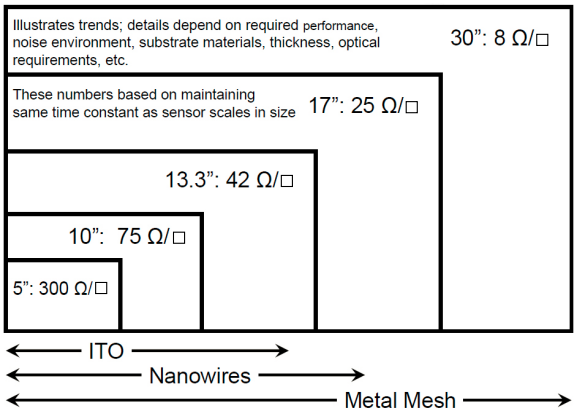

Figure 6.4: Representative maximum acceptable sheet resistance (R_s) as a function of touchscreen size (in inches). The acceptable sheet resistance (R_s) decreases with increasing touchscreen size, in order to deliver an acceptable capacitive response time. Since materials and film deposition considerations do not permit the decreasing of resistivity (ρ) indefinitely, decrease in R_s may realistically be achieved only by increasing thickness (as applicable) of film or of film layer (d). In turn, increasing thickness (as applicable) of film or of film layer (d) leads to a concomitant decrease in film transmission fraction (Tr). The transparent conductive (TC) materials (films) capable of delivering maximum acceptable R_s at minimum acceptable Tr are as indicated. Figure adapted from Walker, 2014.

The (n, μ) region presented in figure 6.5 is as relevant for ISZO films (present study). The contour plots are further respectively to equations 6.4c, 4.11e, and 6.5a. Perusing figures 6.5(a) and 6.5(b) from their respective bottom-right towards top-left, it is evident that while δ (and thereby, Tr) increases, σ ($= 1/\rho$) decreases. Thus, for transparent applications, and assuming that $\mu \geq 10\,\mathrm{cm^2/(V\,s)}$, lower R_s is preferably achieved via increase in μ as opposed to increase in n.

Figures 6.5(a) and 6.5(b) also present the experimentally determined positions of four individual instances of the ISZO material system, viz., F15, F7, F11, F23 (per table 6.5).

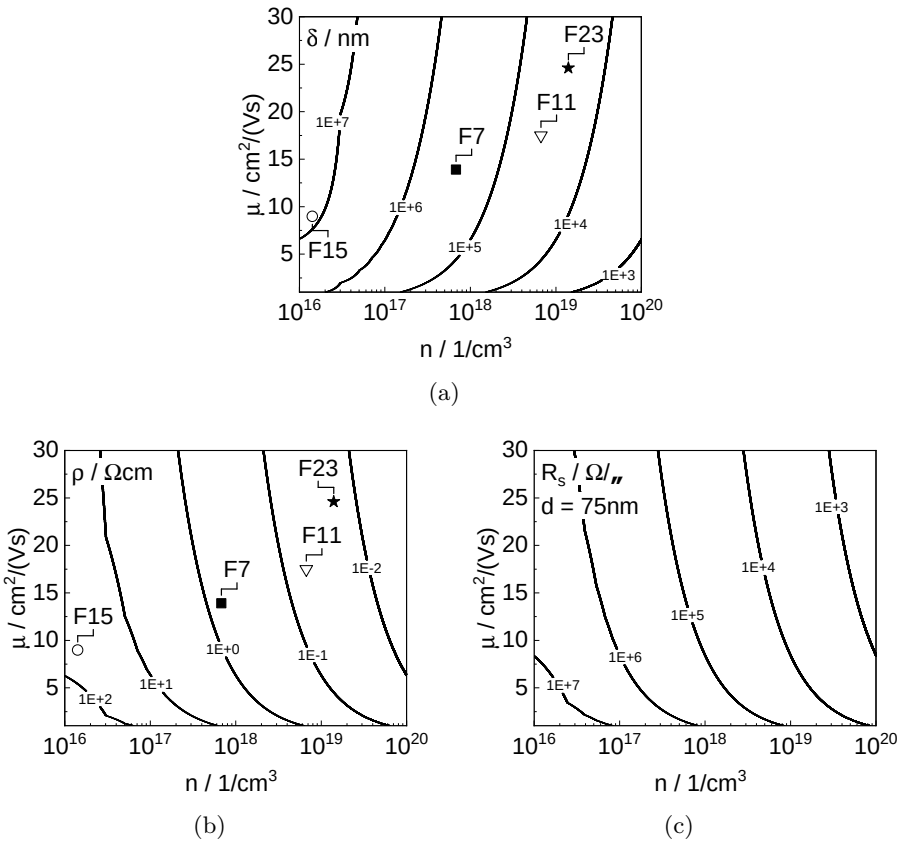

Figure 6.5: (a) Contour-plots, per relation 6.4c, for skin depth (δ) as a function of conduction electron mobility (μ) and conduction electron concentration ($\mathbf{n}$), for the Si doped In_2O_3−$(ZnO)_3$ (ISZO) material system. The plots are for $\lambda_0 = 700\,\mathbf{nm}$, which is the upper limit wavelength of visible light. Given relation 6.4d, it is clear that skin depth (δ), and thereby, transmission fraction ($\mathbf{Tr}$), at all (lower) visible wavelengths will be greater. The estimated location so of δ for four individual instances of the ISZO material system, viz., F15, F7, F11, F23, are shown. (b) Contour-plots, per relation 4.11e, for resistivity (ρ) as a function of μ and $\mathbf{n}$). The experimentally determined values of ρ for four individual instances of the ISZO material system, viz., F15, F7, F11, F23, are shown (refer table 6.5). (c) Contour-plots, per relation 6.5a, for sheet resistance (R_s) as a function of μ and $\mathbf{n}$, and for $\mathbf{d}$ = 75 nm. Note that the contours as plotted are in log progression, while the axes are in log-linear ($\mathbf{n}$-μ) scale. The plots assume $\mathbf{m}^*$(ISZO) = 0.14 (refer table 6.2). Here, wavelength of interest less than λ_p (λ_0), thickness (as applicable) of film or of film layer ($\mathbf{d}$).

6.3.D Optical and electrical determination of room-temperature electronic properties

Table 6.2 presents and compares determinations of electronic properties of films F11 and F23 made on the following two bases: optical (modeling of SE spectra via physically meaningful oscillator models (Fujiwara and Kondo, 2005); refer table 5.2), and electrical ('directly' via measurement of the Hall Effect (HE)). One notes the corroboration of the direct (electrical) determination, of the modeled (optical) one.

The HE results presented in table 6.2 utilized the film thicknesses per table 5.1*.

Further analyses of the electronic state of the ISZO films was proceeded on basis of measurements of the absolute temperature (T) dependences of $\mathbf{n}$ and μ of the ISZO films. Such measurements proved to be feasible only on films F11 and F23, and revealed both films to be semiconducting. Thereby, Brooks-Herring (BH) model of ionized impurity scattering (IIS) (section 6.4), and the Mott theory of the MIT (section 6.5) permitted further analysis.

The film layer structures (refer, table 5.1) permitted modeling of the SE spectra, which yielded the results presented in table 6.2. The analysis also yielded the λ dependence of optical constants (viz., refractive index ($\mathbf{n}$) and extinction coefficient ($\mathbf{k}$)) for each layer, which we consider next.

6.3.E The refractive index and the extinction coefficient

Having determined the film layer structure (viz., layer thicknesses, and their placement relative each other) independently via x-ray reflectometry (XRR)

*As applicable: d_{TFL} (for film F15), or $d_{TFL} + d_{SPL}$ (for films F7, F11, F23). Since d_{SPL} is $\lesssim$10 % of d_{TFL} (with exception of film F7), the error introduced in the estimation of electronic properties due including d_{SPL} in to the film thickness, is not significant for the present purposes.

Property		Film			
		F11		F23	
		SE	HE	SE	HE
n	/ $1/cm^3$	$1.5(1) \times 10^{19}$	$6.7(5) \times 10^{18}$	$1.5(1) \times 10^{19}$	$1.40(4) \times 10^{19}$
μ	/ $cm^2/(V\,s)$	HE value	$1.75(5) \times 10^{1}$	HE value	$2.46(8) \times 10^{1}$
ε_∞		1 (fixed)	NA	1 (fixed)	NA
m^*	/ m_e	$1.2(1) \times 10^{-1}$	NA	$1.4(1) \times 10^{-1}$	NA
A	/ eV	$7.5(2) \times 10^{1}$	NA	$8.4(2) \times 10^{1}$	NA
B	/ eV	6.3(3)	NA	6.0(2)	NA
E_0	/ eV	6.5(1)	NA	6.05(3)	NA
E_g	/ eV	2.38(2)	NA	2.53(1)	NA
MSE		20.8	NA	16.9	NA

Table 6.2: Comparison of electrical (via measurement of Hall Effect (HE)) and optical (via modeling of measured spectroscopic ellipsometry (SE) parameters) determinations of electronic properties of Si doped $In_2O_3-(ZnO)_3$ (ISZO) films F11 and F23. Table 5.2 presents details of the general oscillator model (Tauc-Lorentz plus Drude (TL+D)) that was used for the modeling. The following assumptions were made for the modeling (J. A. Woollam Co., 2014): the high frequency dielectric permittivity (ε_∞) was fixed at unity (Horiba Jobin Yvon, 2006; Lin et al., 2016; Kamiya, Nomura, and Hideo Hosono, 2009), and the infra red (IR) and ultra violet (UV) poles were fixed at 0 eV each. Here, mean square error (MSE), not applicable (NA), conduction electron concentration (n), conduction electron mobility (μ), effective mass of electron in units of rest mass of electron (m^*), rest mass of electron (m_e), amplitude of imaginary part of ε^*_{TL} (A), broadening of imaginary part of ε^*_{TL} (B), energy at peak in imaginary part of TL ε^* (ε^*_{TL}) (E_0), band-gap energy (E_g).

(refer, table 5.1), we are now able to model SE spectra to determine the λ dependence of optical constants (viz., n and k) for each layer.

The determination proceeded via parametrization of complex permittivity (ε^*) of each film layer via KK consistent oscillator models (dispersion functions) per sections 4.4.D and A.3.B. The parametrization yielded the corresponding n^* (refer relations 4.6).

The effect of the film-substrate-combine is to cause a change in the state of polarization of the incident electro-magnetic ray, so that the reflected ray is, in general, elliptically polarized. Thus, given relations 4.6c, the experimentally measured and calculated λ dependence of the ellipsometric parameters (Ψ, Δ), for films F7, F11, and F23 at three representative angle of incident light (α_i), are presented in figure 6.6.

We have employed the KK consistent b-spline dispersion function for performing said parametrization of imaginary part of ε^* (ε_2), and thence (via KK transformation) of real part of ε^* (ε_1), over the experimentally accessed λ-range (210 nm to 1690 nm) (Blaine and Hale, 2008).

With the film layer structure having been determined (per figures 5.3(c) and 5.3(d), and table 5.1), we now determine the λ dependence of optical constants (n, k) of the ISZO films layers, on basis of experimentally recorded SE spectra. This determination is with an eye on the opto-electronic applications potential of the ISZO material system (refer table 7.1).

With film thicknesses as given (refer table 5.1), use of physically meaningful optical model (per table 5.2) for modeling of optical constants was feasible only for the films F7, F11, and F23 (Woollam et al., 1999). Each of these films is bi-layer (BL) (refer table 5.1). The analysis (modeling) proceeds via determination of the ε^* of each film layer (TFL, and sub-plantation layer (SPL)) (refer section 4.4.C).

Figure 6.7 presents the thus modeled ($\mathsf{n}(\lambda)$, $\mathsf{k}(\lambda)$) for the SPL and for the TFL, of the three aforementioned films. The relatively high oxygen percent (O) during film deposition, as also the enhanced concentration of optical scattering centers available due the inherent structural disorder (recall that the films amorphous) likely contribute to the non-zero k(E) in the IR range (Jung et al., 2003; Shimakawa et al., 1998; Hideo Hosono, Yasukawa, and Kawazoe, 1996).

Film transparency ultimately is limited by free carrier absorption (Peelaers, Kioupakis, and Van De Walle, 2012; K. M. Yu et al., 2012). Increased IR transparency may be achieved if the λ_{p} is pushed to higher wavelengths. This is possible via control of film ε^{*}. The same comes to inhere during film fabrication. Thereby, control over it may be exercised via control of the fabrication (deposition and post deposition) process conditions.

The desirable situation would be to exercise such control, while simultaneously obtaining acceptable film n and μ. Indeed, such control has been demonstrated for various material systems and deposition processes (e.g., ITO films deposited via sputtering, and fluorine (F) doped tin(IV) oxide (SnO_2) films deposited via chemical vapour deposition (CVD)) via introduction of suitable impurities (T. Gessert et al., 2011).

Furthermore, modeled ($\mathsf{n}(\lambda)$, $\mathsf{k}(\lambda)$) permit determination of operationally relevant device scale parameters. For example, short wavelength current losses and quantum efficiency are two parameters of interest for evaluating performance of a heterojunction solar cell. Modeling, and consequent optimization, of such parameters becomes feasible given knowledge of the ($\mathsf{n}(\lambda)$, $\mathsf{k}(\lambda)$) of each layer (Holman et al., 2012).

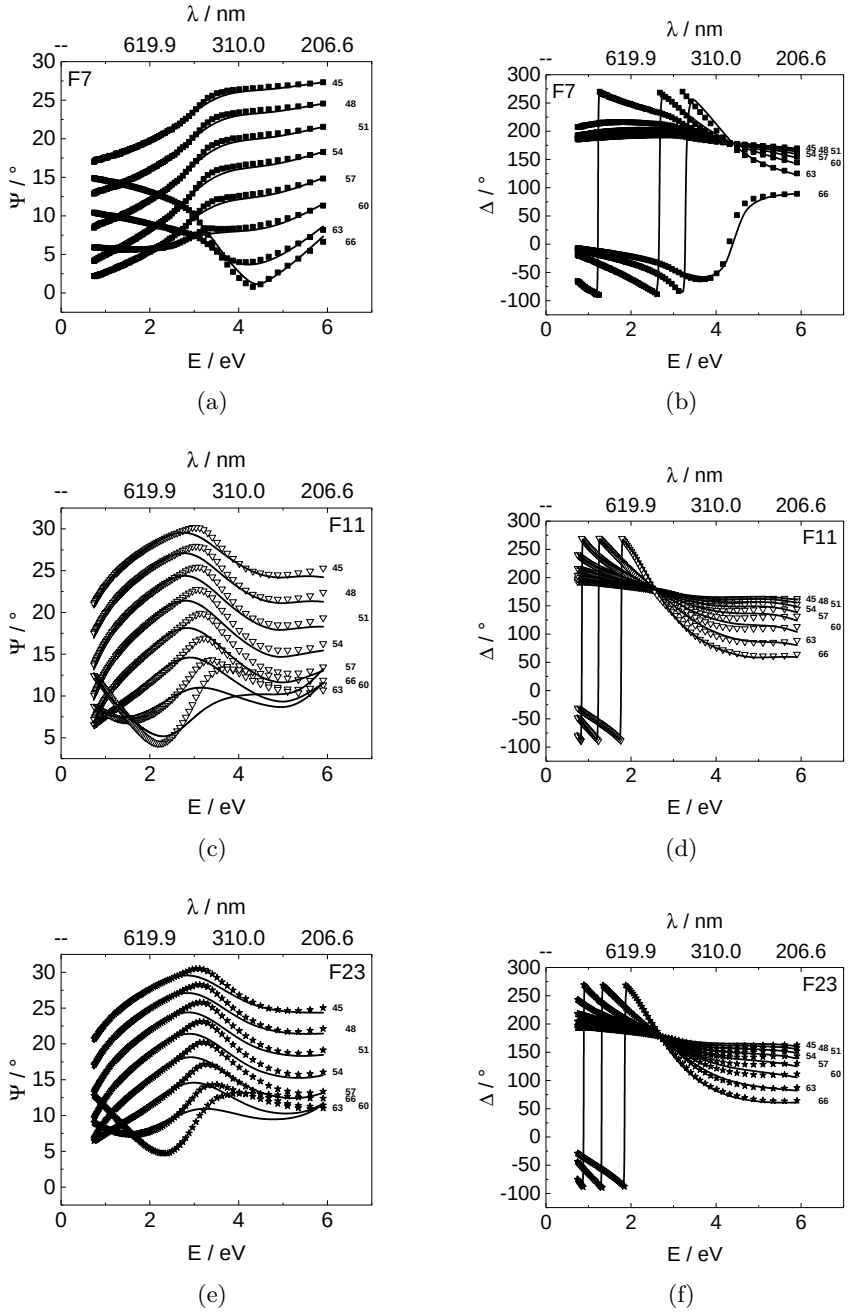

(a) (b) (c) (d) (e) (f)

Figure 6.6: [Caption to this figure is presented on next page.]

Figure 6.6: [Figure corresponding to this caption is presented on the previous page.]
Experimentally obtained (presented as data points) and fitted (presented as curves) energy (E) and wavelength of light (λ) dependences of spectroscopic ellipsometry (SE) parameters (Ψ, Δ), at angle of incident light (α_i) indicated (refer section 4.4.C) for the Si doped $In_2O_3-(ZnO)_3$ (ISZO) films F7, F11, and F23. Each of the films aforementioned is bi-layer (BL). As such, the fitted (Ψ, Δ) curves were obtained via the modeled (n, k) profiles of the two film layers per figure 6.7. The modeled (n, k) profiles so were obtained via fitting of the Kramers Kronig (KK) consistent b-spline dispersion function (at an energy resolution of 0.45 eV) to the BL structure per figure 5.3(d). The E dependence of (Ψ, Δ) was recorded and analyzed in the range $45° \leq \alpha_i \leq 66°$ in steps of 3°. Here, SE Ψ-parameter (Ψ), SE Δ-parameter (Δ), refractive index (n), extinction coefficient (k). (a and b) Film F7, (c and d) film F11, and (e and f) film F23.

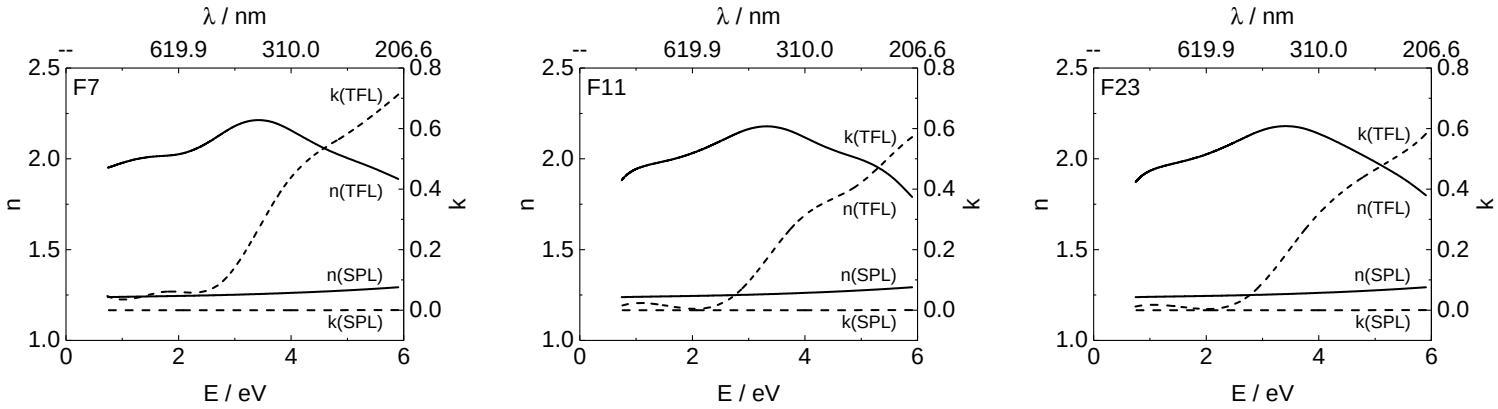

Figure 6.7: The energy (E) dependent refractive index (n) and extinction coefficient (k) of film layers — viz., thin-film layer (TFL) and sub-plantation layer (SPL) — of bi-layer (BL) Si doped In_2O_3−$(ZnO)_3$ (ISZO) films. The modeling was performed on basis of Kramers Kronig (KK) consistent dispersion functions (per table 5.2; refer also figure 6.6). (a) Film F7, (b) film F11, and (c) film F23. Here, wavelength of light (λ).

6.4 Film electronic state I: compensation

6.4.A Introduction

We interrogate the electronic state of our ISZO films on basis of two samples: F11 and F23. Recall that the deposition process conditions for the two aforementioned films differ only in the O content that was provisioned (refer figure 3.3 and table 3.4).

The analysis proceeds from the experimental determination of the T dependence of film electronic properties, viz., μ and n (refer section 4.5.D). We will continue interrogation of the electronic state in section 6.5, also on basis of the two aforementioned films. Further results of room-temperature measurements on the aforementioned two, and of two additional films, viz., F15 and F7, will be considered in section 6.6.

Accordingly, in this section we present experimentally determined T dependence of electronic properties of films F11 and F23 (section 6.4.B). Upon ascertaining its applicability, we analyze the experimentally measured dependences so in terms of the BH model of IIS to obtain quantitative information about the nature of the electronic state of our films (section 6.4.C). Finally, we compare the calculated T dependences of compensation ratio (Γ) of the films F11 and F23 individually, to determine the effect of O incorporation (section 6.4.D).

6.4.B The absolute temperature dependence of conduction electron mobility

Figure 6.8 presents the experimentally determined T dependences of electronic properties, viz., μ, n, and ρ, of the ISZO films F11 and F23.

Notwithstanding the state of the art quality of our ACFHE equipment (refer figure 4.4), the electronic (ρ) and physical (d) properties individually of each

of the seven remaining films of the DE (refer figures 3.3 and 6.13) conspired to present respective (high) R_s values (refer section 4.5.C.2, and definition 6.5a) that precluded T dependent HE measurements[†].

With reference to discussions per section 4.5.D and particularly equation 4.18d, the positive temperature coefficient of mobility (TCM) per figure 6.8(b), foretells the scattering of conduction electrons by ionized impurities. We proceed forth in section 6.4.C on basis of this observation.

6.4.C The Brooks-Herring analysis of ionized impurity scattering

In the previous section, we determined the presence of IIS of conduction electrons within our ISZO films. The determination was on basis of the experimentally determined $\mu(T)$ for films F11 and F23 (per figure 6.8(b)). We now seek, and are able to identify for both aforementioned films, respective T-ranges where IIS is the dominant scattering mechanism (G. Stillman and C. Wolfe, 1976).

With aid of figures 6.9(b) and 6.9(a), it is evident that, over the respective T-ranges shown, $\rho(T) \propto T^{-3/2}$. The $n(T)$ dependences per figure 6.8(a) shows furthermore that for both films, n is constant over the respectively identified T ranges. It follows thereby that $\mu(T) \propto T^{3/2}$ over the respective identified T-ranges (refer relation 4.11e). Thereby, in light of equation 4.18d, over the respective identified T-ranges, IIS is the dominant mechanism of electron scattering in the films F11 and F23.

Having identified T-ranges where IIS is the dominant scattering mechanism, and further to section 4.5.D.1 and particularly to equation 4.20b, we ascertain applicability of the BH model of IIS. For this, we determine the

[†]For two of these seven films, viz., F15 and F7, it proved feasible to measure the HE at room-temperature only (see table 6.5).

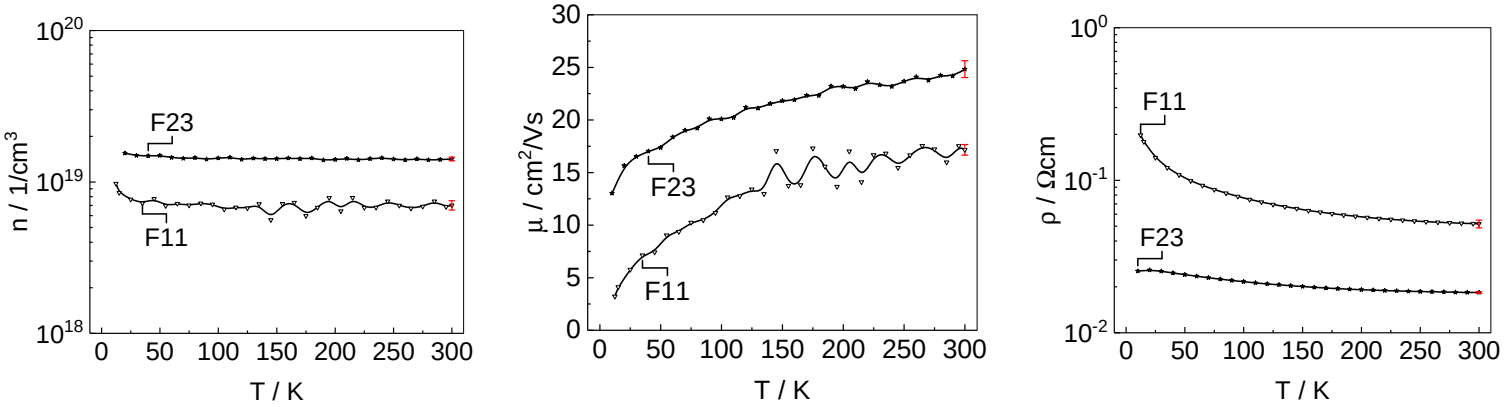

(a) (b) (c)

Figure 6.8: Experimentally measured absolute temperature (T) dependences of electronic properties (viz., conduction electron concentration (n), conduction electron mobility (μ), resistivity (ρ)) of Si doped In_2O_3−$(ZnO)_3$ (ISZO) films F11 and F23. (a) n(T): The films show evidence of non-degeneracy at low temperatures. (b) μ(T): The positive temperature coefficient of mobility (TCM) signals importance of ionized impurity scattering (IIS) for electron conduction (refer equation 4.18d). Furthermore, with reference to experiment design per figure 3.3 and table 3.4, it is evident that increase in oxygen (O) incorporation is accompanied by increase of μ. These observations will be addressed in section 6.4.C. (c) ρ(T): The change in sign of the temperature coefficient of resistivity (TCR) at low temperature in F23 corroborates the Ioffe-Regel analysis per figure 6.12, which revealed this film to be situated close to the metal insulator transition (MIT). Note: The standard error bars in the experimental determinations are indicated.

formal charge on impurity in units of elementary charge (Z) dependence of inverse of screening length (β_s) for the films F11 and F23. The results of the determination at room-temperature (which is within the IIS absolute temperature (T) regime for both films F11 and F23) are presented in table 6.3.

Given the length-scales d_{Si-Si} and d_c (refer table 6.4), table 6.3 reveals Z = 2 as the (lowest) value of Z which recovers, for both F11 and F23, the length-scale $1/\beta_s$ consistent with the BH model of IIS. This Z is a physically reasonable charge state for the impurity (scatterer).

Accordingly, we compute total donor concentration (N_D) and total acceptor concentration (N_A), per the BH model, for films F11 and F23, over the respective T-ranges identified in figures 6.9(a) and 6.9(b). Further to section 4.5.D.1, the computation is on basis of the experimentally determined n(T) and μ(T) per figures 6.8(a) and 6.8(b) respectively.

Appendix B presents the computer program that was developed and used for the computation. The thus computed T dependences, N_D(T) and N_A(T), are presented in figures 6.9(c) and 6.9(d) for F11 and F23 respectively. To recall, in the extrinsic temperature range, n = N_D - N_A (equation 4.20f).

Our estimate of nominal concentration of dopant / Si (N_{Si}) is based on the nominal composition of the target (refer section 4.2.C) wherefrom was sourced the material flux that sourced film deposition. The estimated N_{Si} (assumed independent of T) is presented for reference in both of the figures 6.9(c) and 6.9(d).

Film	Distance				
	$1/\beta_s$ (T = 300 K) / nm		d_{i-i} (T = 300 K) / nm	d_{Si-Si} / nm	d_c (T = 0 K) / nm
			Z (Trial)		
F11	1.8	→	1: 1.2 2: 2.0 3: 2.4 4: 3.1	0.9	0.8 to 1.2
F23	1.3	→	1: 1.1 2: 1.7 3: 2.3 4: 2.7		
Physics	IIS à la Brooks-Herring			NA	MIT à la Mott
T of determination	≲300 K				10.1 K

Table 6.3: Determination of charge on impurity in units of elementary charge (Z) per the Brooks-Herring (BH) model of ionized impurity scattering (IIS). Analysis of (μ(T), n(T)) on basis of the BH model of IIS permits determination of spatial extent of impurities. The analysis proceeds from determination of $1/\beta_s$(Z) for various trial Z values (per equation 4.20b). The BH model assumes that scattering centers / impurities are independent. Accordingly, the condition $d_{i-i} \sim 1/N^{1/3} > 1/\beta_s$ determines a physically reasonable Z (E. Gerlach and Rautenberg, 1978). The table shows that, for both of the films F11 and F23, the aforementioned condition is satisfied for Z = 2 (indicated via respective rightward arrows). This is a physically meaningful impurity charge state (as discussed in the text). Comparison of length-scales $1/\beta_s$ and d_{i-i}, and d_{Si-Si} shows that the impurity may comprise a cluster of two / multiple Si species (in various charge states). This too is a physically plausible outcome given the high nominal dopant / impurity (Si) concentration (refer section 4.2). Finally, with reference to table 6.4, we compare the aforementioned length-scales with the therein estimated d_c(T = 0 K). At low T, neutral impurity scattering determines μ. Here, not applicable (NA), metal insulator transition (MIT), inverse of screening length (β_s), impurity to impurity distance (d_{i-i}), nominal Si to Si distance (d_{Si-Si}), ionized impurity concentration (N), distance between impurity centers at the composition induced MIT (d_c), absolute temperature (T), conduction electron mobility (μ), conduction electron concentration (n), silicon (Si).

6.4.D The compensation ratio

6.4.D.1 The absolute temperature dependence

Consider the T dependence of Γ for films F11 and F23, presented in figures 6.9(e) and 6.9(f) respectively.

First, one observes that, the electronic state of both films F11 and F23 is (highly) compensated.

A second observation is in order on basis of comparison between the computed $\Gamma(T)$ and the experimentally measured $\mu(T)$ of the films. For film F11, one observes (refer figures 6.9(e)) and 6.9(a)) a simultaneous depression in the T dependences of the two aforementioned quantities. On the other hand, for film F23 one observes that $\Gamma(T)$ (per figure 6.9(f)) and $\mu(T)$ (per figure 6.9(b)) are opposite of each other. Since Γ is but a measure of the concentration of ionized impurities, the aforementioned T dependences are physically reasonable (refer section 4.5.D).

6.4.D.2 The oxygen content dependence

We compare the O dependence of Γ for films F11 and F23, as presented respectively in figures 6.9(e) and 6.9(f). One observe that the $\Gamma(\text{F11}) > \Gamma(\text{F23})$ over the common T-range, viz., $252\,\text{K} \lesssim T \lesssim 300\,\text{K}$.

We consider this observation on basis of the sub-gap density of states (DOS) of the amorphous doped In−Zn−O material systems, as presented in figure 6.10 (Ide et al., 2019; Nomura, Kamiya, Yanagi, et al., 2008; Kamiya, Nomura, and Hideo Hosono, 2010b; Kamiya, Nomura, and Hideo Hosono, 2010a). Specifically, we refer to the band of deep sub-gap surface states having width $\sim 1.5\,\text{eV}$ situated in the band-gap close to the energy of maximum of valence band (E_v).

The concentration of sub-gap states (Körner, Urban, and Elsässer, 2013) as

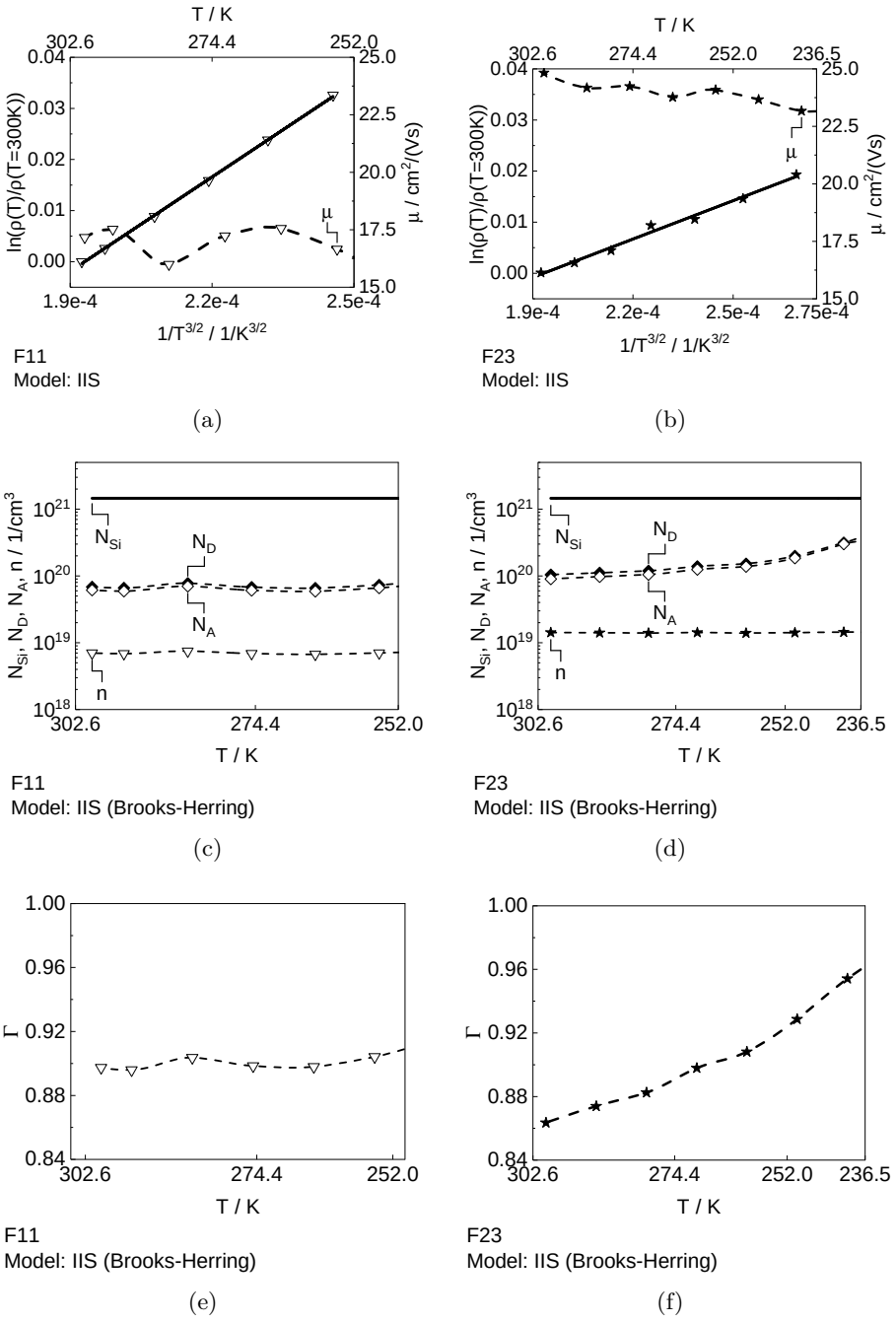

Figure 6.9: [Caption to this figure is presented on next page.]

Figure 6.9: [Figure corresponding to this caption is presented on the previous page.]
Estimation of absolute temperature (T) dependences of total donor concentration (N_D), total acceptor concentration (N_A), and compensation ratio (Γ) for Si doped $In_2O_3-(ZnO)_3$ (ISZO) films, on basis of Brooks-Herring (BH) model of ionized impurity scattering (IIS). The dashed lines are a guide for the eye. For films F11 and F23 respectively: (a and b) The experimentally determined T dependence of conduction electron mobility (μ). In light of equation 4.18d, the positive temperature coefficient of mobility (TCM) signals importance of ionized impurity scattering (IIS) for electron transport. The solid lines are (respective) best-fits to equation 4.18d. Thereby, it is evident that IIS is the dominant electron scattering mechanism over the respective T ranges considered. (c and d) The experimentally determined T dependences of conduction electron concentration (n). Also shown are the calculated — on basis of BH model of IIS; per equations 4.20 — T dependences of N_D and N_A. The calculation was on basis of respective experimentally determined μ(T) and n(T). The nominal concentration of dopant / Si (N_{Si}) (assumed to be temperature independent) is also shown for reference. The same was calculated on basis of the nominal composition of the target employed for sputtering (refer section 4.2). (e and f) The computed Γ(T) (per equation 4.20g).

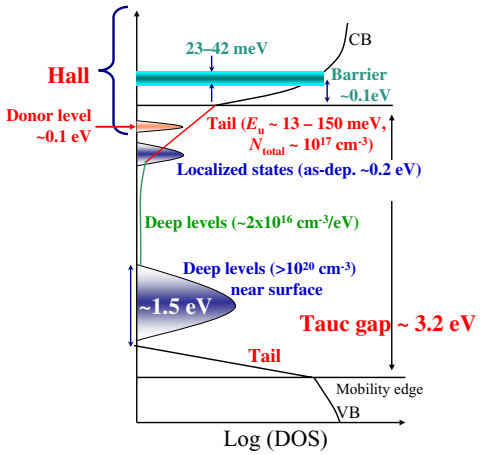

Figure 6.10: The sub-gap density of states (DOS) of the amorphous doped In−Zn−O material systems. The "Tauc gap" is $E_{g,\,Tauc}$ per equation 6.6. Figure adapted from Kamiya, Nomura, and Hideo Hosono, 2010a. Here, conduction band (CB), valence band (VB).

come to inhere in a film (TFL) is a function of TFL density (D_{TFL}), and of oxygen deficiencies. Process control over D_{TFL} may be exercised via TFL deposition-rate (ν_{TFL}), whereas process control over oxygen deficiencies (in the TFL) may be exercised via the process factor O (Kim et al., 2017).

With reference to table 5.1, and to figures 6.21(d) (bottom-right location of which corresponds to F11) and 6.21(f) (bottom-right location of which corresponds to F23), D_{TFL} and ν_{TFL} for both of the films F11 and F23 is the same. Furthermore, the D_{TFL} of both films is close to the density of single-crystalline In_2O_3−$(ZnO)_3$ (refer section 4.3.C).

Also, with reference to experiment design per figure 3.3, the respective deposition process factors set of films F11 and F23 are identical save for the process factor O, which was maintained at levels − and + respectively.

To first order therefore, the process factor O controls the observed excursion of electronic properties of film F11 to those of film F23 (figures 6.8 and 6.9).

One estimates the Tauc gap energy ($E_{g,\,Tauc}$) via a Tauc plot, given the

experimentally determined Tr(E) per figure 5.6 (M.-C. Jun, Park, and Koh, 2012), and the relations:

$$\alpha(E) = \frac{1}{d} \ln \frac{1}{Tr(E)} \tag{6.6a}$$

whereas, for an amorphous semiconductor (Hays et al., 2017),

$$(\alpha E)^2 \propto \left(E - E_{g,\,Tauc}\right) \tag{6.6b}$$

where, absorption coefficient (α), thickness (as applicable) of film or of film layer (d), energy (E), Tauc gap energy ($E_{g,\,Tauc}$).

Thereby, further to equations 6.6, the $E_{g,\,Tauc}$ for films F11 and F23 is determined via the Tauc plots presented in figure 6.11, on basis of onset of absorption rise (signaled by the uptick in α).

Thereby, with reference to figure 6.11 and to table 6.2, it is determined that $E_{g,\,Tauc} > E_g$. This determination is a signature of the band of deep sub-gap surface states per figure 6.10. These sub-gap surface states are electron traps, and among the acceptors referred to in section 6.4.C.

The experimentally observed enhancement of μ in film F23 with respect to film F11 is thus consequent the passivation of such surface states via oxygen incorporation. Consistently, one also observes a slight enhancement of E_g (refer table 6.2).

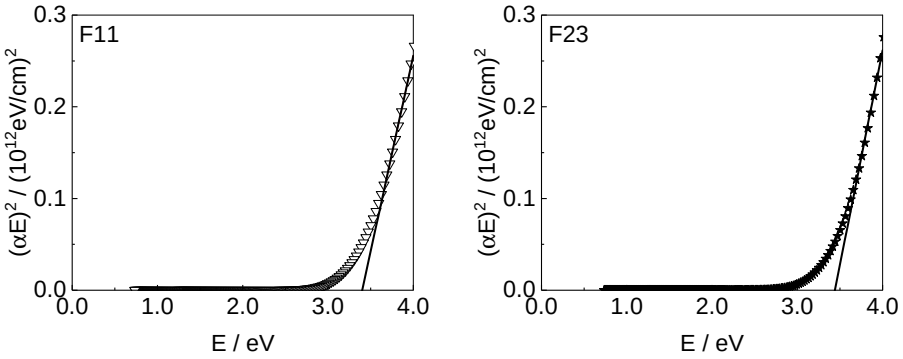

(a) (b)

Figure 6.11: With reference to equation 6.6, to film thicknesses per table 5.1, and to the experimentally determined Tr(E) per figures 5.6(b) and 5.6(c) respectively, one estimates $E_{g,\,Tauc} \simeq 3.4\,eV$ for films (a) F11, and (b) F23. Here, Tauc gap energy ($E_{g,\,Tauc}$), transmission fraction (Tr), energy (E), absorption coefficient (α).

6.5 Film electronic state II: oxygen induced progress towards a metal

6.5.A Introduction

We continue the discussions from section 6.4 re films F11 and F23. With reference to figure 3.3 and table 3.4, the deposition process conditions for the two aforementioned films differ only in the O content that was provisioned. Thus, while film F23 was deposited in oxygen rich conditions (O = +), it is not (expressly) provisioned to the process gas during deposition of film F11 (O = -).

We analyze the electronic state of our ISZO material composition films on basis of the Ioffe-Regel and the Mott theories of the MIT (section 6.5.B).

6.5.B Ioffe-Regel and Mott analyses

The results presented in table 6.2 were obtained at room-temperature. Extending the electrical (HE) measurements down to cryogenic temperatures (refer figures 6.8) permits further interrogation of the electronic state of our ISZO films.

On basis of an Ioffe-Regel criterion analysis (Ioffe and Regel, 1960), and with reference to experiment design per figure 3.3 and table 3.4, we demonstrate progress of said electronic state towards a metal state, as a function of increasing O content. Furthermore, proceeding an analysis of film F23 via the Mott theory of the MIT, we estimate distance between impurity centers at the composition induced MIT (d_c).

Ioffe and Regel, 1960 consider two length-scales: the electron mean free length (l_e), and the wavelength of a free electron at Fermi energy (E_F), viz., $1/k_F$, where magnitude of Fermi wave-vector (k_F), and present thereby expression 6.7a.

They posit that systems in which delocalized wavefunctions (that is, free electrons) exist can but be set up such that the wavelength of the delocalized wavefunction (viz., $1/k_F$) and the free electron mean free path (l_e) are comparable. Thereby, relation 6.7b situates the MIT boundary for a given material system.

$$k_F l_e = \frac{\hbar(3\pi^2)^{2/3}}{e^2} \times \frac{1}{\rho n^{1/3}} \tag{6.7a}$$

whereas,

$$k_F l_e = 1 \qquad \text{... at MIT} \tag{6.7b}$$

Here, reduced Planck constant ($\hbar$), mathematical constant (π), elementary charge (e), resistivity (ρ), conduction electron concentration (n).

Figure 6.12 presents the T dependence of Ioffe-Regel parameter ($k_F l_e$) for films F11 and F23. One notes that, through not yet a metal, compared to film F11, film F23 is situated closer to the MIT boundary.

Recall (refer figure 3.3) that the only difference in the deposition conditions for films F23 and F11 is the O provisioned during their respective depositions, such that O = + for F23 and O = - for F11. Accordingly, it is evident that O incorporation results in progress of the electronic state of our amorphous ISZO films towards a metal state.

Furthermore, according the Mott analysis of the MIT, a metal state manifests at a $\sigma(T = 0\,K) \equiv \sigma_{min}$ (Mott, 1990), such that:

$$\sigma_{min} = \frac{0.026e^2}{\hbar} \times \frac{1}{d_c} \tag{6.8}$$

where, conductivity (σ), elementary charge (e), reduced Planck constant ($\hbar$), distance between impurity centers at the composition induced MIT (d_c).

For purposes of estimation, and under the following two assumptions re film F23:

- that it is situated at the MIT; and
- that its experimentally determined $\sigma(T = 10.1\,K)$ estimates its $\sigma(T = 0\,K)$;

it is possible to estimate d_c via equation 6.8.

Accordingly, table 6.4 presents the estimation of the d_c on basis of low temperature ρ measurements (refer figure 6.8(c)).

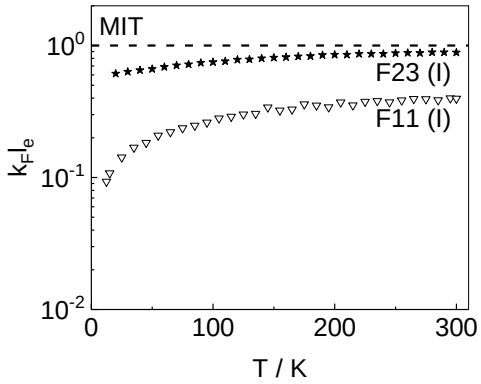

Figure 6.12: The absolute temperature (T) dependences of Ioffe-Regel parameter ($k_F l_e$) for films F11 and F23. The metal insulator transition (MIT) is situated at $k_F l_e = 1$ (refer equation 6.7a). Referring to experiment design per figure 3.3 and table 3.4, it is seen that the process factors set for the two aforementioned films differ only in the amount of oxygen percent (O) presented during film deposition (whereby, O(F23) = 0 % while O(F11) = 20 %). Plausibly therefore, increasing oxygen content results in progress of the electronic state of the Si doped $In_2O_3{-}(ZnO)_3$ (ISZO) film towards a metal.

6.6 Response surface analysis

6.6.A Introduction

We present a RSA of the experimentally measured room-temperature electronic and physical properties of the film (TFL). The RSA results of a given property comprise two (inter-related) types: the pareto plots, and the response surfaces.

The pareto plots make convenient the comparison of magnitude, and of sign, of main and interaction (two-factor or three-factor) effects, of and among the process factors that are at issue. The response surface make convenient the quantitative representation of the property of interest over the process factors space spanned by the DE.

The process factors at issue are RF power (P_{RF}), process gas pressure (p), and O. The process factors space is per figure 3.3 and table 3.4. Properties

F23				ISZO
Experimentally measured		Estimates, MIT à la Mott		Nominal
T	ρ (T)	σ_{min}	d_c	d_{Si-Si}
/ K	/ Ω cm	/ 1/(Ω cm)	/ nm	/ nm
10.1	2.54×10^{-2}	3.94×10^{1}	0.8 to 1.2	0.9

Table 6.4: In light of figure 6.12, assuming that film F23 is situated at the metal insulator transition (MIT), we estimate distance between impurity centers at the composition induced MIT (d_c) according to the Mott theory (refer equation 6.8). The estimation is on basis of the experimental determination of resistivity (ρ) at the lowest experimentally available temperature T = 10.1 K (refer figure 6.8(c)). The estimated d_c may be compared with the nominal Si to Si distance (d_{Si-Si}) (for the ISZO composition at issue; refer section 4.2). Here, Mott minimum metallic conductivity (σ_{min}).

(electronic and physical) of interest are per table 3.1. As discussed in section 5.5.C.2, quantitative comparisons — within and among response surfaces of individual properties of interest — enable simultaneous optimization of multiple film properties (Del Castillo, 1996; Derringer and Suich, 1980).

We present the RSA of film electronic properties (section 6.6.B). This is followed by the RSA of TFL physical properties (section 6.6.C).

6.6.B Film electronic properties

It proved feasible to conduct measurements of electronic properties (via HE measurements) on only the four ISZO films per figure 6.13.

The results so of room-temperature HE measurements are presented in table 6.5. Given the paucity of electronic property results (on but 4 of the 9 films comprising the DE), a rigorous RSA of said properties is not feasible. Nonetheless, we proceeded an RSA on basis of the (limited) electronic property results per table 6.5, for the following two reasons. Accordingly, the RSA results may be expected to be indicative.

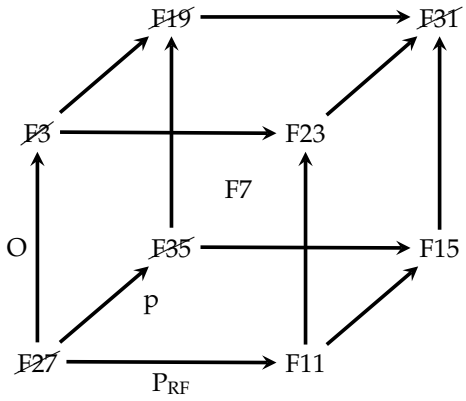

Figure 6.13: Locations, within experiment design per figure 3.3, of those Si doped In_2O_3−$(ZnO)_3$ (ISZO) films that presented electronic properties feasible for measurement. It proved feasible to conduct electrical(Hall Effect (HE)) measurements on only four of the nine films. The names of films on which electrical measurements could not be performed thus are shown struck out. For reference in context of table 6.5.

First, for two of the three process factors — viz., p and O — the full DE range, viz., − to + (refer figure 3.3 and table 3.4), is spanned by the available electronic property measurements. Second, given that each of the films at issue are amorphous (refer figure 6.1) one does not expect a(ny) discontinuity — as a function of film (TFL) microstructure and composition — in room-temperature electronic properties.

Thus, and as indicated, the following caveat may be borne in mind: that the RSA results for film (TFL) electronic properties (as follow) are indicative only. This caveat is the more pertinent within the 'DE volume' in which HE data is not available (refer figure 6.13).

Figure 6.14 presents the β-coefficient obtained upon linear modeling (refer section 3.2.D) of film (TFL) electronic properties, via respective pareto plots.

We next consider the contour plots of electronic properties of interest. Given the role of O in determining the electronic state of ISZO films (refer section 6.5), the scheme for contour plots of electronic properties is as presented in

Film	Factor (CU)			n	μ	ρ	R_s	R_H
	P_{RF}	p	O	/ $1/cm^3$	/ $cm^2/(V\,s)$	/ $\Omega\,cm$	/ $\Omega/\square$	/ cm^3/C
F15	+	+	–	$1.415(7)\times10^{16}$	8.98(5)	$4.91(1)\times10^{1}$	$5.06(2)\times10^{7}$	$4.41(4)\times10^{2}$
F7	0	0	0	6.8×10^{17}	1.39×10^{1}	6.6×10^{-1}	4.0×10^{5}	9.2
F11	+	–	–	$6.7(5)\times10^{18}$	$1.75(5)\times10^{1}$	$5.4(3)\times10^{-2}$	$8.0(4)\times10^{3}$	$9.4(7)\times10^{-1}$
F23	+	–	+	$1.40(4)\times10^{19}$	$2.46(8)\times10^{1}$	$1.82(2)\times10^{-2}$	$2.85(2)\times10^{3}$	$4.4(2)\times10^{-1}$

Table 6.5: Experimentally measured room-temperature electronic properties of Si doped $In_2O_3{-}(ZnO)_3$ (ISZO) films. With reference to figure 6.13, results of Hall Effect (HE) measurements on those Si doped $In_2O_3{-}(ZnO)_3$ (ISZO) films that presented electronic properties feasible for measurement given the AC Field Hall Effect (ACFHE) equipment used. The HE was measured under DC and / or AC magnetic field as feasible. The standard errors in the measured electronic properties are as indicated. The respective process factors set of deposition is also indicated (per figure 3.3 and table 3.4). Electronic properties (conduction electron mobility (μ) and conduction electron concentration (n)) have been referenced elsewhere in this thesis as well (figure 6.8 and table 6.2). Here, coded unit (CU), resistivity (ρ), sheet resistance (R_s), Hall coefficient (R_H), RF power (P_{RF}), process gas pressure (p), oxygen percent (O).

figure 6.15.

Further to the contour plotting scheme presented in figure 6.15, and the linear model corresponding the pareto plot presented in figure 6.14(a), the contour plots for room-temperature n of the film (TFL) are presented in figure 6.16.

Further to the contour plotting scheme presented in figure 6.15, and the linear model corresponding the pareto plot presented in figure 6.14(b), the contour plots for room-temperature μ of the film (TFL) are presented in figure 6.17.

Further to the contour plotting scheme presented in figure 6.15, and the linear model corresponding the pareto plot presented in figure 6.14(c), the contour plots for room-temperature ρ of the film (TFL) are presented in figure 6.18.

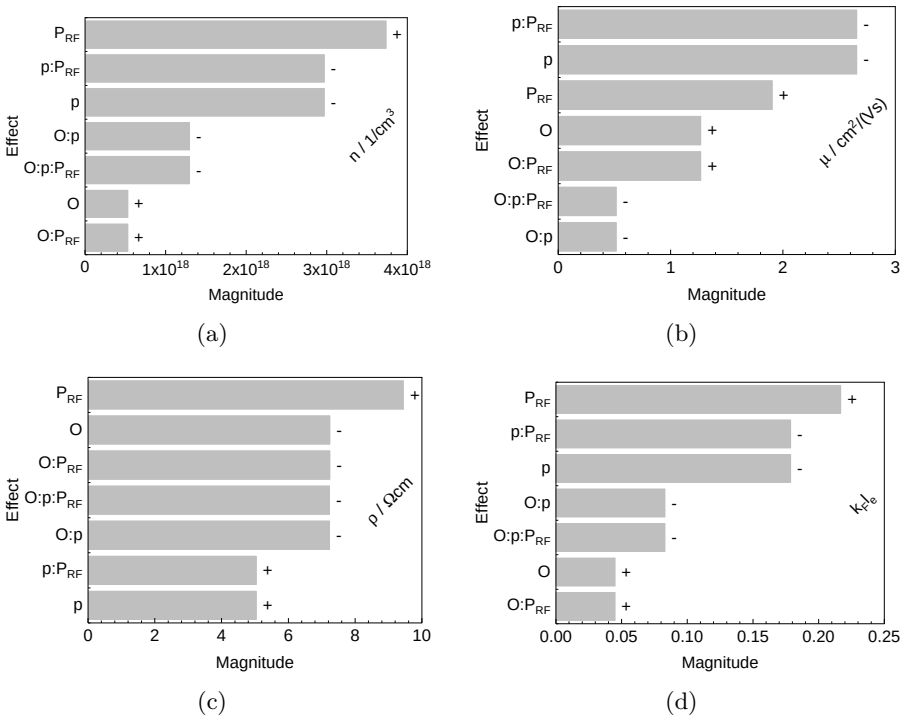

Figure 6.14: The pareto plots of linear models (per equation 3.1 and table 6.5) for room-temperature electronic properties of Si doped In_2O_3−$(ZnO)_3$ (ISZO) films. The discussion of a pareto plot as presented in figure 5.10 applies. Caveat: in light of the paucity (refer figure 6.13) of experimental electronic properties data and related discussions (section 6.6.B), the linear model, and effects (main and / or interaction) determined thereby, may be considered indicative only. (a) conduction electron concentration ($\mathbf{n}$) (refer also figure 6.16), (b) conduction electron mobility (μ) (refer also figure 6.17), (c) resistivity (ρ) (refer also figure 6.18), (d) Ioffe-Regel parameter ($\mathbf{k_F l_e}$) (refer also figure 6.19).

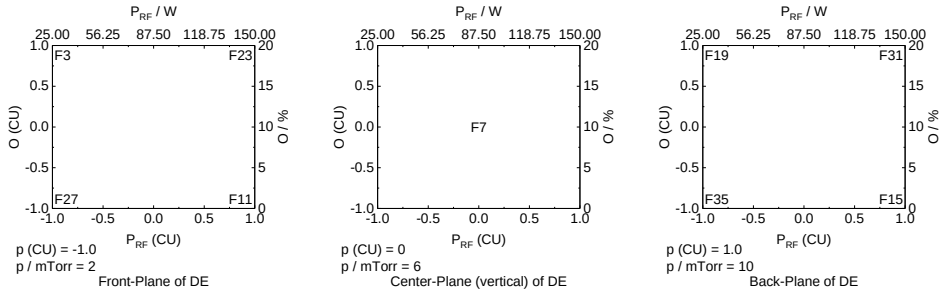

(a) (b) (c)

Figure 6.15: Scheme for contour plots of electronic properties of Si doped In_2O_3−$(ZnO)_3$ (ISZO) films presenting detailed layout of (a) front-plane, (b) center-plane (vertical), and (c) back-plane of the experiment design. The same is for reference in context of contour plots — per figures 6.16 (for conduction electron concentration (n)), 6.17 (for conduction electron mobility (μ)), 6.18 (for resistivity (ρ)), and 6.19 (for Ioffe-Regel parameter ($k_F l_e$)) — of electronic properties of ISZO films. Refer also the 'full' experiment design per figure 3.3 and table 3.4. Here, coded unit (CU), RF power (P_{RF}), process gas pressure (p), oxygen percent (O).

Further to the contour plotting scheme presented in figure 6.15, and the linear model corresponding the pareto plot presented in figure 6.14(d), the contour plots for room-temperature $k_F l_e$ of the film (TFL) are presented in figure 6.19.

6.6.C Thin-Film layer physical properties

Figure 6.20 presents the β-coefficients obtained upon linear modeling (refer section 3.2.D) of film (TFL) physical properties of interest, as respective pareto plots. One observes that each of the three process factors that are at issue — viz., P_{RF}, p, O — are significant for the film (TFL) physical properties in question.

The contour plots constituting the response surface of film (TFL) physical properties of interest will be presented according to the scheme shown in figures 6.21(a) through 6.21(c). This scheme is identical to the one for SPL physical properties per figures 5.11(a) through 5.11(c). Thereby, contour

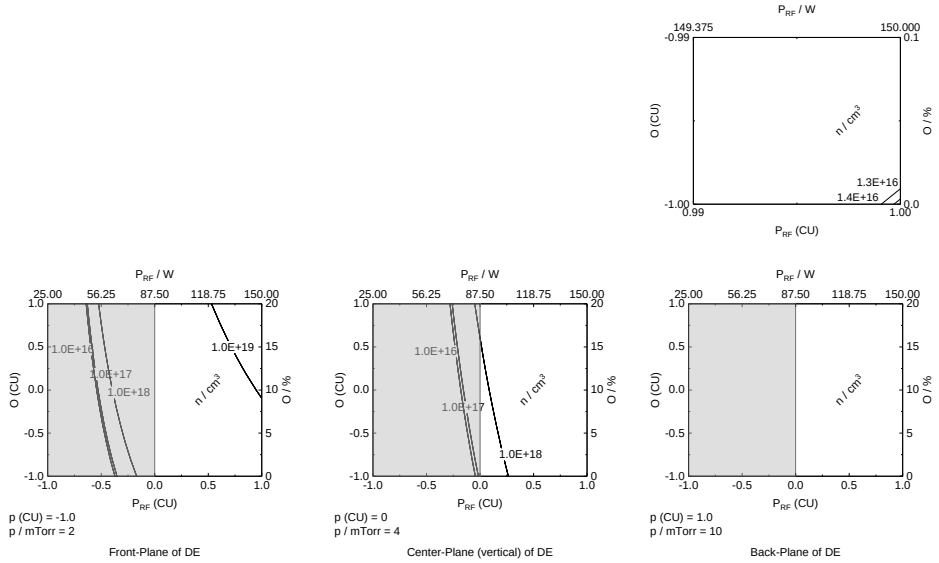

(a) (b) (c)

Figure 6.16: With reference to figure 6.15, the contour plots of linear model as per figure 6.14(a) for room-temperature conduction electron concentration (n) of Si doped In_2O_3−$(ZnO)_3$ (ISZO) films, at (a) front-plane, (b) center-plane (vertical), and (c) at back-plane, of the designed experiment (DE). The caveat noted in figure 6.14 applies. The shaded area indicates (partially) the region of the DE where experimental data is unavailable. Accordingly, the contours, particularly in the shaded area, are indicative only. Here, coded unit (CU), RF power (P_{RF}), process gas pressure (p), oxygen percent (O).

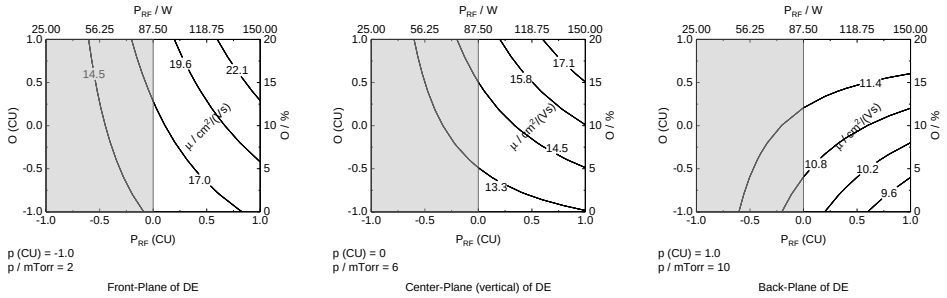

(a) (b) (c)

Figure 6.17: With reference to figure 6.15, the contour plots of linear model as per figure 6.14(b) for room-temperature conduction electron mobility (μ) of Si doped In_2O_3−$(ZnO)_3$ (ISZO) films, at (a) front-plane, (b) center-plane (vertical), and (c) at back-plane, of designed experiment (DE). The caveat noted in figure 6.14 applies. The shaded area indicates (partially) the region of the DE where experimental data is unavailable. Accordingly, the contours, particularly in the shaded area, are indicative only. Here, coded unit (CU), RF power (P_{RF}), process gas pressure (p), oxygen percent (O).

plots sets as plotted, for individual physical properties of the TFL and of the SPL, are readily comparable.

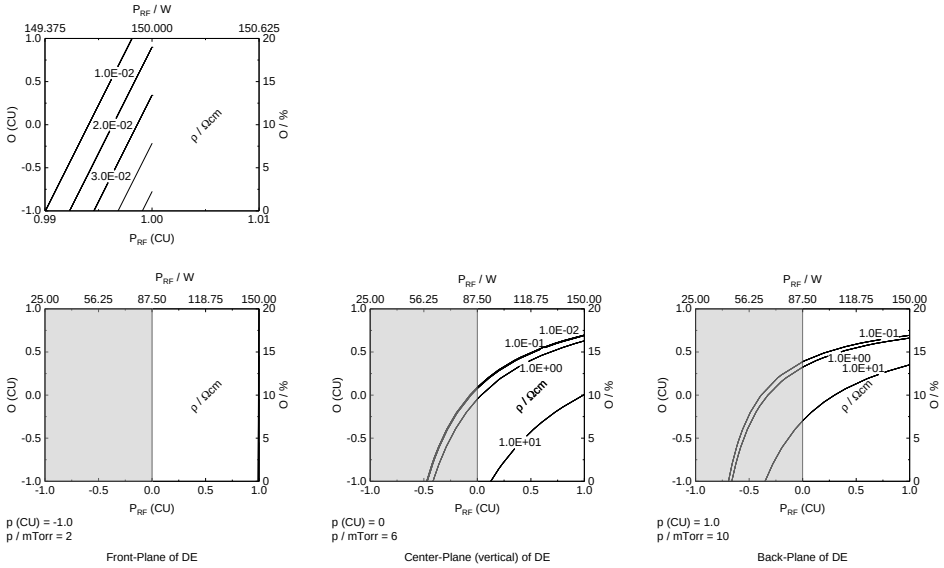

(a) (b) (c)

Figure 6.18: With reference to figure 6.15, the contour plots of linear model as per figure 6.14(c) for room-temperature resistivity (ρ) of Si doped In_2O_3−$(ZnO)_3$ (ISZO) films, at (a) front-plane, (b) center-plane (vertical), and (c) at back-plane, of designed experiment (DE). The caveat noted in figure 6.14 applies. The shaded area indicates (partially) the region of the DE where experimental data is unavailable. Accordingly, the contours, particularly in the shaded area, are indicative only. Here, coded unit (CU), RF power (P_{RF}), process gas pressure (p), oxygen percent (O).

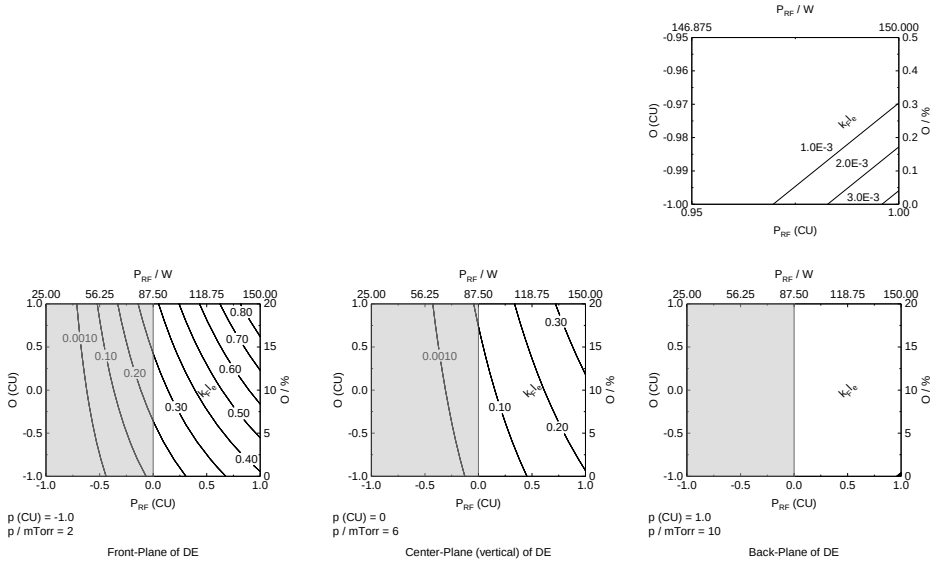

(a) (b) (c)

Figure 6.19: With reference to figure 6.15, the contour plots of linear model as per figure 6.14(d) for room-temperature Ioffe-Regel parameter ($k_F l_e$) of Si doped In_2O_3−$(ZnO)_3$ (ISZO) films, at (a) front-plane, (b) center-plane (vertical), and (c) at back-plane, of designed experiment (DE). The caveat noted in figure 6.14 applies. The shaded area indicates (partially) the region of the DE where experimental data is unavailable. Accordingly, the contours, particularly in the shaded area, are indicative only. Here, coded unit (CU), RF power (P_{RF}), process gas pressure (p), oxygen percent (O).

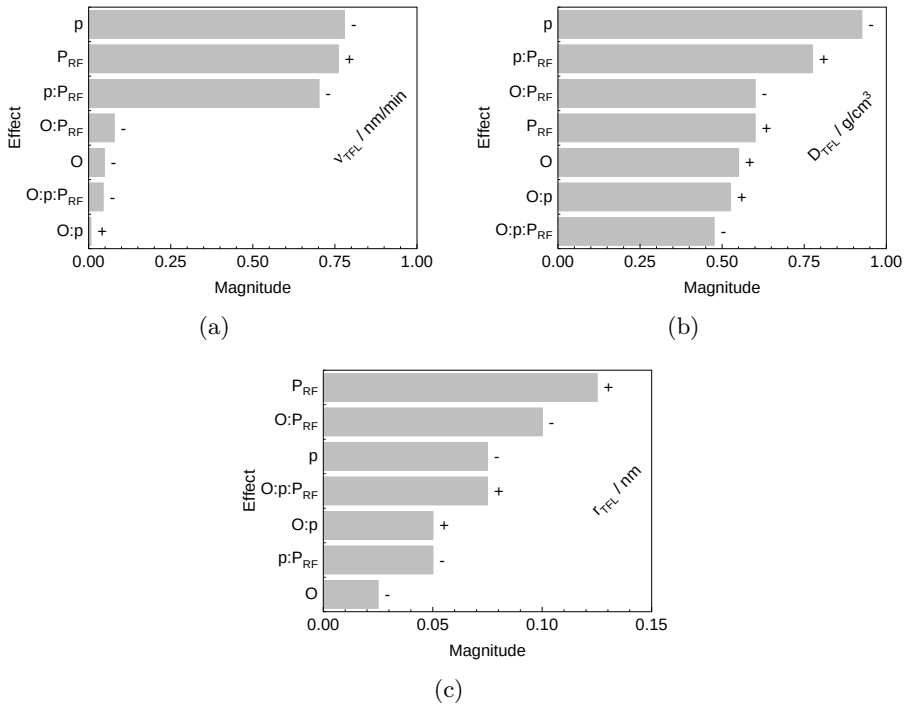

Figure 6.20: The pareto plots of linear models (respective) for room-temperature physical properties of thin-film layer (TFL) of Si doped In_2O_3−$(ZnO)_3$ (ISZO) films. Results of linear modeling (per equation 3.1 and table 5.1) of physical properties of interest of the TFL. Each bar-plot presents the seven β-coefficients corresponding to the main effects (three; terms 3.1b of equation 3.1), two-factor interaction effect (three; terms 3.1c of equation 3.1), and three-factor interaction effect (one; term 3.1d of equation 3.1). The coefficients are presented in descending order of magnitude, with their sign (-, or +) indicated next to the respective bar. Thereby, each bar-plot enables ready comparison of relative magnitude and direction (sign) of the main effects due, and of the interaction effects among, the three experimentally controlled factors, viz., RF power (P_{RF}), process gas pressure (p), and oxygen percent (O). Each of the seven bars in each of the pareto plots bear the label of the effect (individual β-coefficient) which they represent, as follows; main effects: O, p, and P_{RF}; two-factor interaction effects: p:P_{RF}, O:p, and O:P_{RF}; three-factor interaction effect: O:p:P_{RF}. (a) TFL deposition-rate (ν_{TFL}), (b) TFL density (D_{TFL}), and (c) TFL roughness (r_{TFL}). Evidently, for ν_{TFL}, p and P_{RF} are the two principal process factors. Similarly, for D_{TFL} and TFL roughness (r_{TFL}) all three process factors are important.

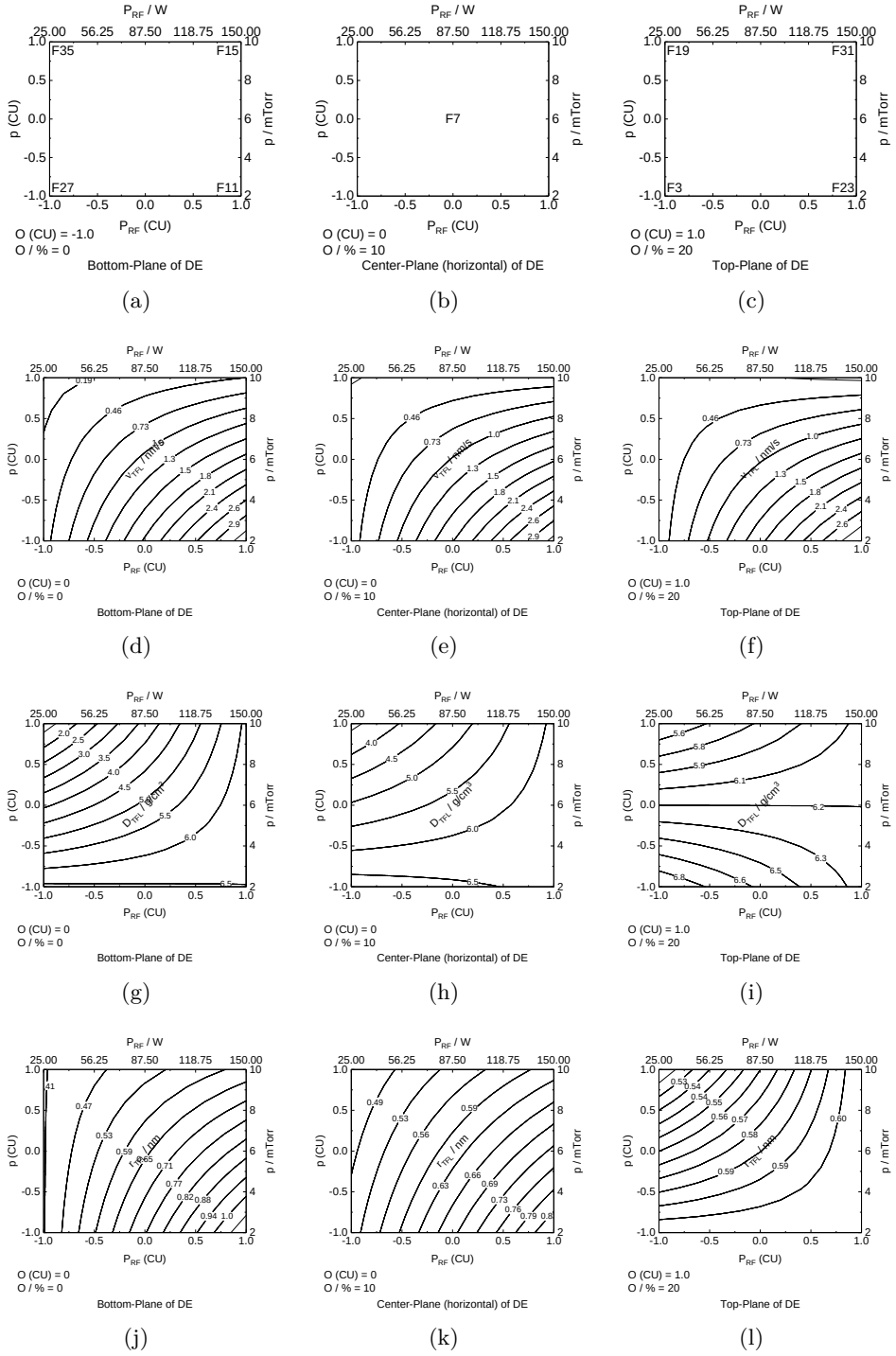

Figure 6.21: [Caption to this figure is presented on next page.]

Figure 6.21: [Figure corresponding to this caption is presented on the previous page.]
With reference to the experiment design per figure 3.3 and table 3.4, thin-film layer (TFL) response surfaces corresponding to the factors set (P_{RF}, p, O) indicated. The response surfaces are presented as contour plots at the bottom-plane, center-plane (horizontal), and top-plane of the experiment design. A simultaneous reading of the response surfaces of each property of interest may be used to determine the deposition process factors set needed to obtain a film (TFL) that manifests a requested set of physical properties. The ranges over which may be varied the individual process factor is determined by the film deposition equipment (Kurt J. Lesker Company (KJLC) model PVD 75, for the present study). (a to c) Respectively the bottom-plane, center-plane (horizontal), and top-plane of experiment design. (d to f) TFL deposition-rate (ν_{TFL}) contours, (g to i) TFL density (D_{TFL}) contours, (j to l) TFL roughness (r_{TFL}) contours. Here, oxygen percent (O), process gas pressure (p), RF power (P_{RF}).

Chapter 7

Conclusions and scope for future work

7.1 Introduction

In this chapter, we summarize the results presented in the preceding chapters. We also consider likely themes for future work on basis of this study. We begin by presenting a ten-thousand-foot-view walk through our results, via a 'ready-reckoner' that highlights the inter-relationships between the contributing experimentation and analysis (section 7.2). We then recapitulate the commercial potential of the results (section 7.3). Thereafter, we signpost potentially fruitful scientific / technological application areas for our results (section 7.4).

7.2 A ready-reckoner

We consider again the various technical aspects of this study, as presented in chapters 3 through 6, to highlight their inter-relationships. Accordingly, figure 7.1 presents a ready-reckoner for this study.

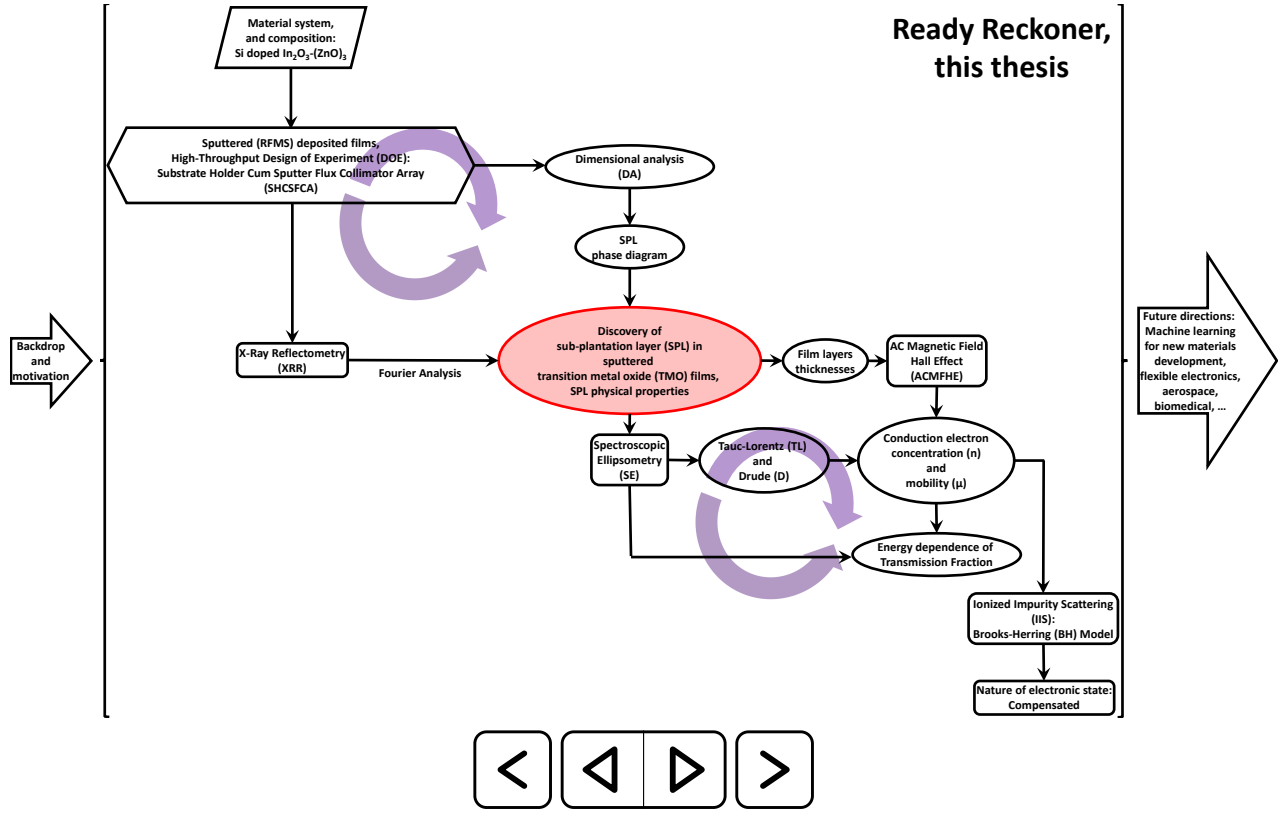

Figure 7.1: [This is an animated figure. The animation sequence may be viewed via Adobe Acrobat software. The control-buttons provided will thence permit manual navigation of the sequence. Caption to this figure is presented on next page.]

Figure 7.1: [Figure corresponding to this caption is presented on the previous page.]
A ready-reckoner (ten-thousand-foot-view walk through starting at the top-left) of this thesis. The individual boxes (various shapes) list an aspect each of this study. The same have been presented in chapters 3 through 6. The straight-line arrows indicate flow (inter-relationships) among such aspects. Two 'wings' (yellow coloured), each anchored on the 'central box' (red coloured) are presented. Each wing, in turn, has two independent arcs of investigation (purple coloured). In the left-wing, the arcs converge-on the central box. In the right-wing, the arcs emerge-from the central box. The central box presents a principal result of this thesis. In the electronic version of this thesis, the sequence in which the arcs appear (upon playing the animation) corresponds to the logical sequence of the investigations. We note however that the logical sequence so, and the chronological sequence of investigations, overlapped but on occasion. That is, the logical sequence is presented with benefit of hindsight. Refer also figure 5.5 and the extended abstract.

Note: The trapezoidal box at top-left houses the material composition arrived upon for investigation (refer chapter 3), the hexagonal box houses film deposition related considerations (refer chapters 3 and 4), the rectangular boxes house characterization modalities (refer chapter 4), and results are housed in elliptical boxes (refer chapters 5 and 6).

7.3 Epilogue

This thesis presents a study of amorphous semiconducting transition metal oxide (TMO) films deposited via the industrially important technique of sputtering. The study has advanced the state of the art re the following film loci:

1. The film-substrate interface. An account of the results obtained was presented in chapter 5.

2. The film electronic state and opto-electronic properties. An account of the results obtained was presented in chapter 6.

The investigations were on basis of new hardware designed and developed expressly for this study, and from scratch.

3. The hardware that enables high-throughput conduct of designed experiments (DEs). An account of the hardware development so was presented in chapter 3.

   The hardware design required dovetailing of multifarious considerations. The considerations emerged from the experimentation framework, from the film deposition technique of choice, and from the requirements of the various characterization techniques.

In the following discussions, we attempt to surface the wide applicability — individually, and more so in combination — of the three results as above. We do so by considering exemplary research themes that may be undertaken on their basis.

7.4 Scope for future work

7.4.A Introduction

We begin by considering the naturally programmatic nature of studies (e.g., this study) that employ the design of experiment (DOE) framework (section 7.4.B). This is followed by a discussion of research themes serviceable on basis on this study (section 7.4.C).

7.4.B Future work: programme development

Endowing a programmatic flow to the addressal of science and technology (S&T) questions can aid the efficient utilization of resources (time and equipment). Experimentation undertaken according to a DOE framework enforces upfront consideration of the following:

- Sample fabrication technique, and factors of (potential or definite) interest.
- Appropriate experiment design; in light of previous.
- Identification and recruitment of characterization modalities; in light of the preceding.
- Consideration of the throughputs, of sample fabrication, and of characterizing measurements and analysis; in light of preceding.
- Sequencing of sample fabrication according the chosen DE, of characterizations as recruited, and of response surface analysis (RSA); in light of preceding.

Detailed consideration of the aforementioned aspects at the onset of a study will confer, naturally, a programmatic flow to the research and development (R&D) efforts.

7.4.C Future work: potential research themes

Table 7.1 presents an overview of selected R&D themes that may be pursued, on basis of this study. In the following, we develop the individual R&D themes as presented.

7.4.C.1 Nature of amorphous state

The nature of the amorphous state, particularly in TMO / transparent conducting oxide (TCO) films, may be addressed on basis of the techniques developed in this study.

Unlike crystallinity, amorphousness does not refer to a unique (if only as an ideal) state (Adler, Schwartz, and Steele, 1985). Indeed, and as shown in figure 7.2, amorphous films are commonly obtained with (individual) properties spanning (respective) ranges (Buchholz, Ma, et al., 2014; Buchholz, Zeng, et al., 2013).

The process factor deposition temperature (T_d) is often used to tune the crystalline fraction of a film. Other studies have proposed that the collimation level of material flux sourcing film growth is another determinant of crystalline fraction of (Demaray, Deshpandey, and Pethe, 2002).

Thereby, the experimentation framework demonstrated by us in this study may help address specific and general questions re the nature of the amorphous state (e.g., in sputtered films).

7.4.C.2 Nature of electronic state

Further to section 6.2.D, figure 7.3(a) is a representation of the electrical conduction pathways as thought to prevail in the In_2O_3–$(ZnO)_k$ (k = 0, 1, 2, 3, …) material system. In similar vein, figure 7.3(b) represents a possible effect of silicon (Si) doping into the same.

In a first order approximation, the following will be the two independent

S. No.	Scientific / technological problem, or application area	Principal characterization			Putative DOEs supported by SHCSFCA per chapter 3 (for R&D involving RFMS deposited films)			
		Quantity	Modality, or measurement	Representative reference(s)	Factors Set	Number of levels	Number of replicates per run	
							4	2
1	Amorphous state, nature of	Pair Distribution Function	GIXRD	Shyam et al., 2016	P_{RF}, O, p, l_{t-s}, ϕ, Ω, T_d	2	2^{7-4}_{III} with center-point	2^{7-3}_{IV} with center-point
2	Electronic state, nature of	Hall Effect	ACFHE	Chapter 5 of this thesis	As previous. Additionally, film composition.		2^{8-5} with center-point	2^{8-4}_{IV} with center-point
3	Experimental data interpretation	Contour Plot / Hypersurface	RSA	Kim et al., 2017	As at issue		As per situation	As per situation
4	Adhesion, Film-Substrate	Film fragmentation, stress, strain	Film fracture	Leterrier, 2003	As at 1. Additionally, substrate.		2^{8-5} with center-point	2^{8-4}_{IV} with center-point
5	Aerospace	Static charge	Opto-Electronic, radiation hardness	Lai, 2000; Sheldahl Inc., 2020	As at 4. Additionally, radiation dose.		2^{9-6} with center-point	2^{9-5}_{III} with center-point
6	Biomedical	Microstructure, composition	Opto-Electronic, biocompatibility	Liu, Pharr, and Salvatore, 2017; Nassar et al., 2018	As at 4. Additionally, film composition.		2^{9-6} with center-point	2^{9-5}_{III} with center-point
7	Experimentation, automation of	Fitness Function	ML	Moon et al., 2020			As per situation	

Table 7.1: [Caption to this table is presented on next page.]

Table 7.1: [Table corresponding to this caption is presented on the previous page.]
Scientific and technological questions and application areas that may be addressed based on this study. The "quantity" and "modality, or measurement" as mentioned are exemplary, and any required quantities or modalities may be recruited in service of addressing the "scientific or technological issue, or application area". In similar vein, the "reference(s)" are exemplary. Accordingly, the "first DOE" as mentioned is putative, in that it proceeds forth from the exemplary "factors set"; and is furthermore constrained by the design of the SHCSFCA (per chapter 4). It is understood that a comprehensive (viz., background knowledge-base, scientific questions of interest, time and costs constraints on experimentation and characterization, constraints on sample due to characterization modalities, necessary number of replicates per DE run, ability to design and develop new hardware and / or associated experimentation protocol, and the like) assessment of the given situation will inform determination of the factors set (and in turn, of the factors number), and of the DOE. Accordingly, the "putative first DOE" mentioned is for the SHCSFCA described in chapter 4, and where four replicates are obtained per DE run. In practice, higher or lower (for instance, two replicates per run) may provision a total number (over the complete DE) of samples such that subsequent linear modeling — of given experimentally determined property of interest — may adequately account for the observed variance in measurement. At any rate, given the self-referencing nature of a DE, the process factor dependent development of a given property of interest — more so, if it is anomalous — is bought into sharp relief forthwith; based on the same, one may reliably proceed with the rationalization of the observation. The notation as used for the two-level DE is as follows (refer figure 3.12): 2^{k-p}_{X}, where "number of levels" equals 2 (as mentioned), number of main factors of the DE (k), reciprocal of fraction level of a two-factor DE (p), resolution of the DE (X) (Dunn, 2016). It is noted that the entries in the right-most column, while exemplary, are in reference to studies involving (as is this study) films deposited via sputtering. The dashed line separates film (or materials) related issues, from others. Here, design of experiment (DOE), designed experiment (DE), substrate holder cum sputter flux collimator array (SHCSFCA), AC Field Hall Effect (ACFHE), response surface analysis (RSA), machine-learning (ML), RF power (P_{RF}), process gas pressure (p), oxygen percent (O), target-substrate distance (l_{t-s}), pressure distance product (ϕ), solid angle (Ω), deposition temperature (T_d).

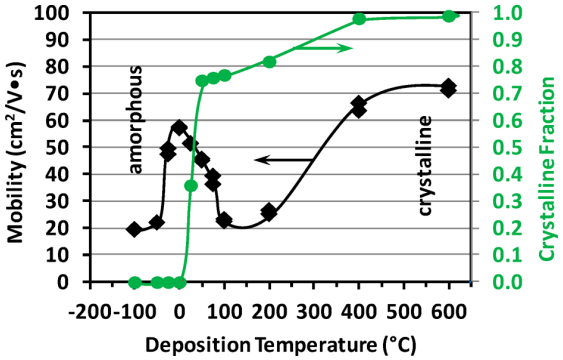

Figure 7.2: The deposition temperature (T_d) dependence of crystalline fraction in indium sesquioxide (In_2O_3) films. The conduction electron mobility (μ) as a function of film 'amorphousness' is presented. Typically, and as shown, the process factor deposition temperature (T_d) is the handle employed to tune crystalline fraction (that is, "amorphousness") of the film. The figure has been adapted from Buchholz, Ma, et al., 2014 and is for $\simeq$350 nm thick films.

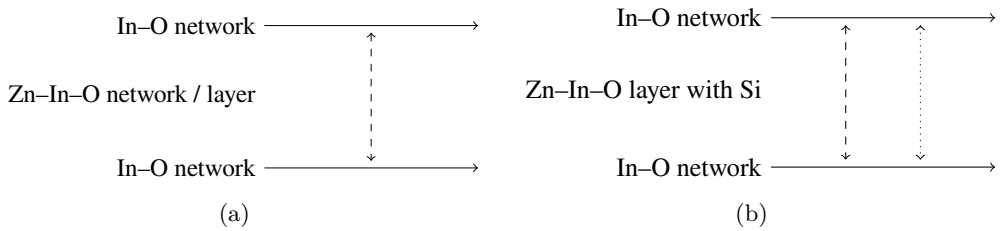

Figure 7.3: (a) Possible representation of electrical conduction through the In_2O_3−$(ZnO)_k$ (k = 0, 1, 2, 3, ...) material system. With reference also to discussions of figure 6.2, the InO_2 networks are, plausibly, the preferred seat of electrical conduction. This is indicated via full arrows running from left to right. The contribution of the mediate Zn−In−O network to electrical conduction, indicated via vertical dashed double arrow, is progressively depressed with increasing k. (b) At low silicon (Si) doping levels, the primary and minor contribution to electrical conduction in a In−Si−Zn−O material system (Si doped In_2O_3−$(ZnO)_3$ (ISZO)), may reasonably be expected to be as at the base homologue (k = 3); refer table 7.2. Progressive doping of Si into the Zn−In−O network, may result in either or both of the following: (i) the Si may donate up to two electrons in to the conduction band and become ionized as a result; and, (ii) the vacant localized states that thus are available at the ionized Si species may provide an additional 'hopping' electrical conduction pathway, indicated via a vertical dotted double arrow, through the Zn−In−O network.

Short name	k	f_{In}	f_{Si}	f_{Zn}	Formula unit	Lattice	Formula units per unit-cell	Unit-Cell volume /Å^3	Length scales of interest: Unit-Cell c-axis /Å	Length scales of interest: Inter-InO_2 plane distance (≡ $2d_1$) /Å	Length scales of interest: Si-Si distance in Zn−In−O layer (≡ d_2) /Å	d_1/d_2
IZO2	2	0.5	0	0.5	$In_2Zn_2O_5$	Hexa.	–	–	–	≤ As in next row	NA	NA
IZO3†	3	0.4	0	0.6	$In_2Zn_3O_6$	Rhom.	3	413.43	c′=42.488	c′/3 ≃ 14	NA	NA
ISZO32*‡	NA	0.38	0.04	0.58	$In_{10}Si_1Zn_{15}O_{32}$	Rhom.	–	–	–	≃ As in previous row	≃9	0.80
IZO6	6	0.25	0	0.75	$In_2Zn_6O_9$	Hexa.	–	–	–	≤ As in next row	NA	NA
IZO7†	7	0.22	0	0.78	$In_2Zn_7O_{10}$	Rhom.	3	698.81	c′=73.699	c′/3 ≃ 25	NA	NA
ISZO76‡	NA	0.22	0.01	0.77	$In_{100}Si_3Zn_{350}O_{506}$	Rhom.	–	–	–	≃ As in previous row	≃16	0.78

Table 7.2: [Caption to this table is presented on next page.]

Table 7.2: [Table corresponding to this caption is presented on the previous page.]
With reference to figure 6.2, structural and physical aspects of selected homologues of the $In_2O_3-(ZnO)_k$ (k = 0, 1, 2, 3, ...) material system in the crystalline state. The entry marked $*$ is the subject of this study. The lattice is hexagonal "Hexa." or rhombohedral "Rhom." for k even or odd respectively. Wherever mentioned, the c-axis length for the homologues marked † are per Yoshinari et al., 2009. The fractions f_{In} and f_{Zn} being maintained at or close to their values for the "base" composition (that is, the composition at the previous row), it is assumed that the introduction of the silicon (Si) (at entries marked ‡) does not disrupt the base structure; as such, the lattice entries are bought forward from the previous row. The fractions f_{Si} for ISZO32 and for ISZO76 were chosen so that the d_1/d_2 (ISZO32) $\simeq$ d_1/d_2 (ISZO76). Such considerations may permit for interpretation of an observed change in conductivity (between the base composition IZO3 and ISZO32; and similarly between IZO7, and ISZO76) in terms of an induced mobility change due addition of Si in the Zn−In−O network (as per the ansatz forwarded via figure 7.3). Given the differential in carrier concentration between the base compositions IZO3 and IZO7 (Negar Naghavi et al., 2000), and the expected concomitant differential in optical band-gap energy (E_g), it may furthermore be possible to fruitfully interpret observed physical property differentials across ISZO32 and ISZO76. The Si-Si distance is estimated as the cube-root of the volume per Si assuming that the unit cell volume and number of formula units at the previous row (that is, of the base homologue) are conserved, and further assuming that each Si is incorporated at a Zn site, and based upon the nominal ratio of Si to Zn from the formula unit of the homologous series of In−Zn−O material system ($In_2O_3-(ZnO)_k$ (k = 0, 1, 2, 3, ...)) material system. Here, metal atomic fraction of In (f_{In}), metal atomic fraction of Zn (f_{Zn}), metal atomic fraction of Si (f_{Si}).

contributors to the corpus of conduction electrons (that is, to conduction electron concentration (n)) of the Si doped In_2O_3−$(ZnO)_k$ (k = 0, 1, 2, 3, …) material system: the original contribution from the In_2O_3−$(ZnO)_k$ (k = 0, 1, 2, 3, …) system, and a contribution of up to 2 electrons per doped Si. This latter contribution will depend on the number of oxygens coordinating an incorporated Si, which in the amorphous state is not fixed.

Incorporation of Si into zinc oxide (ZnO) is known to be possible up to about 5 % of metal sites. Also, polycrystalline films of the Si doped ZnO typically display their best electro-optical properties when about 2 % of metal sites are replaced by Si (V. L. Kuznetsov et al., 2015).

Since we are interested in amorphous phase films, per the discussions of section 6.2.D, the In−Si−Zn−O material systems of our choice possesses Si contents at the upper end of the range of possible incorporation of Si into ZnO (refer table 7.2).

Furthermore, the vacant electronic states of (appropriately spaced and possibly ionized) Si within the Zn−In−O network may provide an additional channel for inter-InO_2 network 'hopping' electronic conduction. Given that the primary pathway for current flow is the InO_2 network, while the Si likely inhabit the Zn−In−O network, it is possible that the expected enhancement of ionized impurity scattering (IIS) due the structural disorder introduced by Si incorporation, is effectively suppressed.

Such considerations led to settlement of the question of amount of Si doping, and the resulting Si doped In_2O_3−$(ZnO)_k$ (k = 0, 1, 2, 3, …) compositions of interest are listed in table 7.2. Sputtering targets of the listed compositions have been procured, and are available for future studies.

7.4.C.3 Data interpretation

Given the ability of RSA to discriminate between main effects of, and interaction effect among, multiple process factor, experimentation conducted according to DOE principles is a valuable aid for data interpretation. In turn, correct data interpretation can guide theory development.

A case in point is presented via figure 7.4. The RSA of the results furnished by an appropriately designed experiment could aid in quantitative discrimination between the effect of oxygen content, and of oxygen partial pressure. The clarity obtained thus can be invaluable for guiding theory development.

7.4.C.4 Film-Substrate adhesion

This study concerns the film-substrate interface of / and amorphous transparent and semi-conductive films (Kamiya and Hideo Hosono, 2010; Nomura, Ohta, Takagi, et al., 2004; Marius Grundmann et al., 2010). The flexible electronics applications area presents a likely playground for exploring the commercial applications of our results (Volinsky, Moody, and Gerberich, 2002; Donald M. Mattox, 2016; Bradley and Huang, 2017; Agaiby, 2018). Accordingly, we consider flexible electronics research themes that may be addressed on basis of our results.

The commercial significance of the problem of film fracture during service is attested to by the development of "more than 200 different methods for measuring adhesion" of film on substrate (Volinsky, Moody, and Gerberich, 2002). Indeed, film fragmentation under stress (e.g., during service) is an outstanding problem impeding commercial success in the field of flexible electronics (Crawford, 2005; Paine, Yeom, and Yaglioglu, 2005; Bouten, Slikkerveer, and Leterrier, 2005; Mattes, 1980).

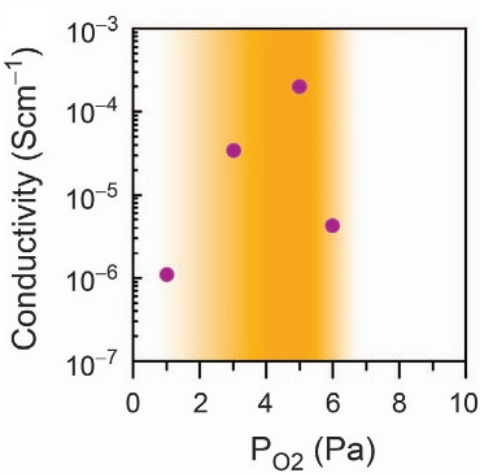

Figure 7.4: The oxygen partial pressure (P_{O2}) dependence of conductivity (σ), showing that low (<1 Pa) and high (>6 Pa) oxygen partial pressure (P_{O2}) result in insulating films. Evidently, the plot conveys that the drop in conductivity (σ) observed above and below $P_{O2} \simeq 5$ Pa is due P_{O2}. The figure is adapted from Kim et al., 2017, and was obtained on amorphous digallium monoxide (a$-Ga_2O_x$) (transition metal oxide (TMO)) films at T = 300 K. Comparison with our results on Si doped $In_2O_3-(ZnO)_3$ (ISZO) films as presented in figures 6.16, 6.17, and 6.19 reveals possible significance of process gas pressure (p) in the reported results.

Evidently, properties of the film-substrate interface determine (at least in part) the fracture dynamics of thin-film devices (Donald M. Mattox, 2016). The discussions of the sub-plantation layer (SPL) (chapters 2 and 6) are of direct relevance to the understanding and control of film fracture and adhesion.

We have demonstrated (refer section 5.10.B) rational macro process control of nanoscale SPL, that is, of film-substrate interface, properties (such as, thickness, roughness, and density).

Adhesion of film on substrate is determined by the mediating interface (e.g., the SPL). Our film deposition / SPL growth process can be of service for deposition of well adhering TMOs films in general. Thus, and for instance, our film deposition process may enable development of upcoming trans-

parent biomedical devices, e.g., ocular devices, that require limited flexing during service. As a matter of fact, TMO films already service a gamut of commercial opto-electronics applications (X. Yu, Marks, and Facchetti, 2016).

It is noted that such niche (low-volume high-value) commercial applications support, that is, require, continual process optimization. Thus, such applications may prove to be a likely market entry point for films and devices per our process (Liu, Pharr, and Salvatore, 2017).

It may also be noted that while our study employed Corning Eagle XG Glass (CEXG) substrates ($\mathsf{d_s} = 700\,\mu\mathsf{m}$), the film deposition process demonstrations are at room-temperature. As such, the process is available for polymer (plastic / flexible) substrates.

It should however be noted, that the surface roughness of polymer substrates are at least an order of magnitude greater than that of CEXG. This will result in additional considerations attending the deposition process, and subsequent characterization (Románszki, Klébert, and Héberger, 2020).

One notes however that 'flexible' CEXG substrates are available in thicknesses as low as $250\,\mu\mathsf{m}$ (Corning Inc., 2017).

Relatedly to the aforementioned, we have demonstrated process control of surface roughness. Such control has implications for utility and performance of microscopic opto-electronic devices (Chee et al., 2018; A. Giri and Hopkins, 2020).

Thereby, the experimentation framework developed in this study may help R&D of commercial applications, particularly, flexible electronics (e.g., opto-electronic device) applications, that require well adhering sputtered films.

7.4.C.5 Aerospace applications

The In_2O_3−$(ZnO)_k$ (k = 0, 1, 2, 3, ...) material system is known to be resilient to radiation damage (Cramer et al., 2016). Also, the opto-electronic performance of the ISZO material composition meets the requirements for thermal control materials for spacecraft and their launch vehicles.

Accordingly, table 7.3 presents exemplary commercial applications that are amenable for development via our material (ISZO), and film-substrate adhesion-relevant (SPL growth) process (see also, Sibin et al., 2018).

The considerations are with specific reference to commercially available products (Sheldahl Inc., 2020). Discussions along these lines have been undertaken with the commercial entity referenced, for further development of their thermal control materials and products. The discussions were in light particularly of upcoming nano-satellite applications.

7.4.C.6 Biomedical applications

All but the luckiest among us know somebody who is suffering from a chronic ailment, be it diabetes, Alzheimer's, depression, or severely impaired vision. The problems are compounded when they occur in the elderly who live alone. 'Always on' medical monitoring technology is a key component of a solutions package addressing the aforementioned situation. However, the utility of such technology presupposes reliable sensing of health indicators.

Exterior and interior loci of a human (animal) body are noisy and challenging environments to perform sensing of, or in. They (particularly, interior loci) are densely packed, are aqueous, and are non-rigid. As such, mechanical attachment and integrity of sensors during service require special consideration.

Our study can be of service in the development of such sensor applications.

Product Type	S. No.	Product Name	Parameters potentially addressable
Special purpose coatings	1	Transparent conductive coatings (ITO) for static charge control	Surface resistance, thickness, abrasion on polyimide, weathering
Perforated interconnects	2		
Static charge control materials	3	ITO coated silver FEP	ITO surface resistivity, intermittent service temperature range, continuous service temperature range, thickness
	4	ITO coated silver FEP tape with 3M 966 acrylic adhesive	ITO surface resistivity, adhesion to stainless steel, intermittent service temperature range, continuous service temperature range
	5	ITO coated silver FEP tape with 3M 9703 adhesive	As previous
	6	Post processing – perforation and embossing of product at s. no. 5	Electrical connection of ITO through the hole to the silver and the conductive adhesive
	7	ITO coated aluminized polyimide	ITO surface resistivity, intermittent service temperature range, continuous service temperature range, thickness
	8	Post processing – perforation of product at s. no. 7	Through hole electrical connection from the ITO to the aluminium surface

Table 7.3: Commercial "product types" — servicing the aerospace industry — that are amenable immediately for development via the materials and processes described in this study. The "product names" / products listed are marketed by Sheldahl Inc., 2020, and permit us to make specific — via listings of the "Parameters potentially addressable" — the potential applications of this study.
[Table continues ...]

Product Type	S. No.	Product Name	Parameters potentially addressable
Laminates	9	Silver coated Fluorinated ethylene propylene, commonly, teflon (FEP) reinforced with polyimide	Addition of ITO to FEP surface, intermittent service temperature range, continuous service temperature range
Thermal control materials	10	Post processing – perforation of product at s. no. 9	For constructions with ITO, the FEP may be perforated prior to coating to provide an electrical connection between the indium tin oxide (ITO) and the silver coatings
	11	Test methods	ITO x substrate x metal: surface resistivity, coating adhesion

Table 7.3: [...Caption to this continuing table is presented earlier.]

Our 'collimated' sputtering protocol can be deployed to endow the surface of a suitable substrate with properties — such as electrical conductivity, adhesiveness, or impermeability — in service of creating reliable implantable or wearable sensors. Such endowment may help obtain robust sensors capable of continuous duty over their lifetime (see chapters 6 and 7).

Furthermore, our DOE and RSA approach has evident utility for efficient experimentation via 'hard-soft' materials development approaches (K. J. Yu et al., 2017).

7.4.C.7 Machine-Learning for automation of experimentation

The technique of RSA (refer chapters 4, 6, and 7) has direct utility for implementing machine-learning (ML) algorithms that automate progress towards a given experimentation goal. An exemplary experimentation goal is described in figure 7.5.

An outstanding industrial quality-control problem relevant to the subject-matter of this study, is the real-time prediction of adjustments to, e.g., a film deposition process that is subject to drifting. Automation of the adjustments process may be achieved via ML approaches based on real-time modeling (RSA) of process output and input conditions. Implementation of data collection and tabulation, and of appropriate characterization modalities, in service of real-time RSA can service such industrial problems (Hubbard, 2014).

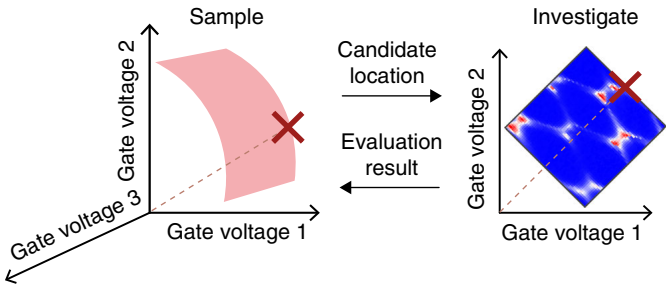

Figure 7.5: The machine-learning (ML) study reported by Moon et al., 2020 for "automatic tuning of a quantum device". The algorithm permits rational determination-of and travel-upon a "hypersurface" to determine locations of single or double quantum dots. Evidently, the left figure is akin figure 3.3 of this study. A real-time determination of effects (main and / or interaction), that is, of linear modelsing, of a system may be utilized for effecting real-time process quality control (tuning) in dynamic environments.

Appendices

Appendix A

Elements of analysis I: refinement and modeling of experimental data

A.1 Introduction

We present further elements of analysis that accompany this study as has been presented in chapters 4 through 6. The elements so, as presented in section A.2, concern x-ray reflectometry (XRR) results. The elements so, as presented in section A.3, concern spectroscopic ellipsometry (SE) results.

A.2 X-Ray reflectometry: further elements of analysis

Refinement of the applicable (on basis of figure 5.2) film layer structures (per figure 5.3) was performed to yield the results presented in table 5.1. Representative (for single-layer (SL) film F15, and for bi-layer (BL) films F7 and F11) modeled Kiessig fringes profile (KFP) are presented in figure 5.4.

Table A.1 presents values of goodness of fit metrics as was obtained for each refinement / film.

A.3 Spectroscopic ellipsometry: further elements of analysis

A.3.A Introduction

We present the Gaussian (G) oscillator model (section A.3.B). The G oscillator model, along with the Tauc-Lorentz (TL) oscillator model as presented in section 4.4.D.1, was used to model the SE spectra (Ψ, Δ) of substrate (Corning Eagle XG Glass (CEXG)) upon which were deposited the films at issue. We thence present results of said modeling (section A.3.C). The measured and fitted (Ψ, Δ) for films F7, F11, and F23 have been presented in section 6.3.E.

A.3.B Gaussian oscillator model

The G oscillator model delivers a Kramers Kronig (KK) consistent lineshape.

The G ε^* (ε^*_G) oscillator model is:

$$\begin{aligned}\varepsilon^*_G = A\Bigg[&\left\{\Gamma\left(\frac{E-E_n}{\sigma}\right)+\Gamma\left(\frac{E+E_n}{\sigma}\right)\right\}\\&+\iota\left\{\exp\left(-\left(\frac{E-E_n}{\sigma}\right)^2\right)-\exp\left(-\left(\frac{E+E_n}{\sigma}\right)^2\right)\right\}\Bigg]\end{aligned} \tag{A.1a}$$

where,

$$\sigma = \frac{B}{2\ln 2} \tag{A.1b}$$

	Film	R – value	χ^2
BL	F27	0.015	0.001 52
	F11	0.035	0.0048
	F23	0.029	0.007 03
	F3	0.034	0.008 25
	F7	0.036	0.0112
SL	F35	0.041	0.0227
	F15	0.056	0.0277
	F31	0.076	0.0512
	F19	0.056	0.0247

Table A.1: Relevant goodness of fit metrics for modeling (representative refinement) Kiessig fringes profile (KFP) of the nine Si doped $In_2O_3-(ZnO)_3$ (ISZO) films (viz., the 5 bi-layer (BL) films F27, F11, F23, F3, F7; and the 4 single-layer (SL) films F35, F15, F31, F19) used for this study. The film layer structure models refined are per figure 5.3(d) (for BL films), and figure 5.3(c) (for SL films). Here, goodness of fit metric for modelling KFP obtained via XRR (R – value), goodness of fit metric for modelling KFP obtained via XRR (χ^2).

where: amplitude of ε^*_G (A), broadening of ε^*_G (B), energy (E), center energy (E_n), convergence series for line-shape of real part of ε^*_G (Γ) (De Sousa Meneses, Malki, and Echegut, 2006; Peiponen and Vartiainen, 1991).

A.3.C Corning Eagle XG Glass substrate

A.3.C.1 Introduction

We present the experimentally measured transmission fraction (Tr) for the CEXG substrate (section A.3.C.2). We present the modeled (n, k) for the CEXG substrate (section A.3.C.3).

A.3.C.2 Transmission Fraction

The wavelength of light (λ) dependence of Tr for the CEXG substrate at issue are presented in figure A.1.

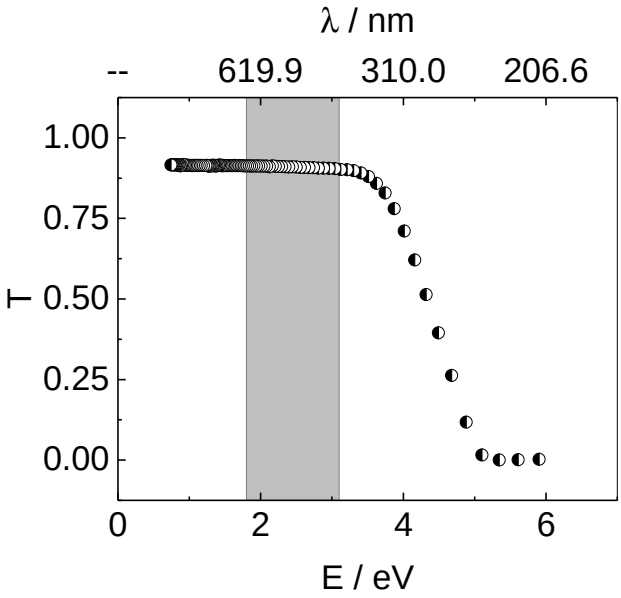

Figure A.1: The energy (E) and wavelength of light (λ) dependences of transmission fraction (Tr) of Corning Eagle XG Glass (CEXG) substrate used in this study. The shaded band represents the visible λ range ($400\,\mathrm{nm} \leq \lambda \leq 700\,\mathrm{nm}$).

A.3.C.3 Refractive index and extinction coefficient

The λ dependence of optical constants (n, k) of the CEXG substrate at issue were modeled via a general oscillator model comprising one G (refer section A.3.B) and one TL (refer section 4.4.D.1) oscillator model. The results are presented in table A.2 and figure A.2.

For reference in context of figures 6.7 and A.2, the following are features of a physically correct λ (modeled) dependence of optical constants (J. A. Woollam Co., 2014):

- $k \geq 0$.
- In λ range where $k = 0$, $n \uparrow$ with $\lambda \downarrow$.
- In λ range where $k > 0$, $n \uparrow$ when $k \downarrow$, and vice versa.

CEXG					
TL			G		
Property			Property		
A	/ eV	1.1×10^{-2}	A	/ eV	8.5×10^{-5}
B	/ eV	8.3×10^{-1}	B	/ eV	1.2
E_0	/ eV	5.4	E_n	/ eV	4.8
E_g	/ eV	4.2			

Table A.2: The spectroscopic ellipsometry (SE) optical model for Corning Eagle XG Glass (CEXG) substrate ($d_s = 700\,\mu m$). The model is based upon ellipsometric data collected in transmission and in reflection. The ellipsometric spectrum was modeled as a general oscillator comprised of one Tauc-Lorentz (TL) and one Gaussian (G) oscillator. The dispersion outside of the measured spectral range, viz., $210\,nm \leq \lambda \leq 1690\,nm$ was modeled via infra red (IR) and ultra violet (UV) poles. The modeling proceeded from the following assumption: the high frequency dielectric permittivity (ε_∞) was fixed at unity. The modeling yielded the infra red (IR) pole amplitude as $1.0 \times 10^{-2}\,eV$, and the ultra violet (UV) pole amplitude and position as $2.0 \times 10^{2}\,eV$ and $1.3 \times 10^{1}\,eV$ respectively (J. A. Woollam Co., 2014). Furthermore, the modeling yielded the CEXG substrate surface roughness of $0.92\,nm$, independently and in agreement with the manufacturer quoted range ($r_{s,\,CEXG} = 0.5\,nm$ to $1\,nm$) (Corning Inc., 2017). Here, for TL: amplitude of imaginary part of ε^*_{TL} (A), broadening of imaginary part of ε^*_{TL} (B), energy at peak in imaginary part of TL ε^* (ε^*_{TL}) (E_0), band-gap energy (E_g); for G: amplitude of ε^*_G (A), broadening of ε^*_G (B), center energy (E_n); substrate thickness (d_s); substrate thickness (d_s).

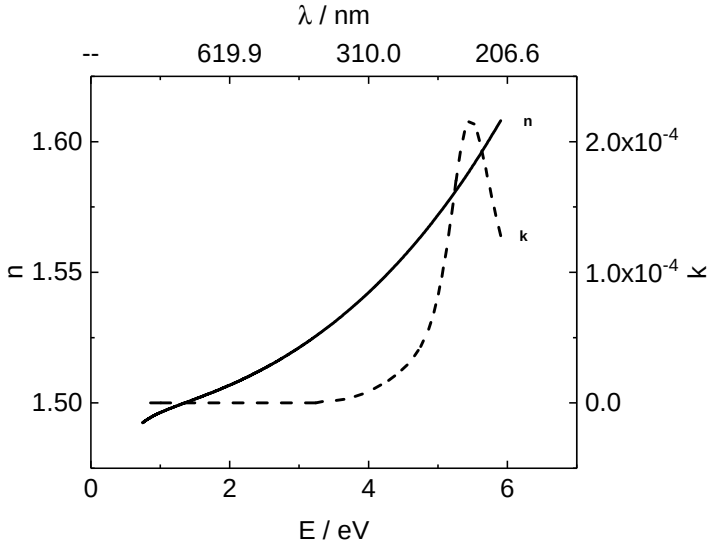

Figure A.2: The energy (E) or wavelength of light (λ) dependent refractive index (n) and extinction coefficient (k) of Corning Eagle XG Glass (CEXG) substrate. The dependence was obtained on basis of Kramers Kronig (KK) consistent dispersion function (Tauc-Lorentz (TL) + Gaussian (G)) fit to the experimentally measured (Ψ, Δ). Here SE Ψ-parameter (Ψ), SE Δ-parameter (Δ).

Appendix B

Elements of analysis II: calculations based on experimental data

B.1 Introduction

In section B.2, and further to section 3.2.D, we present the computer program as was written to compute the linear model of a given physical or electronic property on basis of experimental measurement of said property. The thus computed linear model was used to obtain the pareto plots and response surfaces of the property in question. Refer pareto plots 5.10 (sub-plantation layer (SPL) physical properties), 6.14 (thin-film layer (TFL) electronic properties), and 6.20 (TFL physical properties). The respective response surfaces / contour plots are 5.11 (SPL physical properties), 6.16, 6.17, 6.19, and 6.18 (TFL electronic properties), and 6.21 (TFL physical properties).

In section B.3, and further to section 4.5.D.1, we present the computer program as was written to compute — per the Brooks-Herring (BH) model

— (N_D, N_A)* at a given absolute temperature (T) from the corresponding experimentally measured (μ, n)†.

The computer programs as follow are written in the mathematica programming language‡. For obvious reasons, it was not possible to use symbols as used in the relevant referenced sections. However, the symbols as used in the programs are in close correspondence with those in the relevant sections. Comments are included in the programs for further reference.

B.2 Linear model of layer physical or electronic properties

B.2.A Introduction

An exemplary program for computing the linear model for SPL thickness (d_{SPL}) is presented. The program logic applies to any general property of interest.

B.2.B Computer program

● Computer program begins ●

```
In[690]:= ClearAll["Global`*"];
In[691]:= (*DECLARATIONS.*)
In[692]:= Symbol["RFP"];
Symbol["PGP"];
Symbol["OP"];
Symbol["linearModelVariables"];
Symbol["linearModelFunctions"];
Symbol["linearModelEffectOf"];
Symbol["linearModelEffectOf1"];
Symbol["linearModelEffects"];
Symbol["inputStringBlurb"];
Symbol["importedDataFileAbsoluteName"];
```

*Where, total donor concentration (N_D), total acceptor concentration (N_A).
†Where, conduction electron mobility (μ), conduction electron concentration (n).

```
13 Symbol["importedDataFileName"];
14 Symbol["importedAndForExportDataFilesPath"];
15 Symbol["errorOneMessage"];
16 Symbol["linearModelCoefficients"];
17 Symbol["importedData"];
18 Symbol["propertyType"];
19 Symbol["forContourPlottingInOriginElectronic"];
20 Symbol["forContourPlottingInOriginMechanical"];
21 Symbol["forContourPlottingInOrigin"];
22 Symbol["experimentDesignSampleNameAndPosition"];
23 Symbol["experimentDesignForModelling"];
24 Symbol["relevantSamplePositionAndPropertyValue"];
25 Symbol["relevantSamplePositionAndPropertyValue1"];
26 Symbol["effectAndCoefficient"];
27 Symbol["relevantSamplesNamePositionAndPropertyValue"];
28 Symbol["fileNameForExportRelevantSamplesNamePositionAndPropertyValue"];
29 In[718]:= (*INITIALIZATIONS.*)
30 In[719]:= linearModelVariables={RFP,PGP,OP};
31 linearModelFunctions={RFP,PGP,OP,RFP*PGP,RFP*OP,PGP*OP,RFP*PGP*OP};
32 In[721]:= linearModelEffectOf=Map[ToString,linearModelFunctions];
33 linearModelEffectOf1=StringReplace[linearModelEffectOf," "->":"];
34 linearModelEffects=PrependTo[linearModelEffectOf1,"Intercept"];
35 In[724]:= forContourPlottingInOriginElectronic={OP->y,RFP->x};
36 forContourPlottingInOriginMechanical={PGP->y,RFP->x};
37 In[726]:= inputStringBlurb="Enter absolute name of data-file (full path to
       data-file) in box below. Type carefully or copy-paste the same here;
       ensure that there are no leading or trailing spaces, and that there
      are no surrounding delimiters, such as, for instance, quotation marks.
38
39 I expect a two column file, where first-column is sample-name, and second-
      column is the corresponding value of property sought to be modelled.
40
41 Depending on whether the property is electronic (mechanical) in nature,
      the file-name MUST contain ONE-AND-ONLY-ONE occurence of the string \"
      _ep_\" (\"_mp_\").
42
43 Know that the top-row of the file will be ignored (since the same is
      expected to contain headers).";
44 errorOneMessage="Data-File name MUST contain ONE-AND-ONLY-ONE occurence of
```

```
     the string \"_ep_\" (\"_mp_\"). The data-file name you provide does
    not meet this requirement.";
In[728]:= experimentDesignSampleNameAndPosition={{"F27",{-1,-1,-1}},{"F11
    ",{1,-1,-1}},{"F35",{-1,1,-1}},{"F15",{1,1,-1}},{"F3",{-1,-1,1}},{"F23
    ",{1,-1,1}},{"F19",{-1,1,1}},{"F31",{1,1,1}},{"F7",{0,0,0}}};
relevantSamplesNamePositionAndPropertyValue={};
experimentDesignForModelling={};
In[731]:= importedDataFileAbsoluteName=InputString[inputStringBlurb];
importedDataFileName=FileNameTake[importedDataFileAbsoluteName];
importedAndForExportDataFilesPath=DirectoryName[
    importedDataFileAbsoluteName];
importedData={};
linearModelCoefficients={{"LinearModelTerm","LinearModelTermCoefficient
    "}};
In[736]:= (*LOGIC.*)
In[737]:= If[StringContainsQ[importedDataFileName,"_ep_"],propertyType="
    electronic",If[StringContainsQ[importedDataFileName,"_mp_"],
    propertyType="mechanical",Print[errorOneMessage]]];
forContourPlottingInOrigin=If[propertyType=="electronic",
    forContourPlottingInOriginElectronic,If[propertyType=="mechanical",
    forContourPlottingInOriginMechanical,Print[errorOneMessage]]];
In[739]:= importedData=Import[importedDataFileAbsoluteName,"Table"];
In[740]:= For[i=2,i<=Length[importedData],++i,
For[j=1,j<=Length[experimentDesignSampleNameAndPosition],++j,
If[importedData[[i]][[1]]==experimentDesignSampleNameAndPosition[[j
    ]][[1]],
relevantSampleNamePositionAndPropertyValue=Append[
    experimentDesignSampleNameAndPosition[[j]],importedData[[i]][[2]]];
AppendTo[relevantSamplesNamePositionAndPropertyValue,
    relevantSampleNamePositionAndPropertyValue];,
Null
];
];
];
For[i=1,i<=Length[relevantSamplesNamePositionAndPropertyValue],++i,
relevantSamplePositionAndPropertyValue=Drop[
    relevantSamplesNamePositionAndPropertyValue[[i]],1];
relevantSamplePositionAndPropertyValue1=FlattenAt[
    relevantSamplePositionAndPropertyValue,1];
```

```
69 AppendTo[experimentDesignForModelling,
       relevantSamplePositionAndPropertyValue1];
70 ];
71 In[742]:= linearModel=LinearModelFit[experimentDesignForModelling,
       linearModelFunctions,linearModelVariables];
72 In[743]:= For[i=1,i<=Length[linearModelEffects],++i,
73 effectAndCoefficient=List[linearModelEffects[[i]],linearModel["
       BestFitParameters"][[i]]];
74 AppendTo[linearModelCoefficients,effectAndCoefficient];
75 ];
76 In[744]:= (*EXPORT RELATED.*)
77 In[745]:= fileNameForExportRelevantSamplesNamePositionAndPropertyValue=
       StringJoin[FileBaseName[importedDataFileName],"
       _RelevantSamplesNamePositionAndPropertyValue.txt"];
78 fullPathToOutputFile=StringJoin[importedAndForExportDataFilesPath,
       fileNameForExportRelevantSamplesNamePositionAndPropertyValue];
79 Export[fullPathToOutputFile,relevantSamplesNamePositionAndPropertyValue];
80 In[748]:= fileNameForExportExperimentDesignForModelling=StringJoin[
       FileBaseName[importedDataFileName],"_ExperimentDesignForModelling.txt
       "];
81 fullPathToOutputFile=StringJoin[importedAndForExportDataFilesPath,
       fileNameForExportExperimentDesignForModelling];
82 Export[fullPathToOutputFile,experimentDesignForModelling];
83 In[751]:= fileNameForExportBestFit=StringJoin[FileBaseName[
       importedDataFileName],"_BestFit.txt"];
84 fullPathToOutputFile=StringJoin[importedAndForExportDataFilesPath,
       fileNameForExportBestFit];
85 Export[fullPathToOutputFile,CForm[linearModel["BestFit"]]];
86 In[754]:= fileNameForExportBestFitForContourPlotting=StringJoin[
       FileBaseName[importedDataFileName],"_BestFitForContourPlotting.txt"];
87 fullPathToOutputFile=StringJoin[importedAndForExportDataFilesPath,
       fileNameForExportBestFitForContourPlotting];
88 Export[fullPathToOutputFile,CForm[linearModel["BestFit"]/.
       forContourPlottingInOrigin]];
89 In[757]:= fileNameForExportCoefficients=StringJoin[FileBaseName[
       importedDataFileName],"_Coefficients.csv"];fullPathToOutputFile=
       StringJoin[importedAndForExportDataFilesPath,
       fileNameForExportCoefficients];
90 Export[fullPathToOutputFile,linearModelCoefficients];
```

```
In[759]:= (*DIAGNOSTICS FOR QUALITY-CONTROL.*)
In[760]:= (*THE RAW DATA (SAMPLE VS PROPERTY) AS WAS IMPORTED AND LINEAR-
    MODELLED HERE. COMPARE WITH DATA-FILE TO CONFIRM THAT THE DATA READ
    IS AS INTENDED.*)
In[761]:= Print[importedAndForExportDataFilesPath];
During evaluation of In[761]:= C:\Users\PPEGroup\himanshu\
    oxford_desktop_pc\tco\ucl\lcn\experiments\mathematica\
    files_to_and_from_mathematica\
In[762]:= Print[importedDataFileName];
During evaluation of In[762]:= for_lm_mp_SPLThickness.dat
In[763]:= Print[importedData];
During evaluation of In[763]:= {{Sample,SPLThickness},{F27,3.8},{F11
    ,5.8},{F35,0},{F15,0},{F3,4},{F23,5.1},{F19,0},{F31,0},{F7,4.6}}
In[764]:= Print[experimentDesignSampleNameAndPosition];
During evaluation of In[764]:= {{F27,{-1,-1,-1}},{F11,{1,-1,-1}},{F35
    ,{-1,1,-1}},{F15,{1,1,-1}},{F3,{-1,-1,1}},{F23,{1,-1,1}},{F19
    ,{-1,1,1}},{F31,{1,1,1}},{F7,{0,0,0}}}
In[765]:= Print[linearModelVariables];
During evaluation of In[765]:= {RFP,PGP,OP}
In[766]:= Print[linearModelFunctions];
During evaluation of In[766]:= {RFP,PGP,OP,PGP RFP,OP RFP,OP PGP,OP PGP
    RFP}
In[767]:= Print[linearModelEffects];
During evaluation of In[767]:= {Intercept,RFP,PGP,OP,PGP:RFP,OP:RFP,OP:PGP
    ,OP:PGP:RFP}
In[768]:= Print[linearModel["BasisFunctions"]];
During evaluation of In[768]:= {1,RFP,PGP,OP,PGP RFP,OP RFP,OP PGP,OP PGP
    RFP}
In[769]:= (*THE CHOICES AS WERE MADE —— BASED ON (1) NAME OF THE DATA-
    FILE AND (2) CONTENTS OF DATA-FILE —— BY THE CODE AS IT PROCEEDED TO
    LINEAR MODEL. CHECK TO CONFIRM THAT THEY ARE AS INTENDED.*)
In[770]:= Print[propertyType];
During evaluation of In[770]:= mechanical
In[771]:= Print[forContourPlottingInOrigin];
During evaluation of In[771]:= {PGP->y,RFP->x}
In[772]:= Print[relevantSamplesNamePositionAndPropertyValue];
During evaluation of In[772]:= {{F27,{-1,-1,-1},3.8},{F11,{1,-1,-1},5.8},{
    F35,{-1,1,-1},0},{F15,{1,1,-1},0},{F3,{-1,-1,1},4},{F23
    ,{1,-1,1},5.1},{F19,{-1,1,1},0},{F31,{1,1,1},0},{F7,{0,0,0},4.6}}
```

```
116 In[773]:= Print[experimentDesignForModelling];
117 During evaluation of In[773]:=
        {{-1,-1,-1,3.8},{1,-1,-1,5.8},{-1,1,-1,0},{1,1,-1,0},
118 {-1,-1,1,4},{1,-1,1,5.1},{-1,1,1,0},{1,1,1,0},{0,0,0,4.6}}
119 In[774]:= Print[linearModel["Data"]];
120 During evaluation of In[774]:=
        {{-1,-1,-1,3.8},{1,-1,-1,5.8},{-1,1,-1,0},{1,1,-1,0},
121 {-1,-1,1,4},{1,-1,1,5.1},{-1,1,1,0},{1,1,1,0},{0,0,0,4.6}}
122 In[775]:= (*PIECES OF OUTPUT COMPUTED DURING LINEAR-MODELLING OF IMPORTED
        DATA.  THE SAME WERE EXPORTED AS CONTENT OF GENERATED OUTPUT FILES.*)
123 In[776]:= Print[linearModel["BestFitParameters"]];
124 During evaluation of In[776]:=
        {2.58889,0.3875,-2.3375,-0.0625,-0.3875,-0.1125,0.0625,0.1125}
125 In[777]:= Print[linearModelCoefficients];
126 During evaluation of In[777]:= {{LinearModelTerm,
        LinearModelTermCoefficient},{Intercept,2.58889},{RFP,0.3875},{PGP
        ,-2.3375},{OP,-0.0625},{PGP:RFP,-0.3875},{OP:RFP,-0.1125},{OP:PGP
        ,0.0625},{OP:PGP:RFP,0.1125}}
127 In[778]:= Print[linearModel["BestFit"]];
128 During evaluation of In[778]:= 2.58889 -0.0625 OP-2.3375 PGP+0.0625 OP PGP
        +0.3875 RFP-0.1125 OP RFP-0.3875 PGP RFP+0.1125 OP PGP RFP
129 In[779]:= Print[linearModel["BestFit"]/.forContourPlottingInOrigin];
130 During evaluation of In[779]:= 2.58889 -0.0625 OP+0.3875 x-0.1125 OP x
        -2.3375 y+0.0625 OP y-0.3875 x y+0.1125 OP x y
131 In[780]:= ListPlot[linearModel["FitResiduals"],Filling->Axis]
132 Out[780]=
133 In[781]:= (*GENERATED OUTPUT FILES.*)
134 In[782]:= Print[fileNameForExportExperimentDesignForModelling];
135 During evaluation of In[782]:=
        for_lm_mp_SPLThickness_ExperimentDesignForModelling.txt
136 In[783]:= Print[fileNameForExportBestFit];
137 During evaluation of In[783]:= for_lm_mp_SPLThickness_BestFit.txt
138 In[784]:= Print[fileNameForExportBestFitForContourPlotting];
139 During evaluation of In[784]:=
        for_lm_mp_SPLThickness_BestFitForContourPlotting.txt
140 In[785]:= Print[fileNameForExportCoefficients];
141 During evaluation of In[785]:= for_lm_mp_SPLThickness_Coefficients.csv
```

● Computer program has concluded ●

B.3 The total donor concentration and total acceptor concentration according the Brooks-Herring model for ionized impurity scattering

B.3.A Introduction

It is recalled that determination of validity of the BH model for ionized impurity scattering (IIS) at a given T is a separate consideration. The procedure to determine the T-range over which IIS is the dominant conduction electron scattering mechanism is per the discussion of figures 6.9(b) and 6.9(a).

B.3.B Computer program

The program as follows is written in the mathematica programming language[§]. For obvious reasons, it was not possible to use the symbols per section 4.5.D.1 in the program. Comments are included within the program to make clear the correspondences between the symbols used in the program and per section 4.5.D.1.

● Computer program begins ●

```
1  In[148]:= ClearAll["Global`*"];
2  In[149]:= (*REFERENCES:
3  Electron scattering by ionized impurities in semiconductors, Chattopadhyay
       , D.and Queisser, H. J., Reviews of Modern Physics, 53, 745, 1981.
4  Wolfe, C. M. Stillman, G. E.and Dimmock, J. O., Ionized Impurity Density
       in n–Type GaAs, Journal of Applied Physics, 41, 504, 1970.
5  Korshunov, F. P., Kurilovich, N. F., Murin, L. I., and Prokhorenko, T. A.,
       On the determination of carrier mobility in compensated GaAs,
       Inorganic Materials, 36, 100, 2000.
```

[§]Also known as the Wolfram Language.

```
6  *)
7  (*
8  GLOSSARY:
9  "sub" as in 'subscript'.  As in, "epsilonsubr".
10 "sup" as in 'superscript'.  As in, "msupAST".
11 "AST" as in 'ASTERISK'.  As in, "msupAST".
12 *)
13 outputDirectory=SetDirectory[NotebookDirectory[]];
14 In[150]:= epsilonsubrGaAs=12.9; (*From published literature for material
       indicated.  Noted only for reference --- not used in the present
       calculation.*)
15 epsilonsubrZnO=4; (*From published literature for material indicated.
       Noted only for reference --- not used in the present calculation.*)
16 epsilonsubrIGZO=16; (*Zhang, Jiawei, Li, Yunpeng, Zhang, Binglei, Wang,
       Hanbin, Xin, Qian and Song, Aimin, Flexible indium-gallium-zinc-oxide
       Schottky diode operating beyond 2.45GHz, Nature Communications, 6,
       7561, 2015.  Used in the present calculation.*)
17 Z=2;
18 (*epsilonsubr=epsilonsubrIGZO;*)
19 epsilonsubr=16;
20 In[155]:= msupASTGaAs=0.063; (*From literature for material indicated.
       Noted only for reference --- not used in the present calculation.*)
21 msupASTF11=0.12; (*From modelling of the Spectroscopic Ellipsometry (SE)
       data via a Tauc-Lorentz+Drude model.  Used in the present calculation
       .*)
22 msupASTF23=0.14; (*Same as previous.*)
23 In[158]:= h=6.6261*^-34;(*m2kg/s.*)
24 hbar=h/(2*Pi);
25 kB=1.3806*^-23;(*m2kgs-2K-1.*)
26 me=9.1092*^-31; (*kg.*)
27 e=1.6022*^-19;(*C.*)
28 epsilonsub0=8.8542*^-12; (*m-3kg-1s4A2.*)
29 epsilon=epsilonsub0*epsilonsubr;
30 In[165]:= musubBHPreFactorNumerator=((2)^(15/2))*((Pi)^(1/2))*((epsilon)
       ^(2))*((kB)^(3/2))*((T)^(3/2));
31 musubBHPreFactorDenominator=((m)^(1/2))*((NsubII)^(1))*((Z)^(2))*((e)^(3))
       ;(*NsubII is the "Ionized Impurity Concentration".  Cannot use 'N' as
       a variable name (for instance), since it is the name of a built-in
       function in Mathematica.*)
```

```
32 musubBHPostFactorArgumentNumerator=((24)^(1))*((m)^(1))*((epsilon)^(1))*((
     kB)^(2))*((T)^(2));
33 musubBHPostFactorArgumentDenominator=((n)^(1))*((e)^(2))*((hbar)^(2));
34 In[169]:= musubBHRHS[m_,T_,n_,NsubII_]=((musubBHPreFactorNumerator)/(
     musubBHPreFactorDenominator))*(Log[(musubBHPostFactorArgumentNumerator
     )/(musubBHPostFactorArgumentDenominator)])^(-1);
35 ND[n_,NsubII_]=(n+NsubII)/2;
36 NA[n_,NsubII_]=(-n+NsubII)/2;
37 compensationGamma[n_,NsubII_]=(-n+NsubII)/(n+NsubII); (*Cannot use 'Gamma'
     as a function name (for instance), since it is the name of a built-in
     function in Mathematica.*)
38 In[173]:= inputFileColumnsNames= {"T", "mu", "n"};
39 inputFileColumnsUnits= {"K", "cm2/Vs", "1/cm3"};
40 In[175]:= computedQuantityNames={"N","ND","NA","Gamma"};(*"N" is "NsubII
     ".*)
41 computedQuantityUnits={"1/cm3","1/cm3","1/cm3","1"};
42 In[177]:= outputFileFirstRow=Join[inputFileColumnsNames,
     computedQuantityNames];
43 outputFileSecondRow=Join[inputFileColumnsUnits,computedQuantityUnits];
44 In[179]:= (*F11*)
45 In[180]:= outputFile={};
46 AppendTo[outputFile,outputFileFirstRow]; (*The first three columns of the
     "outputFile" are (respectively) the three columns of the inputFile.*)
47 AppendTo[outputFile,outputFileSecondRow];(*Same as previous.*)
48 In[183]:= inputFile=Import["T:\\oxford_desktop_pc\\tco\\ucl\\lcn\\
     experiments\\mathematica\\mobility\\input_files\\1_hj11_T_mu_n.dat","
     Table"];(*Three columns: column 1 = T in K, column 2 = mu in cm2/Vs,
     column 3 = n in 1/cm3.*)
49 numberOfDataSetsInInputFile=Length[inputFile];
50 In[185]:= m=me*msupASTF11;
51 In[186]:= For[i=1,i<=numberOfDataSetsInInputFile,i++,
52 musubBHLHS=inputFile[[i,2]]*1*^-4;(*mu in m2/Vs.*)
53 musubBHRHS1=musubBHRHS[m,inputFile[[i,1]],inputFile[[i,3]]*1*^6,NsubII];(*
     n in 1/m3.*)
54 NsubII1=NSolve[musubBHLHS == musubBHRHS1,NsubII];
55 NsubII2=NsubII/.Flatten[NsubII1];
56 ND1=ND[n,NsubII]/.Flatten[NsubII1];
57 ND2=ND1/.{n->inputFile[[i,3]]*1*^6};
58 NA1=NA[n,NsubII]/.Flatten[NsubII1];
```

```
59 NA2=NA1/.{n->inputFile[[i,3]]*1*^6};
60 compensationGamma1=compensationGamma[n,NsubII]/.Flatten[NsubII1];
61 compensationGamma2=compensationGamma1/.{n->inputFile[[i,3]]*1*^6};
62 AppendTo[outputFile,{inputFile[[i,1]],inputFile[[i,2]],inputFile[[i,3]],
       NsubII2/1*^6,ND2/1*^6,NA2/1*^6,compensationGamma2}];(*In "outputFile",
        the first two rows have already been populated with header
       information.*)
63 ];
64 In[187]:= Export["T:\\oxford_desktop_pc\\tco\\ucl\\lcn\\experiments\\
       mathematica\\mobility\\output_files\\1_hj11_T_mu_n_N_ND_NA_Gamma.csv",
       outputFile]; (*Six columns: first three columns as for input file,
       column 4 = N in 1/cm3, column 5 = ND in 1/cm3, column 6 = Gamma in
       1.*)
65 In[188]:= (*F23*)
66 In[189]:= outputFile={};
67 AppendTo[outputFile,outputFileFirstRow]; (*The first three columns of the
       "outputFile" are (respectively) the three columns of the inputFile.*)
68 AppendTo[outputFile,outputFileSecondRow];
69 In[192]:= inputFile=Import["T:\\oxford_desktop_pc\\tco\\ucl\\lcn\\
       experiments\\mathematica\\mobility\\input_files\\1_hj23_T_mu_n.dat","
       Table"];(*Three columns: column 1 = T in K, column 2 = mu in cm2/Vs,
       column 3 = n in 1/cm3.*)
70 numberOfDataSetsInInputFile=Length[inputFile];
71 In[194]:= m=me*msupASTF23;
72 In[195]:= For[i=1,i<=numberOfDataSetsInInputFile,i++,
73 musubBHLHS=inputFile[[i,2]]*1*^-4;(*mu in m2/Vs.*)
74 musubBHRHS1=musubBHRHS[m,inputFile[[i,1]],inputFile[[i,3]]*1*^6,NsubII];(*
       n in 1/m3.*)
75 NsubII1=NSolve[musubBHLHS == musubBHRHS1,NsubII];
76 NsubII2=NsubII/.Flatten[NsubII1];
77 ND1=ND[n,NsubII]/.Flatten[NsubII1];
78 ND2=ND1/.{n->inputFile[[i,3]]*1*^6};
79 NA1=NA[n,NsubII]/.Flatten[NsubII1];
80 NA2=NA1/.{n->inputFile[[i,3]]*1*^6};
81 compensationGamma1=compensationGamma[n,NsubII]/.Flatten[NsubII1];
82 compensationGamma2=compensationGamma1/.{n->inputFile[[i,3]]*1*^6};
83 AppendTo[outputFile,{inputFile[[i,1]],inputFile[[i,2]],inputFile[[i,3]],
       NsubII2/1*^6,ND2/1*^6,NA2/1*^6,compensationGamma2}];(*In "outputFile",
        the first two rows have already been populated with header
```

```
    information.*)
84  ];
85  In[196]:= Export["T:\\oxford_desktop_pc\\tco\\ucl\\lcn\\experiments\\
    mathematica\\mobility\\output_files\\1_hj23_T_mu_n_N_ND_NA_Gamma.csv",
    outputFile]; (*Six columns: first three columns as for input file,
    column 4 = N in 1/cm3, column 5 = ND in 1/cm3, column 6 = Gamma in
    1.*)
```

● Computer program has concluded ●

Bibliography

Adachi, Hideaki et al. (2012). *Handbook of sputter deposition technology : fundamentals and applications for functional thin films, nano-materials and MEMS [electronic resource]*. 2nd ed. Waltham, MA: William Andrew.

Adler, David, Brian B. Schwartz, and Martin C. Steele, eds. (1985). *Physical Properties of Amorphous Materials*. Boston, MA: Springer US.

Agaiby, Rouzet (Nov. 15, 2018). *Low temperature processing – a key enabler for large area flexible electronics*. Blog, FlexEnable Limited, UK.

Agura, Hideaki et al. (2005). "Low-resistive and transparent AZO films prepared by PLD in magnetic field". In: *Electrical Engineering in Japan* 151.2, pp. 40–45.

Albrecht, Mark C. et al. (2013). "Experimental Design for Engineering Dimensional Analysis". In: *Technometrics* 55.3, pp. 257–270.

Ali, Saleem H. et al. (Mar. 2017). "Mineral supply for sustainable development requires resource governance". In: *Nature* 543.7645, pp. 367–372.

Altman, Naomi and Martin Krzywinski (Mar. 2015). "Points of Significance: Split plot design". In: *Nature Methods* 12.3, pp. 165–166.

Alzoubi, K. et al. (2011). "Bending Fatigue Study of Sputtered ITO on Flexible Substrate". In: *Journal of Display Technology* 7.11, pp. 593–600.

Anderson, G. S., Wm. N. Mayer, and G. K. Wehner (1962). "Sputtering of Dielectrics by High-Frequency Fields". In: *Journal of Applied Physics* 33.10, pp. 2991–2992.

Armaroli, Nicola and Vincenzo Balzani (2007). "The Future of Energy Supply: Challenges and Opportunities". In: *Angewandte Chemie International Edition* 46.1-2, pp. 52–66.

Babbitt, Callie W. et al. (July 2020). "Disassembly-based bill of materials data for consumer electronic products". In: *Scientific Data* 7.1, p. 251.

Barquinha, Pedro et al. (2012). *Transparent Oxide Electronics: From Materials to Devices*. 1st ed. John Wiley & Sons.

Barranco, Angel et al. (2016). "Perspectives on oblique angle deposition of thin films: From fundamentals to devices". In: *Progress in Materials Science* 76, pp. 59–153.

Bellingham, J., W. Phillips, and C. Adkins (1992). "Intrinsic performance limits in transparent conducting oxides". In: *Journal of Materials Science Letters* 11.5, pp. 263–265.

Bisgaard, S. and D. M. Steinberg (1997). "The Design and Analysis of 2^{k-p} Prototype Experiments". In: *Technometrics* 39.1, pp. 52–62.

Bivour, M. et al. (2014). "Silicon heterojunction rear emitter solar cells: Less restrictions on the optoelectrical properties of front side TCOs". In: *Solar Energy Materials and Solar Cells* 122, pp. 120–129.

Blaine, Johs and Jeffrey S. Hale (2008). "Dielectric function representation by B–splines". In: *physica status solidi (a)* 205.4, pp. 715–719.

Boldy, Robyn et al. (2021). "Understanding the impacts of mining on ecosystem services through a systematic review". In: *The Extractive Industries and Society* 8.1, pp. 457–466. ISSN: 2214-790X.

Bouten, P. C. P., P. J. Slikkerveer, and Y. Leterrier (2005). *Mechanics of ITO on Plastic Substrates for Flexible Displays*, pp. 99–120.

Box, G. E. P. and N. R. Draper (1987). *Empirical Model Building and Response Surfaces*. New York, NY: John Wiley & Sons.

Box, G. E. P. and K. B. Wilson (1951). "On the Experimental Attainment of Optimum Conditions". In: *Journal of the Royal Statistical Society, Series B* 13, pp. 1–45.

Box, George E. P., J. Stuart Hunter, and William G. Hunter (2005). *Statistics For Experimenters: Design, Innovation, and Discovery*. Hoboken, New Jersey: John Wiley & Sons.

Boyd, K. J. et al. (1998). "Semiquantitative subplantation model for low energy ion interactions with surfaces. I. Noble gas ion-surface interactions". In: *Journal of Vacuum Science & Technology A* 16.2, pp. 444–454.

Bradley, Donal D. C. and Wei Huang (2017). "A new flexible venue". In: *npj Flexible Electronics* 1.1, p. 3.

Bright, Clark I. (2008). "Review of Transparent Conductive Oxides (TCO)". In: *SVC Bulletin* Fall, pp. 38–45.

Brooks, Harvey (1955). *Theory of the Electrical Properties of Germanium and Silicon*. Ed. by L. Marton. Vol. 7. Advances in Electronics and Electron Physics. Academic Press, pp. 85–182.

Buchholz, D. Bruce, Qing Ma, et al. (2014). "The Structure and Properties of Amorphous Indium Oxide". In: *Chemistry of Materials* 26.18, pp. 5401–5411.

Buchholz, D. Bruce, Li Zeng, et al. (2013). "Differences between amorphous indium oxide thin films". In: *Progress in Natural Science: Materials International* 23.5, pp. 475–480.

Calnan, S. and A.N. Tiwari (2010). "High mobility transparent conducting oxides for thin film solar cells". In: *Thin Solid Films* 518.7, pp. 1839–1849.

Chapman, B. N. (1974). "Thin-film adhesion". In: *Journal of Vacuum Science and Technology* 11.1, pp. 106–113.

Chattopadhyay, D. and H. J. Queisser (Oct. 1981). "Electron scattering by ionized impurities in semiconductors". In: *Rev. Mod. Phys.* 53 (4), pp. 745–768.

Chee, K. W. A. et al. (2018). "Measurement-based optimization and analysis of α-IGZO/Ag/α-IGZO transparent conducting electrodes fabricated using DC magnetron sputter deposition". In: *Ceramics International* 44.17, pp. 20939–20946.

Chopra, K.L., P.D. Paulson, and V. Dutta (2004). "Thin-film solar cells: An overview". In: *Progress in Photovoltaics: Research and Applications* 12.2-3, pp. 69–92.

Cook, Jeffrey (1999). "Angular distribution of sputtered atoms in physical vapor deposition and collimated sputtering". In: *Thin Solid Films* 338.1, pp. 81–87.

Corning Inc. (2017). *Corning Eagle XG Glass Product Information Sheet.*

Coutts, Timothy J., David L. Young, and Xiaonan Li (2000). "Characterization of Transparent Conducting Oxides". In: *MRS Bulletin* 25.8, pp. 58–65.

Cramer, T. et al. (2016). "Radiation-Tolerant Flexible Large-Area Electronics Based on Oxide Semiconductors". In: *Advanced Electronic Materials* 2.7.

Crawford, Gregory P., ed. (2005). *Flexible Flat Panel Displays.* John Wiley and Sons, Ltd.

Cushman, Cody V. et al. (2016). "Eagle XG glass, optical constants from 230 nm to 1690 nm (0.73 eV to 5.39 eV) by spectroscopic ellipsometry". In: *Surface Science Spectra* 23.1, pp. 55–60.

Daillant, Jean and Alain Gibaud, eds. (1999). *X-Ray and Neutron Reflectivity: Principles and Applications*. Berlin Heidelberg: Springer-Verlag.

Davies, Owen L. (1954). *The design and analysis of industrial experiments.* A sequel to the editor's Statistical methods in research and production, published in 1947. London, New York: Published for Imperial Chemical Industries by Oliver and Boyd; Hafner Pub. Co.

De Sousa Meneses, D., M. Malki, and P. Echegut (2006). "Structure and lattice dynamics of binary lead silicate glasses investigated by infrared spectroscopy". In: *Journal of Non-Crystalline Solids* 352.8, pp. 769–776.

Dehuff, N.L. et al. (2005). "Transparent thin-film transistors with zinc indium oxide channel layer". In: *Journal of Applied Physics* 97.6.

Del Castillo, E. (1996). "Multiresponse Optimization Confidence Regions". In: *Journal of Quality Technology* 28.1, pp. 61–70.

Demaray, Richard Ernest, Chandra Deshpandey, and Rajiv Gopal Pethe (2002). "Collimated sputtering of semiconductor and other films". United States Patent No.: 6,362,097.

Depla, D., S. Mahieu, and J.E. Greene (2010). "Chapter 5 - Sputter Deposition Processes". In: *Handbook of Deposition Technologies for Films and Coatings (Third Edition)*. Ed. by Peter M. Martin. Third Edition. Boston: William Andrew Publishing, pp. 253–296.

Derringer, G. and R. Suich (1980). "Simultaneous Optimization of Several Response Variables". In: *Journal of Quality Technology* 12.4, pp. 214–219.

Dhage, Sanjay R. and Amol C. Badgujar (2018). "Transparent conducting Al:ZnO thin films on large area by efficient cylindrical rotating DC magnetron sputtering". In: *Journal of Alloys and Compounds* 763, pp. 504–511.

DisplayBank Co., Ltd (2021). *Transparent Display Technology and Market Forecast.*

Dunn, Kevin G. (2016). *Process Improvement Using Data.* https://learnche.org/pid/.

Edwards, P. P. et al. (2004). "Basic materials physics of transparent conducting oxides". In: *Dalton Trans.* (19), pp. 2995–3002.

Edwards, Peter P. et al. (2008). "Electron Transfer and Electronic Conduction through an Intervening Medium". In: *Angewandte Chemie International Edition* 47.36, pp. 6758–6765.

Eikon, Refinitiv (2021). *International spot price history of Indium (IND-ING-LON, Indium NWE CIF).*

Ellmer, K (2001). "Resistivity of polycrystalline zinc oxide films: current status and physical limit". In: *Journal of Physics D: Applied Physics* 34.21, pp. 3097–3108.

Ellmer, Klaus (2012). "Past achievements and future challenges in the development of optically transparent electrodes". In: *Nature Photonics* 6.12, pp. 809–817.

Ellmer, Klaus and André Bikowski (2016). "Intrinsic and extrinsic doping of ZnO and ZnO alloys". In: *Journal of Physics D: Applied Physics* 49.41, p. 413002.

Exarhos, Gregory J. and Xiao-Dong Zhou (2007). "Discovery-based design of transparent conducting oxide films". In: *Thin Solid Films* 515.18, pp. 7025–7052.

Feldman, D. and Margolis, R. (2019). *Solar Industry Update Q4/2018 Q1/2019 (NREL/PR-6A20-73992)*. USA.

Fischhoff, Baruch (2015a). "The realities of risk-cost-benefit analysis (Review Summary)". In: *Science (New York, N.Y.)* 350.6260, p. 527.

— (2015b). "The realities of risk-cost-benefit analysis (Review)". In: *Science (New York, N.Y.)* 350.6260, aaa6516.

Fortunato, E. et al. (2006). "High mobility amorphous/nanocrystalline indium zinc oxide deposited at room temperature". In: *Thin Solid Films* 502.1. Selected Papers from the 5th International Conference on Coatings on Glass (ICCG5) - Advanced Coatings on Glass and Plastics for Large-Area or High-Volume Products, pp. 104–107.

Fujiwara, Hiroyuki (2007). *Spectroscopic Ellipsometry*. John Wiley and Sons, Ltd.

Fujiwara, Hiroyuki and Michio Kondo (Feb. 2005). "Effects of carrier concentration on the dielectric function of ZnO:Ga and $In_2O_3 : Sn$ studied by spectroscopic ellipsometry: Analysis of free–carrier and band–edge absorption". In: *Phys. Rev. B* 71 (7), p. 075109.

Funabiki, Fuji, Toshio Kamiya, and Hideo Hosono (2012). "Doping effects in amorphous oxides". In: *Journal of the Ceramic Society of Japan* 120.1407, pp. 447–457.

Gerlach, E. and M. Rautenberg (1978). "Ionized impurity scattering in semiconductors". In: *physica status solidi (b)* 86.2, pp. 479–482.

Gessert, T.A. et al. (2011). "Advantages of transparent conducting oxide thin films with controlled permittivity for thin film photovoltaic solar cells". In: *Thin Solid Films* 519.21, pp. 7146–7148.

Gessert, Timothy A. (2010). "Large-Scale Photovoltaic Energy Production from Thin-Film Modules". In: *SVC Bulletin* Fall, pp. 16–21.

Gibaud, A., M. S. Chebil, and T. Beuvier (2013). "X-Ray Reflectivity". In: *Surface Science Techniques*. Ed. by Gianangelo Bracco and Bodil Holst. Berlin, Heidelberg: Springer Berlin Heidelberg, pp. 191–216.

Ginley, David S. and Clark Bright (2000). "Transparent Conducting Oxides". In: *MRS Bulletin* 25.8, pp. 15–18.

Ginley, David S. and David C. Paine, eds. (2010). Springer.

Giri, A. and P. E. Hopkins (2020). "A Review of Experimental and Computational Advances in Thermal Boundary Conductance and Nanoscale Thermal Transport across Solid Interfaces". In: *Advanced Functional Materials* 30.8.

Giri, Narayan C. and M.N. Das (1979). *Design and Analysis of Experiments*. New York, N.Y: Wiley, pp. 53, 159, 264.

Gordon, Roy G. (2000). "Criteria for Choosing Transparent Conductors". In: *MRS Bulletin* 25.8, pp. 52–57.

Gorse, Christopher, David Johnston, and Martin Pritchard (2020). *dimensional analysis*. 2nd ed. Oxford University Press.

Granqvist, C.G. (2014). "Electrochromics for smart windows: Oxide-based thin films and devices". In: *Thin Solid Films* 564, pp. 1–38.

Granqvist, C.G. and A. Hultåker (2002). "Transparent and conducting ITO films: new developments and applications". In: *Thin Solid Films* 411.1. Proceedings of the 2nd International Symposium on Transparent Oxide Thin Films for Electronics and Optics, pp. 1–5.

Granqvist, Claes G. (2007). "Transparent conductors as solar energy materials: A panoramic review". In: *Solar Energy Materials and Solar Cells* 91.17, pp. 1529–1598.

— (2012). "Preparation of Thin Films and Nanostructured Coatings for Clean Tech Applications: A Primer". In: *SVC Bulletin* Fall, pp. 28–45.

Granqvist, Claes-Göran (2008). "Materials for Good Day-Lighting and Clean Air: New Vistas in Electrochromism and Photocatalysis". In: *SVC Bulletin* Spring, pp. 48–53.

Greene, J. E. (2017). "Review Article: Tracing the recorded history of thin-film sputter deposition: From the 1800s to 2017". In: *Journal of Vacuum Science & Technology A* 35.5, p. 05C204.

Grundmann, M. et al. (2005). "Electrical properties of ZnO thin films and optical properties of ZnO-based nanostructures". In: *Superlattices and Microstructures* 38.4. E-MRS 2005 Symposium G: ZnO and Related Materials, pp. 317–328.

Grundmann, Marius et al. (2010). "Transparent semiconducting oxides: materials and devices". In: *physica status solidi (a)* 207.6, pp. 1437–1449.

Haacke, G. (Sept. 1976). "New figure of merit for transparent conductors". In: *Journal of Applied Physics* 47.9, pp. 4086–4089.

Hagiwara, Y., T. Nakada, and A. Kunioka (2001). "Improved J_{sc} in CIGS thin film solar cells using a transparent conducting ZnO:B window layer". In: *Solar Energy Materials and Solar Cells* 67.1, pp. 267–271.

Hall, E. H. (1879). "On a New Action of the Magnet on Electrical Current". In: *Amer. J. Math* 2 (6), pp. 287–292.

Hartnagel, H. et al. (1995). *Semiconducting Transparent Thin Films*. IOP Publishing, Bristol.

Hays, David C. et al. (2017). "Effect of deposition conditions and composition on band offsets in atomic layer deposited HfxSi1-xOy on InGaZnO4". In: *Journal of Vacuum Science & Technology B* 35.1, p. 011206.

Herrington, R. (2021). "Mining our green future". In: *Nature Reviews Materials*.

Herrington, Richard (2013). "Road map to mineral supply". In: *Nature Geoscience* 6.11, pp. 892–894.

Hill, Russell J., Steve Nadel, and Michael Andreasen (2008). "History of Large Area Coatings". In: *SVC Bulletin* Summer, pp. 38–47.

Hillier, J.A. et al. (2020). "When ellipsometry works best: A case study with transparent conductive oxides". In: *ACS Photonics* 7.10, pp. 2692–2702.

Hoffman, D. W. (1985). "A sputtering wind". In: *Journal of Vacuum Science & Technology A* 3.3, pp. 561–566.

Hoffman, R. L., B. J. Norris, and J. F. Wager (2003). "ZnO-based transparent thin-film transistors". In: *Applied Physics Letters* 82.5, pp. 733–735.

Hoffmann, Winfried (2011). "Thin Films in Photovoltaics: Contribution to a Future Mainstream Electricity Provider". In: *SVC Bulletin* Summer, pp. 20–27.

Holman, Zachary C. et al. (2012). "Current Losses at the Front of Silicon Heterojunction Solar Cells". In: *IEEE Journal of Photovoltaics* 2.1, pp. 7–15.

Honda, N. and A. Honda (2011). "Deposition of Inclined Orientation Film Using Collimated Sputtering". In: *IEEE Transactions on Magnetics* 47.10, pp. 2544–2547.

Horiba Jobin Yvon (2006). *Drude Dispersion Model*.

Hosono, H. (June 2017). "Transparent amorphous oxide semiconductors: Materials design, electronic structure, and device applications". In: *75th Annual Device Research Conference*, pp. 1–2.

Hosono, Hideo (2006). "Ionic amorphous oxide semiconductors: Material design, carrier transport, and device application". In: *Journal of Non-Crystalline Solids* 352.9, pp. 851–858.

— (2010a). *Transparent Amorphous Oxide Semiconductors for Flexible Electronics*. Ed. by David S. Ginley and David C. Paine. Springer. Chap. 13, pp. 459–487.

— (2010b). *Transparent Conductors*. Ed. by David S. Ginley and John D. Perkins. Springer. Chap. 1, pp. 1–25.

Hosono, Hideo, Masahiro Yasukawa, and Hiroshi Kawazoe (1996). "Novel oxide amorphous semiconductors: transparent conducting amorphous oxides". In: *Journal of Non-Crystalline Solids* 203, pp. 334–344.

Hu, Shao-Hwa et al. (2020). "Using a Statistical Experimental Design Method to Confirm the Optimization of Al/Al Doped ZnO Double Layers". In: *Journal of Electronic Materials* 49.10, pp. 5667–5673.

Hubbard, Douglas W. (2014). *How to Measure Anything: Finding the Value of Intangibles in Business*. 3rd ed. Wiley.

Hunter, J. Stuart (1987). "Applying Statistics to Solve Chemical Problems". In: *Chemtech* 03, p. 167.

Ide, Keisuke et al. (2019). "Electronic Defects in Amorphous Oxide Semiconductors: A Review". In: *physica status solidi (a)* 216.5, p. 1800372.

Ioffe, A. F. and A. R. Regel (1960). "Non-crystalline, amorphous and liquid electronic semiconductors". In: *Progress in Seminconductors* 4, p. 237.

J. A. Woollam Co. (2014). *CompleteEASE Software Manual*. Lincoln, NE 68508, USA.

— (2017). *CompleteEASE Software Short Course*. Lincoln, NE 68508, USA.

Jain, Himanshu, Peter P. Edwards, and Michael Pepper (2018). "A filter for a deposition process,related methods, and products thereof". United Kingdom Patent Application Filing No.: GB1806124.2, Filing Date: 13–April–2018.

Jasiński, Dominik et al. (2018). "Assessing supply risks for non-fossil mineral resources via multi-criteria decision analysis". In: *Resources Policy* 58. Special Issue on Mining Value Chains, Innovation and Learning, pp. 150–158.

Jelle, Bjørn Petter, Simen Edsjø Kalnæs, and Tao Gao (2015). "Low-emissivity materials for building applications: A state-of-the-art review and future research perspectives". In: *Energy and Buildings* 96, pp. 329–356.

Jellison Jr., G. E. and F. A. Modine (1996). "Parameterization of the optical functions of amorphous materials in the interband region". In: *Applied Physics Letters* 69.3, pp. 371–373.

Jimenez, F., S. D. Ekpe, and S. K. Dew (2006). "Inhomogeneous rarefaction of the process gas in a direct current magnetron sputtering system". In: *Journal of Vacuum Science & Technology A* 24.4, pp. 1530–1534.

Johs, Blaine et al. (1999). "Overview of variable-angle spectroscopic ellipsometry (VASE): II. Advanced applications". In: *Proc. SPIE* 10294, pp. 29–58.

Jun, Min-Chul, Sang-Uk Park, and Jung-Hyuk Koh (2012). "Comparative studies of Al-doped ZnO and Ga-doped ZnO transparent conducting oxide thin films". In: *Nanoscale Research Letters* 7.1, p. 639.

Jun, Seung-Ik et al. (2005). "A statistical parameter study of indium tin oxide thin films deposited by radio-frequency sputtering". In: *Thin Solid Films* 476.1, pp. 59–64.

Jung, Yeon Sik et al. (2003). "Influence of DC magnetron sputtering parameters on the properties of amorphous indium zinc oxide thin film". In: *Thin Solid Films* 445.1, pp. 63–71.

Kamiya, Toshio and Hideo Hosono (Jan. 2010). "Material characteristics and applications of transparent amorphous oxide semiconductors". In: *NPG Asia Mater* 2, pp. 15–22. ISSN: 1884-4049.

Kamiya, Toshio, Kenji Nomura, and Hideo Hosono (2009). "Electronic structure of the amorphous oxide semiconductor a-$InGaZnO_{4-x}$: Tauc–Lorentz optical model and origins of subgap states". In: *Physica Status Solidi (a)* 206.5, pp. 860–867.

— (2010a). "Present status of amorphous In-Ga-Zn-O thin-film transistors". In: *Science and Technology of Advanced Materials* 11.4, p. 044305.

— (2010b). "Subgap states, doping and defect formation energies in amorphous oxide semiconductor a-InGaZnO4 studied by density functional theory". In: *physica status solidi (a)* 207.7, pp. 1698–1703.

— (2013). "4.1: Invited Paper: Electronic Structure, Carrier Transport, Defects and Impurities in Amorphous Oxide Semiconductor". In: *SID Symposium Digest of Technical Papers* 44.1, pp. 11–13.

Khanal, Rabi et al. (2015). "Composition-dependent structural and transport properties of amorphous transparent conducting oxides". In: *Phys. Rev. B* 91 (20), p. 205203.

Khuri, A. I. and J. A. Cornell (1987). *Response Surfaces*. New York, NY: Marcel Dekker.

Kiessig, Von Heinz (1931). "Interferenz von Röntgenstrahlen an dünnen Schichten". In: *Annalen der Physik* 402.7, pp. 769–788.

Kim, Junghwan et al. (2017). "Conversion of an ultra-wide bandgap amorphous oxide insulator to a semiconductor". In: *NPG Asia Materials* 9.3, e359–e359.

Kılıç, Çetin and Alex Zunger (2002). "Origins of Coexistence of Conductivity and Transparency in SnO_2". In: *Physical Review Letters* 88.9, p. 095501.

Kobrinsky, V. et al. (2008). "Tailoring the gas sensing properties of ZnO thin films through oxygen nonstoichiometry". In: *Applied Physics Letters* 93.11, p. 113502.

Körner, Wolfgang, Daniel F. Urban, and Christian Elsässer (2013). "Origin of subgap states in amorphous In-Ga-Zn-O". In: *Journal of Applied Physics* 114.16, p. 163704.

Korshunov, F. P. et al. (Feb. 2000). "On the determination of carrier mobility in compensated GaAs". In: *Inorganic Materials* 36, pp. 100–104.

Kowalski, Scott M. and Kevin J. Potcner (Nov. 2003). "How to Recognize a Split–Plot Experiment". In: *Quality Progress: Journal of the American Society for Quality*, pp. 60–66.

Kumar, Mukesh et al. (2013). "Optimizing amorphous indium zinc oxide film growth for low residual stress and high electrical conductivity". In: *Applied Surface Science* 283, pp. 65–73.

Kurt J. Lesker Company (2010). *Practical Proceess Tips*, pp. 1–4.

— (2012). *PVD75 Thin Film Deposition System Operation Manual*. 1925, Route 51, Jefferson Hills, PA 15025, USA.

Kuznetsov, V. and P. Edwards (2010). "Functional Materials for Sustainable Energy Technologies: Four Case Studies". In: *ChemSusChem* 3.1, pp. 44–58.

Kuznetsov, Vladimir L. et al. (2015). "Electronic transport in highly conducting Si–doped ZnO thin films prepared by pulsed laser deposition". In: *Applied Physics Letters* 107.23, p. 232103.

Lai, S. T. (2000). "The Mott transition as a cause of anomalies on spacecraft". In: *IEEE Transactions on Plasma Science* 28.6, pp. 2097–2102.

Lakeshore Cryotronics Inc. (2020). *8400 Series Hall Effect Measurement Systems*.

Lampert, Carl (2012). "Flexible Electronics: Are we there yet?" In: *SVC Bulletin* Summer, pp. 54–55.

LaPuma, Peter and Martin Zimmermann (2010). *Bruker Good Diffraction Practice Webinar Series*. https://www.bruker-webinars.com.

Leterrier, Y. (2003). "Durability of nanosized oxygen-barrier coatings on polymers". In: *Progress in Materials Science* 48.1, pp. 1–55.

Lifshitz, Y., S. R. Kasi, and J. W. Rabalais (Mar. 1989). "Subplantation model for film growth from hyperthermal species: Application to diamond". In: *Phys. Rev. Lett.* 62 (11), pp. 1290–1293.

Lifshitz, Y., S. R. Kasi, J. W. Rabalais, and W. Eckstein (May 1990). "Subplantation model for film growth from hyperthermal species". In: *Phys. Rev. B* 41 (15), pp. 10468–10480.

Lin, K.-M. et al. (2016). "Spectroscopic ellipsometry study of the optoelectrical properties of In2O3:Sn-ZnO:Al thin films deposited through alternating sputtering". In: *Journal of the Ceramic Society of Japan* 124.5, pp. 528–531.

Lindemuth, Jeffrey (2020). Ed. by Brad C. Dodrill. Lake Shore Cryotronics, Incorporated.

Lindemuth, Jeffrey and Shin-Ichiro Mizuta (2011). "Hall measurements on low-mobility materials and high resistivity materials". In: *Proc. SPIE* 8110, pp. 1–7.

Liu, Yuhao, Matt Pharr, and Giovanni Antonio Salvatore (2017). "Lab-on-Skin: A Review of Flexible and Stretchable Electronics for Wearable Health Monitoring". In: *ACS Nano* 11, pp. 9614–9635.

Look, D. C. et al. (2011). "Self-compensation in semiconductors: The Zn vacancy in Ga-doped ZnO". In: *Phys. Rev. B* 84 (11), p. 115202.

Lundstrom, Mark (2000). *Fundamentals of carrier transport*. Second edition. Cambridge core. Cambridge.

Macco, B. et al. (2014). "High mobility In2O3: H transparent conductive oxides prepared by atomic layer deposition and solid phase crystallization". In: *Physica Status Solidi - Rapid Research Letters* 8.12, pp. 987–990.

Maier, Wilhelm F., Klaus Stöwe, and Simone Sieg (2007). "Combinatorial and High-Throughput Materials Science". In: *Angewandte Chemie International Edition* 46.32, pp. 6016–6067.

Mallick, A., S. Ghosh, and D. Basak (2020). "Highly conducting and transparent low-E window films with high figure of merit values based on RF sputtered Al and In co-doped ZnO". In: *Materials Science in Semiconductor Processing* 119.

Matsubara, K et al. (2002). "Room-temperature deposition of Al-doped ZnO films by oxygen radical-assisted pulsed laser deposition". In: *Thin Solid Films* 422.1, pp. 176–179.

Mattes, Brenton L. (1980). "Growth and Structure of Amorphous and Polycrystalline Thin Films". In: *Polycrystalline and Amorphous Thin Films and Devices*. Ed. by Lawrence L. Kazmerski. Academic Press.

Mattox, D. M. (1965). *Interface formation and the adhesion of deposited thin films*. U.S. Atomic Energy Commission and Sandia Corporation monograph; SC-R-65-852. Albuquerque, New Mexico: Technical Information Division, Sandia Corportion, p. 6.

— (1978). *Thin-film Adhesion and Adhesive Failure - A Perspective*. Ed. by K. L. Mittal. West Conshohocken, PA: ASTM International, pp. 54–62.

Mattox, Donald M. (2004). "Vacuum coating — An Enabling Technology". In: *SVC Bulletin* Summer, pp. 21–24.

— (2010a). *Chapter 6: Vacuum Evaporation and Vacuum Deposition*. Norwich, United States: William Andrew.

— (2010b). *Chapter 7: Physical Sputtering and Sputter Deposition (Sputtering)*. Norwich, United States: William Andrew.

— (2011). "Glass as a Substrate Material". In: *SVC Bulletin* Fall, pp. 28–29.

— (2013). "History of Vacuum Deposition Using Energetic Ions of Condensable Materials". In: *SVC Bulletin* Spring, pp. 36–38.

— (2014). "A short history of *in situ* cleaning in vacuum for Physical Vapor Deposition (PVD)". In: *SVC Bulletin* Fall, pp. 50–53.

— (2015a). "A Short History: Film Deposition by Pulsed Laser Deposition (PLD)". In: *SVC Bulletin* Spring, pp. 38–39.

— (2015b). "A Short History: Magnetron Sputter Deposition". In: *SVC Bulletin* Summer, pp. 42–45.

— (2016). "A short history: Adhesion, interface formation, and stress in PVD coatings". In: *SVC Bulletin* Spring, pp. 32–37.

Messier, R., A. P. Giri, and R. A. Roy (1984). "Revised structure zone model for thin film physical structure". In: *Journal of Vacuum Science & Technology A: Vacuum, Surfaces, and Films* 2.2, pp. 500–503.

Minami, T. et al. (1989). "Influence of substrate and target temperatures on properties of transparent and conductive doped ZnO thin films prepared by r.f. magnetron sputtering". In: *Thin Solid Films* 171.2, pp. 307–311.

Minami, Tadatsugu (2005). "Transparent conducting oxide semiconductors for transparent electrodes". In: *Semiconductor Science and Technology* 20.4, S35–S44.

Minami, Tadatsugu et al. (1986). "Highly Conductive and Transparent Silicon Doped Zinc Oxide Thin Films Prepared by RF Magnetron Sputtering". In: *Japanese Journal of Applied Physics* 25.9A, p. L776.

Montgomery, D.C. (2000). *Design and Analysis of Experiments*. 5th. New York, NY: John Wiley & Sons.

Moon, H. et al. (Aug. 2020). "Machine learning enables completely automatic tuning of a quantum device faster than human experts". In: *Nature Communications* 11.1, p. 4161.

Morales-Masis, M. et al. (2015). "Low-Temperature High-Mobility Amorphous IZO for Silicon Heterojunction Solar Cells". In: *IEEE Journal of Photovoltaics* 5.5, pp. 1340–1347.

Mott, N. F., ed. (1990). *Metal Insulator Transition*. London: Taylor and Francis.

Myers, Raymond H., Douglas C. Montgomery, and Christine M. Anderson-Cook (2011). *Response Surface Methodology: Process and Product Optimization Using Designed Experiments*. Somerset: John Wiley & Sons.

Naghavi, N. et al. (2001). "Systematic study and performance optimization of transparent conducting indium–zinc oxides thin films". In: *Electrochimica Acta* 46.13-14, pp. 2007–2013.

Naghavi, Negar et al. (2000). "Structural and physical characterisation of transparent conducting pulsed laser deposited In_2O_3–ZnO thin films". In: *J. Mater. Chem.* 10 (10), pp. 2315–2319.

Nair, V. N. (1992). "Taguchi's parameter design: a panel discussion". In: *Technometrics* 34.2, pp. 127–161.

Nassar, Joanna M. et al. (2018). "Compliant lightweight non-invasive standalone "Marine Skin" tagging system". In: *npj Flexible Electronics* 2.1, p. 13.

Nolot, E. and A. André (2011). "Systematic combination of X-ray reflectometry and spectroscopic ellipsometry: A powerful technique for reliable in-fab metrology". In: *Thin Solid Films* 519.9, pp. 2782–2786.

Nomura, Kenji, Toshio Kamiya, Hiromichi Ohta, et al. (2004). "Carrier transport in transparent oxide semiconductor with intrinsic structural randomness probed using single-crystalline InGaO3(ZnO)5 films". In: *Applied Physics Letters* 85.11, pp. 1993–1995.

Nomura, Kenji, Toshio Kamiya, Hiroshi Yanagi, et al. (2008). "Subgap states in transparent amorphous oxide semiconductor, In-Ga-Zn-O, observed by bulk sensitive x-ray photoelectron spectroscopy". In: *Applied Physics Letters* 92.20, p. 202117.

Nomura, Kenji, Hiromichi Ohta, Akihiro Takagi, et al. (Nov. 2004). "Room–temperature fabrication of transparent flexible thin–film transistors using amorphous oxide semiconductors". In: *Nature* 432.7016, pp. 488–492.

Nomura, Kenji, Hiromichi Ohta, Kazushige Ueda, et al. (2003). "Thin-Film Transistor Fabricated in Single-Crystalline Transparent Oxide Semiconductor". In: *Science* 300.5623, pp. 1269–1272.

Ohring, Milton (2002). *Chapter 4 - Discharges, Plasmas, and Ion-Surface Interactions*. Ed. by Milton Ohring. Second Edition. San Diego: Academic Press, pp. 145–202.

Ohta, Hiromichi and Hideo Hosono (2004). "Transparent oxide optoelectronics". In: *Materials Today* 7.6, pp. 42–51.

Paine, David C., Hyo-Young Yeom, and Burag Yaglioglu (2005). "Transparent Conducting Oxide Materials and Technology". In: *Flexible Flat Panel Displays*. Ed. by Gregory P. Crawford. John Wiley and Sons, Ltd, pp. 79–98.

Palmer, Andrew C. (2008). *Dimensional Analysis and Intelligent Experimentation*. World Scientific.

Pasquarelli, R.M., D.S. Ginley, and R. O'hayre (2011). "Solution processing of transparent conductors: From flask to film". In: *Chemical Society Reviews* 40.11, pp. 5406–5441.

Pauw, L. J. van der (1958). "A Method of Measuring Specific Resistivity and Hall Effect of Discs of Arbitrary Shapes". In: *Philips Res. Repts* 13 (6), pp. 1–9.

Peelaers, H., E. Kioupakis, and C.G. Van De Walle (2012). "Fundamental limits on optical transparency of transparent conducting oxides: Free-carrier absorption in SnO_2". In: *Applied Physics Letters* 100.1.

Peiponen, K.-E. and E. M. Vartiainen (Oct. 1991). "Kramers-Kronig relations in optical data inversion". In: *Phys. Rev. B* 44 (15), pp. 8301–8303.

Peng, C., T. P. Dhakal, et al. (2014). "Strained Growth of Aluminum-Doped Zinc Oxide on Flexible Glass Substrate and Degradation Studies Under Cyclic Bending Conditions". In: *IEEE Transactions on Device and Materials Reliability* 14.1, pp. 121–126.

Peng, C., M. M. Hamasha, et al. (2013). "Electrical and Optical Degradation Studies on AZO Thin Films Under Cyclic Bending Conditions". In: *IEEE Transactions on Device and Materials Reliability* 13.1, pp. 236–244.

Peng, C.-Y. et al. (2012). "Performance of aluminum-doped zinc oxide thin films under bending fatigue conditions". In: *2012 IEEE Long Island Systems, Applications and Technology Conference, LISAT 2012*. Article no.: 6223196.

Perkins, J.D. et al. (2002). "Discovery and optimization of In-Zn-Sn-O based transparent conductors by combinatorial and pulsed laser deposition ap-

proaches". In: *Conference Record of the IEEE Photovoltaic Specialists Conference*, pp. 1126–1129.

Phillips, C. S. G. and R. J. P. Williams (1965). *Inorganic Chemistry. Volume 1, Principles and Non–Metals*. Oxford University Press, p. 540.

Porch, Adrian et al. (2004). "Electromagnetic absorption in transparent conducting films". In: *Journal of Applied Physics* 95.9, pp. 4734–4737.

Powell, Ronald A. and Stephen M. Rossnagel (1999). *PVD for Microelectronics: Sputter deposition applied to semiconductor manufacturing*. Vol. 26. Thin Films. Elsevier.

Quinto, Dennis. T. (2007). "Twenty-five years of PVD coatings at the cutting edge". In: *SVC Bulletin* Fall, pp. 17–22.

Rashidi, Nazanin et al. (2013). "Highly conducting and optically transparent Si-doped ZnO thin films prepared by spray pyrolysis". In: *Journal of Materials Chemistry C* 1.42, pp. 6960–6969.

Raw materials for a truly green future (2021). "Raw materials for a truly green future". In: *Nature Reviews Materials* 6.6, pp. 455–455.

Rezaei, S.D., S. Shannigrahi, and S. Ramakrishna (2017). "A review of conventional, advanced, and smart glazing technologies and materials for improving indoor environment". In: *Solar Energy Materials and Solar Cells* 159, pp. 26–51.

Robbins, Joshua J. and Colin A. Wolden (2003). "High mobility oxides: Engineered structures to overcome intrinsic performance limitations of transparent conducting oxides". In: *Applied Physics Letters* 83.19, pp. 3933–3935.

Románszki, Loránd, Szilvia Klébert, and Károly Héberger (2020). "Estimating Nanoscale Surface Roughness of Polyethylene Terephthalate Fibers". In: *ACS Omega* 5.7, pp. 3670–3677.

Rose, Aimee and Gregory J Exarhos (1997). "Ellipsometric studies of thermally induced transformation phenomena in oxide films". In: *Thin Solid Films* 308-309, pp. 42–49.

Rossnagel, S. M. (1988). "Gas density reduction effects in magnetrons". In: *Journal of Vacuum Science & Technology A* 6.1, pp. 19–24.

— (1999). "Sputter deposition for semiconductor manufacturing". In: *IBM Journal of Research and Development* 43.1.2, pp. 163–179.

— (2003). "Thin film deposition with physical vapor deposition and related technologies". In: *Journal of Vacuum Science & Technology A* 21.5, S74–S87.

— (1995). "Directional and preferential sputtering-based physical vapor deposition". In: *Thin Solid Films* 263.1, pp. 1–12.

Rowell, Michael W. and Michael D. McGehee (2011). "Transparent electrode requirements for thin film solar cell modules". In: *Energy Environ. Sci.* 4 (1), pp. 131–134.

Ruske, Florian (2012). *Deposition and Properties of TCOs*. Ed. by Wilfried G. J. H. M. van Sark, Lars Korte, and Francesco Roca, pp. 301–330.

Sakurai, Kenji and Atsuo Iida (1992). "Fourier Analysis of Interference Structure in X-Ray Specular Reflection from Thin Films". In: *Japanese Journal of Applied Physics* 31.2A, p. L113.

Schreiber, Frank and Alexander Gerlach (2004). *X-Ray and Neutron Reflectivity for the Investigation of Thin Films: A Short Tutorial*, pp. 1–9.

Shah, A. et al. (1999). "Photovoltaic Technology: The Case for Thin-Film Solar Cells". In: *Science* 285.5428, pp. 692–698.

Shannon, R. D. (Sept. 1976). "Revised effective ionic radii and systematic studies of interatomic distances in halides and chalcogenides". In: *Acta Crystallographica Section A* 32.5, pp. 751–767.

Sheldahl Inc. (Jan. 24, 2020). The Red Book, Static Charge Control Materials. Sheldahl Flexible Technologies, Inc., pp. 69–78.

Shimakawa, K et al. (1998). "Free carrier absorption in highly conducting amorphous oxides". In: *Journal of Non-Crystalline Solids* 227-230, pp. 513–516.

Shyam, Badri et al. (Aug. 2016). "Measurement and Modeling of Short and Medium Range Order in Amorphous Ta2O5 Thin Films". In: *Scientific Reports* 6.1, p. 32170.

Sibin, K.P. et al. (2018). "Environmental stability of transparent and conducting ITO thin films coated on flexible FEP and Kapton® substrates for spacecraft applications". In: *Solar Energy Materials and Solar Cells* 176, pp. 134–141.

Simon, Andrew H. (2012). *Sputter Processing*. Ed. by Krishna Seshan. Third Edition. Oxford: William Andrew Publishing, pp. 55–88.

Simon, Michael (2019). "3 obstacles that folding phones like Samsung's Galaxy Fold and Huawei's Mate X must overcome." In: *PCWorld* 37.4, pp. 10–12.

— (2020a). "Samsung Galaxy Z Fold 2: Killer specs in search of killer purpose." In: *PCWorld* 38.10, pp. 20–23.

— (2020b). "Samsung's new Galaxy Fold Z 2 is vastly improved, but now it needs a purpose." In: *PCWorld* 38.9, pp. 11–13.

Simon, Volker, Bernhard Weigand, and Hassan Gomaa (2017). *Dimensional analysis for engineers*. Cham, Switzerland.

Sinha, S. K. et al. (Aug. 1988). "X-ray and neutron scattering from rough surfaces". In: *Phys. Rev. B* 38 (4), pp. 2297–2311.

Slocombe, Daniel et al. (2012). "The Mott transition and optimal performance of transparent conducting oxides in thin-film solar cells". In: *Energy Environ. Sci.* 5 (1), pp. 5387–5391.

Somekh, R. E. (1984). "The thermalization of energetic atoms during the sputtering process". In: *Journal of Vacuum Science & Technology A* 2.3, pp. 1285–1291.

Sonin, A. A. (2001). *The Physical Basis of Dimensional Analysis*. 2nd ed. https://web.mit.edu/2.25/www/pdf/DA_unified.pdf. Department of Mechanical Engineering, MIT, Cambridge, MA 02139, pp. 1–57.

Sproul, William D. (2008). "The need to understand how the process works". In: *SVC Bulletin* Spring, pp. 28–29.

Statista (2020). *Distribution of In reserves in year* 2009 *by country*.

— (2021). *Distribution of In production in year* 2020 *by country*.

Stierle, Andreas and Elias Vlieg (2012). "Surface-Sensitive X–Ray Diffraction Methods". In: *Modern Diffraction Methods*. Wiley-VCH Verlag GmbH & Co. KGaA, pp. 221–257.

Stillman, G.E. and C.M. Wolfe (1976). "Electrical characterization of epitaxial layers". In: *Thin Solid Films* 31.1, pp. 69–88.

Suzuki, Akio et al. (2002). "Highly conducting transparent indium tin oxide films prepared by pulsed laser deposition". In: *Thin Solid Films* 411.1. Proceedings of the 2nd International Symposium on Transparent Oxide Thin Films for Electronics and Optics, pp. 23–27.

Synowicki, R. A. (2008). "Suppression of backside reflections from transparent substrates". In: *physica status solidi c* 5.5, pp. 1085–1088.

Taguchi, G. and S. Konishi (1987). *Orthogonal Arrays and Linear Graphs*. Dearborn, MI: ASI press.

Talagrand, C. et al. (2015). "Ellipsometry study of process deposition of amorphous Indium Gallium Zinc Oxide sputtered thin films". In: *Thin Solid Films* 590, pp. 134–140.

Taylor, M.P. et al. (2008). "The remarkable thermal stability of amorphous In-Zn-O transparent conductors". In: *Advanced Functional Materials* 18.20.

U.S. Department of Energy Solar Energy Technologies Office (n.d.). *Photovoltaics Innovation Roadmap Request for Information Summary*. USA.

Vai, Alex T. et al. (2014). "The Transition to the Metallic State in Polycrystalline n-type Doped ZnO Thin Films". In: *Zeitschrift für anorganische und allgemeine Chemie* 640.6, pp. 1054–1062.

Vidal, Olivier, Bruno Goffé, and Nicholas Arndt (Nov. 2013). "Metals for a low-carbon society". In: *Nature Geoscience* 6.11, pp. 894–896.

Volinsky, A. A., N. R. Moody, and W. W. Gerberich (2002). "Interfacial toughness measurements for thin films on substrates". In: *Acta Materialia* 50.3, pp. 441–466.

Wager, John F, Douglas A. Keszler, and Rick E Presley (2008). *Transparent electronics*. New York: Springer.

Walker, Geoff (2014). *Part 1: Fundamentals of Projected-Capacitive Touch Technology*. http://www.walkermobile.com/Touch_Technologies_Tutorial_Latest_Version.pdf, slide 81.

Walsh, Aron, Juarez L. F. Da Silva, and Su–Huai Wei (2011). "Multi–component transparent conducting oxides: progress in materials modelling". In: *Journal of Physics: Condensed Matter* 23.33, p. 334210.

Wang, R. et al. (1996). "Nonstoichiometric zinc oxide and indium–doped zinc oxide: Electrical conductivity and ^{111}In–TDPAC studies". In: *Journal of Solid State Chemistry* 122.1, pp. 166–175.

Wasa, Kiyotaka, Makoto Kitabatake, and Hideaki Adachi (2004). *Thin film materials technology : sputtering of compound materials [electronic resource]*. Norwich, NY : Heidelberg: William Andrew Pub. ; Springer.

Weeks, S. P. (1985). "Measurements". In: *Quick reference manual for silicon integrated circuit technology*. Ed. by W. C. Beadle, J. C. C. Tsai, and R. D. Plummer. John Wiley & Sons.

Wehner, G. K. and D. Rosenberg (1960). "Angular Distribution of Sputtered Material". In: *Journal of Applied Physics* 31.1, pp. 177–179.

Wei, Su-Huai (2004). "Overcoming the doping bottleneck in semiconductors". In: *Computational Materials Science* 30.3-4. Theory, modeling and simulation of materials for advanced technologies: Proceedings of the International Conference on Materials for Advanced Technologies (ICMAT 2003) and IUMRS International Conference in Asia (IUMRS-ICA 2003), pp. 337–348.

Weiser, Annika et al. (2015). "Understanding the modes of use and availability of critical metals — An expert-based scenario analysis for the case of indium". In: *Journal of Cleaner Production* 94, pp. 376–393.

Wilson, Gregory M et al. (2020). "The 2020 photovoltaic technologies roadmap". In: *Journal of Physics D: Applied Physics* 53.49, p. 493001.

Wilson, S.R., C.J. Tracy, and Jr. Freeman J.L., eds. (1993). *Handbook of Multilevel Metallization for Integrated Circuits - Materials, Technology, and Applications*. William Andrew Publishing/Noyes, p. 206.

Winters, Harold F. et al. (Apr. 1990). "Energy transfer from rare gases to surfaces: Collisions with gold and platinum in the range 1–4000 eV". In: *Phys. Rev. B* 41 (10), pp. 6240–6256.

Wolfe, C. M., G. E. Stillman, and J. O. Dimmock (1970). "Ionized Impurity Density in n-Type GaAs". In: *Journal of Applied Physics* 41.2, pp. 504–507.

Woollam, John A. et al. (1999). "Overview of variable-angle spectroscopic ellipsometry (VASE): I. Basic theory and typical applications". In: *Proc. SPIE* 10294, pp. 3–28.

Wooten, F (1972). *Optical properties of solids.* New York: Academic Press.

Yasaka, Miho (2010). "X-Ray thin-film measurement techniques: V. X-ray reflectivity measurement". In: *The Rigaku Journal* 26 (2), pp. 1–9.

Yoshinari, Atsushi et al. (2009). "Crystal and electronic band structures of homologous compounds $Zn_kIn_2O_{k+3}$ by Rietveld analysis and first–principle calculation". In: *Materials Research Bulletin* 44.2, pp. 432–436.

Yu, Ki Jun et al. (Sept. 2017). "Inorganic semiconducting materials for flexible and stretchable electronics". In: *npj Flexible Electronics* 1.1, p. 4.

Yu, Kin Man et al. (2012). "Ideal transparent conductors for full spectrum photovoltaics". In: *Journal of Applied Physics* 111.12, p. 123505.

Yu, Xinge, Tobin J. Marks, and Antonio Facchetti (Apr. 2016). "Metal oxides for optoelectronic applications". In: *Nature Materials* 15, pp. 383–396.

Zalm, P. C. (1988). "Quantitative sputtering". In: *Surface and Interface Analysis* 11.1-2, pp. 1–24.

Zardetto, Valerio et al. (2011). "Substrates for flexible electronics: A practical investigation on the electrical, film flexibility, optical, temperature,

and solvent resistance properties". In: *Journal of Polymer Science Part B: Polymer Physics* 49.9, pp. 638–648.

Zervos, Harry (2015). "Vacuum Deposition vs. Printing in the Flexible Electronics Era". In: *SVC Bulletin* Fall, pp. 50–52.

Zweibel, K. (1999). "Issues in thin film PV manufacturing cost reduction". In: *Solar Energy Materials and Solar Cells* 59.1, pp. 1–18.

— (2000). "Thin film PV manufacturing: Materials costs and their optimization". In: *Solar Energy Materials and Solar Cells* 63.4, pp. 375–386.

Zweibel, Ken (1995). "Thin Films: Past, Present, Future". In: *Progress in Photovoltaics: Research and Applications* 3.5, pp. 279–293.